TECHNISCHE UNIVERSITÄT MÜNCHEN
Ingenieurfakultät Bau Geo Umwelt
Professur für Hydromechanik

Experimental Study of the Flow Field Around a Scouring Bridge Pier

Ulrich Peter Jenssen

Vollständiger Abdruck der an der Ingenieurfakultät Bau Geo Umwelt der Technischen Universität München zur Erlangung des akademischen Grades eines

Doktor-Ingenieurs

genehmigten Dissertation.

Vorsitzender: Prof. Dr. sc. techn. D. Straub
Prüfer der Dissertation:

                            1. Prof. Dr.-Ing. M. Manhart
                            2. Prof. Dr. rer. nat. C.J. Kähler
                            3. Prof. Dr.-Ing. O. Link

Die Dissertation wurde am 14.11.2018 bei der Technischen Universität München eingereicht und durch die Ingenieurfakultät Bau Geo Umwelt am 03.05.2019 angenommen.

Abstract

In wall-junction flows, an obstacle interferes with the flow generating a horseshoe vortex, which stretches around this obstacle. Such flow configurations can be found in many Mechanical and Civil Engineering applications, for example, wing-body junction of an aircraft or a bridge pier embedded in a river bed. In the latter case, local scour can occur due to this vortex affecting the structural stability of the bridge.

To study the flow field at a scouring bridge pier, particle image velocimetry experiments were designed and measurements were conducted in the symmetry plane upstream of a cylinder on a flat bed as well as around a scoured cylinder, in the hydraulic laboratory of the Professorship of Hydromechanics at the Technical University of Munich. Three different Reynolds numbers were studied: $Re = 20{,}000$, $39{,}000$, and $78{,}000$, whereas the highest Re was only studied in the flat-bed configuration. The inflow condition was validated to be a fully developed turbulent boundary layer.

The wall-mounted cylinder represented the initial stage of the scour development at which the balance equation of the turbulent kinetic energy (TKE), the time-averaged flow fields, the probability density functions (PDF) of the velocity components, and the wall shear stress distribution were analysed. The distribution of the TKE revealed the c-shape as reported in the literature. At the wall underneath the horseshoe vortex, the streamwise velocity component has a bimodal distribution referring to the *back-flow* and *zero-flow* mode. The agreement of the results with data from of a companion project by Dr. Wolfgang Schanderl, who performed a Large-Eddy Simulation, validated the present experiments. Moreover, the data converged statistically and the third central moment of the velocity PDFs was estimated with an error of less than 5%.

In addition, measurements were conducted around a scoured cylinder to study the influence of the developing scour hole on the flow structures. The geometry of the scour hole was taken from the literature and built as a fixed shape. The c-shaped TKE distribution was observed in the scour hole, too. The similarity between the flow fields in front of the wall-mounted and the scoured cylinder was large and became even more apparent after transforming the Cartesian into a scour-oriented coordinate system. However, differences also occurred as the bimodality of the wall-parallel velocity component was less pronounced and the intensity of the near-wall flow was smaller than in the flat-bed case. As a consequence, the wall shear stress distribution along the scour surface was different, too. Furthermore, a shear layer detaching from the scour edge, which brought additional TKE into the horseshoe vortex system, occurred only in the scoured stage.

Finally, coherent flow structures were identified using the proper orthogonal decomposition. Furthermore, the spatial joint probability density functions of the horseshoe vortex centre showed that the vortex oscillated in both configurations parallel to the bounding wall and to a similar extend.

Kurzfassung

Bei der Umströmung von im Flussbett gegründeten Brückenpfeilern wird ein Hufeisenwirbel erzeugt, der sich um den Pfeiler herum erstreckt und lokalen Kolk entstehen lassen kann, der wiederum die Stabilität der Brücke beeinträchtigt. Eine solche Strömungssituation ist jedoch von interdisziplinärer Bedeutung, da sie auch bei der Verbindung von Rumpf und Tragflächen eines Flugzeugs beobachtet werden kann.

Um das Strömungsfeld an einem auskolkenden Brückenpfeiler zu untersuchen, wurden Particle-Image-Velocimetry Experimente konzipiert und Messungen in der Symmetrieebene vor einem Zylinder auf ebener Platte, sowie um einen ausgekolkten Zylinder, im Hydrauliklabor der Professur für Hydromechanik an der Technischen Universität München durchgeführt. Es wurden drei verschiedene Reynoldszahlen ($Re = 20000$, 39000 und 78000) mit einer voll entwickelten turbulenten Grenzschicht als Einlaufrandbedingung untersucht, wobei die höchste Re nur im ebenen Fall Anwendung fand.

Der Zylinder auf ebener Platte stellte den Ausgangszustand der Kolkentwicklung dar, bei dem die Bilanzgleichung der turbulenten kinetischen Energie (TKE), die zeitlich gemittelten Strömungsfelder, die Wahrscheinlichkeitsdichtefunktionen (PDF) der Geschwindigkeiten und die Wandschubspannungsverteilung analysiert wurden. Die Verteilung der TKE ergab die in der Literatur beschriebene C-Form. An der Wand unter dem Hufeisenwirbel wies die horizontale Geschwindigkeitskomponente eine bimodale Verteilung auf (*back-flow* und *zero-flow mode*). Die Übereinstimmung der Ergebnisse mit denen einer Large-Eddy Simulation, die von Dr. Wolfgang Schanderl durchgeführt wurde, validierte die vorliegenden Experimente und das dritte zentrale Moment der Geschwindigkeits-PDFs wurde mit einem Fehler von weniger als 5% geschätzt.

Ferner, wurden Messungen an einem ausgekolkten Zylinder durchgeführt, um den Einfluss des entstehenden Kolklochs auf die Strömungsstrukturen zu untersuchen. Die Kolkgeometrie wurde der Literatur entnommen und als feste Form eingebaut. Die c-förmige TKE-Verteilung wurde auch im Kolk beobachtet. Die Ähnlichkeit zwischen den Strömungsfeldern im ebenen und im ausgekolkten Zustand war groß und zeigte sich noch deutlicher, nachdem das kartesische in ein kolkorientiertes Koordinatensystem transformiert wurde. Es traten jedoch auch Unterschiede auf: die Bimodalität der wandparallelen Geschwindigkeit war im Kolk weniger ausgeprägt und die Intensität der wandnahen Strömung geringer. Infolgedessen war auch die Wandschubspannungsverteilung entlang der Kolkoberfläche unterschiedlich. Des Weiteren trat im ausgekolkten Zustand eine Scherschicht auf, die sich vom Kolkrand ablöst und zusätzliche TKE in das Hufeisenwirbelsystem einbringt.

Kohärente Strömungsstrukturen wurden mit der Hauptkomponentenanalyse identifiziert und die bivariaten räumlichen Wahrscheinlichkeitsverteilungen des Hufeisenwirbelzentrums bestimmt. Der Wirbel oszillierte in beiden Fällen in ähnlichem Ausmaß parallel zur begrenzenden Oberfläche.

Preface

In my opinion, doing a doctorate is a process that represents much more than aiming just for the academic title "Dr.-Ing.", but opens up many opportunities to grow personally and professionally. My limits did not hesitate to appear more than once during this process, and I am very happy to finish this dissertation as my personal endurance test, which was only possible due to the great support and cooperation of companions.

First of all, I would like to thank you, dear Michael! For your great support while supervising this doctorate, for your helpful advice and trust, and for the deeply digging and precious discussions that brought me always forward and kept me motivated until the end.

I would like to express my gratitude to Prof. Dr. Christian Kähler, and to Prof. Dr. Oscar Link for the interest in this work and for being the second and third referee, respectively, and to Prof. Dr. Daniel Straub for taking over the chairmanship of the committee.

An experimental research would not be possible without the valuable support of the craftsmen in the laboratory. Dear Christian Schmid, Jan Oelze, and Philip Schneider, I thank you very much for your cooperation and for all of your valuable suggestions while designing and manufacturing the experimental set-up with the highest accuracy. I could always rely on your support and your ideas, thank you!

I would like to thank my lovely colleagues for the wonderful time and discussions we shared. Each and everyone of you has contributed to this dissertation in your own way while discussing about PIV, POD, flow structures, chess, and many many other topics! My warmest thanks from the bottom of my heart (in alphabetic order) to: Dr. Alexander McCluskey (keep on fighting!), Dr. Claudia Strobl, Dr. Daniel Quosdorf, Dr. Evelyn Wegner, Dr. Florian Mintgen, Hao Zeng, Julian Brosda, Lukas Unglehrt, Dr. Sheema Kooshapur, Tianshi Sun, Dr. Wolfgang Schanderl, and Dr. Yoshiyuki Sakai.

Thank you to my parents and to my family (in-law) for your support, your love and your belief in me.

Last but not least, I would like to thank you, Johanna, for your understanding, support, motivation, and for being my love, my life, my darling, my wife!

Thank you!

Contents

List of Tables

List of Figures

XV

Nomenclature

Abbreviations

CCD   Charge-Coupled Device

EF   Energy fraction of the POD modes

FFT   Fast Fourier Transform

FOV Field of View

Fr   Froude Number

HGS Hollow Glass Spheres

HV   Horseshoe vortex

IW   Interrogation Window

jPDF Joint Probability Density Function

Nd:YAG Neodymium-doped yttrium aluminum garnet; $Nd : Y_3Al_5O_{12}$

PDF Probability Density Function

PIV   Particle Image Velocimetry

POD Proper Orthogonal Decomposition

Re   Reynolds Number

SNR   Signal-to-Noise Ratio

SSE   Sum of Squares due to Error

TKE Turbulent Kinetic Energy

Greek Letters

δ	Uncertainty of a variable	
δ_{ij}	Kronecker delta	
ϵ	Dissipation rate of turbulent kinematic energy	[m^2/s^3]
η_{K}	Kolmogorov length scale: $\sqrt[4]{\nu^3/\epsilon}$	[m]
κ	von Kármán constant: 0.41	[−]
λ	Eigenvalue	
λ	Laser wavelength	[nm]
λ^*	Friction factor	[−]
ω	Vorticity vector of a velocity field	[1/s]

μ	Dynamic viscosity of fluid	[Ns/m^2]
ν	Kinematic Viscosity of fluid: $\nu = \mu/\rho$	[m^2/s]
Φ^*	Complex conjugate of Φ	
$\Phi_k(\mathbf{x})$	k^{th} basis function of vector field $\mathbf{u}(\mathbf{x}, t)$, spatial POD mode	
ρ	Density of fluid	[kg/m^3]
ρ_{P}	Density of particles	[kg/m^3]
$\tau(\mathbf{X})$	Particle image pattern	[$-$]
$\tau_{\eta_{\mathrm{K}}}$	Kolmogorov time scale: $\sqrt{\nu/\epsilon}$	[s]
τ_{inertial}	Time scale of inertial forces	[s]
τ_{P}	Particle relaxation time	[s]
τ_{viscous}	Time scale of viscous forces	[s]
τ_{w}	Wall shear stress	[N/m^2]
τ_{ij}	Stress tensor of a continuum	[N/m^2]
θ	Shields parameter of sediment	
$\Theta(x)$	Momentum thickness of boundary layer	[m]
θ_{c}	Critical Shields parameter of sediment	
ε	Relative error of a variable: $(u - \langle u \rangle) / \langle u \rangle \cdot 100$	
$\varepsilon_{\mathrm{std}}$	Standard error	
Ω	Spatial domain	
φ	Angle of rotation for the Cartesian coordinate system	
ϱ	Linear correlation coefficient of two random variables	

Mathematical Operators

Δ	Difference	
$\langle \ \rangle$	Temporal Average	
∇	Nabla Operator	
∂	Partial Differential	

Roman Letters

Δt	Time delay between frame A and B	[μs]
$\mathbf{a}$	Acceleration **vector**	[m/s^2]
$\tilde{x}$	Wall-parallel coordinate normalized by the postioin of the horseshoe vortex	[$-$]
A	Cross section of rectangular flume	[m^2]
$a_k(t)$	k^{th} time coefficient of decomposed vector field $\mathbf{u}(\mathbf{x}, t)$, temporal POD coefficient	
B	Constant of log-law: 5.2	[$-$]

b	Width of flume	[m]
C	Temporal correlation function	$[-]$
c_{f}	Friction coefficient	$[-]$
D	Diameter of cylinder	[m]
d_{τ}	Particle image diameter	[m]
D_{a}	Diameter of the lens aperture	[mm]
d_{diff}	Diffraction limit	[m]
d_{P}	Particle diameter	[µm]
d_{s}	Scour depth	[m]
D_h	Hydraulic diameter: $D_{\mathrm{h}} = 4 \cdot R_{\mathrm{h}}$	[m]
d_z	Focal depth	[m]
F	Mapping function of Stereo-PIV calibration	$[-]$
f	Focal length	[mm]
$f_{\#}$	$f-$number, ratio of focal length to aperture diameter	$[-]$
f_{s}	Sampling frequency	[Hz]
f_{v}	Vortex shedding frequency	[Hz]
Fr	Froude number, based on y_0: $\frac{u_{\mathrm{b}}}{\sqrt{g \cdot y_0}}$	$[-]$
Fr_D	Froude number, based on D: $\frac{u_{\mathrm{b}}}{\sqrt{g \cdot D}}$	$[-]$
k	Turbulent kinetic energy	$[\mathrm{m}^2/\mathrm{s}^2]$
K_i	Factors for modelling the local scour depth	[]
L	Entry length	[m]
L_{c}	Characteristic length scale	[m]
M_{n}	n^{th} Central Moment of a velocity component	$[(\mathrm{m/s})^n]$
N	Number of valid samples	
$p(u)$	Probability density function of u	
Q	Flow rate	$[\mathrm{m}^3/\mathrm{s}]$
R	Spatial correlation function	$[-]$
R_{h}	Hydraulic radius: $R_{\mathrm{h}} = \frac{A}{U}$	[m]
Re	Reynolds number, based on D: $\frac{u_{\mathrm{b}} \cdot D}{\nu}$	$[-]$
Re_{h}	Reynolds number, based on hydraulic radius: $Re_{\mathrm{h}} = \frac{u_{\mathrm{b}} \cdot 4R_{\mathrm{h}}}{\nu}$	$[-]$
Re_{P}	Reynolds number, based on particle diameter and shear velocity u_{τ}: $\frac{u_{\tau} \cdot d_{\mathrm{P}}}{\nu}$	$[-]$
Re_{Θ}	Reynolds number, based on momentum thickness: $\frac{u_{\infty} \cdot \Theta}{\nu}$	$[-]$

St Strouhal number: $\frac{f_v \cdot D}{u_b}$ $[-]$

St_k Stokes number: $\frac{\tau_P}{\tau_{\eta_K}}$ $[-]$

T Transformation matrix $[-]$

T_u Turbulence intensity of streamwise velocity component: $\frac{\sqrt{u'^2}}{\langle u \rangle}$ $[-]$

U Wetted perimeter of flume: $U = 2 \cdot y + b$ $[m]$

u', v', w' Velocity fluctuations in $x-$, $y-$ and $z-$ direction $[m/s]$

u, v, w Cartesian velocity vector components in $x-$, $y-$ and $z-$ direction $[m/s]$

u^+ Dimensionless velocity in wall units $[-]$

u_{η_K} Kolmogorov velocity scale: $\sqrt[4]{\nu \epsilon}$ $[m/s]$

u_∞ Free stream velocity $[m/s]$

u_τ Friction velocity $[m/s]$

u_b Bulk velocity: cross-sectional average $u_b = \frac{Q}{A}$ $[m/s]$

u_r, u_n, u_a Scour-oriented vector components in x_r-, x_n- and x_a- direction $[m/s]$

u_s Slip velocity of a particle in a viscous fluid $[m/s]$

x, y, z Cartesian coordinates $[m]$

x_r, x_n, x_a Scour-oriented coordinates $[m]$

y^+ Dimensionless wall distance in wall units $[-]$

y_0 Flow depth $[m]$

1 Introduction

Bridges crossing rivers have always been important for human civilizations and still fascinate, as the design of such adventurous constructions requires a high level of engineering knowledge and craftmanship, and a large amount of money. In the Middle Ages, for example, bridges across wide rivers such as the Danube were unique, and the few existing ones created a bottleneck for salesmen, troops or pilgrims. The Stone Bridge in Regensburg, Germany, is a well-known example for such an important infrastructure. Built in 1135 A.D., this bridge is still in excellent condition more than 870 years later, and an example of outstanding engineering skills. Completed after only 11 years of construction, legends have emerged concerning otherworldly support, since the builder was said to have signed a contract with Satan himself to complete such a solid construction. A more likely explanation for this outstanding achievement, however, is given by Resch & Bösner (1821), who mentioned an international cooperation of experts from all over Europe, which itself was an achievement.

The Stone Bridge crosses the Danube on 16 supporting abutments, the majority of which are embedded in the river bed. To withstand the permanent impact of the flow, ice loads or floods, the bridge piers are reinforced by hydrodynamically favourably shaped elliptical islands that taper towards the front and rear. Therefore, the approaching flow is deflected sideways and passes the piers without developing a downflow that would cause considerable erosion of the river bed.

This example shows that the hazard of scouring around bridge piers has been known for a long time, but this does not imply that all bridges are protected from damage due to scour, and the flow around obstacles, like bridge piers, is not yet fully understood. Investigations on this topic are still required to advance the level of knowledge and to provide new data, in order to derive reliable morphodynamic models that improve the prediction of scour processes (Government of Queensland (AUS), 2013).

1.1 Scour Phenomenon

1.1.1 Types of scour

Scour in a hydrodynamic context refers to the erosion of sediment material, river banks or soil in general, due to the wall shear stress exerted by the flow onto the river bed (Richardson & Davis, 2001). Melville & Coleman (2000) classify this phenomenon according to three different types: (i) *General Scour*, (ii) *Contraction Scour*, and (iii) *Local Scour*.

General Scour The first type of scour is a long-term erosion process of the Thalweg of a river on a geological time scale (Melville & Coleman, 2000). The Grand Canyon of the

Colorado River in Arizona, USA, or alpine gorges like the Partnachklamm near Garmisch-Partenkirchen in Germany, are impressive examples of such ongoing erosion of solid rock by flowing water, formed over millions of years. General scour is constantly developing over time, independent of any human activity; therefore, it is of minor importance for civil engineers, as the time span of road infrastructures is very limited compared to the one of the general scour.

Contraction Scour   The second scour category, however, can be directly related to human intervention in nature. River engineering has long been of interest for human civilizations, such as the Romans, in order to redirect water for irrigation, to develop shipping, or to use hydro power. For such purposes, natural streams have been channelised, narrowing the cross section of a river. Compared to the undisturbed state, the channelised river must discharge the same amount of water. Therefore, the flow velocity accelerates and, subsequently, the shear stress at the river bed and at the banks increases, sediment is eroded and scour due to this contraction occurs.

Local Scour   As the name indicates, this type of scour occurs on a small spatial scale around obstacles in a flow. Due to the local disturbance of the flow, a three dimensional vortex structure develops, amplifies the shear stress on the river bed, and leads to erosion of sediment surrounding that obstacle. A bridge pier, for example, struggles with local scour problems. However, the understanding of this phenomenon can also help to identify buried objects in a marine environment such as unexploded ordnance. On the one hand, the shape of the scour is proportional to the shape of the obstacle causing it. On the other hand, obstacles begin to move or become buried in the first place due to scour (Rennie *et al.*, 2017). Therefore, the analysis of scour geometries in the Baltic Sea, for example, may locate dangerous objects and support their removal.

1.1.2 Effect of flow intensity

Water flowing over a solid surface exerts a certain shear stress. In case of an open channel flow with loose bed material, this shear stress stemming from the velocity gradient is responsible for transporting sand grains when a critical threshold has been exceeded. This critical value depends on the *Shields parameter* θ (Shields, 1936) and on the particle Reynolds number Re_P:

$$\theta = \frac{\tau_w}{(\rho_\mathrm{P} - \rho)g d_\mathrm{P}}, \tag{1.1}$$

$$Re_\mathrm{P} = \frac{u_\tau d_\mathrm{P}}{\nu}. \tag{1.2}$$

The Shields parameter θ refers to the ratio between the wall shear stress of the approaching flow, acting on a grain, and its reduced weight due to buoyancy. Re_P is the relation between the inertia of a particle and the viscosity of the surrounding flow. Figure 1.1 shows a qualitative Shields diagram. For a given type of sediment exposed to a flow, this diagram helps to determine if this sediment is in motion or at rest.
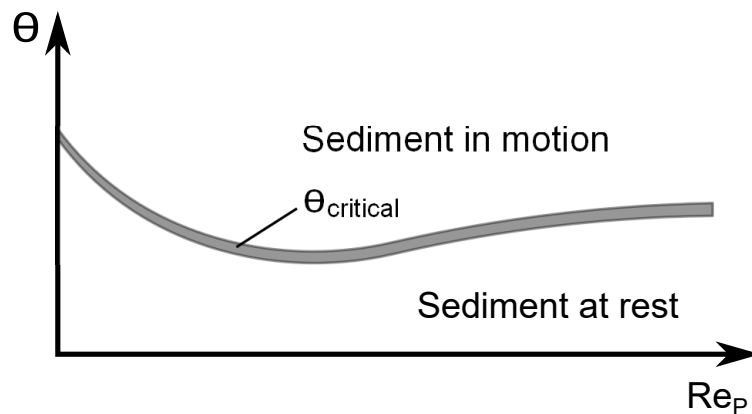
Figure 1.1: Qualitative Shields diagram to determine the critical shear stress for a type of sediment

When $\theta < \theta_c$, the sediment is not in motion and the flow is in a *clear-water* condition, i.e. there is no supply of sediment by the flow from upstream. The scour depth d_s in front of a bridge pier, for example, increases monotonically with the flow intensity until it reaches a maximum value, the so-called *threshold peak* (Melville & Coleman, 2000), when $\theta = \theta_c$.

However, when the shear stress of the undisturbed flow has already exceeded the critical Shields parameter, i.e. bed material is in motion ($\theta > \theta_c$), the flow condition is called *live-bed*, which typically occurs during flood events. The scour depth in a live-bed condition is fluctuating around a live-bed average depth (Chabert & Engeldinger, 1956), due to the constant entrainment of sediment from upstream. The final scour depth is reached when the scouring and the refilling processes are in equilibrium (Melville & Coleman, 2000).

Furthermore, in both flow conditions, clear-water and live-bed, the distribution of the grain size of the sediment influences the scour development, as well. The more the particle diameter varies, the larger the flow intensity has to be, in order to reach the threshold peak in clear-water conditions. The larger grains protect the smaller particles from being entrained by the flow, due to the *armouring effect* of sediment (Ettema, 1976). Moreover, the maximum scour depth is smaller compared to the one with uniform sediment. The impact of armouring becomes less significant with increasing flow intensity as all sediment particles are in motion at some point, and a live-bed peak is reached independently of the sediment gradation (Melville & Coleman, 2000).

1.1.3 Size of bridge pier

When estimating the expected scour depth around a bridge pier or abutment, the so-called *flow shallowness* has to be taken into account. With this ratio of the pile diameter (or length of the abutment) to the flow depth (D/y_0), the foundation can be classified from narrow to wide, and from short to long, respectively. The depth of the expected local scour is proportional to D when the size of the bridge pier is small compared to the flow depth (narrow pier); whereas, the scour depth depends only on the flow depth in case of wide bridge piers (Melville & Chiew, 1999).

1.1.4 Scour model parameters

In order to model the scour and to estimate the expected final scour depth, a whole series of parameters is required, due to the complexity of this process. According to Melville & Sutherland (1988), factors related to flow intensity (K_I) and shallowness (K_y), the sediment grain size (K_d) and the armouring effect due to its gradation (K_σ) have to be taken into account, as well as the shape of the pier (K_s) and its alignment (K_α) with respect to the flow direction. Further, the time scale (K_t) of the scouring process is important (Melville & Chiew, 1999) for clear-water conditions, as the equilibrium scour depth is reached asymptotically over time. The shape of the approaching channel geometry (K_G), however, is negligible for bridge piers and for rectangular channels. Only in case of abutments and irregular cross sections this factor has to be considered (Melville & Coleman, 2000). Laboratory experiments modelling real scour set-ups face the limitation of sediment cohesion, i.e. the sediment size is not arbitrarily small selectable, in order to scale the grain-to-pier-diameter ratio. Ettema *et al.* (1998) showed that the relationship between scour depth and pier diameter is not linear except for a pure geometric similitude between pier diameter, flow configuration and sediment, which is rarely the case. Therefore, this effect should be considered for laboratory set-ups. Melville & Coleman (2000), however, ignore this factor for field applications and suggest the following relation to estimate the final scour depth d_s:

$$\frac{d_s}{D} = K_I K_y K_d K_\sigma K_s K_\alpha K_t K_G. \tag{1.3}$$

The given factors are not discussed in detail here as it is not within the scope and purpose of this dissertation, but specifically quantified by Melville & Coleman (2000). The development of the scour geometry as been studied extensively e.g. Breusers *et al.* (1977); Melville & Chiew (1999); Ettema *et al.* (2006), and consequently many models exist to estimate the equilibrium scour depth for a certain set-up. Nevertheless, the uncertainty of predicting the equilibrium scour depth is still quiet large. For example, Pfleger (2011) measured the development of a scour hole around a circular cylinder under laboratory conditions and observed large uncertainties using existing equations to calculate the equilibrium scour depth. Furthermore, Qi *et al.* (2016) compared the most common scour models and report that some scour models, which provide good results for laboratory set-ups, do not predict correctly the scour depth in field measurements or vice versa. Some of the input parameters influence the outcome significantly, and therefore, the sensitivity of the models with respect to these parameters is also large. The critical velocity, for instance, is one of the parameters, which should be considered carefully as the performance of scour models depends strongly on this value, and on the contrary, the flow depth does not have such strong influence on the scour depth, according to Qi *et al.* (2016).

1.2 Significance of the Topic and Literature Review

Even though flow eroding bridge bearings is a known phenomenon, numerous examples of bridges that failed due to scour exist. Shirhole & Holt (1991) reported that 60% of the 823 bridge failures in the USA since 1950 were due to scour, which agrees with the study of Wardhana & Hadipriono (2003), who reported that 50% of the bridge failures in the USA between 1989 and 2000 were caused by scour. Moreover, a much larger number of bridges (more than 85,000) are considerably vulnerable to scour damage (Sumer & Fredsøe, 2012). Melville & Coleman (2000), too, describe the tremendous damage caused by scour of bridge piers and the subsequent failure: in the USA, two major flood events in 1964 and 1972 caused damages to road facilities of about 100 million USD each. Furthermore, the government of New Zealand spends about 18 million NZD per year for scour-damaged bridges. However, the costs for temporary measures incurring after a failure exceed those of replacing the actual bridge by 50% (Melville & Coleman, 2000). Both, evaluating the vulnerability of an existing bridge, and increasing the resistance to scour eroding the bridge foundation would save a considerable amount of money.

Therefore, to improve the understanding of the physics of local scour is of high economical interest, and consequently, a large number of scientific studies has been conducted, in order to derive models for predicting the expected scour depth more accurately. In New Zealand alone, 37 research projects dealing with bridge scour were funded in the period from 1975 to 1994 (Melville & Coleman, 2000). But this flow phenomenon is highly complex involving a large set of different parameters such as flow intensity, ratio of flow depth to pier diameter, blockage ratio, grain size of the soil, geometry of the pier, and time, and they were used to derive empirical equations for the scour depth prediction (Melville & Coleman, 2000; Qi *et al.*, 2016).

However, the prediction of the scour depth around a bridge pier is a daunting task, due to its high level of complexity. The results of existing scour models around both single piers (Qi *et al.*, 2016) as well as pile groups (Baghbadorani *et al.*, 2017) vary widely. The reason for such large variability lies in the manifold parameters used to build these empirical scour models. For example, the time a scour hole could develop during an experiment is one of the crucial factors. The scour depth approximates typically a logarithmic trend (Link, 2006), and therefore, it is difficult to determine when the final equilibrium state was reached. Pfleger (2011) compared a set of such empirical models with experimental data, and observed a divergence from −40% to +50% after 20h elapsed time. Baghbadorani *et al.* (2017) pointed out that such deviation may come from the different runtime on which the corresponding models are based. By considering the effect of the time span, they could reduce the error in predicting the final scour depth by about 10%; thus, defined a period of validity for the tested models.

Scour around bridge piers has been in focus of scientific studies for almost 80 years (Tison, 1940), and is still one of the basic research topics. Laursen & Toch (1956) studied the model-prototype relation by conducting field measurements of the scour geometry and compared it to a scour occurring around a corresponding model in a laboratory experiment. The predictive accuracy of scour models, the role of the model parameters, and finally, protection measures were extensively discussed by Breusers *et al.* (1977).

Whereas, the flow structure in a developing scour hole was observed by Melville & Raudkivi (1977). Further, design rules for estimating the expected scour depth were suggested and improved by Raudkivi & Ettema (1983); Melville & Sutherland (1988); Melville & Chiew (1999).

Conducting a Large-Eddy simulation (LES), Kirkil *et al.* (2005) investigated the influence of the turbulence of the approaching flow on the vortex dynamics around a scoured cylinder based on experimental bathymetric data. They found several coherent vortex structures that strongly vary depending on the angle of rotation around the cylinder caused by high pressure fluctuations and turbulent kinetic energy levels. Ettema *et al.* (2006) found that the ratio d_s/D decreases when the diameter of the cylinder increases, and they related the equilibrium scour depth in front of a cylinder to the vorticity in its wake. According to Ettema *et al.* (2006), the scaling of the cylinder diameter, the grain size of the sediment, and the flow depth interfere with each other and disrupt the similitude of different experiments or prototypes. Therefore, they introduced a correction factor to overcome these scaling difficulties.

Roulund *et al.* (2005) simulated experimentally and numerically the time development of a scour geometry in live-bed conditions and observed a matching trend of the temporal evolution of the topology; however, the scour depth differed up to 15% upstream the cylinder. According to Roulund *et al.* (2005), the Reynolds number, based on the cylinder diameter, has a major impact on the vortex structure inside the scour hole. Further, they measured the wall shear stress distribution using a hot-film device and found the largest amplification in the region of 45° to 70° at the side of the cylinder, which agrees with Link (2006); Link *et al.* (2008), who observed the initiation of the scour process in this region.

The approaching flow leads to a downflow in front of the cylinder (see section 3.1.1). The influence of this downward directed flow for the scour development was studied by Dey *et al.* (2008), and they found that under similar flow conditions, the scour depth decreases when a cylinder is submerged rather than protruding from the water. This result may seem intuitive, but emphasizes the importance of the flow-depth-to-cylinder-diameter ratio on the one hand, and on the other hand, the role of the boundary layer thickness with respect to the diameter of the cylinder.

Experimental investigations of the flow field inside the scour hole developed around a vertical cylinder were commonly conducted using intrusive devices such as hot wire anemometers (Melville & Raudkivi, 1977) or acoustic Doppler velocimeters (ADV) (Dey & Raikar, 2007), and the flow is distorted by the presence of the measurement device itself. In other studies, the experimental set-up was also simplified by a quasi three-dimensional approach: a half sided scour geometry was glued to the transparent side wall of a channel to be able to observe the flow inside the scour hole perpendicularly from the side (Unger & Hager, 2007) or to measure the flow structure by ADV (Afzalimehr *et al.*, 2018).

1.3 Contribution of this Study

The mentioned studies mainly aimed to derive or to improve existing scour models, or intended to provide design rules for practical applications, in order to protect single bridge piers or abutments from scour. Moreover, the focus of recent scour studies has shifted as the

flow around pile groups or in-line piers is investigated instead (Baghbadorani *et al.*, 2017; Keshavarzi *et al.*, 2018; Quezada *et al.*, 2018). Anyway, the existing experimental scour research lacks of data that show fluctuating flow structures like Reynolds stresses, as well as the distribution, production and dissipation of turbulent kinetic energy. Furthermore, a non-intrusive and fully three dimensional approach with high spatial resolution is required to study the coherent flow structures of the vortex system.

This project is continuing the work of Pfleger (2011), who recorded the naturally developed scour geometry around a cylindrical pier for the flow case $Re = 36,000$, based on the set-up of Dargahi (1989). Pfleger (2011) measured the velocity along three axes (0°, 30°, and 60°) with respect to the approaching flow direction using the laser Doppler velocimetry (LDV). Therefore, a hollow glass cylinder had to be intruded into the water body by approximately 0.04m, in order to let the laser beams enter the flow. By traversing the probe head to each measurement point separately, and adjusting its orientation to record all three components of the velocity vector at a wall distance of 0.004m, the spatial resolution was comparatively coarse, and the effort following this strategy was tremendously high.

The aim of this research project is to provide experimental data for both flow in front of a wall-mounted cylinder, i.e. flat-bed case, and for the flow around a scoured cylinder, i.e. inside a scour hole. Furthermore, the dependency of the flow field with varying Reynolds number (Re) based on the cylinder diameter is one of the key issues this dissertation intends to investigate. Therefore, three different flow cases within the intermediate range $Re = 20,000$, 39,000, and 78,000 are studied in the flat-bed case, whereas the flow around a scoured cylinder is measured for $Re = 20,000$ and 39,000.

In order to observe the flow field with high spatial resolution using a non-intrusive measurement device, the particle image velocimetry (PIV) in the mono and in the stereo set-up is applied. And to the author's knowledge, this is the first approach providing PIV data using a stereoscopic set-up in a fully three dimensional scour hole. Unger (2006), however, applied Mono-PIV and reduced the set-up to a semicircular cylinder. Additionally, the focus of Unger (2006) was on large-scale observations; thus, he recorded approximately one vector per 10mm². The data provided by this dissertation fill the gap between the numerical studies comprehensively simulating the flow around a scoured cylinder, and the limited, mostly intrusive, experimental observations.

1.4 Outline

In this chapter the phenomenon of scour was highlighted generally, before the significance of studying the scour phenomenon around bridge piers has been expounded. The further outline of this dissertation is structured as follows: the characteristics of fluids and the governing equations describing a turbulent flow are discussed next, before the focus shifts to the flow physics around wall-mounted obstacles. The principle of the applied measurement technique, the experimental set-up, and the measurement validation are explained, and finally, the obtained results are presented and concluded.

2 Turbulent Flows

This chapter deals with the basic concepts of turbulent flows in open channels. Further, the mathematical notation used in this dissertation is introduced, and the analysed flow statistics are explained.

2.1 Characteristics of Fluids

Real fluids can either be *Newtonian*[1] or *non-Newtonian*, and were often simplified as being *ideal* in the past. Ideal fluids are of hypothetical character, as they show no viscous stresses, which is a sufficient approximation to describe the motion of waves, for instance (Schlichting & Gersten, 2006).

The assumption of ideal fluids fails at the latest when rigid bodies or walls come into play. Considering the flow of a fluid along an infinite plate driven by an external force (such as gravity or pressure gradient). The fluid would stick to the body's surface due to adhesion, but still keeps flowing driven by the external force. Consequently, a velocity gradient occurs in the fluid, which entails both internal and external shear forces. Inner friction is called *viscosity*, which is a characteristic material quantity like the density of a fluid. Moreover, the friction from the fluid to a body is also known as *wall shear stress*, and defined as:

$$\tau_{\mathrm{w}} = \mu \frac{\partial u}{\partial y}\bigg|_{y=0}. \tag{2.1}$$

Normalizing the wall shear stress by the density of the fluid and by the reference velocity of the flow, it is alternatively referred to as the friction coefficient c_{f}:

$$c_{\mathrm{f}} = \frac{\tau_{\mathrm{w}}}{\frac{\rho}{2} \cdot u_{\mathrm{ref}}^2}. \tag{2.2}$$

This description is dated back on Newton saying that friction is linearly proportional to the velocity gradient in wall-normal direction times the dynamic viscosity of the fluid μ. Further, the resistance of Newtonian fluids with respect to external forces is small. Whereas, non-Newtonian fluids show considerable resistance to external forces, and require some time to react. Asphalt or human blood can be named representatively for such fluids, and are studied in rheology (Truckenbrodt, 1987).

Newtonian fluids such as water or air are of major interest for practical applications in

---

[1]Sir Isaac Newton (⋆1643, †1727)

fluid mechanics. Therefore, the term *fluid* stands synonymously for a Newtonian fluid from here on.

2.2 Turbulent Flows

2.2.1 General aspects

The flow of a fluid can either be *laminar* or *turbulent*. According to Schlichting & Gersten (2006), a laminar flow can be described as "layers" moving with different velocities with no significant exchange of mass, momentum, energy or temperature apart from the Brownian[2] motion. Turbulence is simply the opposite of this state, while being irregular in space and time with fluctuating motions on a large range of scales, amplified mixing, and dissipation of kinetic energy; thus, turbulent flows are of chaotic behaviour, which is complicated to predict. This fundamental classification of flow states can be dated back on Osborne Reynolds[3] who conducted 1883 a pipe flow experiment that demonstrated the transition from laminar to turbulent flow with increasing flow velocity (Schlichting & Gersten, 2006).

Basically, a (turbulent) flow is a non-linear mechanical system with a large number of degrees of freedom (Monin & Yaglom, 2007). Therefore, the description of the turbulent motion of a fluid is generally of statistical rather than deterministic nature (Pope, 2013). Furthermore, statistical attempts require a large number of samples to achieve sufficient validity.

A fluid represents a continuous media and can be considered as the accumulation of infinitesimal volumes. The forces acting on such fluid volumes occur due to: (i) the inertia caused by the mass / density ρ of the fluid; (ii) the friction, which is proportional to the viscosity μ; (iii) pressure and (iv) gravity (Schlichting & Gersten, 2006). Reynolds (1883) found that the ratio of inertia to friction forces, acting in the fluid, can be applied to quantify the similarity of flow configurations, and to distinguish between a laminar and a turbulent behaviour of the flow. This ratio is, therefore, known as the *Reynolds number* (see eq. 2.3).

The inertial forces are responsible for introducing mixing and disturbances, i.e. generation of turbulence; whereas, viscous forces (friction) damp such perturbations (Monin & Yaglom, 2007). The inertial force per fluid volume is equal to $\rho Du/Dt$. The term $\frac{D}{Dt}$ stands for the material derivative, which reduces to $\rho u \partial u/\partial x$ for steady state flows.

The friction is responsible for the momentum transport between two neighbouring fluid elements (Oertel *et al.*, 2015), which is defined by the shear stress acting on the surface of an infinitesimal fluid volume. The net shear force per fluid volume is described by the divergence of the stress tensor τ_{ij}; thus, a fluid volume that moves in $x-$direction observes a net shear force $\partial\tau/\partial y\,\mathrm{d}x\mathrm{d}y\mathrm{d}z$, which leads to the expression of the friction force per volume $\partial\tau/\partial y$ and by applying eq. 2.1 to $\mu\partial^2 u/\partial y^2$, i.e. the friction force per volume is dependent on the

---

[2]Robert Brown (⋆1773, †1858)
[3](⋆1865, †1911)

velocity gradient tangential to the surface of the fluid volume.

$$Re = \frac{\text{inertial forces}}{\text{viscous forces}} \propto \frac{\rho u \partial u / \partial x}{\mu \partial^2 u / \partial y^2} \propto \frac{\rho u^2 / L_\text{c}}{\mu u / L_\text{c}^2} = \frac{u L_\text{c}}{\nu} \tag{2.3}$$

The time scales of the inertial force is $\tau_\text{inertial} = L_\text{c}/u$, whereas the viscous time scale is $\tau_\text{viscous} = L_\text{c}^2/\nu$. According to the Reynolds number, considering the ratio of the forces due to inertia and friction, the time scales can be related likewise: $Re = \tau_\text{viscous}/\tau_\text{inertia}$, which leads to the same expression as eq. 2.3. This perspective concerning the time scales, however, clarifies the meaning and interpretation of the Reynolds number: in case of turbulent flows, the inertial exceed the viscous forces. Furthermore, the time scale of the turbulence production is smaller than the one of damping processes due to viscosity, which means that turbulence is faster produced than dissipated and, therefore, the value of Re is large for turbulent flows in comparison with laminar flows, and vice versa.

Turbulent energy is introduced on large spatial scales (e.g. diameter of an obstacle in the flow) and, consequently, the initial source disturbing the fluid represents the largest scale of instabilities in the flow. This energy, however, is dissipated on the smallest scales. Therefore, a transfer of energy between these scales is required. The introduced instabilities (e.g. large eddies) break up into smaller ones, which in turn decay to eddies of even smaller size and so on. This process is known as the *Richardson cascade*[4] describing the transfer of energy from large unstable eddies to the smallest possible scale, where the energy is irreversibly dissipated into heat by viscosity. This cascade can be subdivided into three regions with decreasing size of scales: production - energy transfer - dissipation.

The ability of inertial forces actuating turbulent motion decays "downstairs" the cascade until it reaches an equilibrium state with the damping viscous forces. As a consequence, the Reynolds number of the cascading flow structures decreases with each breakup and has to equal one at a certain scale (at least theoretically). Kolmogorov[5] found the following relations between the kinematic viscosity $\nu = \mu/\rho$ and the dissipation ϵ to describe the smallest length, time and velocity scales occurring in a turbulent flow until equilibrium is reached (Pope, 2013), for which it holds true that $Re = 1$:

$$\eta_\text{K} = \left(\frac{\nu^3}{\epsilon}\right)^{\frac{1}{4}}, \tag{2.4}$$

$$\tau_{\eta_\text{K}} = \sqrt{\frac{\nu}{\epsilon}}, \tag{2.5}$$

$$u_{\eta_\text{K}} = (\nu \epsilon)^{\frac{1}{4}}. \tag{2.6}$$

The dissipation takes place on the smallest scales and is, therefore, difficult to be directly measured (Tanaka & Eaton, 2007). However, for designing an experiment or a numerical simulation it might be useful to know the dissipation rate in advance (e.g. to choose appropriate tracer particles or interrogation window size, see chapter 4). To overcome this conflict, the dissipation can be estimated presumably using the characteristic *macro*

---

[4]Lewis Fry Richardson (⋆1881, †1953)
[5]Andrey Nikolaevich Kolmogorov (⋆1903, †1987)

scales of velocity and length: $\epsilon \propto \frac{u^3}{L_c}$. With growing knowledge of the investigated flow configuration, this first rough estimation has to be updated by measured data (see section 2.3).

2.2.2 Continuity equation

The conservation of mass, or continuity equation, for fluids is defined as (Kundu & Cohen, 2004):

$$\frac{\partial \rho}{\partial t} + \nabla (\rho \mathbf{u}) = 0, \tag{2.7}$$

and describes the balance of the change in density (ρ) and the change in volume for a fluid element; $\mathbf{u} = (u, v, w)^T$ represents the velocity vector. According to the *Boussinesq*[6] *approximation*, the density and other physical properties[7] of water are "constant" (Kundu & Cohen, 2004). Water is, therefore, considered to be *incompressible*, as the rate of change in density is small with respect to the velocity gradients. Therefore, eq. 2.7 simplifies to:

$$\nabla \mathbf{u} = 0,$$
$$\frac{\partial u}{\partial x} + \frac{\partial v}{\partial y} + \frac{\partial w}{\partial z} = 0, \tag{2.8}$$

and is also knowns as the *divergence* of the velocity vector.

2.2.3 Equations of motion

The motion of an infinitesimal volume of any continuum is described according to Newton's law of motion. Hereby, the acceleration of a fluid element is related to the body forces (e.g. gravity) and surface forces (e.g. friction) that act on an element (Pope, 2013), which is known as the momentum or *Cauchy*[8] equations:

$$\rho \frac{Du_i}{Dt} = \rho g_i + \frac{\partial \tau_{ij}}{\partial x_j}, \tag{2.9}$$

with τ_{ij} representing the stress tensor, which describes the deformation of a fluid (or continuum) element by the so-called *constitutive equation* (Kundu & Cohen, 2004):

$$\tau_{ij} = \underbrace{-p_{\text{th}} \delta_{ij}}_{\text{static}} + \underbrace{\sigma_{ij}}_{\text{dynamic}} . \tag{2.10}$$

---

[6]Joseph Valentin Boussinesq (⋆1842, †1929)
[7]Such as the dynamic viscosity μ, the specific heat at constant pressure and the thermal conductivity
[8]Augustin-Louis Cauchy (⋆1789, †1857)

The first term of the stress tensor (static part) is the thermodynamic pressure p_{th} of the fluid multiplied with the Kronecker[9] delta, as it is *isotropic*, i.e. only normal stresses are relevant, they are independent of the orientation of the fluid element. The second part σ_{ij} is related to the motion of the fluid, thus, to the velocity gradients. Further, the dynamic part is the *deviatoric stress tensor* and *non-isotropic*. It consists of a symmetric and an antisymmetric part: the first one describes the strain rate tensor, whereas, the latter stands for the rotation without deformation. For incompressible fluids, p_{th} can be substituted by the mean pressure p; thus, eq. 2.10 simplifies to (Kundu & Cohen, 2004):

$$\tau_{ij} = -p\delta_{ij} + \mu \left(\frac{\partial u_i}{\partial x_j} + \frac{\partial u_j}{\partial x_i} \right). \tag{2.11}$$

2.2.4 Navier-Stokes equations

By inserting eq. 2.11 in eq. 2.9, and by taking the conservation law of mass (eq. 2.8) into account, the motion of an incompressible fluid obeys the so-called *Navier-Stokes*[10] *equations*:

$$\underbrace{\rho \frac{\partial u_i}{\partial t}}_{\text{local derivative}} + \underbrace{\rho u_j \frac{\partial u_i}{\partial x_j}}_{\text{convective derivative}} = \underbrace{-\frac{\partial p}{\partial x_i}}_{\text{pressure term}} - \underbrace{\rho g_i}_{\text{gravity}} + \underbrace{\mu \frac{\partial^2 u_i}{\partial x_j^2}}_{\text{viscous term}}. \tag{2.12}$$

2.2.5 Reynolds averaged Navier-Stokes equations (RANS)

Reynolds (1895) introduced the decomposition of a turbulent quantity into a fluctuating (denoted by $'$) and a (time-)averaged part (denoted by $\langle \cdot \rangle$):

$$u(x,t) = u(x,t)' + \langle u(x,t) \rangle. \tag{2.13}$$

With this decomposition, the continuity equation (eq. 2.8) yields:

$$\frac{\partial u'}{\partial x} + \frac{\partial v'}{\partial y} + \frac{\partial w'}{\partial z} = 0, \tag{2.14}$$

$$\frac{\partial \langle u \rangle}{\partial x} + \frac{\partial \langle v \rangle}{\partial y} + \frac{\partial \langle w \rangle}{\partial z} = 0, \tag{2.15}$$

and applied to eq. 2.12 the *Reynolds (averaged Navier-Stokes) equations (RANS)* are ob-

---

[9]Leopold Kronecker (⋆1823, †1891)
[10]Claude Louis Marie Henri Navier (⋆1785, †1836)
   Sir George Gabriel Stokes (⋆1819, †1903)

tained:

$$\rho \frac{\partial \langle u_i \rangle}{\partial t} + \rho \langle u_j \rangle \frac{\partial \langle u_i \rangle}{\partial x_j} = -\frac{\partial \langle p \rangle}{\partial x_i} - \rho g_i + \mu \frac{\partial^2 \langle u_i \rangle}{\partial x_j^2} - \rho \frac{\partial \langle u_i' u_j' \rangle}{\partial x_j}. \tag{2.16}$$

Reynolds stress tensor The last term of eq. 2.16 appears due to the decomposition (see eq. 2.13) of the non-linear convective part $\rho u_j \partial u_i / \partial x_j$ in eq. 2.12. This *additional* stress term is called *Reynolds stress tensor* (see eq. 2.17), and consists of the normal stresses σ_{ii} (in principle diagonal) and the shear stresses τ_{ij} (remaining entries) acting on a fluid element due to the turbulent motion.

$$\rho \langle u_i' u_j' \rangle = \rho \begin{bmatrix} \langle u'u' \rangle & \langle u'v' \rangle & \langle u'w' \rangle \\ \langle v'u' \rangle & \langle v'v' \rangle & \langle v'w' \rangle \\ \langle w'u' \rangle & \langle w'v' \rangle & \langle w'w' \rangle \end{bmatrix} \tag{2.17}$$

Alternatively, the trace of the Reynolds stress tensor describes the *"mean kinetic energy per unit mass in the fluctuating velocity field"* (Pope, 2013, p. 88), thus, the *turbulent kinetic energy (TKE)*:

$$k = \frac{1}{2} \left(\langle u_i' u_i' \rangle \right) = \frac{1}{2} \left(\langle u'u' \rangle + \langle v'v' \rangle + \langle w'w' \rangle \right). \tag{2.18}$$

As already mentioned in section 2.2.1, turbulent motions are preferably described by statistical methods. Considering the decomposition according to Reynolds (cf. eq. 2.13), and the stress tensor in eq. 2.17, the entries can be rewritten as:

$$\langle u_i' u_j' \rangle = \frac{1}{n} \sum \left(u_i - \langle u_i \rangle \right) \left(u_j - \langle u_j \rangle \right), \tag{2.19}$$

which is the covariance of two random variables u_i and u_j in case of $i \neq j$, and the variance of u_i for $i = j$. Furthermore, by applying the Reynolds decomposition to the constitutive equation of an incompressible fluid (see eq. 2.11), the total stress tensor in the RANS-framework reads:

$$\tau_{ij} = -p\delta_{ij}\mu \left(\frac{\partial \langle u_i \rangle}{\partial x_j} + \frac{\partial \langle u_j \rangle}{\partial x_i} \right) - \rho \langle u_i' u_j' \rangle. \tag{2.20}$$

In turbulent flows, the contribution of the Reynolds stresses predominates the one of viscous stresses, and therefore, the latter can be assumed to be negligible in free shear flows. However, in the case of wall bounded flows, e.g. in an open channel, the viscous stresses prevail in a proximity range up to approximately 15 wall units (see section 2.4.1) depending on the Reynolds number (Pope, 2013).

Closure problem In order to determine the temporal averaged fields for the velocity and the pressure, eq. 2.16 and eq. 2.15 can be applied; that means a set of four equations containing the four unknowns $\langle \mathbf{u} \rangle$ and $\langle p \rangle$. Additionally, the Reynolds stress tensor represents a set of unknowns, too. Thus, the Reynolds equations are *unclosed*, and additional information have to be collected. Therefore, a balance equation for the TKE is required and introduced in section 2.3. However, by doing so, other unknowns such as velocity-pressure correlations appear, and consequently, reveal a closure problem. This issue is treated by applying turbulence models to describe these additional correlations (Schlichting & Gersten, 2006).

2.3 Budget of Turbulent Kinetic Energy

Section 2.2.1 introduced the concept of producing and damping contributors, as well as the energy transfer in turbulent flows. Hence, the turbulent kinetic energy k of a velocity field is produced, transported, and dissipated, and all contributors of the following equations (Pope, 2013) balance each other; thus, the total sum equals to zero:

$$0 = \underbrace{C}_{\text{convection}} + \underbrace{\nabla T}_{\text{diffusion}} + \underbrace{P}_{\text{production}} - \underbrace{\epsilon}_{\text{dissipation}} , \tag{2.21}$$

$$\text{with} \quad C = -\frac{\partial k}{\partial t} - \langle u_i \rangle \frac{\partial k}{\partial x_i}, \tag{2.22}$$

$$T = \underbrace{-\frac{1}{2}\langle u_i' u_j' u_j' \rangle}_{\text{turbulent fluctuations}} \underbrace{-\frac{1}{\rho}\langle u_i' p' \rangle}_{\text{pressure transport}} \underbrace{+2\nu\langle u_j' s_{ij} \rangle}_{\text{viscous diffusion}} , \tag{2.23}$$

$$P = -\langle u_i' u_j' \rangle \frac{\partial \langle u_i \rangle}{\partial x_j}, \tag{2.24}$$

$$\epsilon = 2\nu\langle s_{ij} s_{ij} \rangle, \tag{2.25}$$

$$\text{and} \quad s_{ij} = \frac{1}{2}\left(\frac{\partial u_i'}{\partial x_j} + \frac{\partial u_j'}{\partial x_i}\right). \tag{2.26}$$

The first term on the right hand side of eq. 2.21 stands for the time-averaged *convection* of k, thus, the mean substantial derivative. Therefore, the local derivative $\partial/\partial t$ in eq. 2.22 vanishes as the convection is time-invariant for steady-state flows.

T represents the transport of k in space due to turbulent and pressure fluctuations, as well as by viscous diffusion. The first term in eq. 2.23 contains triple velocity correlations, and refers to the time-averaged transport of Reynolds normal stresses $u_j' u_j'$ by u_i'. The second term refers to the transport of TKE by pressure fluctuations (or pressure-velocity correlations), and the last term stands for the diffusion of TKE due to viscosity. All three terms together are summed up as the *diffusion* of TKE.

When the *production* of the TKE in eq. 2.24 is positive, *turbulent* kinetic energy is generated from the *mean* kinetic energy; and vice versa for negative values of P.

The *dissipation* rate ϵ (see eq. 2.25) is positive semi-definite, and represents the transformation of TKE into internal energy (i.e. heat) due to viscosity acting on the smallest

scales of the flow. Consequently, a high spatial resolution is required, in order to measure experimentally the fluctuating rate-of-strain tensor s_{ij}. The strain rate tensor in eq. 2.26 consists of the spatial gradient of the velocity fluctuations, which are usually small compared to the mean velocity. However, this is not the case for the corresponding gradients, as $\partial u_i'/\partial x_j \gg \partial \langle u_i \rangle/\partial x_j$, which is a characteristic feature of turbulent flows (Rotta, 2010).

2.4 Longitudinal Flow Along a Plate

2.4.1 Boundary layer theory

The interaction of the flow with an adjacent wall introduces turbulence, and has to be considered in many fluid dynamical applications. Ludwig Prandtl[11] extensively studied this interaction, and coined the term *boundary layer* for the region in a flow, which is located close to an adjacent solid surface. Therefore, a wall-bounded flow is distinguished by two main regions: the inner and the outer region.

The outer region has a certain free stream velocity and the fluid can be approximated by nearly inviscid behaviour (Schlichting & Gersten, 2006), whereas, the flow velocity is zero directly at the wall (no-slip) due to the viscosity of the fluid. Here, a thin layer develops along the solid surface. Therefore, a velocity profile connecting the inviscid outer region with the no-slip wall has to develop: the boundary layer. Within this layer, viscous effects have to be taken into account, and it can either appear to be laminar or turbulent.

The presence of a solid wall parallel to the main flow direction decelerates the fluid due to its viscosity, which in turn exerts a shear stress to the wall (cf. section 2.1). In order to describe the viscous effects within the boundary layer, the velocity and length scales are respectively expressed as:

$$u_\tau = \sqrt{\frac{\tau_\mathrm{w}}{\rho}}, \tag{2.27}$$

$$\text{and} \quad \delta_\nu = \nu\sqrt{\frac{\rho}{\tau_\mathrm{w}}} = \frac{\nu}{u_\tau}. \tag{2.28}$$

The Reynolds number based on these scales is equal to one (Pope, 2013). For characterising and comparing boundary layers of different flow configurations, the mentioned scales in eq. 2.27 and eq. 2.28 are used to normalize the flow variables such as the wall distance:

$$y^+ = \frac{y}{\delta_\nu} = \frac{yu_\tau}{\nu}, \tag{2.29}$$

---

[11]($\star$1875, $\dagger$1953)

and the time-averaged velocity:

$$u^+ = \frac{\langle u \rangle}{u_\tau}. \tag{2.30}$$

These dimensionless scales (length y^+ and velocity u^+) are the so-called *wall units*, and describe the behaviour of a wall-bounded velocity profile as explained in the remaining chapter.

2.4.2 The log law

As mentioned in section 2.4.1, the boundary layer is the link between the no-slip condition at the surface of a solid wall, and the bulk velocity of the outer region; the mean profile of the boundary layer can be described by (Pope, 2013):

$$\langle u \rangle = u_\tau f\left(\frac{y}{\delta}, Re_\tau\right). \tag{2.31}$$

with Re_τ as the friction Reynolds number δ/δ_ν and $f(\cdot)$ as a non-dimensional function. Eq. 2.31 is of universal character as fully developed turbulent wall-bounded flows are similar to each other by revealing this ubiquitous mean profile. By differentiating eq. 2.31, dynamic quantities such as viscous stresses or TKE production can be obtained:

$$\frac{d\langle u \rangle}{dy} = \frac{u_\tau}{y}\Phi\left(\frac{y}{\delta_\nu}, \frac{y}{\delta}\right). \tag{2.32}$$

By inserting eq. 2.29 and eq. 2.30 into eq. 2.32, the dimensionless differential equation can be obtained:

$$\frac{d\langle u^+ \rangle}{dy^+} = \frac{1}{y^+}\Phi\left(y^+\right). \tag{2.33}$$

The viscosity included in the function $\Phi\left(y/\delta_\nu\right)$ is negligible for large values of y^+. Thus, for $y_0/y \ll 1$ and $y^+ \gg 1$ the function Φ takes the constant value $\Phi(y^+) = 1/\kappa$, and the time-averaged velocity gradient in this region becomes:

$$\frac{\partial u^+}{\partial y^+} = \frac{1}{\kappa y^+}. \tag{2.34}$$

Finally, the integration of eq. 2.34 leads to the expression for the universal *log law* derived in 1930 by Theodore von Kármán[12]:

$$\int \frac{\partial u^+}{\partial y^+} dy^+ = u^+ = \frac{1}{\kappa}ln\left(y^+\right) + B, \tag{2.35}$$

---

[12] (⋆1881, †1963)

with B as the integration constant, and κ refers to the von Kármán constant. According to Pope (2013), in open channel flows these parameters are usually considered as $\kappa \approx 0.41$ and $B \approx 5.2$ with an uncertainty of $\pm 5\%$, respectively.

2.4.3 The wall regions

Turbulent boundary layers can basically be subdivided into three regions (Pope, 2013): viscous sublayer (for $y^+ < 5$), buffer layer (for $5 < y^+ < 30$), and log-law region (for $y^+ > 30$). Figure 2.1 shows the alignment of these regions within a turbulent boundary layer using a semi-logarithmic scale; thus, the linear relation of the velocity and the wall distance in the viscous sublayer ($u^+ = y^+$) appears as a curve (dotted line). Further, the straight dashed line of the velocity profile in the log-law region refers to the logarithmic relation of eq. 2.35. The transition between the linear viscous and the turbulent logarithmic layer is empirically described by the buffer layer.
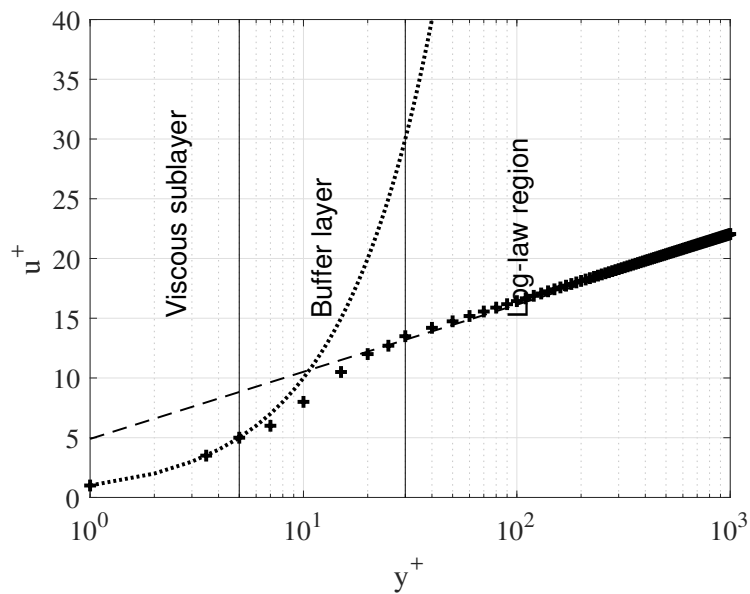
Figure 2.1: Wall regions of an exemplary turbulent boundary layer (black crosses)

3 Wall-junction Flows

Local scour, as introduced in chapter 1, occurs due to the local interference of the flow by a wall-mounted obstacle. Examples for such a wall-junction flow are bridge piers embedded in a river bed, aircraft-wing joints, pillars supporting wind turbines on the ground, or flow around turbine blades. A simplification of such flow configurations would be a cylindrical pier on a flat plate, and therefore, the flow around a vertical cylinder has been intensely studied, and will be summarized in the following chapter as a background for the flow inside a scour hole.

3.1 Wall-mounted cylinder

3.1.1 Flow in the symmetry plane in front of a cylinder

The flow approaching a vertical cylinder is sketched in the symmetry plane as side view in Figure 3.1 a). The $x-$axis is oriented in streamwise direction, the $y-$axis in wall-normal, and the $z-$axis in transverse direction, further, the coordinate system is located in the centre of the cylinder at the level of the bottom plate. The turbulent boundary layer approaches the cylinder and decelerates, therefore, the pressure increases in streamwise direction, i.e. adverse pressure gradient ($\frac{\partial p}{\partial x} > 0$). At the flow facing side of the cylinder, the flow splits up: the very top part is redirected upwards forming the surface roller and a bow wave, whereas the remaining upper part of the flow is directed towards the bottom of the channel. This *downflow* transports high momentum fluid while forming a boundary layer along the surface of the cylinder. This downwash impinges at the bottom wall, i.e. decelerates in vertical direction and, therefore, separates from the cylinder. The downflow is deflected at the bottom plate in all directions forming an upstream directed wall-parallel jet (e.g. Dargahi (1989); Devenport & Simpson (1990); Martinuzzi & Tropea (1993)). This jet exerts high wall shear stress in this region (Dargahi, 1989) as a consequence to the high acceleration inducing a large velocity gradient $\partial u/\partial y$. In the same manner a jet is pointing towards the cylinder, too, and generating a small-scale vortex while meeting the downflow from above in the corner of the cylinder-wall-junction.

The upstream directed jet meets the approaching boundary layer and blocks the parts of the incoming flow close to the wall forming a recirculation zone. Due to the adverse pressure gradient, the flow destabilizes and reveals increased levels of turbulence intensity (Simpson *et al.*, 1981). The part of the approaching velocity profile above that recirculation zone separates from the wall, and is dragged by the strong downflow to form the main vortex that is bending around the cylinder like a horseshoe (see dashed line in Figure 3.1 b); thus, called *horseshoe vortex* (HV) (e.g. Hjorth (1975); Baker (1979, 1980)).

a: Side view
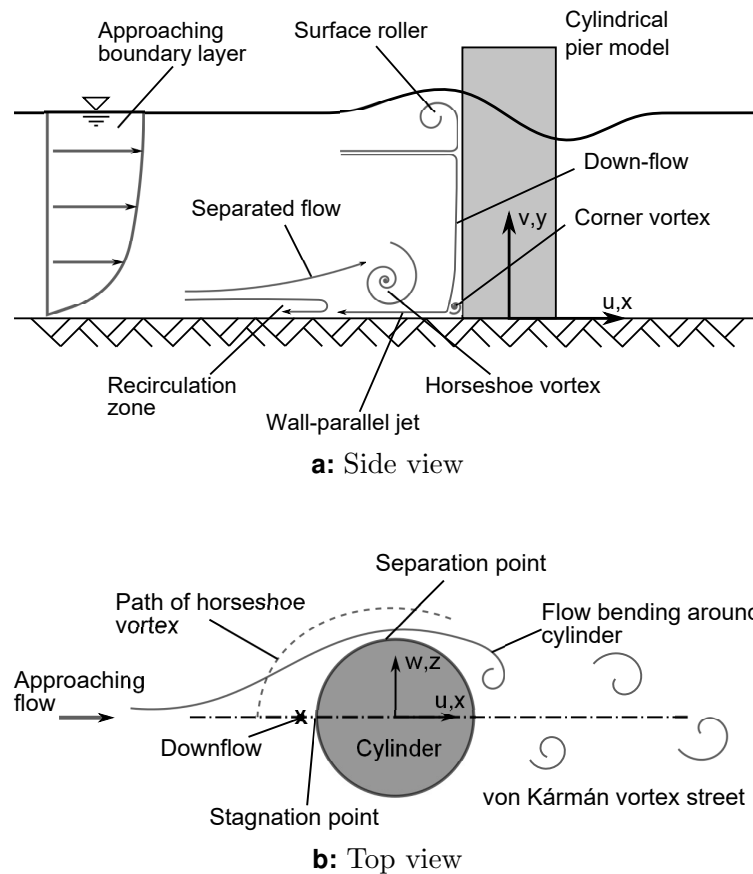
b: Top view

Figure 3.1: Sketch of flow around a vertical cylinder: a) side view; b) top view dash-dotted line indicates the symmetry plane based on Sumer & Fredsøe (2012).

3.1.2 Horseshoe vortex

According to Sumer & Fredsøe (2012), the formation of the horseshoe vortex is triggered when the approaching boundary layer has a sufficient thickness δ, and an adverse pressure gradient in front of the cylinder forces this boundary layer to detach. Such a boundary layer follows a logarithmic shape (see section 2.4) revealing a gradient of streamwise velocity in vertical direction $(\partial u(y)/\partial y)$ causing the downflow, which in turn drives the horseshoe vortex.

The horseshoe vortex oscillates horizontally in streamwise direction and the wall-parallel jet reveals a bimodal characteristic. Devenport & Simpson (1990) measured the probability density functions (PDF) of the horizontal component of the velocity vector in the jet underneath the horseshoe vortex, and found two major flow modes: the *back-flow* and the *zero-flow* mode. Kirkil *et al.* (2008); Kirkil & Constantinescu (2010) confirmed these oscillations and observed such bimodal behaviour of the horseshoe vortex around a scoured cylinder as well.

In Figure 3.2, a bimodal process is sketched as an example, and reveals both a strong event with negative mean velocity (back-flow) and a second event with zero mean (zero-flow). The overall mean value of the whole process is somewhere in the middle of these two modes, and is of minor importance and not as likely to occur as the two dominant
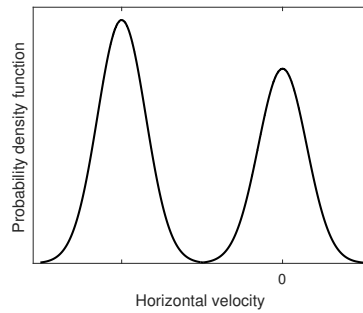
Figure 3.2: Sketch of bimodal probability density function of the horizontal velocity component

modes.

During the back-flow mode, the wall-parallel jet is directed upstream exerting amplified shear stress to the wall and driving the horseshoe vortex. In the zero-flow mode the jet detaches from the bottom plate indicated by an increased vertical velocity (Escauriaza & Sotiropoulos, 2011) pushing the HV towards the cylinder. These oscillations entail highly fluctuating velocities in the region of movement of the HV, and subsequently, high levels of turbulent kinetic energy (TKE) are generated, which follow a c-shaped spatial distribution that has been consistently observed by Paik *et al.* (2007); Escauriaza & Sotiropoulos (2011); Kirkil & Constantinescu (2015); Apsilidis *et al.* (2015); Schanderl & Manhart (2016).

Schanderl & Manhart (2016) studied the influence of the approaching boundary layer on the horseshoe vortex by comparing a fully turbulent boundary layer and a time-averaged logarithmic profile (both $\delta/D = 1.5$) with a block profile ($\delta/D = 0.2$): in their results, the block-profile, i.e. thin boundary layer thickness compared to the obstacle diameter, reveals a large velocity gradient directly at the wall ($y < \delta$), but nearly a zero-gradient for $y > \delta$. Therefore, the horseshoe vortex cannot develop due to the suppressed downflow and boundary layer separation. Consequently, the turbulence structure and the wall shear stress distribution differ from the results with a thick boundary layer. The flow in front of a cylinder with steady logarithmic inflow profile shows a similar structure as the one with a turbulent boundary layer. However, the lack of turbulent fluctuations results in a premature separation of the approaching flow; thus, to a qualitatively wrong estimation of the wall shear stress distribution.

The findings of Schanderl & Manhart (2016) allow the conclusion that the turbulence structure, as well as the shape of the inflow profile is of major importance for representing the horseshoe vortex correctly. Therefore, the approaching flow conditions are studied first in this dissertation, before the flow around a wall-mounted and around a scoured cylinder is tackled, respectively.

3.2 Flow around a cylinder and the induced vortex shedding

The incoming flow passes the cylinder sideways left or right forming a boundary layer along the perimeter of the cylinder when following a streamline outside the symmetry plane. De-

pending on the Reynolds number of the flow, this boundary layer separates at some point from the cylinder surface (see Figure 3.1b), caused by the instability of the wake region; vortices are shedding alternately as a consequence and are evolving a *von Kármán vortex street*. The wide range of $300 < Re < 3 \cdot 10^5$ is characterized by a turbulent wake region and a laminar boundary layer attached to the cylinder surface, and is called the *subcritical* flow regime (Sumer & Fredsøe, 2006).

In this regime, the force lifting the cylinder in transverse direction is zero in average due to the symmetric behaviour of the laminar boundary layer. The mean drag force, summing up the drag due to the shape of the obstacle and the friction caused by the surface roughness, remains nearly constant, and goes in hand with the vortex shedding behaviour that is constant, too, in the subcritical range. The *Strouhal number*[1] (see eq. 3.1) describes this process as the product of the vortex shedding frequency f_v and the characteristic time scale of the flow D/u_b taking usually a value of 0.2. Therefore, the lift and the drag force both show a periodical trend alternating around zero or around a certain mean, respectively.

$$St = \frac{f_v \cdot D}{u_b} \tag{3.1}$$

However, when the Re exceeds the upper limit of the subcritical range, the boundary layer becomes turbulent, too, from the point of separation on towards the stagnation point in front of the cylinder resulting in an asymmetric separation process: on one side of the cylinder the boundary layer is turbulent, whereas, on the opposite side it remains laminar. This state is called the critical flow regime (Sumer & Fredsøe, 2006), and the turbulent and laminar characteristic of the boundary layer can occasionally change sides. Due to this asymmetry, the mean lift force is no longer zero experiencing a sudden increase in norm while omitting oscillations.

When shifting from the subcritical to the supercritical flow regime, the separation points (S_1 and S_1') move downstream as qualitatively sketched in Figure 3.3; thus, the boundary layer is attached to the cylinder for a longer time. The drag force breaks down abruptly as a result, which is known as the *drag crisis* (Sumer & Fredsøe, 2006). This effect is directly related to the change of pressure distribution at the cylinder surface: before the boundary layer separates from the body, the pressure along the surface is negative, and remains at a constant (negative) level after the detachment; owing to the delayed separation (change from S_1 to S_2), the pressure along the surface becomes more negative (i.e. increased suction at the surface). However, after the boundary layer separated from the body in the supercritical state, the pressure level between S_2 and S_2' is less negative compared to the subcritical regime (Achenbach, 1968). Therefore, the width of the wake (proportional to $\overline{S_i S_i'}$) decreases, and simultaneously induces a higher vortex shedding frequency, thus, Strouhal number.

The flow passing laterally the cylinder is important for the formation of the scour, as Roulund *et al.* (2005) identified the largest amplification of wall shear stress at approximately $54°$ with respect to the stagnation point P in Figure 3.3. Furthermore, Pfleger (2011) observed the initiation of the scour process in that region.

---

[1]Vincent Strouhal ($\star$1850, $\dagger$1922)
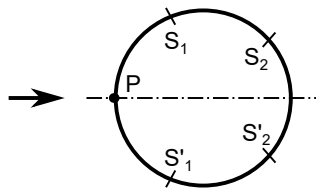
Figure 3.3: Change of separation point depending on flow regime. Arrow indicates direction of flow, dash-dotted line the symmetry plane

4 Particle Image Velocimetry

The measurement technique applied here is the *particle image velocimetry* (PIV), which is based on the measurement of flow velocities using particles and image processing tools. Therefore, it is also described as a *non-intrusive*, *indirect*, and *whole field* technique: the flow is not disturbed by any device; the velocities of the particles are measured in place of the flow; and the image processing provides instantaneous data for a whole region at the same time. Adrian (1984) and Pickering & Halliwell (1984) recognised the significance of particle images for experimental fluid mechanics, and PIV has developed to the state-of-the-art in this field over the last thirty years.

As the capability of the devices, such as computer processing power, storage volumes, and camera resolution, just to mention a few, is growing exponentially, the overall field of application for PIV is multifaceted and certainly not finite. The spectrum of usage varies from the basic planar up to the time-resolved volumetric PIV, and for a comprehensive overview of PIV, see Adrian (1984), Adrian & Westerweel (2011), and Raffel *et al.* (2007). To provide a background for this dissertation, the principle of the planar PIV set-up with one camera (Mono) is briefly described, before the key components as seeding particles, laser, optical devices, and the image processing techniques are introduced. Finally, the set-up employing two cameras (Stereo) together with calibration techniques are presented in this chapter.

4.1 Principle of Planar PIV

Figure 4.1 shows the main components of a planar monoscopic PIV set-up capable of recording a flow field in a two dimensional (2D) plane and evaluating two components of the velocity vector (2C). *Seeding particles* are added to the fluid fulfilling the requirement to follow the flow; thus, the particle velocity stands representatively for the one of the fluid. These particles are illuminated by a quasi-2D *light sheet* generated from a coherent monochromatic pulsed laser beam, which passes a cylindrical-planar lens. The particles scatter the laser light that is recorded by a *CCD-camera*. In the 2D-2C application, this camera is mounted perpendicularly to the light sheet to avoid aberration errors such as astigmatism. The recorded image pairs (frame A and B) are evaluated by cross-correlation, in order to gain a displacement vector field (Keane & Adrian, 1992).
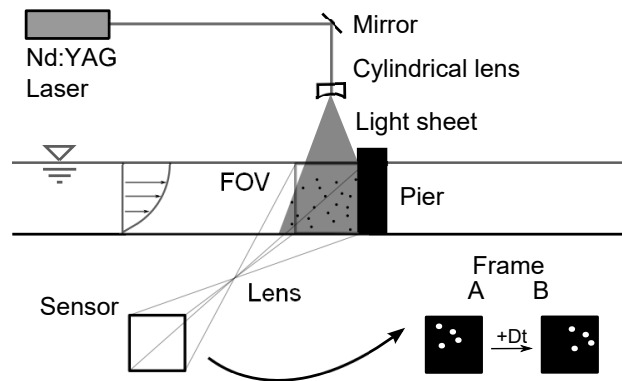
Figure 4.1: Principle of 2D-2C particle image velocimetry

4.2 Seeding Particles

One of the key issues of a successful PIV measurement is the selection of the tracer particles visualizing the velocity of the flow field. A trade-off is made in every experiment while choosing appropriate seeding particles trying to fulfil contrary requirements. On the one hand, the particles should be as small as possible to follow the fluid motions accurately, i.e. no damping of small velocity scales by high inertia, moreover, the properties of the fluid must not be changed by the tracer. On the other hand, particles should have a high scattering behaviour of the laser light; thus, should be as large as possible to allow high quality particle images. Ideally, the density of the seeding material is close to the one of the fluid, the shape of the tracer particles is spherical to provide particle images independent of their rotation and to keep the centre of mass in the central point of the particle image (Adrian & Westerweel, 2011).

In practice, there exist many types of seeding with different characteristics and diameters, ranging from one or even less microns up to several hundred microns depending on the set-up (Melling, 1997). Wind tunnel applications often use oil droplets, smoke, soap bubbles, or micro-balloons, whereas polymer particles, hollow glass spheres (HGS), or hydrogen bubbles are commonly used in water. For measuring the flow dynamics in combustion engines or flames, however, chemically inert solid particles are applied, e.g. aluminium oxide (Al_2O_3). Furthermore, special types of seeding can be found, like fluorescent or metallic-coated particles.

4.2.1 Tracking behaviour

Considering a spherical particle suspended in a turbulent flow, four main forces can be identified: gravitation, lift force, drag force, and the force due to inertia. But, no exact analytical equation exists to calculate the forces acting on a particle (Adrian & Westerweel, 2011), especially when the particle Reynolds number (e.g. eq. 1.2) becomes large. However, the particles' behaviour of following the flow can be assessed by two assumptions: firstly, the diameter of the particle is small compared to the smallest length scale of the flow, which is the Kolmogorov length scale, see eq. 2.4. Consequently, the flow field or acceleration is constant over the cross-section of the particle; and secondly, the flow around the particle is a creeping Stokes flow.

With these assumptions the slip velocity vector $\mathbf{u_s}$ can be determined as follows (Raffel *et al.*, 2007):

$$\mathbf{u_s} = d_P^2 \frac{(\rho_P - \rho)}{18\mu} \mathbf{a}. \tag{4.1}$$

With $\mathbf{a}$ as the acceleration vector, d_P and ρ_P as the particle diameter and density, respectively, ρ stands for the fluid density and μ for its dynamic viscosity. Again, a conflict occurs as the slip velocity has to be kept small, in order to observe high fidelity of particles following the flow. However, a certain velocity lag is necessary to apply a drag force from the fluid that brings the particles into motion.

To quantify if particles are following the flow, the Stokes-number St_k, eq. 4.3, can be taken into account (Raffel *et al.*, 2007; Rapp, 2009). It describes the ratio between the particle response time suspended in a viscous fluid, the so-called relaxation time τ_P (see eq. 4.2) and the smallest time scale of the flow (see eq. 2.5). In other words, St_k gives an answer for the question: how long does it take the particle to follow sudden changes in the fluid motion? Figure 4.2 illustrates this simple question. The above mentioned forces lead to a small difference between a hypothetical fluid element moving along a streamline of the flow and a suspended particle that only approximates this motion. Thus, there might be a certain deviation from the particle motion and the one of the fluid. This error in approximation can be ignored if $St_k \ll 1$.

$$\tau_P = \frac{d_P^2}{18\nu} \frac{\rho_P}{\rho} \tag{4.2}$$

$$St_k = \frac{\tau_P}{\tau_{\eta_K}} \tag{4.3}$$
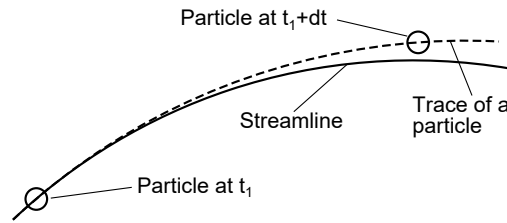
Figure 4.2: Tracer particle following the motion of the fluid

4.2.2 Light scattering behaviour

The particles are illuminated by the light sheet. Subsequently, they scatter the incoming light in all directions, which is recorded by the camera. The theory of the scattering of coherent light was described by Lorenz and Mie[1] as a solution for Maxwell's[2] equations (van de Hulst, 1957). The characteristic scattering behaviour known as *Mie scattering* is formed by several

---

[1]Ludvig Valentin Lorenz ($\star$1829, $\dagger$1891)
   Gustav Adolf Feodor Wilhelm Ludwig Mie ($\star$1868, $\dagger$1957)
[2]James Clerk Maxwell ($\star$1831, $\dagger$1879)

parameters such as diameter, type, shape, and refractive index of the particles in relation to the one of the fluid, furthermore, wavelength and polarization of the incoming coherent light (Raffel *et al.*, 2007; Adrian & Westerweel, 2011). The intensity of the scattered light differs depending on the angle of observation. Consequently, there is *forward* scattering when the angle of observation is larger than 90°, and *backward* scattering when the angle of observation is less than 90° with respect to the incident light. In the centre of the sketch in Figure 4.3, an illuminated particle is located. The light intensity in the forward scattering exceeds generally the one of the backward scattering or at a 90°-scattering-angle by several orders of magnitude (Adrian & Westerweel, 2011).

In the Mono-PIV set-up one camera is used. To avoid image distortion, the angle of observation is 90°, and therefore, the camera arrangement is given (see red dash-dotted line). In the Stereo-PIV approach, however, two cameras are used (see section 4.6), and therefore, the arrangement of both cameras needs to be considered, in order to record the scattered light of the particles in a favourable angle. As the intensity of the scattered light in the forward scattering is stronger than the backward scattering, it is recommended to arrange the cameras in such a way (see dark grey area) to run the experiments with reduced laser energy, for example.

However, due to constructional constraints in the Stereo-PIV set-up of this study, the observation angle was 45° and 315° (see blue dash-dotted lines) for both cameras, respectively. From the Mie scattering appears that this arrangement is in the backward scattering (see light grey area), which can be disadvantageous as the recorded light intensity might be low. To overcome this effect, the energy of the laser beam can be increased, which in turn can cause other unfavourable effects such as increased surface reflections at the walls of the test facility, for instance. These considerations refer to the scattering behaviour of one single particle. In the case of high seeding density of the flow, a multiscattering effect can occur. The recorded light stems not only from direct illumination, but also from re-scattering of the scattered light of neighbouring particles, which can lead to inhomogeneous intensities of the particle images (Raffel *et al.*, 2007).
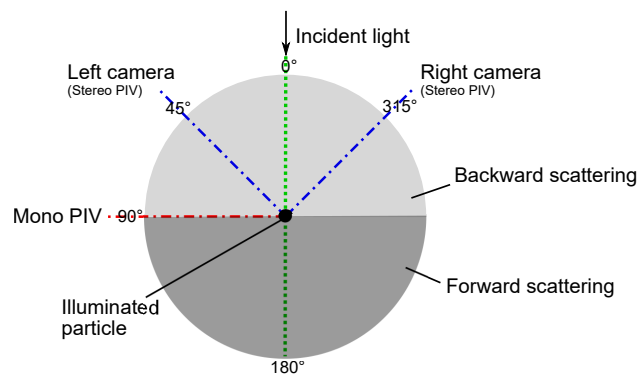
Figure 4.3: Camera arrangement of the Mono-PIV and Stereo-PIV set-up with respect to the Mie scattering of a seeding particle

4.3 Illumination and Light Sheet

4.3.1 Laser

PIV is a laser-assisted optical measurement technique illuminating seeding particles with very small diameters (in the range of microns). Therefore, the application of precise and powerful light sources is essential to capture sharp images with high quality. Lasers[3] have been proved of value emitting monochromatic coherent polarized light with constant power, and precise duration of exposure. The time of exposure t_{dur} has to be short (i.e. several nanoseconds) to avoid blurring in the particle images. Adrian & Westerweel (2011) recommend that the ratio between the pulse duration and the time delay Δt between two sequent pulses should be $t_{\mathrm{dur}}/\Delta t \ll 0.1$.

Lasers can either generate a constant wave (CW) or a pulsed beam. As for PIV a sequence of short flashes is required to illuminate the particles with a time delay Δt, the beam of a CW-laser would have to be "chopped" which wastes energy. Therefore, the pulsed system with two cavities, i.e. separate beams for each frame, is more commonly in use (Adrian & Westerweel, 2011).

Atoms of the laser medium are excited by an energy pump (flash lamp), i.e. increasing their energy level (absorption). Due to *spontaneous emission*, the atoms would jump back from the excited state to the original energy level, and emit a photon with random phase and time within a limited range of wavelengths, and as a consequence, the emitted light would not be coherent. To enhance this process, a population inverse can be built up by pumping with appropriate frequency that is higher than the one of the spontaneous emission. I.e. the photons of the pump raise the energy levels of the atoms, such that more atoms are in the excited state than in the original one. When the photons of the pump hit the excited atoms, a second photon is emitted with the same phase as the stimulating one (*stimulated emission* and *light amplification*).

The laser medium is surrounded by two different mirrors: one is fully reflecting the light and the second is partially transmitting the energy. With this arrangement, the light wave within the laser cavity is oscillating until a defined energy threshold of the so-called *Pockels cell*[4] is reached, and the high-power beam is generated at a precise instant of time (Stanislas & Monnier, 1997).

In PIV, the most commonly used is the solid-state *neodymium-doped yttrium aluminum garnet* (Nd:YAG), as it provides high energy with short pulse durations (Cao *et al.*, 2014).

4.3.2 Light sheet

The light sheet of a PIV experiment is a crucial point for the resolution of the obtained results. A particle (cluster) should be recognisable in both frames, i.e. being paired, in order to contribute to the correlation function (cf. section 4.5.1). Otherwise they will increase the noise of the correlation that decreases the quality of the result. This would either be the case for flow situations with a strong out-of-plane component (e.g. flow in front of a cylinder), or for poorly aligned laser beams, i.e. jumping light sheet between frame A

---

[3]Light amplification by stimulated emission of radiation
[4]Friedrich Carl Alwin Pockels ($\star$1865, $\dagger$1913)

and B. Grayson *et al.* (2018) found for a Gaussian intensity profile of the beams that a mismatch between each beam of 1.35σ (standard deviations) lead to 45% more incorrect vectors.

Generating a light sheet requires basically the combination of a diverging cylindrical lens with negative focal length (front view) and a converging spherical lens with positive focal length (side view), as sketched in Figure 4.4 (Stanislas & Monnier, 1997; Adrian & Westerweel, 2011). The light beam enters the cylindrical lens from left, which spans a triangular shape of the light sheet and defines the main measurement plane of the PIV set-up; thus, it is commonly referred to as the *in-plane* dimension. Further, the spherical lens is used to let the light sheet converge in z-direction. The in-plane spatial resolution is linked to the light sheet thickness; thus, it is highly desirable to work with "thin" light sheets in most cases (Raffel *et al.*, 2007). This dimension is defined as the *out-of-plane* direction. The focal point of the second lens should be in the region of interest where the highest accuracy is required. Due to this geometrical shape of the light sheet, it is often described as quasi-two-dimensional.
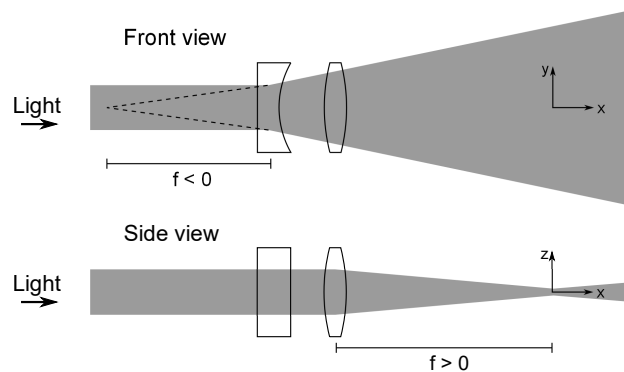
Figure 4.4: Front and side view of the light sheet generation

4.4 Imaging

4.4.1 Gauss theory of thin lens imaging

The basics of imaging a point onto an image plane is sketched in Figure 4.5. This simplified ideal mapping is free from aberrations following the Gauss theory of thin lenses (Jenkins & White, 2001), i.e. sheer geometric imaging. Three parallel planes collude while mapping an object onto an image: object plane, lens plane, and image plane.

The object plane (light sheet in PIV) contains a point source (illuminated particle) at location B, for instance. The distance to the lens plane is Z_0, which is between the object and the image plane (CCD-sensor). The distance from lens to image plane is indicated by z_0.

The optical axis links these three planes perpendicularly, i.e. infinitesimal objects on this axis would be mapped onto the image plane without refraction. The omni-directionally scattered light stemming from object B enters the lens with different incidence angles, since the lens has a finite size it receives only a spherical segment of these light rays. Among this

cone-shaped bundle, one ray passes through the lens centre (*Chief ray*), and experiences no refraction (Adrian & Westerweel, 2011). The position of the image on the sensor is defined by the intersection of the Chief ray and the image plane (see B').

Another ray within this bundle enters the lens parallel to the optical axis ($\overline{BC_2}$), but off-centred; thus, it is refracted to map the object at location B'. Therefore, it crosses the optical axis between the lens and the image plane. The distance of this point of intersection to the lens plane is known as the *focal length f* of the lens. Likewise, a different ray has crossed the optical axis at the focal length in front of the lens plane, too, before it has been deflected parallel to the optical axis ($\overline{BC_1B'}$).

From this geometric imaging, and assuming the same media (air) on both sides of the lens, the *Gaussian lens law* can be derived (Jenkins & White, 2001; Raffel *et al.*, 2007; Adrian & Westerweel, 2011). If eq. 4.4 holds true, a certain imaged object will be in focus.

$$\frac{1}{z_0} + \frac{1}{Z_0} = \frac{1}{f}. \tag{4.4}$$
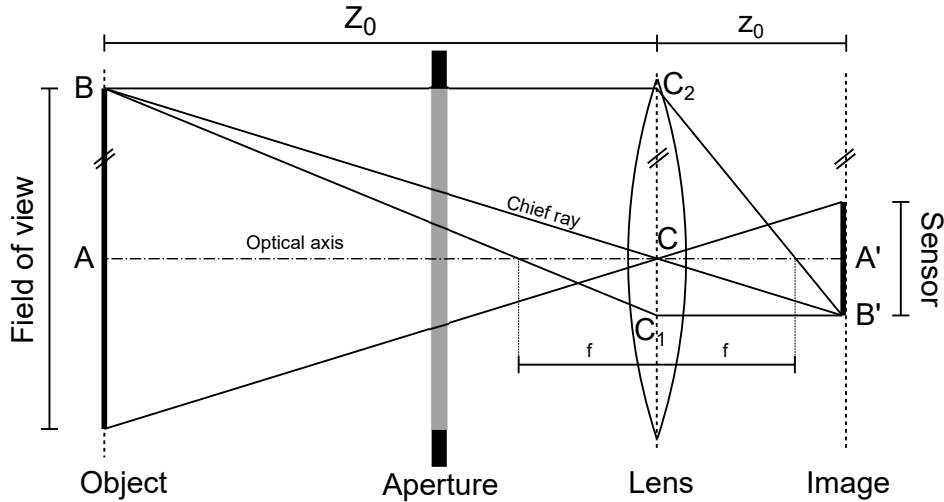
Figure 4.5: Principle of ideal lens geometric imaging

4.4.2 Magnification factor

While mapping an object geometrically, the size of its image depends on the ratio of the distances image-lens to object-lens, see Figure 4.5, and considering the second statement of the intercept theorem:

$$\frac{\overline{A'B'}}{\overline{AB}} = \frac{\overline{CA'}}{\overline{CA}} = \frac{z_0}{Z_0}, \tag{4.5}$$

the magnification factor is defined as:

$$M = \frac{z_0}{Z_0}. \tag{4.6}$$

The size of the CCD-sensor is fixed for each camera, whereas the size of the field of view (FOV) varies from set-up to set-up. When performing Mono-PIV, the FOV can be determined via the calibration (see section 4.7.1), however, in many applications it is not easy to determine the values for z_0 and Z_0. Therefore, taking eq. 4.5 and eq. 4.6 into account the magnification factor can be rewritten as follows:

$$M = \frac{2\overline{A'B'}}{2\overline{AB}} = \frac{\overbrace{\text{Pixel size sensor} \cdot n_{\text{px}}}^{\text{Size of sensor}}}{\underbrace{\text{Pixel size image} \cdot n_{\text{px}}}_{\text{FOV}}}, \tag{4.7}$$

with n_{px} as the number of pixel on the square sensor, thus within the image. The pixel size in the image is the *scaling* factor [µm/px] that is used in eq. 4.17 to calculate the velocity from the displacement.

4.4.3 Diffraction limit

Imaging a point source as described in section 4.4.1 results in an image, which is a point as well. However, the impact of the wavelength of the scattered light, and of the diameter of the lens / aperture D_{a} (see Figure 4.5) have to be considered, too, as they cause *diffraction* (Jenkins & White, 2001). The plane waves of the coherent laser light are refracted at both sides of the lens (entrance and exit), due to *Snell's law*[5] (Goodman, 2005) such that a point spread function is imaged to be known as the *Airy pattern*[6].

Figure 4.6 a) shows the point spread function of a point source passing a thin lens with finite aperture. This pattern was synthetically calculated from the square of the first-order Bessel's equation[7] and "represents the Fourier[8] transform of the aperture's [transmittance] distribution" Raffel *et al.* (2007). The diameter of the first black ring defines the diffraction limit, which is a measure for the smallest possible object to be imaged. In other words, the diffraction limit defines the maximum resolution achievable for a specific optical system (Goodman, 2005). Plotting the intensity normalised by its maximum along a profile through the centre of the Airy discs (dashed line $y/x_0 = 0$) shows the size of the diffraction limit, as it is the first position along the x-axis[9] where the intensity equals zero.

Depending on the magnification and on the wavelength of the light λ, the diffraction-

---

[5] Willebrord van Roijen Snell ($\star$1580, $\dagger$1626)
[6] Sir George Airy ($\star$1801, $\dagger$1892)
[7] Friedrich Wilhelm Bessel ($\star$1784, $\dagger$1846)
[8] Jean Baptiste Joseph Fourier ($\star$1768, $\dagger$1830)
[9] Normalised by the radius of the diffraction limit x_0

limited diameter can be calculated as:

$$d_{\text{diff}} = 2.44 f_{\#}(M + 1)\lambda. \tag{4.8}$$

In the literature, $f_{\#}$ is referred to as either *f-value* (Jenkins & White, 2001) or *f-number* (Goodman, 2005), however, it describes the ratio of the focal length f to the lens aperture diameter D_{a}.

From eq. 4.8 appears that the larger the aperture diameter becomes, the smaller the diffraction limit gets, i.e. small f-number. Whereas, a large magnification increases the diffraction limit.

a: Airy discs   **b:** Intensity profile through centre
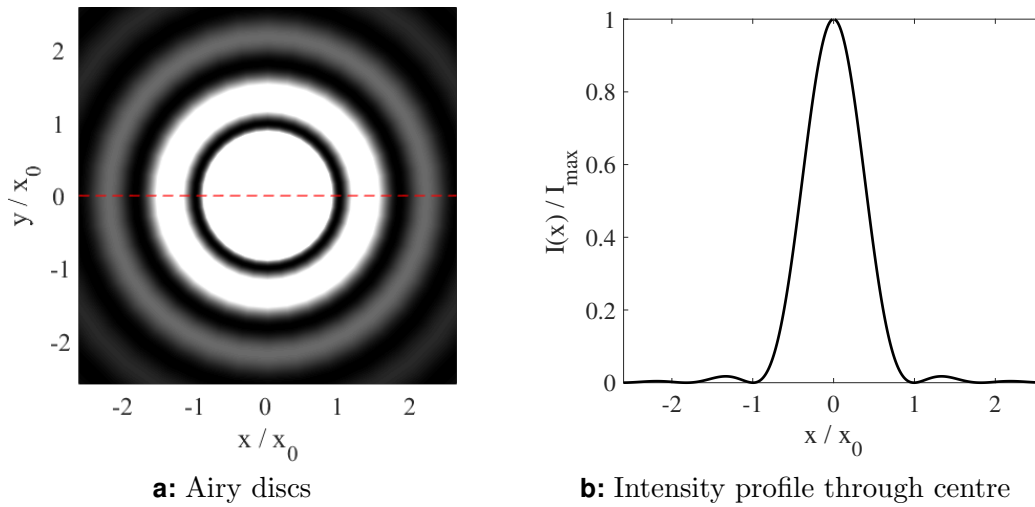
Figure 4.6: Airy pattern

4.4.4 Particle image diameter

Recapitulating the previous sections (4.4.1 to 4.4.3), the ideal particle image consists of two parts: the geometric and the diffraction-limited imaging. However, in reality lens aberrations may occur disturbing the particle image (Adrian & Westerweel, 2011).

Either the geometric or the diffraction-limited part becomes more dominant, depending on the optical configuration. A dominant geometric imaging applies for large magnification M, or large particles d_{P}, and vice versa. Therefore, the particle image diameter, i.e. the size of the particle image on the sensor can be estimated by (Raffel *et al.*, 2007):

$$d_{\tau} = \sqrt{(Md_{\text{P}})^2 + d_{\text{diff}}^2}. \tag{4.9}$$

The particle image diameter plays an important role in PIV as the uncertainty of the velocity measurement is proportional to d_{τ}. According to Raffel *et al.* (2018), the minimum

recommended particle image diameter is 2px, and is associated with the *sub-pixel accuracy* described in section 4.5.3.

4.4.5 Focal depth

So far, the object plane (light sheet) was assumed to be planar. As the light beam has a certain diameter, the light sheet will be quasi-two-dimensional (see section 4.3). The thickness of the light sheet is about one order of magnitude smaller than its in-plane dimensions; though, a very important parameter when designing an experiment.

Due to diffraction-limited imaging (cf. section 4.4.3), objects within a certain range rather than in a selective distance are in focus. A camera cannot distinguish between the distance of two different objects located in this range, which is commonly known as *focal depth* d_z.

$$d_z = 2f_\# d_{\text{diff}} \frac{M+1}{M^2} \tag{4.10}$$

The definition of the focal depth in eq. 4.10 (Raffel *et al.*, 2007) reveals a strong influence of both the f-number (aperture diameter), and the magnification, as it can be seen when substituting d_{diff} by eq. 4.8:

$$d_z = 2f_\# \overbrace{2.44 f_\# (M+1)\lambda}^{d_{\text{diff}}} \frac{M+1}{M^2} = 4.88 f_\#^2 \lambda \frac{M^2 + 2M + 1}{M^2}. \tag{4.11}$$

In experimental set-ups, the magnification can be modified by using lenses with different focal lengths. The sensor size does influence this parameter, too, but varying this parameter is hardly feasible as it is fixed for a certain camera model. For PIV applications, the focal depth of the imaging set-up should cover the whole thickness of the light sheet (see section 4.3.2) in order to image all particles in good shape. Otherwise, the image would contain both focussed and blurred particles, that would affect the quality of the spatial correlation function.

4.5 Processing

4.5.1 Spatial cross-correlation

To gather information on the flow velocity stored in images, the spatial cross-correlation is applied (Keane & Adrian, 1992). Following the *Single-Exposure Double-Frame Recording* method, the camera records "two subsequent exposures on separate frames" related to one instant of time: frame A and frame B separated by the time interval Δt. Particles spotted in the first frame are entrained by the flow, and re-illuminated, i.e. recorded in a second frame. If Δt is correctly chosen, a motion from frame A to B can be observed. In PIV, the particle

image density is generally too large in order to track every single particle[10]. Therefore, a statistical method, the spatial cross-correlation, is applied to quantify the motion of particle clusters, cf. eq. 4.12 Adrian & Westerweel (2011).

First, the image is sub-divided into smaller areas, the interrogation windows (IW). For each IW a displacement vector will be analysed by cross-correlation, and the size of the IW defines the spatial resolution of the experimental data.

Second, the particle image pattern τ_1 in a frame[11] at location $\mathbf{X}$ consists of the recorded light intensity $I_1(\mathbf{X})$ of one interrogation window $W_1(\mathbf{X} - \mathbf{X_{I_1}})$. $\tau_1(\mathbf{X})$ of frame A is similar to the one in frame B, but shifted by the displacement vector $\mathbf{s}$, i.e. $\tau_2(\mathbf{X} + \mathbf{s})$. By multiplying and integrating the light intensities of both frames, i.e. spatial correlation, the best match, i.e. the shift from frame A to B can be found. Subsequently, the correlation function $R(s)$ in eq.4.12 reveals the information of displacement between frame A and frame B.

$$R(s) = \int_\Omega \tau_1(\mathbf{X})\tau_2(\mathbf{X} + \mathbf{s})d\mathbf{X} \tag{4.12}$$

Theoretically, one single particle image of frame A can be matched to all particle images recorded in frame B; this results in several possible solutions, as every single particle image in both frames could be related to each other by a certain displacement. Every match generates a certain correlation that is reproduced by a peak in the correlation function. Repeating this seek for related partners for every particle image all possible displacements are summed up by the integration in eq.4.12. The correlation function R contains many different low peaks (noise), but ideally only one large main peak that represents the most likely combination of the whole particle image *pattern*. The location of this peak in relation to the centre of the interrogation window corresponds to the displacement vector $\mathbf{s}$ represented by that interrogation window at position $\mathbf{X}$. As a result, only one vector can be identified for each IW; thus, it acts as a spatial filter on the real velocity field.

4.5.2 Correlation using fast Fourier transform (FFT)

The correlation function in eq. 4.12 is also called *direct correlation*. An image is discretised by the pixel array of the CCD-sensor, therefore, the integration in space in eq.4.12 is substituted by a double summation over $N \times N$ multiplications for each pixel separately. With N as the size of the interrogation window. The total direct correlation requires, therefore, $(2N \times 2N)^2$ multiplications (Adrian & Westerweel, 2011; Tropea *et al.*, 2007). To reduce this computational effort, a frequency domain based correlation (Raffel *et al.*, 2007) can be used instead such as the fast Fourier transform (FFT). Applying an FFT-based correlation requires only $2N^2 \log_2 N$ operations (Adrian & Westerweel, 2011; Raffel *et al.*, 2007).

---

[10]Such method is called particle tracking velocimetry (PTV). As it is not part of this work it will not be further discussed. For more information the reader is referred to Adrian & Westerweel (2011)

[11]The analysis described here refers always to one interrogation window at the same location $\mathbf{X}$ in frame A and B. For simplicity the term "frame" stands simultaneously for "interrogation window" in this section

According to Adrian (1991); Raffel *et al.* (2007), the cross-correlation in Fourier space of the particle image pattern from an interrogation window can be computed by the multiplication of the Fourier transformed light intensity of frame A with the complex conjugate of the Fourier transform of frame B. Finally, the cross-correlation in real space is obtained by the inverse Fourier transform of this product.

4.5.3 Sub-pixel accuracy

As discussed in section 4.5.1, the location of the maximum peak of the spatial correlation function represents the most likely displacement vector of the corresponding interrogation window pair. Therefore, the accuracy of the procedure finding this peak is of central importance in PIV.

The images are recorded on pixel arrays; thus, the light intensities are stored as discretised information, and the cross-correlation function of eq. 4.12 will be discretised, as well. Searching for the location of the maximum peak would result in an integer displacement vector, due to the discrete input data. Figure 4.7 shows the influence of the fractional displacement on the shape of the correlation function. Case a) has no fractional displacement, thus only integer values. The correlation function has a symmetric shape with its peak exactly at the centre of the corresponding integer pixel. When the fractional displacement is equal to 0.5px (cf. case c) the correlation function is still symmetric but reveals two equal peaks at the surrounding pixel centres. And, in case b) the fractional displacement is 0.25px, the shape of the corresponding correlation function is no longer symmetric, and searching for the maximum value of this correlation function would lead to zero fractional displacement, thus to an error in the sub-pixel range. The same applies for a 0.75px fractional displacement. The maximum would then be found at 1.0.

To avoid this bias, a Gaussian distribution (dashed line in Figure 4.7) can be fitted in the correlation function, and the location of the peak (see cross symbols) of the fitted function indicates the fractional displacement. This approach can increase the sub-pixel accuracy tremendously to 0.1px for low spatial resolution imaging.
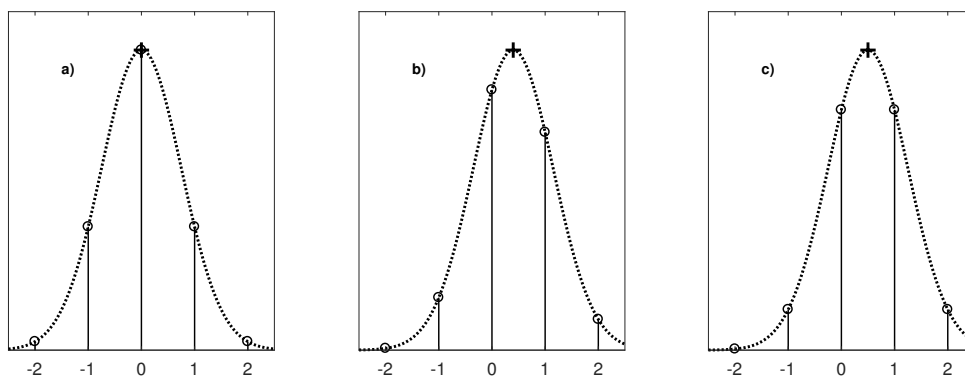
Figure 4.7: Fractional displacement a) 0, b) 0.25, and c) 0.5 influences shape of correlation function, according to Westerweel (1997)

4.5.4 Influence of velocity gradients on the correlation function

The cross-correlation function acts as a spatial filter on the velocity field, irrespectively of the direct (see section 4.5.1) or frequency domain based correlation (see section 4.5.2). In case of an uniform vector field with high seeding density and ignoring other sources of error, the correlation function would contain the true particle displacement independently of the size of the interrogated area.

However, when investigating turbulent flows, velocity fluctuations, eddies, and strong velocity gradients can occur entailing large differences in velocity within an interrogation window. The time interval Δt between two frames is set to catch the particle displacements within an IW as best as possible, i.e. a trade-off has to be made. Figure 4.8 depicts the effect of in-plane losses of particle images (Westerweel, 2008): the observed flow has a gradient transporting the particles in the upper part of the IW faster than the ones in the lower part. The black dots represent particles at time t_1 (frame A), and the circles those at time $t_1 + \Delta t$ (frame B) both contributing to the correlation function.

While correlating frame A and B, the most likely displacement will generate the highest peak in the correlation function. When particles are likely to be lost from frame A to frame B, i.e. circles located outside of the right hand side of the interrogation window, they do no longer contribute to the correlation function. Furthermore, new particles are just as well likely to occur in frame B from upstream, but they had not been present in frame A (crosses in Figure 4.8). Both, sudden in-plane loss and gain of particle images between frame A and frame B undermine the quality of the correlation function by decreasing the signal-to-noise ratio (SNR) that biases systematically the estimation of the displacement vector in the end.
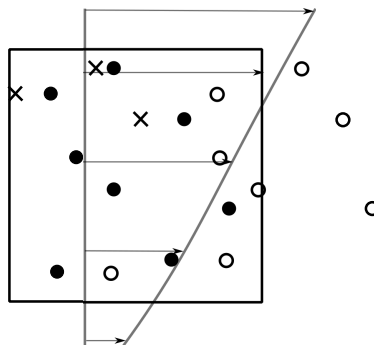
Figure 4.8: In-plane losses due to velocity gradient

Window offset and deformation correlation   To overcome this unfavourable effect in complex flows, the shear, rotation and deformation acting on the particles, and therefore, on the particle image pattern should be taken into account by likewise deforming the interrogation windows. That reduces the in-plane loss of particles, and thereby, enhances the strength of the maximum correlation peak (Adrian & Westerweel, 2011).

Huang *et al.* (1993*a,b*) and Ashforth-Frost *et al.* (1993) proposed an "improvement of PIV" based on correcting the particle image pattern due to a linear velocity gradient for the first time.

Jambunathan *et al.* (1995) suggested to iteratively correct the correlation function by rebuilding the second image. This reconstruction is based on the a priori estimation of the vector field and its deformation (rotation and shear), and came with an improvement in accuracy of about 50% depending on the investigated flow situation. This work was continued by Nogueira *et al.* (1999) who achieved to resolve structures smaller than the interrogation window size.

Numerous approaches for iterative correlation techniques to increase the accuracy of PIV were further elaborated (e.g. Scarano & Riethmuller (1999, 2000)); thus, no standard algorithm exists (Astarita & Cardone, 2005). While processing the PIV images of this study, the built-in *image deformation* algorithm of the commercial software INSIGHT 4G of TSI was applied.

4.6 Stereoscopic PIV

In the stereoscopic PIV application an additional camera is installed to be able to measure the three components of the velocity vector. This gain in information entails a number of changes compared to the basic Mono-PIV set-up, however, the light sheet remains planar. For performing Stereo-PIV, two different configurations exist, which are shortly discussed first.
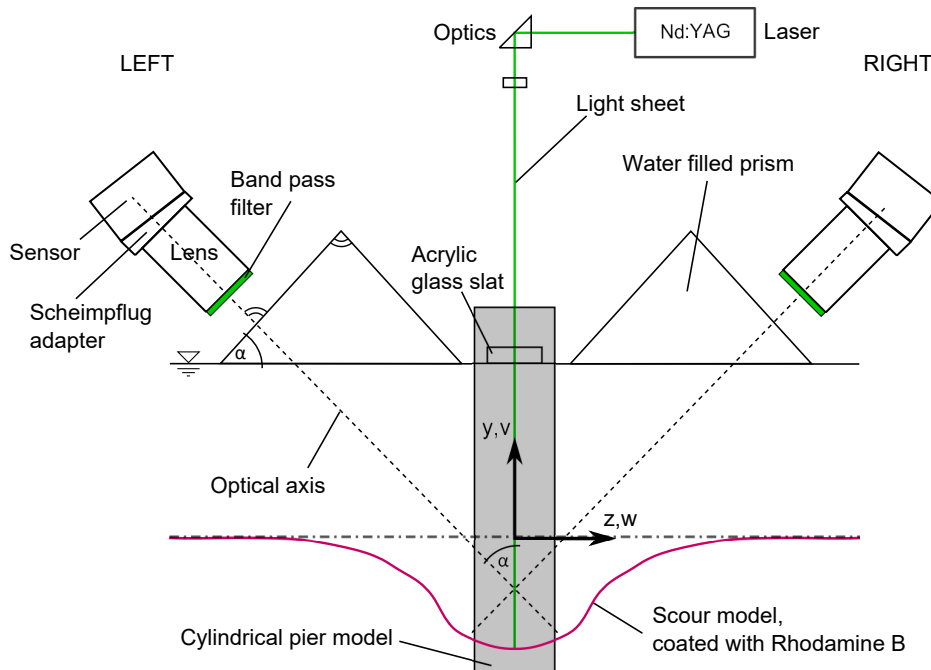
Figure 4.9: Angular Stereo-PIV set-up; view in streamwise direction in front of a scoured cylinder

4.6.1 Set-up

The cameras of a Stereo-PIV set-up can be installed in two different configurations (Raffel *et al.*, 2007):

a) lens translation method

b) angular lens displacement

In the first case, the sensor remains parallel to both the lens and the object plane, but is shifted laterally with respect to the lens plane. While the advantage of this method lies in undistorted imaging (constant magnification within an image), the range of application is very limited (Adrian & Westerweel, 2011), as the optical aberrations increase for large viewing angles.

When using the second method, the cameras are mounted with an angle to each other. This entails a perspective distortion of the images, as the sensor, lens and object plane are no longer parallel to each other. I.e. the imaging properties can no longer be assumed to be Gaussian; thus, do not follow the imaging described in section 4.4. Consequently, the image is not homogeneously focussed any more. Therefore, introducing such an inclination requires additional constructional and methodological effort, in order to regain Gaussian imaging properties.

In order to obtain optimum measurement accuracy for the displacements in all three dimensions equally, the opening angle between both cameras should be approximately $90°$ (Raffel $et\ al.$, 2018; Adrian & Westerweel, 2011). Figure 4.9 shows a sketch of the applied Stereo-PIV set-up following the angular lens displacement method. The inclination of the cameras by $45°$, however, provokes refraction at the interface of water and air (Jenkins & White, 2001), which can be avoided by installing water filled prisms directly at the water surface (see section 4.6.2). Further, the inclined set-up requires so-called $Scheimpflug\ adapters$, which are discussed in more detail in section 4.6.3.

The flow field is observed from two different angles in Stereo-PIV; thus, the same particle displacement leads to two different results depending on the perspective, and this information can be used to reconstruct the real velocity field (see section 4.6.4).

4.6.2 Water filled prism

Working with water entails an additional constructional device to be applied in the experimental set-up (see Figure 4.9). As the cameras are mounted with an inclination with respect to the water surface (e.g. $\alpha = 45°$) and outside the water medium, refraction occurs. When the optical axis does not cross the water-air-interface perpendicularly, the particle images would be distorted. Therefore, Prasad & Jensen (1995) suggested to install a water filled prism slightly submerged at the interface to overcome this unfavourable distortion. The lens facing side of the prism should be normal to the optical axis, and the prism has to be filled with water, i.e. a medium with the same refractive index as the working fluid, to translate the original water surface onto a plane, which is inclined by the angle α.

4.6.3 Scheimpflug condition

The basic background of ideal (Gaussian) imaging was described in section 4.4. The ability to homogeneously focus on the entire object plane arises from a constant magnification factor within the image that is achieved when the three planes object plane, lens plane, and image

plane intersect in one line, according to the so-called *Scheimpflug*[12] condition (Adrian & Westerweel, 2011; Tropea *et al.*, 2007; Prasad, 2000).

In the Mono-PIV case, the optical axis of the camera and the light sheet are mounted perpendicularly, hence, all three planes intersect in infinity; thus, there is no limitation in focussing an object.

However, when mounting cameras in the Stereo-PIV set-up with an angular displacement, these three planes do not intersect in one line any more, as the sensor and the lens plane are parallel to each other (see left hand side of Figure 4.10). As a consequence, only one part of the image can be focussed, whereas the remaining part stays blurred. To be able to focus on all particles homogeneously throughout the entire image when conducting Stereo-PIV, an additional angle between lens and image plane is introduced by the Scheimpflug adapter. Thus, by fulfilling the Scheimpflug condition, and by restoring the intersection of the three planes in one line, the object plane can be clearly focussed without restrictions (see right hand side of Figure 4.10).
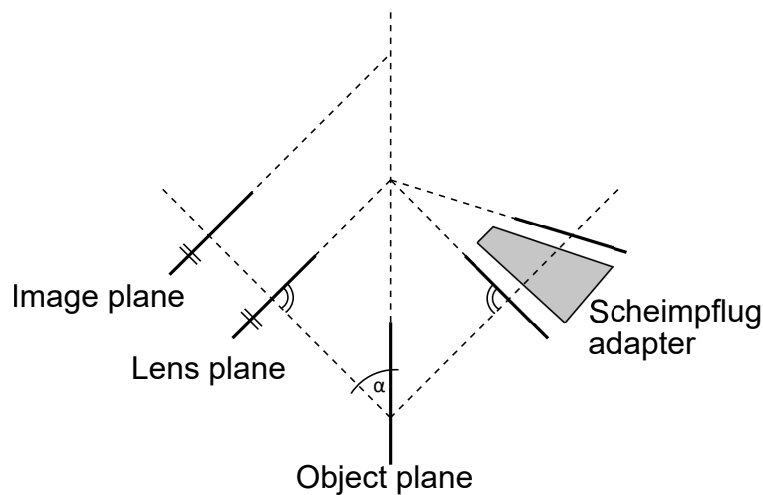
Figure 4.10: Angular Stereo-PIV set-up without (left) and with (right) Scheimpflug adapter

4.6.4 Reconstruction of the vector field

The vector field has to be reconstructed when applying Stereo-PIV, since the in-plane displacement of a particle is recorded from two different point of views, whereas the out-of-plane component is not recorded directly. However, the measured in-plane particle displacement differs due to this third component normal to the light sheet; thus, the cameras provide varying information about the same particle displacement. Using the data from both cameras allows the precise reconstruction of the three dimensional velocity vector as depicted in Figure 4.11.

The object plane represents the light sheet centre, i.e. $z = 0$, where a particle at time t_0 is located. After the time delay dt, this particle is displaced in space by the vector $\mathbf{u} = (u_0, v_0, w_0)^T$. The particle is projected onto the object plane by both cameras; in this example, the left camera records a larger horizontal component u_L with respect to the true

---

[12]Found by Theodor Scheimpflug ($\star$1865, $\dagger$1911)

value u_0, whereas, the right camera observes this velocity as u_R, which is smaller than u_0. That means different in-plane displacements are observed, and none of the two cameras can detect the out-of-plane component w_0 directly. The same concept applies for the vertical displacement v_0, as Figure 4.11b) shows.

Using both values from left and right camera, and taking the angle of view into account, allows the reconstruction of the true vector $\mathbf{u}$ as follows (Raffel $et\ al.$, 2007):

$$u_{0,\text{reconstr.}} = \frac{u_\text{L}\tan\alpha_\text{R} + u_\text{R}\tan\alpha_\text{L}}{\tan\alpha_\text{L} + \tan\alpha_\text{R}}, \tag{4.13}$$

$$v_{0,\text{reconstr.}} = \frac{v_\text{L}\tan\beta_\text{R} + v_\text{R}\tan\beta_\text{L}}{\tan\beta_\text{L} + \tan\beta_\text{R}}, \tag{4.14}$$

$$w_{0,\text{reconstr.}} = \frac{u_\text{L} - u_\text{R}}{\tan\alpha_\text{L} + \tan\alpha_\text{R}}. \tag{4.15}$$

α and β refer to the angles within the YZ and XZ planes, respectively. The first is intended to be approximately 45°, while the latter is close to 0°. Therefore, the reconstruction of v_0 reduces to the arithmetic mean of v_L and v_R according to Raffel $et\ al.$ (2007), as eq. 4.14 can be rewritten as:

$$v_{0,\text{reconstr.}} = \frac{v_\text{L} + v_\text{R}}{2} + \frac{u_\text{L} - u_\text{R}}{2}\left(\frac{\tan\beta_\text{L} - \tan\beta_\text{R}}{\tan\alpha_L + \tan\alpha_\text{R}}\right). \tag{4.16}$$

a: Top view   **b:** Front view
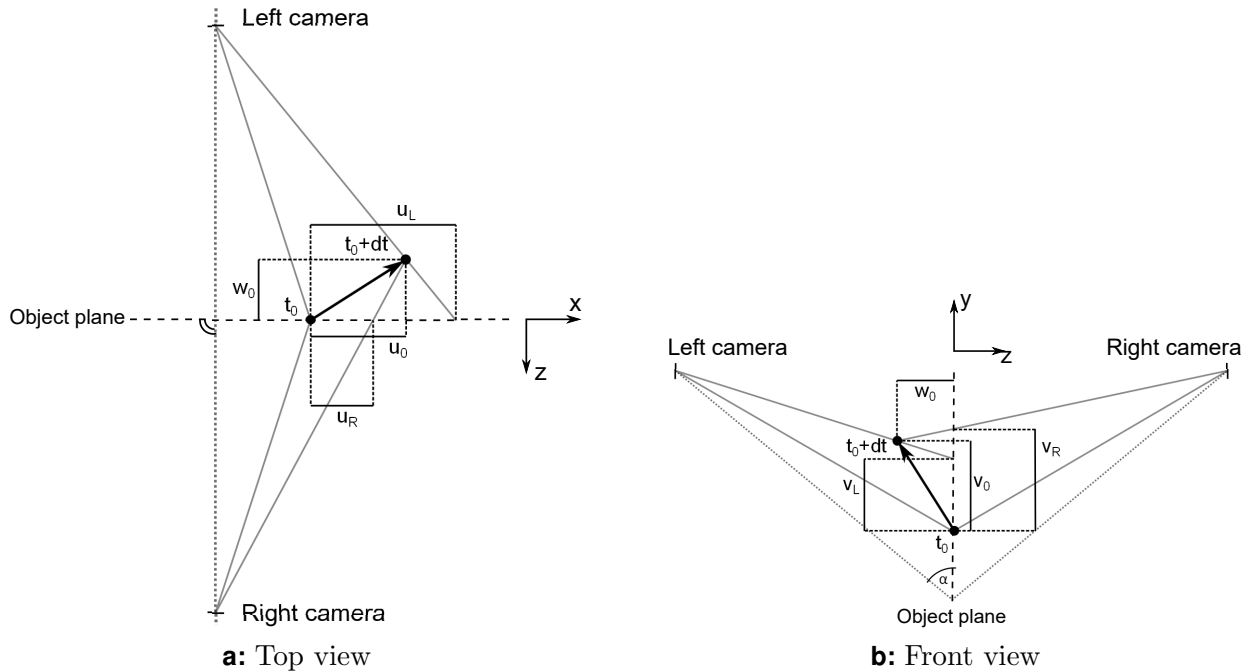
Figure 4.11: Geometric sketch of particle displacement using the angular lens displacement set-up.

4.7 Calibration

The result of the cross-correlation (see section 4.5) is a field of displacement vectors for each instantaneous image pair in pixel units. The velocity field can be computed by dividing the pixel displacement by the time delay dt between frame A and B, and by applying the spatial calibration, which transforms pixels into real world units. In the following, the calibration procedures for both the Mono-PIV and the Stereo-PIV are described.

4.7.1 Mono-PIV

In case of using only one camera, a target of known size has to be placed in the object plane (light sheet) as sketched in Figure 4.12. For the Mono-PIV measurements, a chequerboard pattern of 5mm size was used (see Figure 4.13), and the red lines mark the location of the surface of the bottom of the channel and of the cylinder front, respectively. The object plane and the camera axis are arranged perpendicularly, and the calibration target has to be aligned with the light sheet to ensure the optical set-up to be calibrated for the same position as the particle images will be recorded during the experiment.

A calibration image is recorded, and the number of pixels covered by the object in the image are counted that a calibration factor in [μm/px] can be obtained. Each black and white square covered approximately 136px in horizontal and vertical direction, which yields a constant scaling factor f_{scal} of 36.86μm/px for the entire image. Finally, the displacement can be transformed into a velocity vector using eq. 4.17.

$$\mathbf{u} = \mathbf{u_{px}} \frac{f_{\text{scal}}}{\Delta t} \tag{4.17}$$

4.7.2 Stereo-PIV

When conducting a PIV experiment with two cameras recording simultaneously and arranged by the angular displacement method (cf. section 4.6), the calibration procedure becomes more complex. Both cameras are mounted inclined with respect to the light sheet that the camera axes intersect in the object plane. Therefore, a perspective distortion occurs, and avoids a homogeneous focusing within the image; thus, makes it impossible to compute one single, constant scaling factor representing the entire image. As the stereoscopic set-up enables the reconstruction of all three components of the velocity vector (cf. section 4.6.4), three dimensional spatial information of the object "plane" has to be provided, following one of the two common techniques:

Traversing   A plane target, like the one for Mono-PIV, is traversed through the light sheet[13] along the out-of-plane-axis. Doing so, calibration images are recorded at several positions

---

[13]The light sheet is a quasi-two-dimensional plane; thus, the in-plane dimensions are about one order of magnitude larger than the out-of-plane one. I.e. the light sheet is a slender volume rather than a proper sheet.
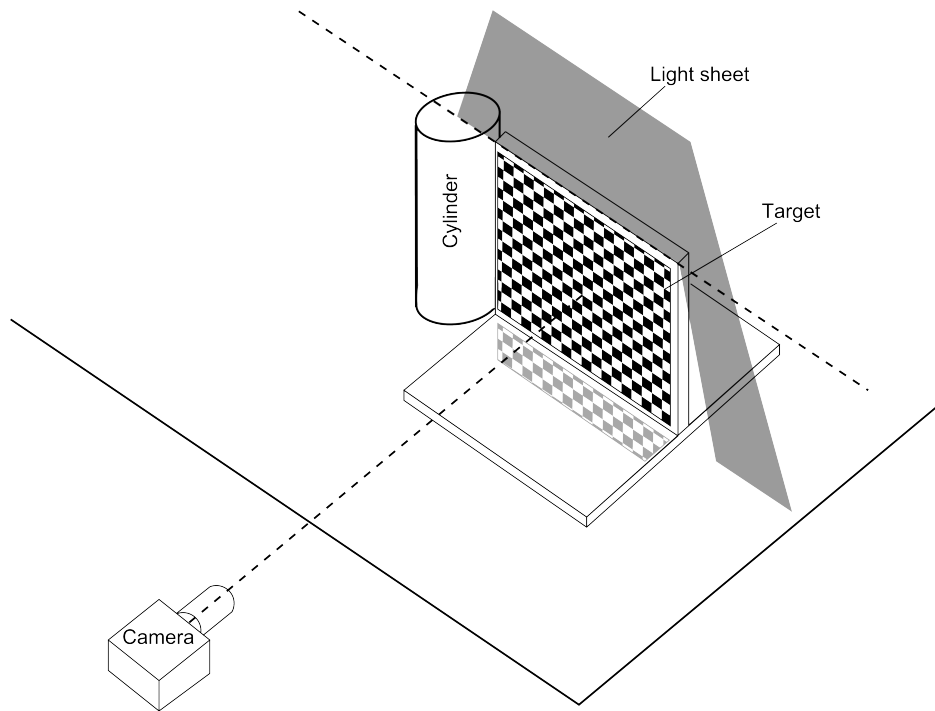
Figure 4.12: Sketch of calibration set-up in Mono-PIV

on this axis to gather three dimensional information in space. From this calibration grid mapping functions can be calculated to reconstruct the undistorted object plane at $z = 0$. This method appears to be precise, but comes along with the effort of exact traversing, which is not always feasible in the experimental environment.

Multi-plane target   If the traversing technique is not possible to apply, a multi-plane target can be used instead (see Figures 4.14 a and b). Such a four-plane target is constructed as a relief-like structure with an equally spaced dot pattern on the calibration planes (Z_1 and Z_2) of both sides. The centre marker (white cross) serves thereby as a reference point that is identified in the grids from the left and right camera to link them in the same point. The light sheet is aligned with the centre of the target (dash-dotted line), and each camera is focused for example on one side of the fixed target and records the dot pattern without traversing the target in $z-$direction. The centre of gravity of the dots on each individual plane is determined, in order to be used as coordinates in the object planes (Z_1 and Z_2).

Furthermore, a mapping function F can be computed using the coordinates of the dots on the object planes $\mathbf{X} = (X_{\mathrm{obj}}, Y_{\mathrm{obj}}, Z_{\mathrm{obj}})^T$, which are projected on the image plane with the corresponding coordinates $\mathbf{x} = (x_{\mathrm{img}}, y_{\mathrm{img}})^T$ by a direct linear transformation that assumes
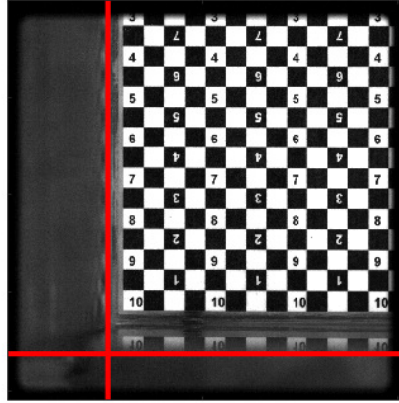
Figure 4.13: Calibration image in Mono-PIV

an idealized imaging (Raffel *et al.*, 2007):

$$w_i \begin{bmatrix} x_\text{img} \\ y_\text{img} \\ 1 \end{bmatrix} = F^{3\times 4} \cdot w_o \begin{bmatrix} X_\text{obj} \\ Y_\text{obj} \\ Z_\text{obj} \\ 1 \end{bmatrix}. \tag{4.18}$$

The weighting factors w_i and w_o are constant and can be normalized (w_i/w_o) and eliminated such that eq. 4.18 reads:

$$\begin{aligned} x_\text{img} &= \frac{f_{11}X_\text{obj} + f_{12}Y_\text{obj} + f_{13}Y_\text{obj} + f_{14}}{f_{31}X_\text{obj} + f_{32}Y_\text{obj} + f_{33}Z_\text{obj} + f_{34}}, \\ y_\text{img} &= \frac{f_{21}X_\text{obj} + f_{22}Y_\text{obj} + f_{23}Y_\text{obj} + f_{24}}{f_{31}X_\text{obj} + f_{32}Y_\text{obj} + f_{33}Z_\text{obj} + f_{34}}, \end{aligned} \tag{4.19}$$

with $f_{34} = 1$.

The coefficients f_{11} to f_{33} are found by using a nonlinear least-squares solver[14]. For both cameras (left and right) the mapping function F is determined separately and the relief depth $\overline{Z_1 Z_2}$ as well as the thickness of the target ($\overline{Z_1 Z_1'}$ and $\overline{Z_2 Z_2'}$) are used to provide information on the z-direction. With this information, the object plane ($Z = 0$) and the particle displacements in $z-$direction can be reconstructed as well as a constant scaling factor for the entire image determined.

The mapping procedure of the Stereo-PIV is of central importance, as the raw frames of an experiment that are distorted due to the perspective alignment of the cameras, are de-warped in a first step by the back-projection of eq. 4.19 before the particle displacements are computed by the spatial cross-correlation. Finally, the three-dimensional velocity vector is reconstructed by using eq. 4.13 to 4.15 and the transformation from the pixel displacements

---

[14]Raffel *et al.* (2007) suggest the Levenberg-Marquardt algorithm

into velocities of eq. 4.17.

a: Dot pattern

b: Relief-like structure of
a four-plane target
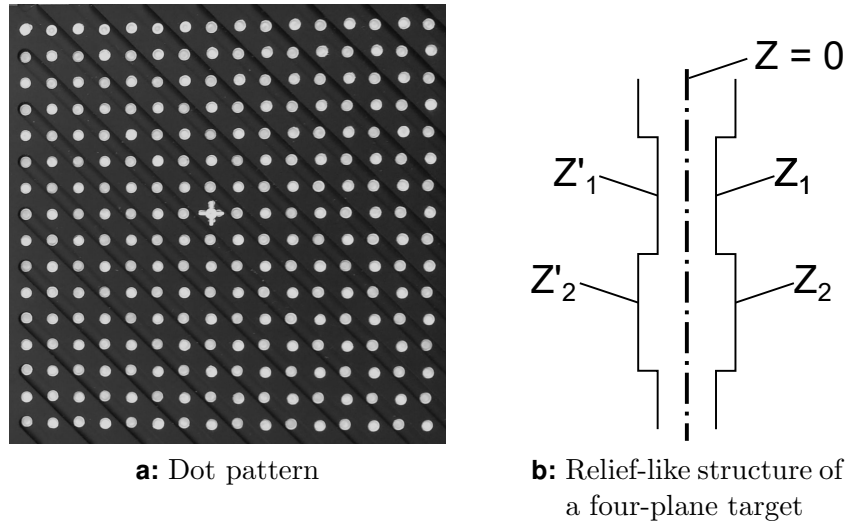
Figure 4.14: Multi-plane calibration target for Stereo-PIV

4.8 Conclusion

Summing this chapter up that introduced the theoretical background of particle image ve-
locimetry, leads to the following set of key issues, which are important when designing a
PIV experiment, and may conflict with each other, and require trade-off decisions to be
made:

- the Kolmogorov scales (see eq. 2.4 to eq. 2.6) have to be estimated in advance to choose
  appropriate particle size, time delay, and interrogation window size
- the diameter of the seeding particles should be on the one hand large to ensure bright
  light scattering, i.e. large and nicely focussed particle images. One the other hand,
  however, the size of the particles interfere with their sensitivity to small turbulent
  scales by high inertia
- for the imaging configuration a small f-number is desired, i.e. large aperture diameter,
  to let the sensor capture more light; the diffraction limit decreases, which leads to
  higher spatial resolution. However, this shortens the focal depth at the same time,
  which in turn entails a higher fraction of blurred particles, and more noise in the
  correlation function. Further, the particle image diameter is decreasing with increasing
  f-number; thus, undermines the sub-pixel accuracy in the correlation function.

5 Experimental Strategy

The following chapter deals with the experimental infrastructure to generate the flow configurations $Re = 20{,}000$, $39{,}000$, and $Re = 78{,}000$. Further, the hydraulic design of the experiments is discussed, before the set-ups for studying the flow in front of a wall-mounted cylinder and around a scoured cylinder are described. Treatment strategies with respect to damp surface reflections are presented, and finally, the position of the wall in the images is determined.

5.1 Experimental Set-up

5.1.1 Hydraulic set-up

Figure 5.1 shows the sketch of the laboratory infrastructure at the Professorship of Hydromechanics of the Technical University of Munich. A 1.17m wide rectangular flume is fed by a high-level water tank that ensures a constant pressure height, while a magneto-inductive flow meter measures the flow rate Q. At about 3m after the inlet, a flow straightener is installed consisting of four sheets of punched stainless steel to mitigate the disturbances of the inlet, and surface waves are damped by using a floating body at the beginning of the entry length L.

This 20m long part of the straight flume allows a turbulent boundary layer to develop, but as discussed later in section 6.2, the relative entry length of the flume changed with respect to the hydraulic diameter D_h. To support the turbulence generating performance of the flume, a set of vortex generators are installed, designed according to Counihan (1969) (see Figure 5.2). The height and width of these quarter ellipses are set to one flow depth y_0, and one half of y_0, respectively. The triangular cross section has an angle of 12°; thus, the thickness is one tenth of y_0, and the spacing is recommended to be about $\frac{3}{5}y_0$. In front of the aligned generators, the installed fence tripping the near wall flow has a height of $\frac{1}{8}y_0$.

5m after the measurement section a sluice gate is mounted defining the outlet of the flume and controlling the flow depth before the water recirculates driven by a pump. To study the approaching flow conditions (cf. section 6.2), the bridge pier model was removed that the inflow profile could be observed at this position without any disturbances.

The cylinder of the experiments conducted in the sections 5.3 and 5.4 induced surface waves, which disturbed the light sheet when entering the water body. For this reason, a slender plate of acrylic glass with a length of 0.15m, a width of 0.05m, and submerged by approximately 0.01m was mounted at the water surface. The influence of this component on the approaching flow condition is documented for $Re = 39{,}000$ in section 6.3.
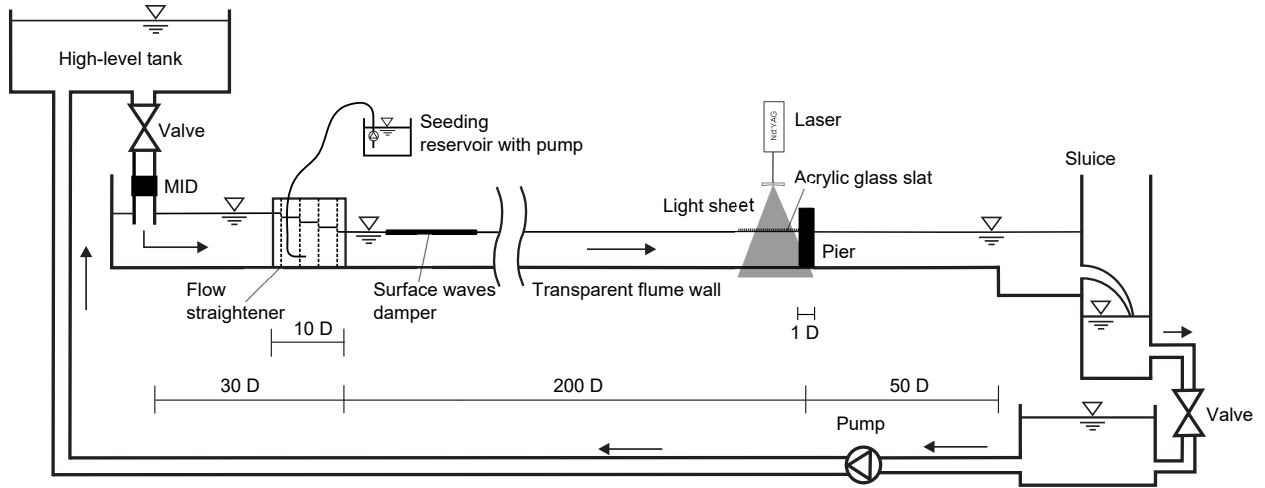
Figure 5.1: Experimental set-up edited from Pfleger (2011)
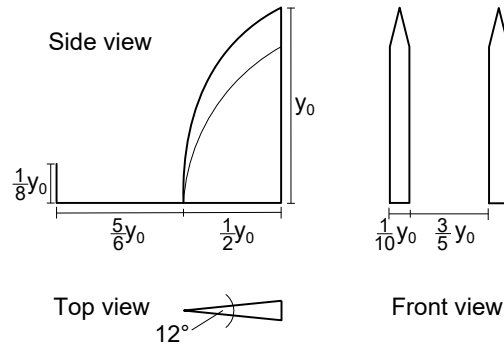
Figure 5.2: Vortex generators according to Counihan (1969)

5.1.2 Illumination

A Nd:YAG laser Evergreen 200 from Quantel was used as a light source. The pulsed light beam had a wavelength of 532nm and a maximum energy of 200mJ. The pulse width was 10ns and the near field beam diameter < 6.35mm. This high-power beam was directed by a set of mirrors, with optimized reflectivity ($> 99.8\%$) for this particular wavelength, and a damage threshold[1] > 10J/cm^2. The triggering for the laser and the camera was synchronized to a repetition rate of 7.25Hz. The light sheet was generated using a diverging and a converging lens (see Figure 4.4) and had a thickness of about 2mm.

5.1.3 Seeding particles

During all experiments, hollow glass spheres (HGS) from Dantec with a median diameter $d_P = 10\mu$m and a density $\rho_P = 1100$kg/m^3 were suspended to the flow as tracer particles. Using a macro estimation of the dissipation rate $\epsilon \propto \frac{u_b^3}{L_c}$, which is the bulk velocity u_b to the power of three divided by the characteristic length scale L_c, the Kolmogorov time scales τ_{η_K} of each set-up were computed according to eq. 2.5. In case of the approach flow tests, the

---

[1]According to EN-ISO-11254-2: s-on-1 test

hydraulic diameter D_h was used for L_c; whereas, for all experiments with the cylinder (on flat bed and in the scour hole) its diameter was considered to be the representative length scale.

Further, eq. 4.2 yielded $\tau_\mathrm{P} = 6.11 \cdot 10^{-6}$s as the particle relaxation time, which led to the Stokes numbers listed in Table 5.1. The Stokes number is the ratio of the particle relaxation time to the smallest time scale of the flow. St_k is much smaller than one for all cases, therefore, the selected particles were suitable for the investigated flow configurations, and were able to follow the flow accurately. Furthermore, the approximation error of the particles following the trajectories of the flow was less than 1%, as $St_\mathrm{k} < 0.1$ (Tropea $et\ al.$, 2007).

5.1.4 Constructional set-up

The support for mounting the measurement devices such as laser head, mirrors and light sheet optics and cameras, was constructed using so-called "X95"[2] aluminium beams. Two horizontal foundations on top of each side wall of the flume and a pair of crossing beams connecting both sides formed the basic structure.

When applying PIV, all devices must be mounted as tightly as possible to ensure precise calibration and measurements. However, in this set-up, a full rotation of the light sheet, i.e. optical components, and cameras was required to be able to measure at any angle of rotation around the cylinder. Additionally, the flow inside a three dimensional scour hole is of interest, therefore, all devices were mounted above the water channel to ensure best optical accessibility (cf. Figure 4.9). Every rearrangement of the devices requires, usually, a new calibration procedure from the very beginning.

Facing the challenge of installing all components as firmly as possible, but allowing a 360° rotation of the set-up around the centre axis of the cylinder, a turntable disc with a highly precise cross roller bearing was constructed, and mounted underside the pair of X95 crossbeams (see Figure 5.3a)). This rotatable part supported the entire construction for mounting both cameras, the water filled prisms, and the optical devices generating the light sheet. The crux of this design consisted of directing the laser beam by mirror 1 from above the cross beams into the rotary axis of the turntable disc. Therefore, any angle of rotation could be set without readjusting the optical components. A second mirror redirected the light beam out of the vertical centre axis towards a third mirror on the optical bench, which was mounted vertically at the required position of the light sheet. According to the description in section 4.3.2, the light sheet was generated by a diverging cylindrical ($f = -15$mm) and a converging spherical lens ($f = 500$mm).

The optical bench was supported by two horizontal X95 beams holding the camera support, too. Thus, the cameras could be aligned with the laser beam following the angular lens displacement strategy (cf. section 4.6.1). By traversing these three components simultaneously in the horizontal direction, the field of view (FOV) could be set at any position in radial direction with respect to the cylinder. The camera support allowed a third degree of freedom to adjust the optical axis of the cameras within the FOV, as the cameras could be moved perpendicularly in horizontal direction away from the light sheet.

Figure 5.3b) shows the supporting structure of the water filled prisms that are required

---

[2]X-shaped cross-section with 95mm edge length

in a stereoscopic set-up working with water (cf. section 4.6.2). The supporting structure of the acrylic glass plate, which suppressed surface waves, was mounted on top of the cylinder independently of the remaining devices; thus, had to be readjusted separately for each angle of rotation.

When studying the flow in front of the cylinder on a flat plate as described in section 5.3, the light sheet generation was identical to the one in the scour set-up (see section 5.4). However, the camera was mounted perpendicularly outside the water channel, i.e. the flow field was observed only in the symmetry plane in front of the cylinder at 0° with respect to the approach flow (see Figure 5.7).
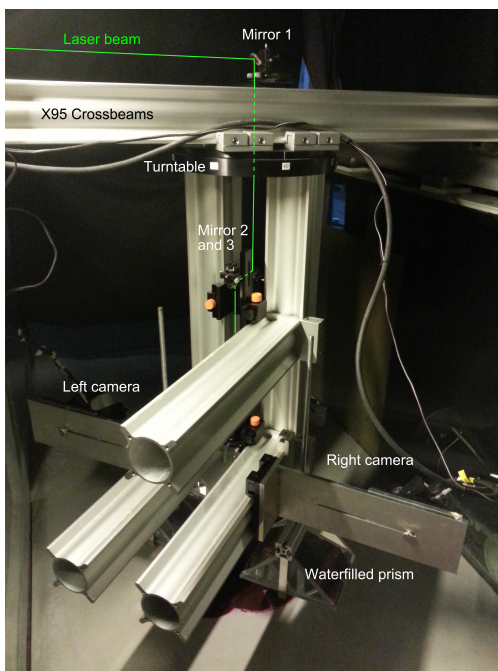
a: X95 Structure supporting measurement devices
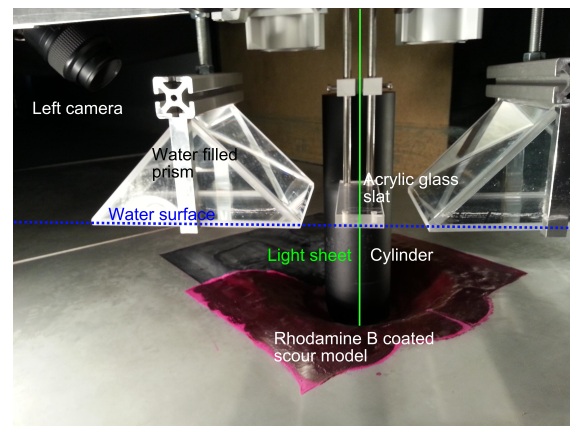
b: Water filled prisms at 45° angle of rotation with respect to approach flow

Figure 5.3: Constructional set-up supporting the measurement devices

5.2 Design and Scaling of the Experiments

The scour geometry, which is used to study the flow field around a scoured cylinder (see section 5.4), was taken from Pfleger (2011), who conducted scour experiments in the same laboratory under similar conditions, and intended to study the flow at $Re = 36,000$. However, as an acrylic glass plate covering the entire water surface at the measurement section to enhance the optical accessibility was mounted, the effective Reynolds number increased to 39,600 due to channelling effects.

Therefore, $Re = 39,000$ was set to be the initial situation for this study. To represent scaling effects occurring with different Reynolds numbers, the cases $Re = 20,000$ and

$Re = 78{,}000$ were additionally investigated; thus, the scaling factor between the flow configurations was $\frac{Re_2}{Re_1} \approx 2$. The flow-depth-to-cylinder-diameter ratio was kept constant at $\frac{y_0}{D} = 1.5$.

Table 5.1 provides an overview of the a priori estimation of the Kolmogorov micro scales (cf. section 2.2). The temperature varied between 18°C and 21°C; thus, the influence on the fluid properties such as density ρ and kinematic viscosity ν had to be considered, which is discussed in section 6.4.

The Reynolds numbers were computed based on the cylinder diameter D and the bulk velocity $u_\mathrm{b} = Q/A$. As the measurements were conducted in the symmetry plane of the flume, the depth-averaged value of the approaching velocity profile measured in the symmetry plane of the flume was considered to be the more suitable reference value than u_b to normalize all turbulence metrics in front of the (scoured) cylinder, e.g. Reynolds stresses, TKE, production, and dissipation rate. The depth-averaged velocity was determined according to eq. 5.1, and exceeded the bulk velocity by 2% to about 7% depending on Re due to the secondary flow structure of the rectangular flume. However, the measurement of the approach flow did not reach the water surface and the bottom wall exactly, therefore, the velocity profiles were linearly extrapolated towards $y = y_0$ and $y = 0$ before the integration as shown in Figure 5.4. The measured samples are represented by the black markers, whereas the linear extrapolation is indicated by the red lines and markers. Furthermore, the small plots zoom to the lower and upper end of the measured velocity profiles, respectively.

$$u_\mathrm{ref} = \frac{1}{y_0} \int\limits_0^{y_0} u(y)\, dy \tag{5.1}$$
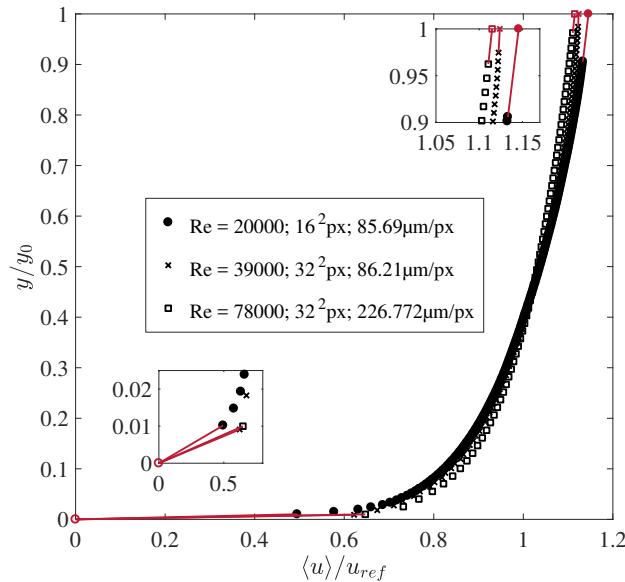
Figure 5.4: Time-averaged velocity profiles (black markers) of the approach flow for all Re normalized by the depth averaged velocity in the symmetry plane. Red markers and solid lines indicate the linear extrapolation towards the bottom of the flume and the water surface.

$\mathbf{Re = 20{,}000}$	Approach flow	Cylinder	Scour
T [°C]	20.0	18.4	21.1
ν [m²/s]	$1.01 \cdot 10^{-6}$	$1.0502 \cdot 10^{-6}$	$0.9837 \cdot 10^{-6}$
ρ [kg/m³]	998.22	998.53	997.99
u_{b} [m/s]	0.2	0.2	0.2
u_{ref} [m/s]	0.2091	0.2091	0.2091
L_{c} [m]	0.48	0.1	0.1
$\epsilon_{\text{macro}} \propto \frac{u_{\text{b}}^3}{L_{\text{c}}}$ [m²/s³]	0.0167	0.08	0.08
η_{K} [m]	$8.867 \cdot 10^{-5}$	$6.1686 \cdot 10^{-5}$	$5.8733 \cdot 10^{-5}$
$\tau_{\eta_{\text{K}}}$ [s]	$7.74 \cdot 10^{-3}$	$3.54 \cdot 10^{-3}$	$3.54 \cdot 10^{-3}$
$u_{\eta_{\text{K}}}$ [m/s]	0.0114	0.017	0.0167
$St_{\text{k}} = \tau_{\text{P}}/\tau_{\eta_{\text{K}}}$	$7.9 \cdot 10^{-4}$	$1.73 \cdot 10^{-3}$	$1.73 \cdot 10^{-3}$
Resolution [m/px]	$8.569 \cdot 10^{-5}$	$3.686 \cdot 10^{-5}$	$3.792 \cdot 10^{-5}|3.713 \cdot 10^{-5}$
$\mathbf{Re = 39{,}000}$	Approach flow	Cylinder	Scour
T [°C]	20.0	18.4	20.2
ν [m²/s]	$1.01 \cdot 10^{-6}$	$1.0502 \cdot 10^{-6}$	$1.005 \cdot 10^{-6}$
ρ [kg/m³]	998.22	998.53	998.18
u_{b} [m/s]	0.39	0.39	0.39
u_{ref} [m/s]	0.3986	0.3986	0.3986
L_{c} [m]	0.48	0.1	0.1
$\epsilon_{\text{macro}} \propto \frac{u_{\text{b}}^3}{L_{\text{c}}}$ [m²/s³]	0.1236	0.5932	0.5932
η_{K} [m]	$5.3734 \cdot 10^{-5}$	$3.7382 \cdot 10^{-5}$	$3.6172 \cdot 10^{-5}$
$\tau_{\eta_{\text{K}}}$ [s]	$2.84 \cdot 10^{-3}$	$1.30 \cdot 10^{-3}$	$1.30 \cdot 10^{-3}$
$u_{\eta_{\text{K}}}$ [m/s]	0.0188	0.0281	0.0278
$St_{\text{k}} = \tau_{\text{P}}/\tau_{\eta_{\text{K}}}$	$4.7 \cdot 10^{-3}$	$4.7 \cdot 10^{-3}$	
Resolution [m/px]	$8.621 \cdot 10^{-5}$	$3.686 \cdot 10^{-5}$	$3.807 \cdot 10^{-5}|3.735 \cdot 10^{-5}$
$\mathbf{Re = 78{,}000}$	Approach flow	Cylinder	Scour
T [°C]	21.0	20.7	–
ν [m²/s]	$0.986 \cdot 10^{-6}$	$0.993 \cdot 10^{-6}$	–
ρ [kg/m³]	998.01	998.07	–
u_{b} [m/s]	0.49	0.49	–
u_{ref} [m/s]	0.5219	0.5219	–
L_{c} [m]	0.48	0.16	–
$\epsilon_{\text{macro}} \propto \frac{u_{\text{b}}^3}{L_{\text{c}}}$ [m²/s³]	0.1730	0.7353	–
η_{K} [m]	$4.852 \cdot 10^{-5}$	$3.397 \cdot 10^{-5}$	–
$\tau_{\eta_{\text{K}}}$ [s]	$2.40 \cdot 10^{-3}$	$1.17 \cdot 10^{-3}$	–
$u_{\eta_{\text{K}}}$ [m/s]	0.0203	0.0292	–
$St_{\text{k}} = \tau_{\text{P}}/\tau_{\eta_{\text{K}}}$	$2.55 \cdot 10^{-3}$	$5.22 \cdot 10^{-3}$	–
Resolution [m/px]	$3.623 \cdot 10^{-5}$	$3.629 \cdot 10^{-5}$	–

Table 5.1: Estimation of the Stokes number and the Kolmogorov scales for all experiments

5.3 Wall-mounted Cylinder

The experimental set-up in front of a wall mounted cylinder is depicted in Figure 5.5. The light sheet entered the flow from above through the acrylic glass plate in the centre line of the rectangular flume (symmetry plane) parallel to the streamwise direction. The camera of the Mono-PIV configuration was mounted perpendicularly to the light sheet plane outside of the flume; thus, a rotation of the set-up around the cylinder centre was not possible during that measurement. The cylinder was mounted on the glass bottom of the flume that allowed the light sheet to pass through, and the coordinate system was aligned with the centre of the cylinder and the surface of the bottom wall. The field of view (FOV) was upstream of the cylinder, thus, in negative $x-$direction.

For both measurement configurations, i.e. approaching flow without cylinder, and in front of the cylinder, the locations of the corresponding field of view (FOV) are sketched in Figure 5.5, respectively. In order to study the turbulent boundary layer covering the entire flow depth, the grid resolution ineluctably turned out to be coarse. The size of one pixel varied between 86μm/px and 227μm/px in the approach-flow measurements depending on Re. The results of these measurements are further discussed in section 6.2.

The field of view in the measurements in front of the wall-mounted cylinder was concentrated on the most relevant area around the horseshoe vortex, which is directly at the cylinder wall junction, the spatial resolution could be increased to about 37μm/px, i.e. the size of one pixel in the images was smaller than the Kolmogorov length scales, (see Table 5.1).
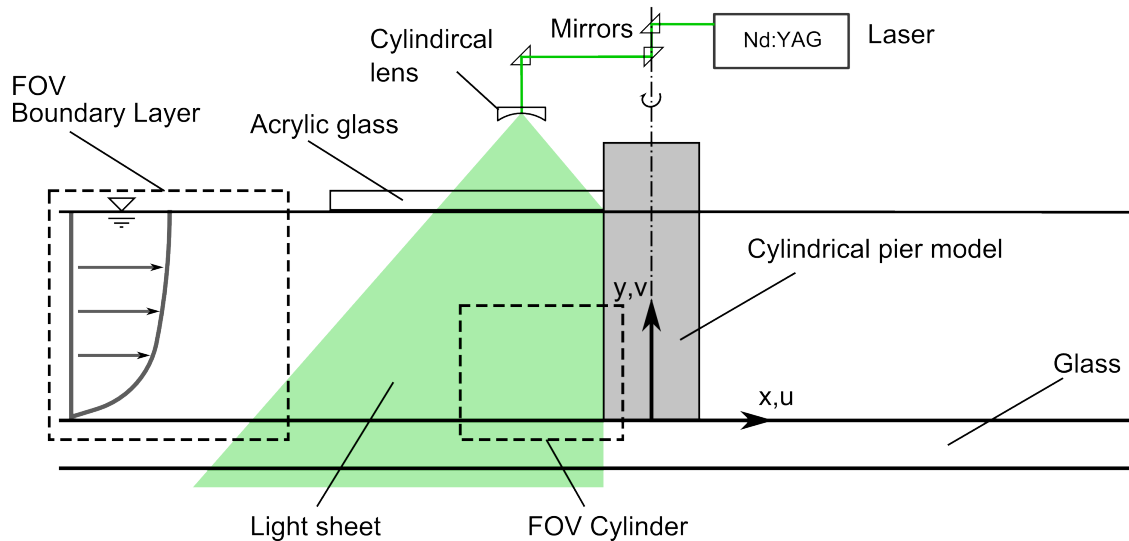
Figure 5.5: Detail of experimental set-up in front of a cylinder on flat plate including coordinate system

5.4 Scour Geometry

The set-up for the measurements around the scoured cylinder was similar to the one of the flat bed case; except of the scour model, which was installed instead of the transparent

bottom wall (see Figure 5.6). The coordinate system remained in the centre of the cylinder and at the height of the flat bed. Therefore, the measurement position in the scour hole was located in both negative $x-$ and $y-$direction. The spatial resolution was kept to be high at about 37 μm/px, therefore, the image sections of the cameras were too small to cover the entire region of the horseshoe vortex system including the cylinder. Consequently, two separate measurements with different FOV positions, one concentrating on the horseshoe vortex and another on the cylinder-wall-junction, had to be conducted for each Re as sketched in Figure 5.6, and the time-averaged fields were patched up in the end. Moreover, both FOV were recorded in the symmetry plane (0°) as well as at a lateral position (135°) around the scoured cylinder, which are illustrated in Figure 5.7; the lateral position of the light sheet at the scoured cylinder was, therefore, at 45° with respect to the inflow direction. Thus, eight different experimental runs were carried out in total to measure the flow for $Re = 20,000$ and 39,000 at 0° and 45°.

In order to patch up the corresponding data recorded at both FOV positions in either the symmetry plane or at an 45° angle, the data were interpolated to a common grid. Doing so, the FOV concentrating on the centre of the horseshoe vortex was taken as a starting point. The grid was expanded towards the cylinder, in order to cover the entire area of both measurement positions together, and the data of the FOV containing the cylinder-wall-junction was interpolated onto the global grid as the positions of the vectors of each FOV were not identical. Furthermore, the streamwise velocity profiles extracted at the same horizontal position in the centre of the overlapping region of both FOV were analysed with respect to the mutual conformity.

The rearrangement of the cameras when changing from one FOV to the other required to repeat the entire fine-adjustment and calibration process, which made it impossible to measure both FOV positions during the same experiment with identical experimental boundary conditions such as discharge or temperature. Therefore, both velocity profiles were not perfectly matching (see Figure 5.8 a) due to the variability in reproducing the experiment, which is further discussed in section 6.4. To overcome this effect, the ratio of both velocity profiles at $x/D = -0.85$ was determined at each vertical position and the median value of this ratio served as conformity factor to let both profiles match (see Figure 5.8 b).

Each time-averaged field such as the velocity components, the Re stresses, TKE and the corresponding budget terms were modified by this conformity factor. Applying this procedure resulted in time-averaged fields containing the information of both measurements. In the overlap region, both data sets were averaged after the application of the conformity factor to include both measurements equally, whereas the patched up grid outside the overlapping region consisted of the data of one or the other measurement. The overall quality of this procedure to put together the time-averaged fields based on the individual measurements was acceptable. However, the conformity factor could not entirely ensure that all fields matched equally, so that artefacts from this procedure can be seen in some fields at the boundary of the overlap region, but these artefacts do not affect the plausibility of the data.

The geodetic data of the scour were taken from Pfleger (2011), who measured the scour geometry that naturally developed in sand of median grain diameter $d_{50} = 1.9$mm. The experiment was stopped after one hour, which corresponded to about $14400D/u_{\mathrm{b}}$, and Pfleger

(2011) recorded the geometry using a laser distance sensor on a 5mm × 5mm grid. In order to investigate the flow field inside this scour hole, the geometry had to be fixed, i.e. reproduced as a steady model using the geodetic data of Pfleger (2011). A digital 3D-model was constructed, which was the basis for the milling process, documented in Figures 5.9a) to f): a solid block of aluminium of the size 469mm×390mm×100mm (length × width × depth) was mounted on the table of a vertical CNC-milling machine.

Figures 5.9a) and b) show the rough machining process using a 12mm radius cutter that modelled the contour of the scour geometry coarsely. Subsequently, the scour surface was smoothed during the finish machining step applying a 12mm radius finishing cutter (see Figure 5.9c) and d). Further, a cylindrical pier model of the diameter $D = 0.1$m was built using a turning lathe, and fitted into the circular pocket at the bottom of the scour hole to support the cylinder by a through-hole with thread (Figure 5.9 e). Finally, to increase the ageing resistance of the aluminium, and to alleviate the reflective behaviour of the surface, the entire scour-cylinder model was black anodized and installed in the test section of the water channel, shown in Figure 5.9 f).
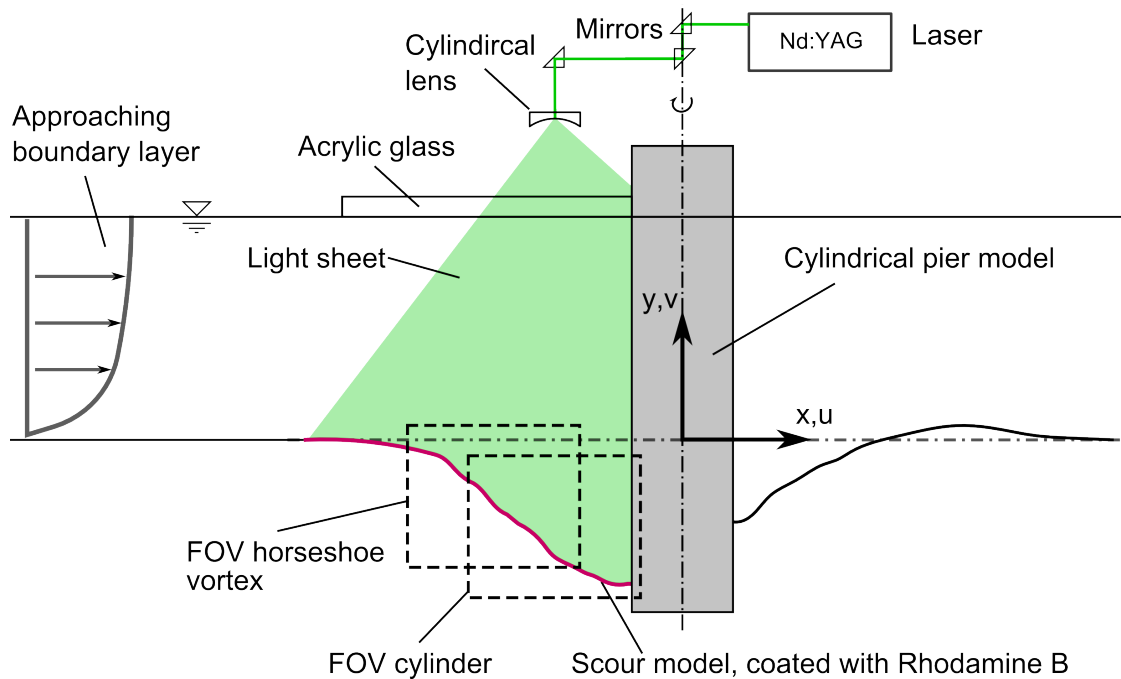
Figure 5.6: Detail of experimental set-up inside scour hole with coordinate system
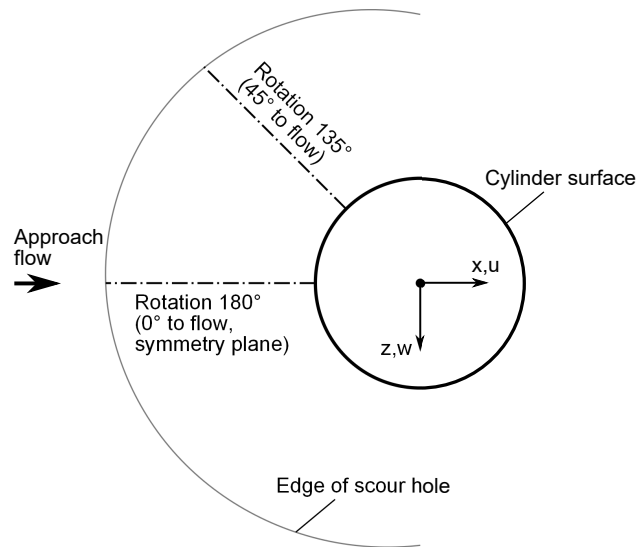
Figure 5.7: Top view of measurement positions 0° and 45° inside scour hole with coordinate system

a: Without conformity factor   **b:** With conformity factor
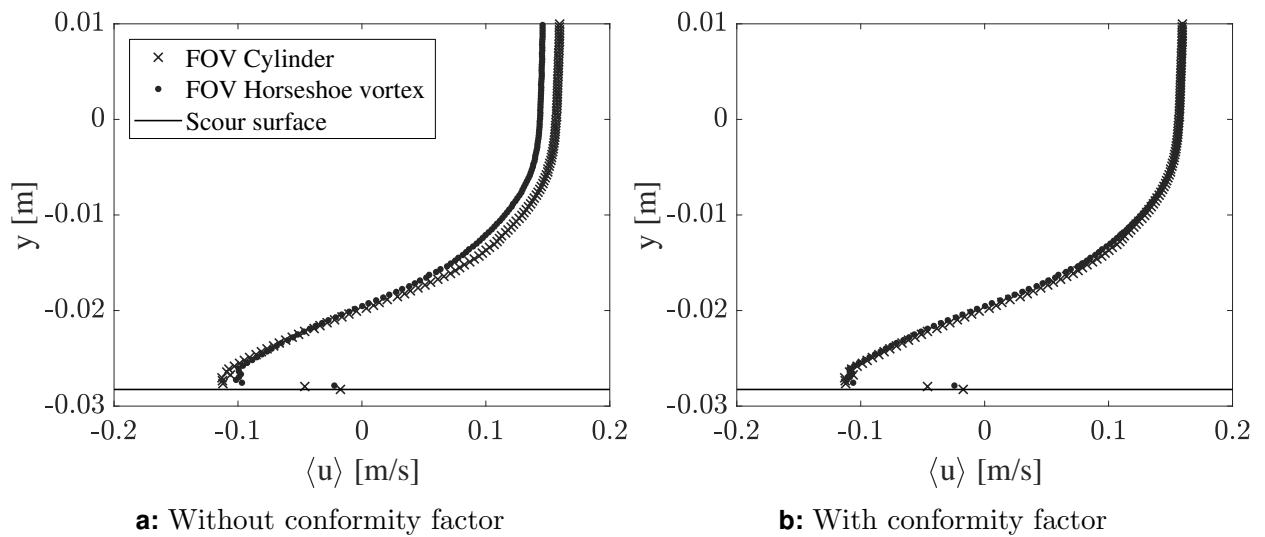
Figure 5.8: Time-averaged streamwise velocity profiles in the symmetry plane of the scoured cylinder at $x/D = -0.85$ stemming from both FOV at $Re = 20{,}000$, before (left) and after (right) the application of the conformity factor
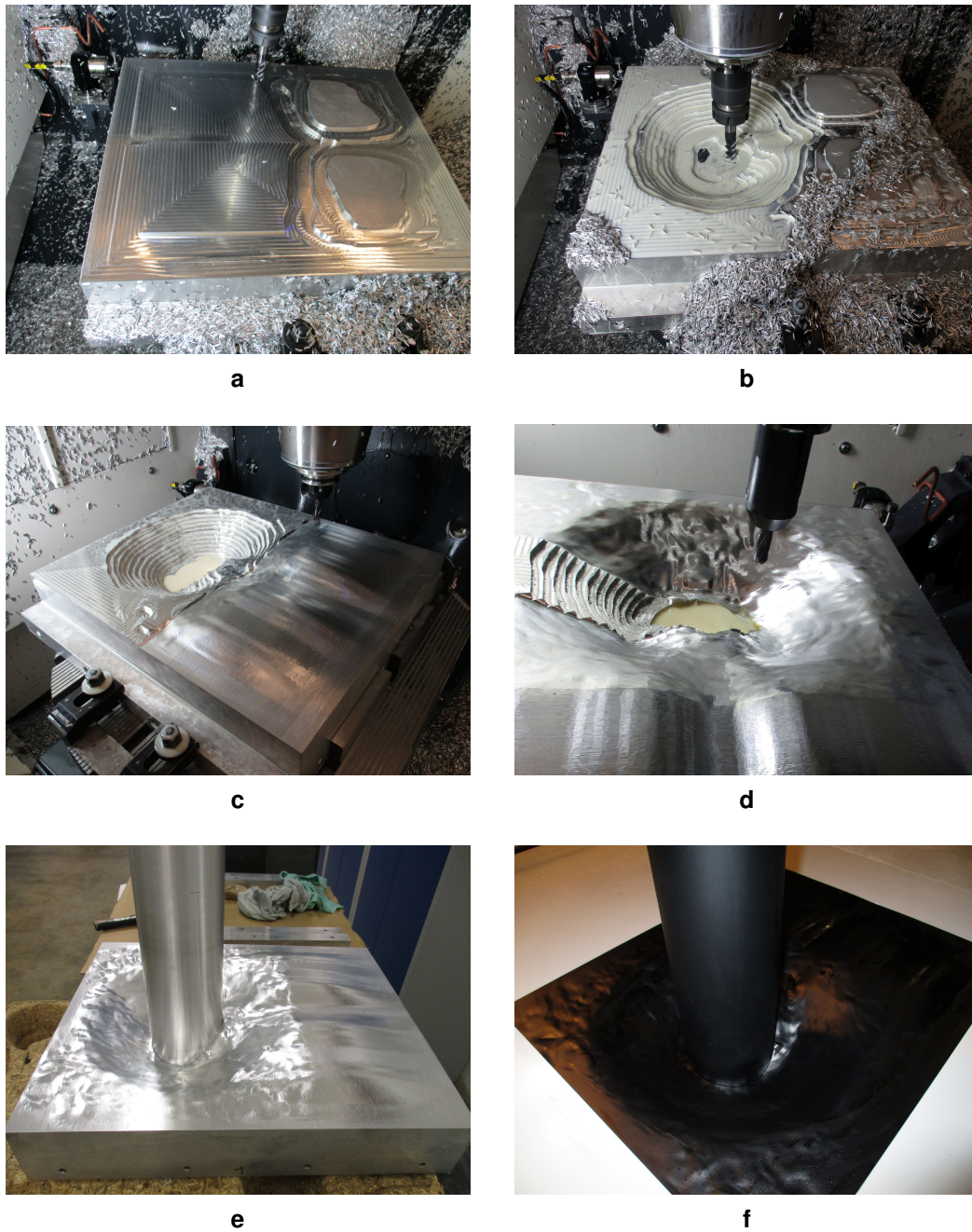
Figure 5.9: Milling process of scour geometry (images in courtesy of P. Schneider, TUM)

5.5 Surface Reflection

Surface reflections can cause many errors in PIV measurements. Highly exposed pixels of a CCD sensor add a high level of noise to the correlation function (cf. section 4.5) by lowering the contrast between moving particles and the stationary wall, which falsifies the results. In case of very strong exposure, the pixels start to show the so-called *blooming* effect (Adrian & Westerweel, 2011): a pixel array can be simplified as an array of empty buckets. The exposure of each pixel to light is represented by a certain amount of water in such a bucket; meaning that every pixel has a certain capacity for light, like a bucket that can accumulate water. When the maximum capacity is reached, a bucket would spill over to the neighbouring buckets starting a cascade of spilling buckets until a bucket can completely absorb the additional water load from the previous one. The same principle applies for pixels being over-exposed to light, when the light intensity in an image starts to flow or to "bloom", and in the worst case, this can damage the CCD sensor.

Therefore, surface reflections have to be avoided, in order to achieve high-quality PIV-images. Paterna *et al.* (2013) studied the performance of certain wall-treatment techniques in comparison of black painted wood, in order to suppress surface reflections of smooth plates effectively. They followed three main strategies of:

- absorbing the light energy
- directed reflection
- transmitting materials.

All three strategies contained several treatment techniques that performed differently. For the absorbing materials, a fluorescent paint showed the highest reflection reduction coefficient, which was 22.5 times higher than the one of black painted wood. The idea of a fluorescent wall coating is to shift the incoming wavelength of the absorbed light, and subsequently, to emit light with a different wavelength, which in turn will be blocked by a band pass filter mounted in front of the camera lens. When directing the reflection with a glass mirror the reduction coefficient became 21.1, whereas a transparent glass could reduce the reflections by a factor of 30.7.

The results of Paterna *et al.* (2013) indicate that a strategy should be chosen depending on the individual experimental situation, as each wall-treatment comes with several advantages and drawbacks. Rostamy *et al.* (2012), for instance, successfully applied black anodized aluminium to measure the flow field behind and on top of a submerged vertical cylinder. In the frame of this study, the reflective behaviour of different surface treatment techniques or materials such as Rhodamine B (Rh-B) coated polyvinyl chloride (PVC), black anodized aluminium, and acrylic glass were tested for the specific scour model shown in Figure 5.6. For simplicity, only one half of the 3D model was used, and the camera was perpendicularly mounted to the symmetry plane of the model, which was aligned with the light sheet approaching from above. I.e. the camera and the incoming light sheet formed a 90° angle. The local curvature of the scour surface had a strong influence on the suppressing performance of the strategies (Schuster *et al.*, 2015).

All three techniques suppressed the surface reflections significantly. However, the transmitting technique (acrylic glass) was not recommended since the transmitted light illuminated the whole model, which led to high background noise (Schuster *et al.*, 2015). Especially when the full set-up would be applied (cf. Figure 4.9), this bright background would add an

unacceptable level of noise to the particle images.

The Rh-B coated PVC model showed the lowest background noise due to the essential band pass filter that had a centre wavelength of 532nm and a band width of 10nm. Furthermore, it reduced the width of the reflection layer in the images above the surface, but this layer contained still very high intensity values. Especially in concave regions of the surface no reduction of the peak intensity could be noticed.

Working with Rh-B requires special precautions as both the car finish, which was used as substrate and the Rh-B pigments are noxious. Furthermore, the coating should be applied carefully to ensure that dust particles would not restrict the fluorescent characteristics. The quantum efficiency of Rh-B depends on several factors such as the applied solvent, the pH value, and the ambient temperature (Karstens & Kobs, 1980), and can also be reduced by the so-called *quenching effect* (Lindon *et al.*, 2016).

Finally, the black anodized aluminium showed low surface reflections independently of the curvature and very low background noise, while being robust and long-lasting. Taking these studies into account, the suppression strategies of surface reflections during the experiments were chosen as follows:

a) approach flow conditions (Mono-PIV): transmitting material (glass)

b) wall-mounted cylinder on flat plate (Mono-PIV): transmitting material (glass)

c) flow around a scoured cylinder (Stereo PIV): absorbing coating (black anodized aluminium).

For the experiments of campaigns a) and b), the considered strategies performed very well, and led to very low of surface reflections. The black anodized aluminium of the scour model (strategy c), however, did not show the desired performance when the cameras were mounted according to the Stereo-PIV set-up (cf. Figure 4.9), as the background noise and the surface reflections disrupted the particle images. This unfavourable position of the cameras observing the surface, thus all reflections with an angle of 45° from above, required the fluorescent coating strategy. Therefore, the black anodized aluminium scour model was coated with a transparent two component car finish including 10% Rhodamine B pigments. This wall treatment method reduced both the surface reflections and the background noise significantly, and provided good quality particle images (see Figure 5.10). However, due to the high-power laser irradiation during a measurement, the operating time of the Rh-B coating was limited, as the light sheet left a burnt imprint; thus, a periodic renovation of the finish was required.

Figure 5.16 a) shows the dewarped and binarized particle image of a measurement in front of the scoured cylinder using the Rh-B coating as surface treatment, whereas Figure 5.16 b) shows the method for determining the thickness of the reflective layer. In a first step, the original particle image was binarized and an edge detection method applied according to Canny (1986). This resulted in a black and white image showing the extracted surface reflection as a broad white strip (represented as ones), whereas the rest of the image remained black (zero), including the particles, which were filtered out in that way, see Figure 5.16 a) and b). The image matrix was scanned for the index of the first ”1” in each column, beginning from the upper and lower margin of the image, in order to detect the upper and lower bound of the reflection, respectively (see red dots in Figure 5.16 b)).

The thickness t was obtained by the vertical $\Delta\hat{y}$ and horizontal $\Delta\hat{x}$ distance between the upper and lower bound of the reflection layer forming a rectangular triangle. Further, the
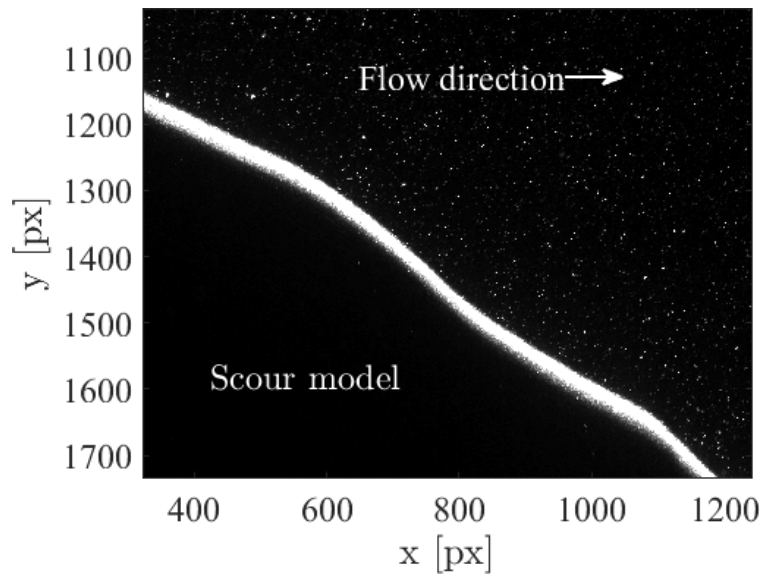
Figure 5.10: Dewarped particle images in front of a scoured cylinder with Rh-B coated model. Note that the seeding density is intentionally low to facilitate the determination of the reflection layer thickness.

height t of such a rectangular triangle corresponded to the thickness of the reflective layer and was computed as:

$$t = \frac{\Delta \hat{x} \cdot \Delta \hat{y}}{c}, \tag{5.2}$$

with c is the hypotenuse of the triangle. Repeating this procedure for the entire image, the average thickness of the reflective layer was $\langle t \rangle = 24.9$px.

Intending to improve the quality of PIV-images, Sciacchitano & Scarano (2014) suggested to apply a temporal high-pass filter on the snapshot time series, since particles that cross a pixel irregularly and surface reflections illuminating a pixel steadily can be expressed as two different frequencies: a high frequency corresponds to a particle following the flow, and a low frequency represents the surface reflection. By setting a certain threshold, these two frequency domains can be separated, and the lower one, which is related to disturbing surface reflections, can be filtered out. However, Sciacchitano & Scarano (2014) confine the efficiency of this filter as the minimum factor that separates the considered frequency domains should be equal to three.

While testing the Stereo-PIV set-up for the cylinder-on-flat-bed case (see section 5.3), this filter performed well and enhanced the quality of the images tremendously. Figures 5.11 a) and b) show a particle image in front of the wall-mounted cylinder on a glass surface recorded by Stereo-PIV. The horizontal and vertical red lines indicate the position of the bottom surface and of the cylinder, respectively. In this test, using the Stereo-PIV calibration target (see Figure 4.14) was sufficiently accurate to determine both positions of the wall and of the cylinder. Due to the installation of the cameras above the water surface and the resulting 45° viewing angle, the reflected laser light and the occurring background noise disrupted the quality of the particle images. The thickness of the reflective layer was approximately

20px wide, which corresponded to $6.54 \cdot 10^{-4}$m. By filtering the same particle image using a temporal high-pass filter suggested by Sciacchitano & Scarano (2014), the background noise as well as the surface reflection could be totally reduced (see Figures 5.12 a) and b)), and the only remaining part were the particle images following the flow. Figure 5.13 shows the impact of this filter by comparing the time-averaged streamwise velocity along a vertical line through the centre of the horseshoe vortex. The red dots correspond to the evaluation of the original particle images in which no valid vector could be obtained below approximately 3mm wall distance and the overall trend of the profile appears to be affected by the background noise. In contrast, using the filtered particle images the profile seems to be on one hand smoother and on the other hand the region close to the wall could be evaluated as well, as the first vector is located $4.37 \cdot 10^{-4}$m or 13.37px above the wall. Note, that the interrogation window size of the data without applying the filter was 32×32px, whereas including the filter 16×16px interrogation windows could be applied. A finer resolving evaluation of the original particle images, however, was not satisfying.

When applying the same method to snapshots corresponding to the scour experiment (cf. section 5.4), the image quality could not be improved, unfortunately, and the surface reflections were not successfully filtered, as the specified requirement of having sufficient distance between the two frequency domains was probably not fulfilled. After the application of this filtering technique, some particle images appeared to be corrupt and additional fake ones occurred as artefacts adding random noise to the image, thus, to the spatial correlation function (see eq. 4.12). Therefore, the high-pass filter was not applied to the scour experiment.

a: Original particle image   **b:** Zoom to reflection
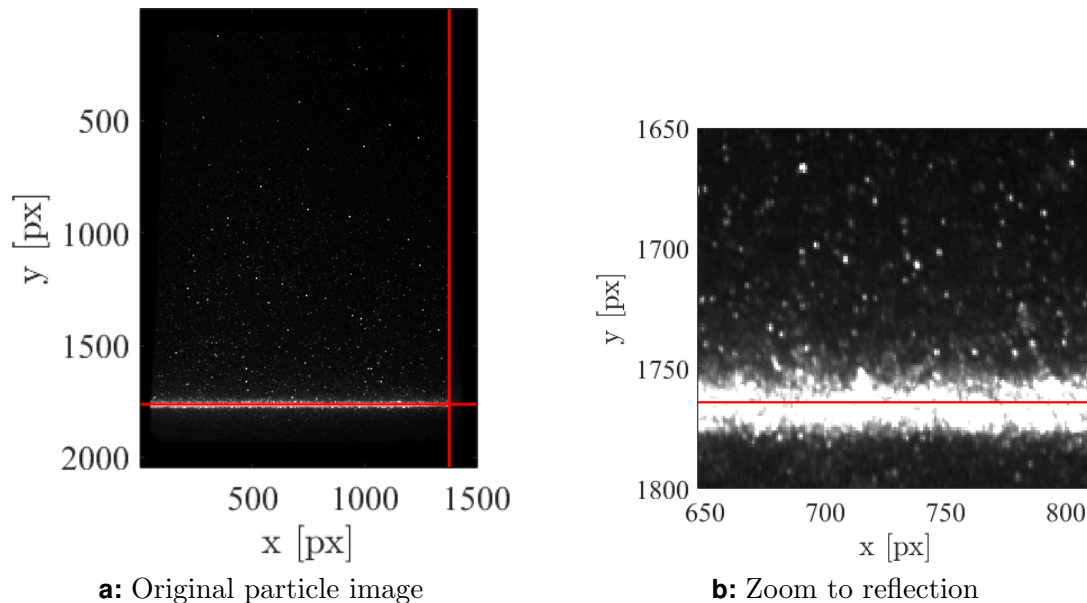
Figure 5.11: Particle image recorded by the Stereo-PIV in front of a wall-mounted cylinder on a glass surface

a: Original particle image   **b:** Zoom to reflection
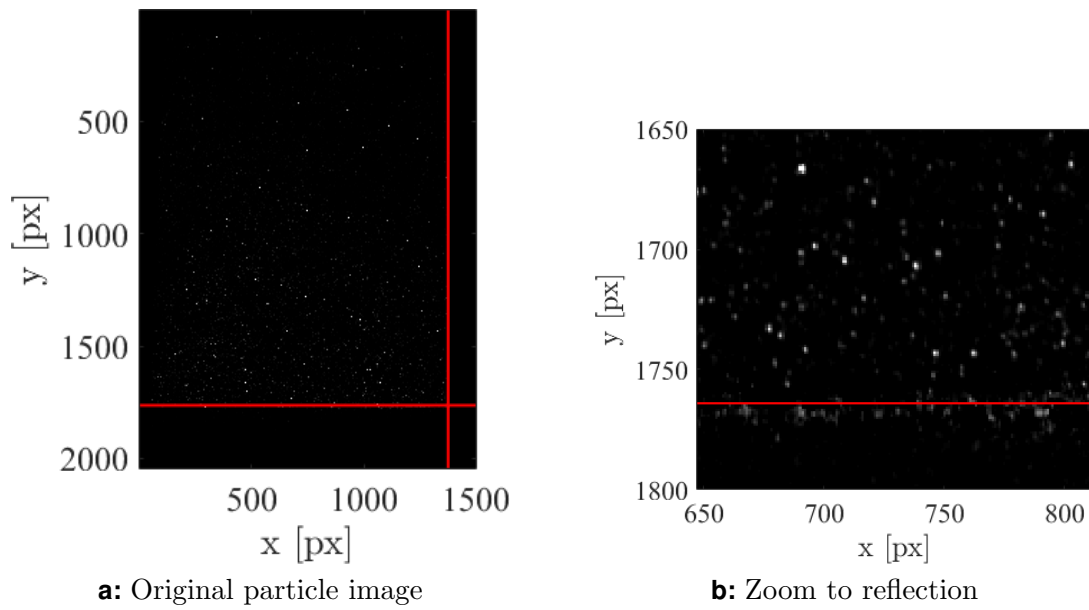
Figure 5.12: Enhanced particle image using a temporal high-pass filter (Sciacchitano & Scarano, 2014) recorded by the Stereo-PIV in front of a wall-mounted cylinder on a glass surface
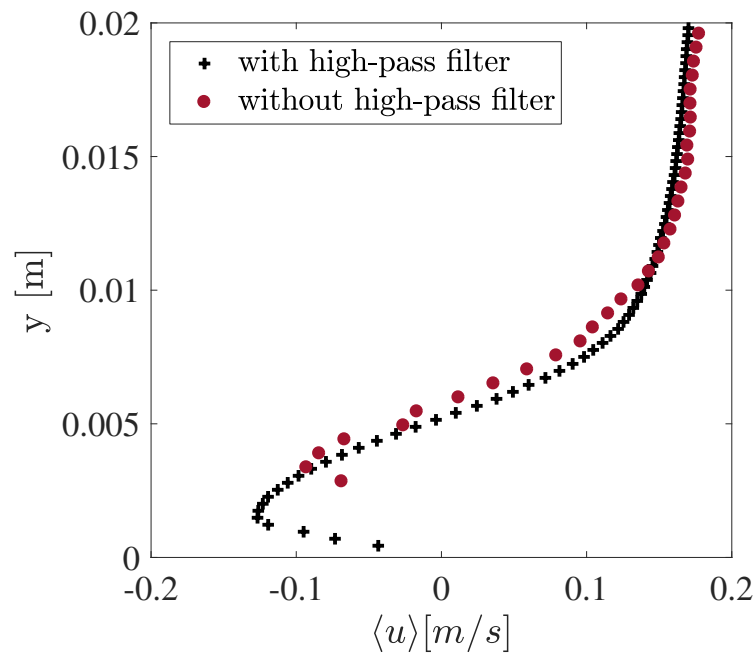
Figure 5.13: Time-averaged velocity profile along a vertical line at $x = x_{V1}$ of Stereo-PIV data with and without the application of a temporal high-pass filter

5.6 Position of the Wall in the Images

The determination of the position of the wall in the PIV-images should be handled carefully, especially when computing the wall shear stress. Extracting the wall from calibration images alone leads to a rough estimation of the position of the wall as:

- the target could be tilted or shifted with respect to the light sheet
- the target itself could contain uncertainties in representing the position of its markers
- defining the position of the markers in the calibration image is not fully objective, and depends on several parameters, e.g. the binarization threshold.

Furthermore, the wall is represented by a reflection layer in the particle images of 2 to 3px width (see Figure 5.14). When deriving the position of the wall from the position of the reflection layer in the particle images, the accuracy, therefore, is 2 to 3px, too. The viscous sublayer was estimated using the friction coefficient $c_f = -0.01$ in the wall-parallel jet obtained by Schanderl $et\ al.$ (2017) conducting a Large-Eddy simulation with high wall-resolution. The wall-shear stress can be obtained by $\tau_w = c_f \cdot u_{\text{ref}}^2 \cdot \rho/2$; further, with the friction velocity u_τ (see eq. 2.27) the thickness of the viscous sublayer is determined by $\Delta y^+ = 5 = \Delta y \cdot u_\tau/\nu$. Inserting the values of the experiment at $Re = 39{,}000$ in front of the wall-mounted cylinder yields $\Delta y_{\text{viscous}} = 1.863 \cdot 10^{-4}$m or 5.05px. At first glance, the accuracy of defining the position of the wall within 3px seems to be sufficient compared to the 5px thickness of the viscous sublayer, but the first vector is located above the wall at $y_1 = 2.76 \cdot 10^{-4}$m, which corresponds to about 7.5px, which is just above the viscous sublayer. Considering now the accuracy of 3px shows that the sensitivity of the wall shear stress estimation concerning the wall position is large and, therefore, defining the position of the wall in the particle images or by using the calibration target would not be sufficiently accurate, and more advanced approaches have to be followed.

Wall-mounted cylinder / Mono-PIV As sketched in Figure 5.5, the bottom of the flume was made from transparent glass; thus, the particle images were mirrored at the glass surface (see Figure 5.14). By applying a cross-correlation based PIV algorithm, the displacements and, subsequently, the velocity vectors were computed for the entire image represented by the interrogation windows. As the particle image pairs in the frames A and B were mirrored at the glass surface, the interrogation windows above and below the glass surface contained identical particle images, which led automatically to symmetric velocity profiles (see Figure 5.15). Therefore, the following two ideas were tested to determine the position in the PIV-images:

- fitting a polynomial in both the real and the mirrored velocity profiles, and seeking the point of intersection according to Jenssen $et\ al.$ (2016a)
- identifying particle clusters and their mirrored partners in the particle image to locate the reflecting surface.

The applied polynomial was assumed to be of second order as Schanderl & Manhart (2016) showed that the flow in front of a wall-mounted cylinder is in a non-equilibrium state and the velocity profiles are of second order near the wall. Hypothetically, the fitted models should intersect with each other at the location that meets the condition $u(y = 0) = 0$; thus, defines the position of the wall. However, this condition was only approximatively met as indicated in Figure 5.15 a) and b) where the models (dashed lines) intersect each other close

to the zero velocity, but not precisely.

Furthermore, the number of velocity samples that contributed to the fitting procedure had a major influence on the final result. Since the interrogation-window-cross-correlation technique is prone to generate biased vectors near the wall (Kähler *et al.*, 2012), outliers occurred and undermined the quality of the fit, thus, wall estimation. Therefore, the number of velocity samples supporting the fit had to be adjusted in all conscience, and was, consequently, rather arbitrarily than objectively set.

In order to overcome a possible misalignment of the camera with respect to the horizon, i.e. the bottom of the flume, the procedure was repeated for several locations within the image. However, this led to strongly varying results for the location of the glass surface (± 5px), and appeared to be too sensitive regarding the outliers near the wall. Although, the fitting method seemed to be unbiased and sophisticated in the first place, this approach contained too many sources of error, and could not be applied.

However, the second approach that intended to identify particle clusters within the images directly, led to more promising results than the fitting method, and appeared to be the simpler and more efficient technique. The surface of the flume bottom was assumed to be plane; thus, appeared linearly in an image. Therefore, at three different locations at the left, in the centre, and at the right edge of the image, the positions of several characteristic particle images and their mirrored partners were identified, and half the distance between each particle and its mirrored partner resulted in the position of the reflecting surface. This procedure suffered only from the uncertainty of locating the coherent particle images, which was estimated to be within the range of $1 - 2$px; thus, the wall was determined using this method in the Mono-PIV images.

Scoured cylinder / Stereo-PIV   Unlike the measurements in front of the wall-mounted cylinder with a plane transparent glass bottom reflecting the particle images and allowing to identify the wall position, the experiments around the scoured cylinder using Stereo-PIV could not benefit from this feature. As sketched in Figure 4.9, the cameras were mounted to observe the light sheet inside the scour hole, i.e. observing the surface reflection with an 45° angle from above.

Therefore, a particle image was binarized and filtered, in order to determin the upper and lower bound of the reflective layer (cf. section 5.5). Assuming a symmetric reflection with respect to the object plane ($z = 0$), the wall surface was finally determined by averaging the bounds at each column of the image (red squares in Figure 5.16 b). This approach resulted in a first approximation of the position of the scour surface within an image. Furthermore, the estimated position of the surface had to be refined in a second step: the Cartesian vectors of the measured flow field were transformed into a scour-oriented coordinate system (a detailed description of this transformation is given in appendix 10). Doing so, the vectors were oriented parallel and normal to the surface, and the distance from each vector perpendicular to the scour surface was calculated using the individual normal vectors (see dashed blue lines in Figure 5.17 a)).

In the interrogation window based PIV technique, each vector represents the spatial average of the corresponding area of an IW. When the interrogation window (indicated by the dotted lines in Figure 5.17 a) is intersected by some boundary (e.g. scour surface, solid line

in Figure 5.17 a)), the corresponding vector turns out to be corrupt in terms of the location, as the true position would rather be in the centroid of the remaining area than in the centre of the IW. Therefore, the data points closest to the wall in Figure 5.17 b) deviate from the apparently linear trend of the data points directly above.

The wall-normal distance, at which this bend occurs, correlates with half the diagonal length of the interrogation window, i.e. when an IW starts to be intersected by the scour surface. The vectors that have a wall-normal distance smaller than this critical threshold are highlighted in Figure 5.17 a) by dashed red lines. Furthermore, a first order polynomial was iteratively fitted with increasing number of data points above that critical distance starting with three samples. The correlation coefficient ρ_{fit} (see eq. 5.3) was applied, in order to find the number of data points supporting best the linear fit. This coefficient was calculated using the covariance of the model and the input data, divided by the corresponding standard deviations, which refers to the linear correlation between the data points u_{meas} and the considered model of first order $f^1(u_{\mathrm{meas}})$.

$$\rho_{\mathrm{fit}} = \frac{cov(f^1(u_{\mathrm{meas}}), u_{\mathrm{meas}})}{\sigma_{f^1(u_{\mathrm{meas}})}\sigma_{u_{\mathrm{meas}}}} \tag{5.3}$$

The profile of the wall-parallel component of the vectors $\langle u_{\mathrm{r}} \rangle$ along the scour-surface-normal distance X_{n} is plotted in Figure 5.17 b). The data points were extracted at the horizontal position $x/D \approx -0.94$, which corresponds to the foot of a normal vector with respect to the scour surface and pointing in the direction of the HV centre. In addition, to increase the number of data points four neighbouring velocity profiles were combined to one profile before the linear fit was applied.

The maximum linear correlation was found for the first nine data points (encircled) above the mentioned critical distance (dotted red line); thus, the velocity profile was assumed to be linear in that region, and the first order polynomial supported by these first nine data points was used to extrapolate the velocity profile towards the wall (see Figure 5.17 b). Due to the no-slip condition (see section 2.4.1), the velocity must be equal to zero at $X_{\mathrm{n}} = 0$. However, this was not the case here; therefore, the position of the scour surface had to be corrected by $2.9165 \cdot 10^{-4}$m, which corresponded to 7.85px, in order to meet the no-slip condition.

The effect of the corrected wall position shows Figure 5.18. The viscous shear stress normalized by the gradient of the corresponding linear fit along X_{n} is plotted for the uncorrected (grey 'x'), and for the corrected data based on the fit including nine data points (black dots). Since a secondary maximum of the correlation coefficient appeared when five points were included, the corrected data based on a corresponding fit (hollow red squares) are presented, too. The blue crosses represent data in front of the wall-mounted cylinder and reveal a similar decay of the wall shear stress with increasing wall distance, but indicating no constant level of the wall shear stress and that no linear trend between the velocity and the wall distance could be obtained. Schanderl *et al.* (2017) observed an underestimation of the wall shear stress using the same PIV data.

Without correcting the estimated position of the wall, the wall shear stress does not approximate a constant trend; thus, does not indicate linearity. However, due to the correction method, the wall shear stress scatters around a plateau and confirms a linear trend, before

it strongly decreases with increasing distance to the wall. The decay starts after nine data points in both cases; hence, defines a limit for the linear fit (vertical line), and verifies the correction of the position of the estimated scour surface. Moreover, the width of the scatter in the linear region can be taken as uncertainty of the estimated wall shear stress, which is 10% in this case.

This method seems to indicate a linear relation between the wall-parallel velocity and the wall distance. The reliability of the presented results, however, have to be further approved to be able to derive a linearity based on these data. On one hand, the vector field in Figure 5.17 a) reveals a strong wall-normal component close to the scour surface, which is counter intuitive, and therefore has to be further investigated. On the other hand, the velocity profile in Figure 5.17 b), shows a sudden kink after the quasi-liner trend, and might be the result of a zero-pressure gradient at this location. However, due to these reasons, the data near the wall have to be treated with caution particularly when estimating the wall-shear stress.
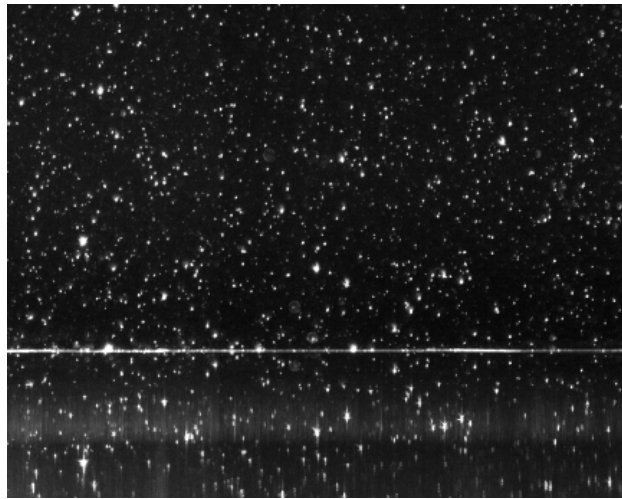
Figure 5.14: Mirrored particle image and the $2 - 3\text{px}$ wide reflective layer along the glass surface

a: $x \approx -1.0D$ **b:** $x \approx -0.73D$
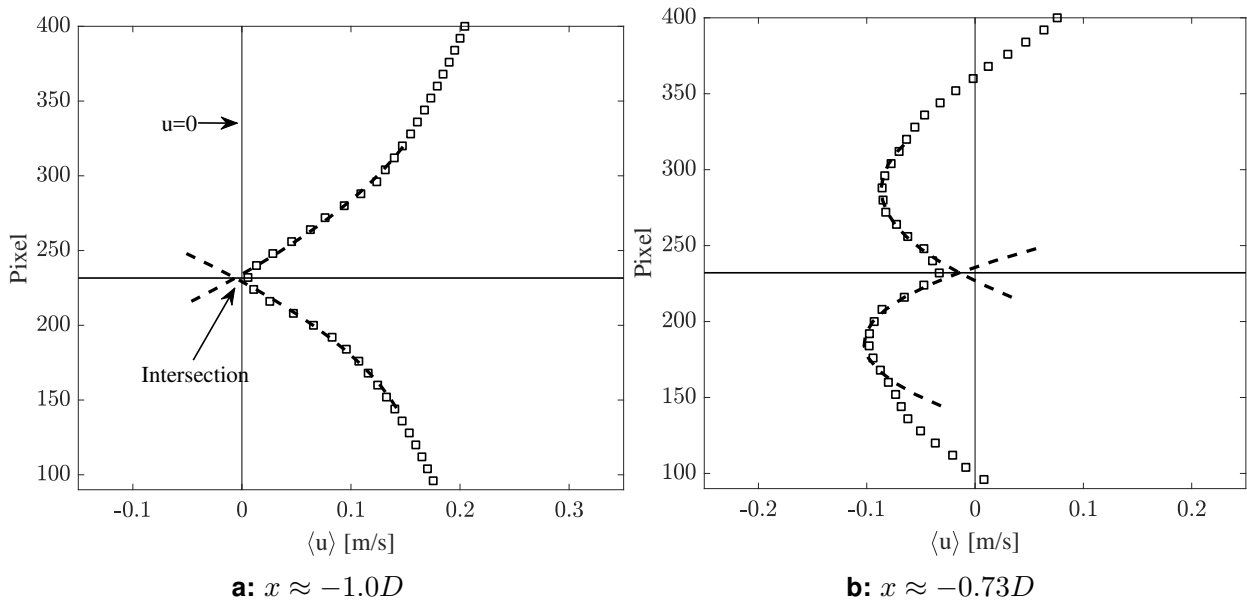
Figure 5.15: Mirrored time-averaged velocity profiles in front of a wall-mounted cylinder including second order polynomial fit (Jenssen *et al.*, 2016*a*)

a: Dewarped image **b:** Zoom to reflection
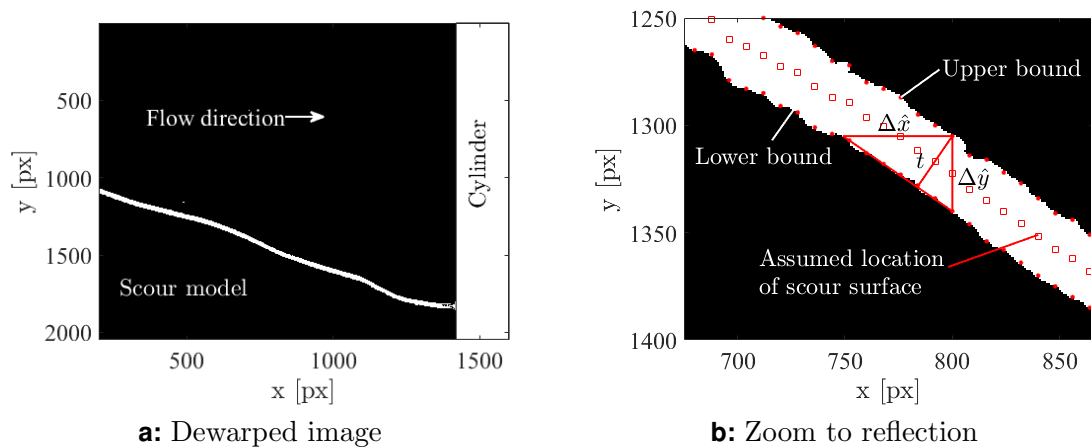
Figure 5.16: Binarized particle image in front of a scoured cylinder with Rh-B coated model

a: Vector field in the scour hole

b: Profile of surface-parallel component along the wall normal coordinate
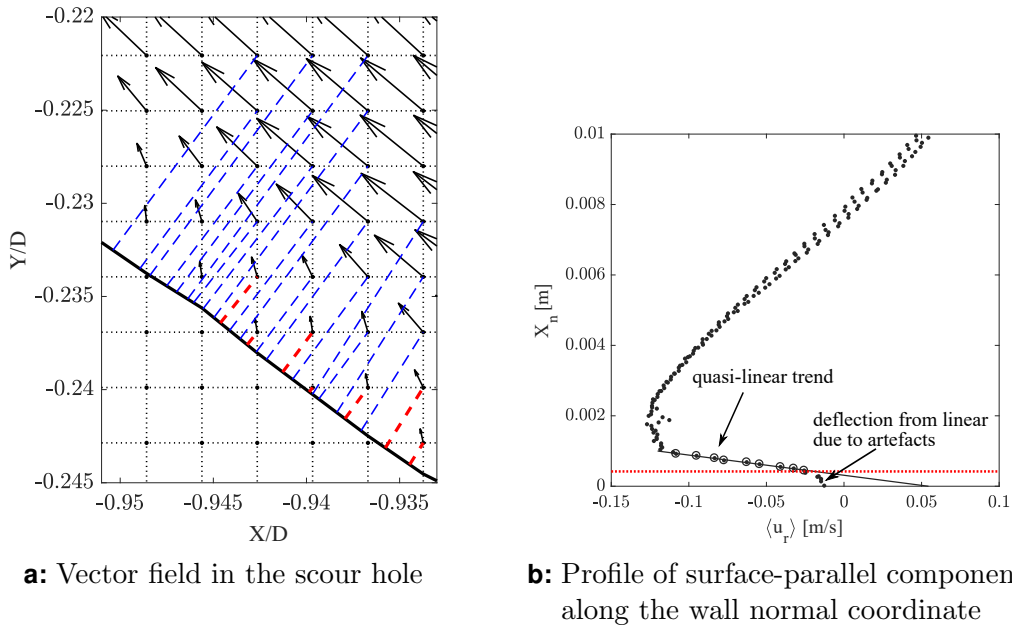
Figure 5.17: Wall correction in the scour experiment at the horizontal position $x/D \approx -0.94$
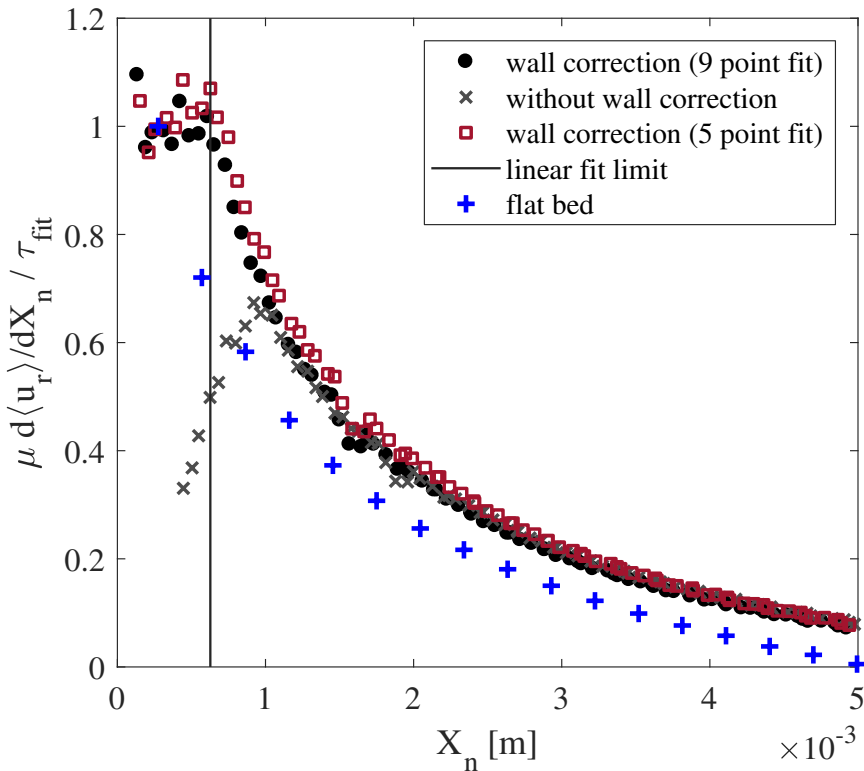
Figure 5.18: Profile of viscous shear stress normalized by the gradient of the polynomial fit along the corrected and uncorrected scour-normal distance at $x/D \approx -0.94$

6 Measurement Validation

Numerous sources of errors can occur while conducting PIV experiments; thus, comparing the results to accepted benchmarks in the literature is necessary to validate the quality of the experimental set-up. Here, the results of the approaching flow, i.e. the hydraulic boundary conditions, are used to verify the experiments. An other crucial task is to ensure that the measurements are reproducible and that the observed values are statistically converged. In this study, two PIV approaches were employed (Mono- and Stereo-PIV); thus, their performance and reliability is tested by mutually comparing the results for the same flow configuration.

6.1 Determination of the Wall Shear Stress in the Approaching Flow

To study the flow approaching the cylinder, measurements without an obstacle were performed (see section 6.2). The field of view within those measurements was chosen to cover the whole flow depth, which resulted in a lack of spatial resolution, as the area that was projected onto the camera sensor was larger compared to the measurements including a cylinder.

If the first measurement point is located in the linear region (viscous sublayer), the wall shear stress can be determined directly from eq. 2.1 by calculating the velocity gradient at the wall $\frac{\partial u}{\partial y}\big|_{y=0}$. However, the size of a pixel in an image covering the whole flow depth varied from about 87µm/px up to 226µm/px depending on the Reynolds number. These resolutions appeared to be too coarse to calculate the wall shear stress τ_w correctly.

To deal with this problem, Clauser (1954) suggested to iteratively calculate the friction coefficient c_f instead of the gradient at the wall. This method assumes that the velocity profile matches the log-law region somewhere in the outer layer ($y^+ > 50$, cf. Pope (2013)). On both sides of eq. 6.1, the unknown u_τ appears; therefore, the common equation for the log-law

$$\frac{\langle u(y)\rangle}{u_\tau} = \frac{1}{\kappa} ln\left(\frac{yu_\tau}{\nu}\right) + B \tag{6.1}$$

is rearranged by including the following relation with u_∞ as the free-stream velocity:

$$c_\mathrm{f} = 2\left(\frac{u_\tau}{u_\infty}\right)^2. \tag{6.2}$$

Furthermore, when multiplied by u_τ/u_∞ the new equation reads (Wei *et al.*, 2005):

$$\underbrace{\frac{\langle u(y)\rangle}{u_\infty}}_{\text{known}} = \frac{1}{\kappa}\sqrt{\frac{c_\mathrm{f}}{2}}ln\left(\frac{yu_\infty}{\nu}\right) + \frac{1}{\kappa}\sqrt{\frac{c_\mathrm{f}}{2}}ln\left(\sqrt{\frac{c_\mathrm{f}}{2}}\right) + B\sqrt{\frac{c_\mathrm{f}}{2}}, \qquad (6.3)$$

where c_f is the remaining unknown appearing only on the right hand side of eq. 6.3, and is determined iteratively. The friction velocity u_τ is then obtained from eq. 6.2 and the wall shear stress τ_w is calculated as:

$$\tau_\mathrm{w} = u_\tau^2\rho. \qquad (6.4)$$

To confirm the generic assumption of Clauser (1954) that the velocity profile would match the log-law, an additional measurement of the approach flow $Re = 78,000$ was performed zooming in to the near-wall region to determine the wall shear stress directly supported by a high spatial resolution; thus, to verify the method of Clauser (1954) for this set-up. Therefore, the spatial resolution could be increased to approximately 36µm/px, and the first data point was located in the viscous sublayer at $y^+ = 4.4$, which enabled the direct calculation of the wall shear stress by using eq. 2.1, and subsequently of the friction velocity u_τ using eq. 2.27.

The corresponding results are listed in Table 6.1: the method of Clauser (1954) seems to slightly underestimate the wall shear stress by about 4% with respect to the direct calculation using the near-wall velocity gradient. As the friction velocity and the wall shear stress are linked quadratically, the relative error in u_τ decreases to about 2%. By considering the uncertainty of reproducing identical flow conditions at two different days, these differences become acceptable as the total uncertainty of the Reynolds number is already 1.55% at $Re = 78,000$ (see section 6.4)). Therefore, the method of Clauser (1954) could be validated for this set-up on the one hand, and on the other hand the validity of this method is transferred to the other configurations ($Re = 20,000$ and $Re = 39,000$). The direct calculation of the wall shear stress of $Re = 78,000$ is considered to be the most uncertain one, as the viscous sublayer is the smallest for this Re and reveals the largest potential error.

	τ_w	u_τ
Direct method	0.5223 N/m^2	0.02285 m/s
Clauser (1954)	0.5006 N/m^2	0.02237 m/s
ϵ	4.15%	2.10%

Table 6.1: Relative error in the wall shear stress estimation directly obtained from high resolution data and by the method of Clauser (1954) for $Re = 78,000$

6.2 Approaching Flow Conditions

6.2.1 Short entry length

To begin of this study, the experimental set-up was a little different to the description in section 5.1 as the full length of the channel was not available. The flume was initially about 6m long, which corresponded to $40y_0$ at $Re = 39,000$. The approaching flow conditions with this short entry length were studied first, but the time-averaged streamwise velocity profile appeared not to be fully developed after this distance. For this reason several methods to enhance the development of the logarithmic boundary layer were implemented at the beginning of the flume and tested: (i) a 2m long rough gravel layer with median grain diameter $d_{50} = 3.5$mm; (ii) vortex generators suggested by Armitt & Counihan (1968) and improved by Counihan (1969) (see Figure 5.2); (iii) a combination of the roughness layer and the vortex generators.

Figure 6.1 compares these three approaches of working with a short entry length to generate a fully developed turbulent boundary layer by showing the time-averaged streamwise profiles, which were normalized by their depth averaged value. As a reference, the boundary layer simulated by Schanderl (2018), the streamwise velocity profile measured by Pfleger (2011) in the same channel as the present study, and the boundary layer developed along the entire entry length were added[1]. The three approaches show strongly varying results and none of them seems to have generated satisfactorily a fully developed turbulent boundary layer.
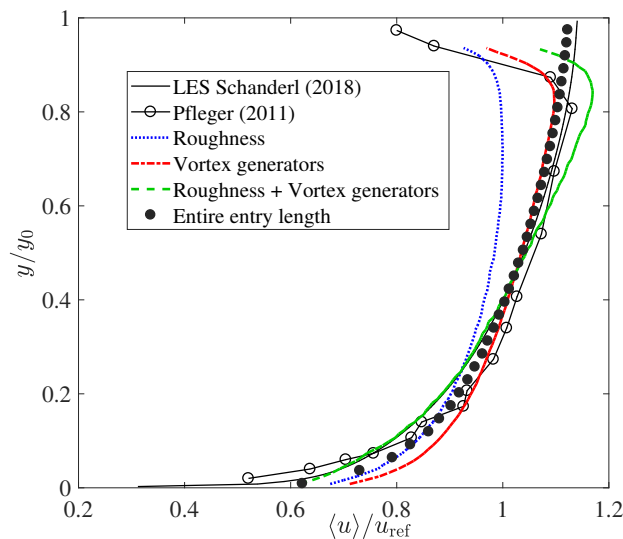
Figure 6.1: Time-averaged streamwise profiles of the approach flow for $Re = 39,000$ normalized by the depth averaged velocity in the symmetry plane

---

[1] The decay of some of the velocity profiles was caused by an acrylic glass plate at the water surface covering the whole width of the flume, which was installed to reproduce the same configuration as Pfleger (2011). This large plate was, however, not used in other measurements and should not be mistaken with the slender slat described in section 5.1.

6.2.2 Entire entry length

After the approach failed to generate a fully developed logarithmic boundary layer with the short entry length of the flume, the inlet of the flume was moved further upstream such that the test section was located 20m after the inlet (cf. section 5.1). As for $Re = 78,000$ a larger diameter D and flow depth y_0 were used, the relative entry length decreased from $133y_0$ at ($Re = 20,000$ and $Re = 39,000$) to $83y_0$ at $Re = 78,000$ (more details are provided in Table 9.1 in appendix 9).

Experiments on the secondary current patterns suggest an entry length of 60 to 70 hydraulic diameters D_h, which is defined as four times the hydraulic radius R_h, in order to generate fully developed secondary current structures (Gessner, 1973; Demuren & Rodi, 1984). However, the results of Tominaga *et al.* (1989) and Blanckaert *et al.* (2010) show secondary flow structures with a relative entry length of only $25D_h$ and $13D_h$, respectively. In the set-up of this study, the entry length was 30 to $40D_h$.

Figure 6.2 shows the time-averaged velocity profiles for all three Reynolds numbers in the symmetry plane of the flume normalized by the flow depth and the depth-averaged streamwise velocity (see eq. 5.1). In all three cases, the approaching velocity profiles follow a logarithmic shape. Moreover, the known *Re*-dependency of turbulent boundary layers becomes apparent as the velocities in the lower third of the profiles tend to accelerate with increasing Re, whereas those in the upper third decrease likewise.

Graphs a) to e) of Figure 6.3 show the results for the approach flow of each *Re* in the inner scaling, i.e. using the wall units y^+. Data from the literature are used as a reference to validate the present findings. The paper of Fernholz & Finley (1996) combines several data sets from the literature to provide a review of the turbulent boundary layer of incompressible flows with zero pressure gradient. The data extracted from Fernholz & Finley (1996) were measured by Bruns *et al.* (1992) using a hot wire anemometer.

The field of view was chosen to represent the whole flow depth to document the complete velocity profile. The method of Clauser (1954) was applied to compensate for the lack of spatial resolution and to determine the wall shear velocity (cf. section 6.1). In case of $Re = 78,000$ additional measurements were performed with higher spatial resolution in the near-wall region to gather data within the viscous sublayer.

As seen in Figure 6.3 a), all profiles show the theoretical logarithmic behaviour. The measurement data for $Re = 20,000$ and $Re = 39,000$ reach the buffer layer $5 < y^+ < 30$ (Pope, 2013), whereas the $Re = 78,000$ data cannot resolve any near-wall pattern as the first point is located at $y^+ \approx 50$.

The profiles for the Reynolds normal stresses ($\langle u'^2 \rangle$ and $\langle v'^2 \rangle$) and the Reynolds shear stress ($\langle u'v' \rangle$) are normalized with u_τ^2 and depicted respectively in the plots b), c), and d) of Figure 6.3. All experimental data follow approximately the results of Bruns *et al.* (1992) in trend and amplitude. The data are classified using the *Re* based on the momentum thickness $\Theta(x)$, defined in eq. 6.5 and eq. 6.6.

$$\Theta(x) = \int_0^\infty \frac{\langle u \rangle}{u_\infty} \left(1 - \frac{\langle u \rangle}{u_\infty} \right) dy \qquad (6.5)$$

$$Re_\Theta = \frac{u_\infty \Theta}{\nu} \tag{6.6}$$

The turbulence intensity of the streamwise velocity component of all cases (see Figure 6.3 graph e)) match the reference results as well. Furthermore, the turbulent kinetic energy k, defined in eq. 2.18 and normalized with u_τ^2, is given in the outer scaling (y/y_0). The data of this study match the reference profiles in the near-wall region and coincide in the outer region; thus, indicate similarity of the experimental set-up (Fernholz & Finley, 1996). Due to these findings, the approaching turbulent flow conditions are considered to be fully developed and validated.
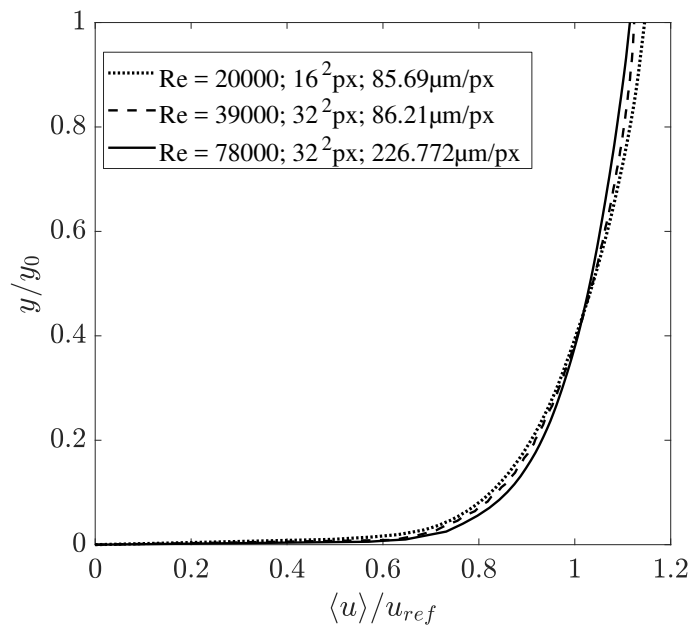
Figure 6.2: Time-averaged velocity profiles of the approach flow for all Re normalized by the depth averaged velocity in the symmetry plane
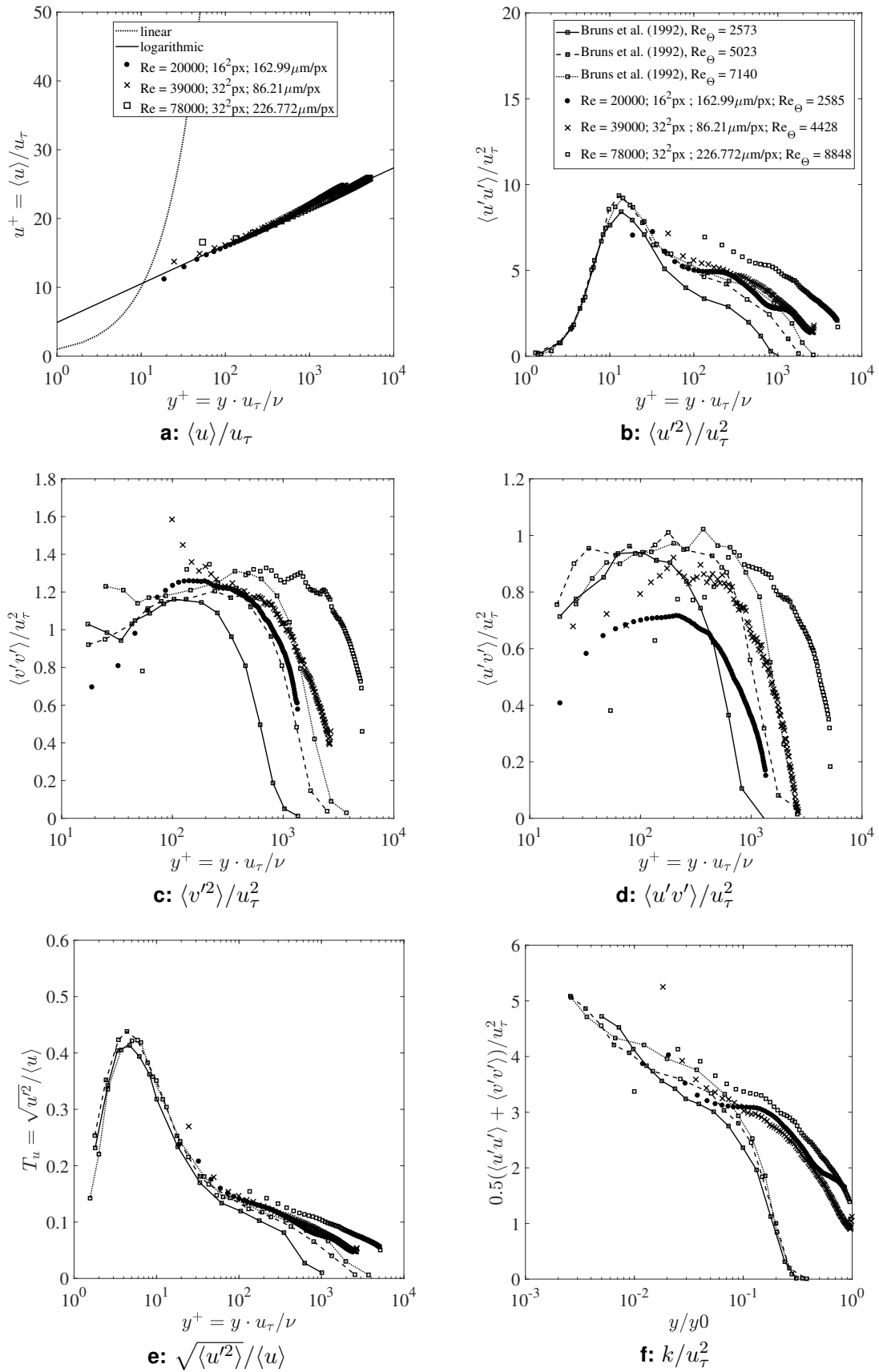
Figure 6.3: Time-averaged profiles of turbulence statistics of the approach flow for all *Re*. Note: graphs a) to e) are in inner scaling, whereas f) is given in outer scaling.

6.3 Influence of the Acrylic Glass Plate on the Water Surface

As described in section 5.1, a small plate of acrylic glass had to be mounted on top of the water surface to suppress occurring waves and to let the light sheet enter the flow without interference; especially during the experiments around a cylinder. However, any component of the set-up submerged into the flow, provoked disturbances, i.e. errors with respect to the intended situation.

The impact of this plate on the flow pattern in front of a cylinder is impossible to quantify experimentally with the set-up designed here. Surface waves are generated directly upstream the cylinder that prevent any optical accessibility from above. Therefore, a numerical case study was conducted by Alfaya (2016) showing that the influence of this component on the flow structure is mainly limited to the surface, and therefore, the vortex system at the cylinder-wall-junction remains nearly unchanged by this plate. Additionally, the influence of this plate on the approach flow conditions was investigated experimentally at $Re = 39,000$ to support the validity of the numerical conclusions on the experimental set-up.

Doing so, the acrylic glass plate was removed and the light sheet entered the water body from above directly through the water surface and the approaching flow could be measured with and without the acrylic glass plate. Figure 6.4 shows the comparison between the results with and without plate at the water surface for $Re = 39,000$ measured by Mono-PIV with a spatial resolution of $86.21\mu m$/px and evaluated by 32×32px interrogation windows. Moreover, the approach flow was measured using the Stereo-PIV with the acrylic glass plate on the water surface, in order to validate the reliability of the results. The spatial resolution was $91.75\mu m$/px and the IW size identical to the Mono-PIV (32×32px). In the Mono-PIV set-up, the Reynolds number based on the momentum thickness Re_Θ (see eq. 6.6) was 4428 and 6124 for the free surface and the case with acrylic glass plate, respectively. Whereas, in the Stereo-PIV experiment Re_Θ was 2999.

Considering the profiles of the logarithmic boundary layer, horizontal Re-stresses and of the turbulence intensity (see Figures 6.4 a, b and e), the impact of the acrylic glass plate on the flow structure is small, and the results stemming from Mono-PIV and Stereo-PIV match each other sufficiently, and allow to trust both methods equally. Moreover, the difference between the Stereo-PIV results and the Mono-PIV results seems to be larger than the difference of the Mono-PIV results with and without the acrylic glass plate on the surface.

The profiles containing the wall-normal fluctuation v' (see Figures 6.4 c, d and f) reveal a large difference between the three measurements. Since the wall-normal velocity component of the approaching boundary layer is about one order of magnitude smaller than the streamwise velocity and the resolution of the images is necessarily coarse, in order to cover the entire flow depth, the uncertainty of the corresponding wall-normal Re-stresses is large. Therefore, all statistics containing the v'-fluctuation especially in Figure 6.4 c) reveal a large difference comparing the three measurements. The Re-shear stress profiles $\langle u'v' \rangle$ (Figure 6.4 d)) indicate a matching trend between the Mono-PIV data with and without the acrylic glass plate on the surface and, therefore, it can be concluded that the divergence of the presented results did not stem from the presence of the acrylic glass plate and, thus, its

impact is considered to be small. Furthermore, the wall shear stress was estimated using both the Mono-PIV measurements with and without the acrylic glass plate on the water surface and the did not seem to be affected as the corresponding difference was less than 0.4%.
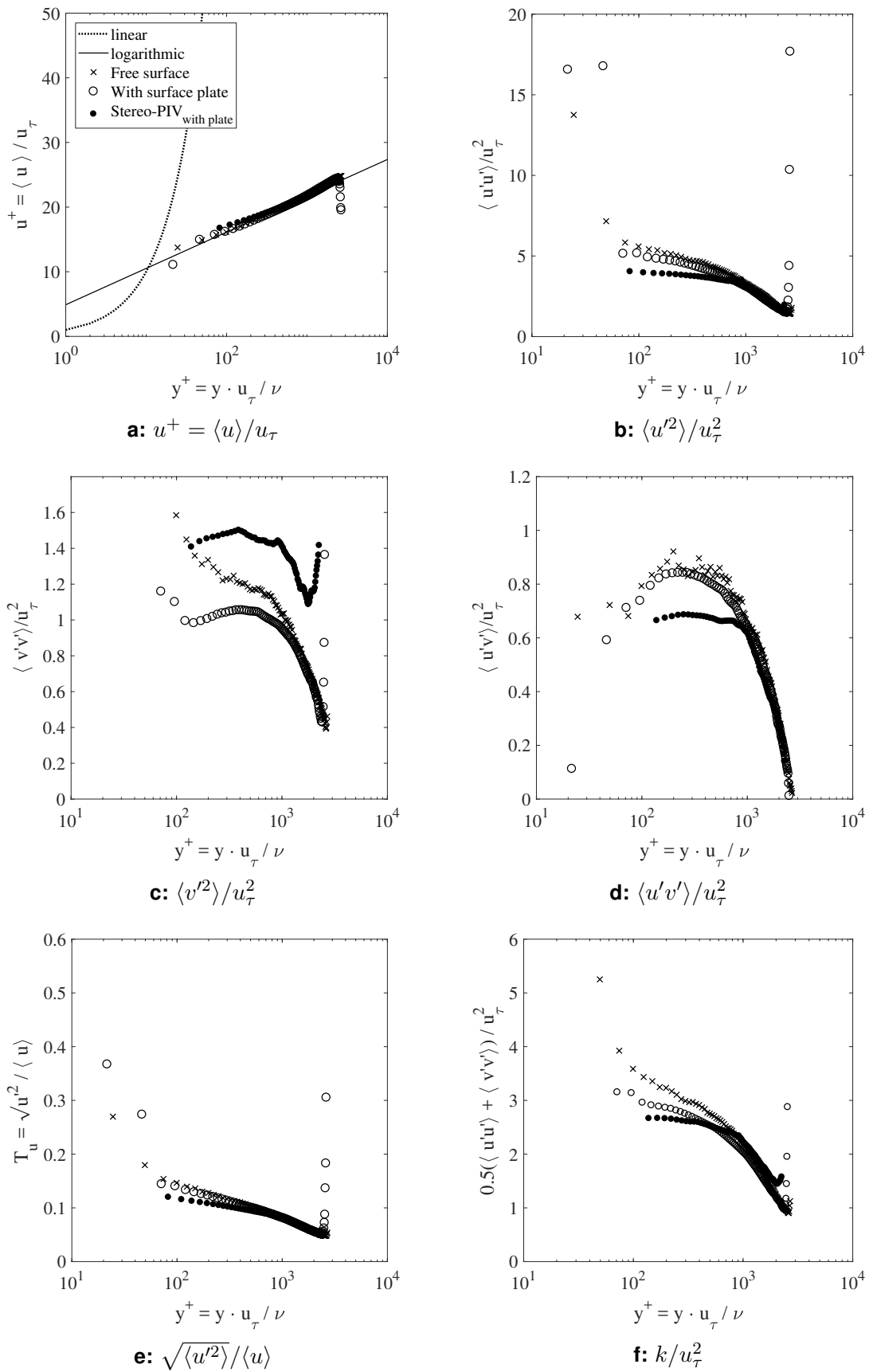
Figure 6.4: Time-averaged profiles of turbulence statistics of the approach flow for $Re = 39{,}000$ with (o) and without (x) acrylic glass plate on the water surface obtained from Mono-PIV, and from Stereo-PIV with surface plate ($\bullet$). All graphs are given in inner scaling.

6.4 Reproducibility of the Experiment

Flow conditions in a flume with rectangular cross section can be compared using the Reynolds number. When Re is identical for two different experimental runs, the flow can be considered to be similar and reproducible. And the reproducibility of an experiment augments the reliability of the obtained results; therefore, the PIV-measurements in front of the wall-mounted cylinder at $Re = 39,000$ were repeated on three different days: in November 2015 (Mono-PIV), in February 2016 (Mono-PIV), and in June 2017 (Stereo-PIV).

Figure 6.5 shows the time-averaged velocity profiles $\langle u(y) \rangle$ at a position upstream the cylinder ($x/D = -0.9$). The absolute values of the streamwise velocity show a significant discrepancy as the profiles deviate with increasing proximity (see Figure 6.5 a); thus, the flow conditions, which are supposed to be identical, do not indicate similarity and reveal a considerable uncertainty.

These variations in the velocity profiles and differences in the flow structures are caused by the uncertainty of the Reynolds number itself, which is computed as $Re = QD/by_0\nu$. According to the propagation law of stochastic errors (see eq. 6.7), the total uncertainty of Re can be calculated using the uncertainties of each input variable, which are assumed to be normally distributed (Tropea $et\ al.$, 2007). In this case, the discharge Q, the flow depth y_0, and the kinematic viscosity ν are suspected of introducing errors. Whereas, the width b of the flume, and the diameter D of the cylinder are expected to be precisely determined and, therefore, constant.

$$\delta(Re) = \sqrt{\left(\frac{\partial Re}{\partial Q}\Delta_Q\right)^2 + \left(\frac{\partial Re}{\partial y_0}\Delta_{y_0}\right)^2 + \left(\frac{\partial Re}{\partial \nu}\Delta_\nu\right)^2} \tag{6.7}$$

In the experimental set-up (see Figure 5.1), the discharge was measured by a magneto-inductive flowmeter (MID[2]) and rounded to $0.001\mathrm{m}^3/\mathrm{s}$. The required discharge for $Re = 39,000$ was $Q = 0.068445\mathrm{m}^3/\mathrm{s}$, and thus, could either be set to 0.068 or $0.069\mathrm{m}^3/\mathrm{s}$. However, when the display showed $0.068\mathrm{m}^3/\mathrm{s}$, the true flow rate could have varied between 0.0676 and $0.0684\mathrm{m}^3/\mathrm{s}$ due to the rounding. Therefore, the absolute uncertainty of Q was conservatively estimated as $\Delta_Q = 0.0694 - 0.0676 = 0.0018\mathrm{m}^3/\mathrm{s}$. Further, the viscosity of a fluid depends on its temperature. During each experiment the variation of the temperature was about $0.3°\mathrm{C}$, which corresponded to an uncertainty of the kinematic viscosity of $\Delta_\nu = 7.314 \cdot 10^{-9}\mathrm{m}^2/\mathrm{s}$. Lastly, the flow depth was measured with an accuracy of $\Delta_{y_0} = 0.001\mathrm{m}$. Using eq. 6.7, the total uncertainty in reproducing a certain flow configuration and bulk velocity is estimated, and the corresponding absolute and relative errors for all Re are listed in Table 6.2.

The solid red line in Figure 6.5 a) and b) represents the mean of the three measured velocity profiles, and the uncertainty range (dashed red lines) corresponds to $\pm\delta_{Re}$ with respect to the mean of all measurements. Considering the total uncertainty of Re, the velocity profiles were varied by multiplying with $(1 \pm \delta_{Re})$, which resulted in coinciding velocity profiles (see Figure 6.5 b). The results of the Mono-PIV measurement conducted in February 2016 (black

---

[2]From German: **M**agnetisch-**i**nduktiver **D**urchflussmesser
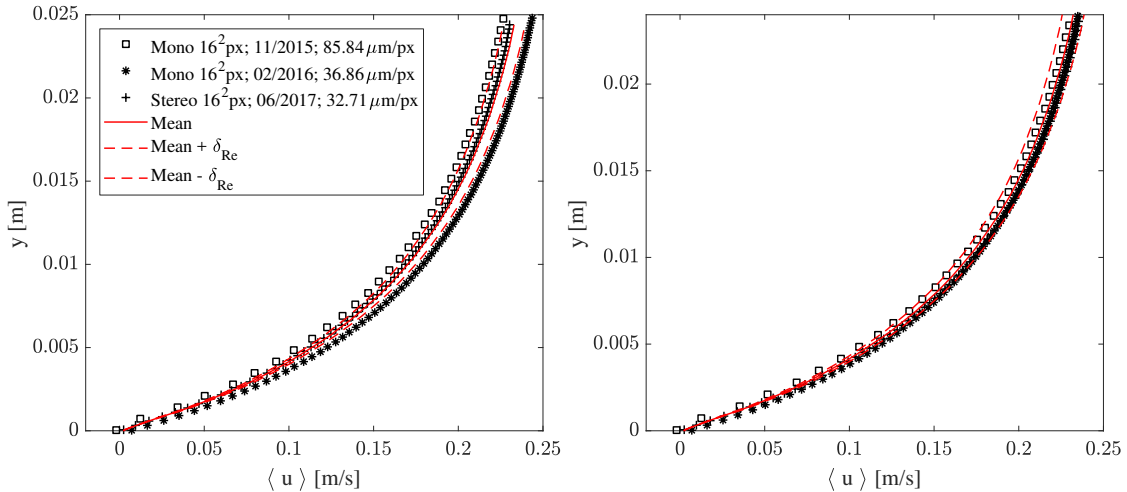
a: Time-averaged streamwise velocity pro- **b:** Time-averaged streamwise velocity pro-
files   files including the uncertainty of Re

Figure 6.5: Streamwise velocity profiles in wall normal direction: $\langle u(y) \rangle$ at $x/D = -0.9$ in front of wall-mounted cylinder

Re	20,000	39,000	78,000
$\Delta(Re)$	1034	1086	1207
δ_{Re}	5.17%	2.78%	1.55%

Table 6.2: Absolute and relative uncertainty estimating the Reynolds number

asterisks) were reduced by the factor of $(1 - \delta_{Re})$, whereas the remaining data were increased by $(1 + \delta_{Re})$. In other words, each velocity profile was modified by the same factor, which represented the expected uncertainty of the experimental infrastructure. As the deviation in the velocity profiles using different measurement techniques (Mono and Stereo-PIV) is smaller than the uncertainty δ_{Re} of reproducing the experiment itself (irrespectively of the applied measurement device), this test reveals that the results gained from Mono-PIV and Stereo-PIV match sufficiently well, which means that both strategies are reliable and that the experiment is reproducible.

6.5 Evaluation of the PIV-Processing Parameters

When performing a PIV experiment, many parameters can be adjusted and influence the obtained results. Setting the interrogation window size and the signal-to-noise ratio (SNR), applying the window deformation technique or vector interpolation techniques in the post-processing step are most commonly varied, and preferential settings of these parameters are based on experience. However, as every experimental set-up is unique, the optimal settings for the PIV-processing were evaluated empirically for the measurements at the wall-mounted cylinder (cf. section 5.3) and $Re = 39,000$.

For the cross-correlation function (see section 4.5.1), the SNR value is typically set to 1.5, meaning that the ratio of the maximum peak to the second highest peak of the correlation function must be greater than this threshold. In order to find the optimal value for this set-up, the SNR has been varied by $\pm 10\%$, but set to 1.5 as no improvement of the quality of the vector fields could be observed.

Due to a local lack of particle image pairs in the PIV-images, for example, the evaluation of the cross-correlation can fail, and vectors are missing at these locations undermining the reliability of the final results. Therefore, the post-processing provides the possibility to detect outliers and to fill holes in the instantaneous vector fields by interpolation from the surrounding vectors, and other methods can be applied to smooth the instantaneous vector fields in the end. However, as the impact of such filling and smoothing methods can bias the result, they have not been applied. Instead, more image pairs have been recorded, in order to obtain a converging trend in the statistical estimators.

Regarding the size, overlap, and the shape of the interrogation windows, the following parameter variations were tested:

1. 16×16px, 50% overlap, standard evaluation ($\square$)
2. 16×16px, 50% overlap, window deformation ($*$)
3. 32×32px, 75% overlap, standard evaluation ($\triangledown$)
4. Combined results: case 2 merged with 3. ($+$)

The interrogation windows were either set to a size of 16×16px or 32×32px. The larger the size of the IW, the more particle image pairs are included in the calculation of the correlation function, and the more reliable the result becomes. However, the PIV evaluation acts as a spatial filter with the size of an IW on the flow field; therefore, larger IW lead to coarser results in sense of spatial resolution, and small scales of the velocity field might be damped and not represented correctly.

The IW are typically overlapping each other by 50%, and as each vector is located in the centre of an IW, the spacing of the final grid sampling the vector field is half the length of an IW. In case of a larger overlap (e.g. 75%), the vector field becomes denser. However, the spatial resolution is related to the size of the IW and cannot be increased by a larger overlap.

The *standard evaluation* stands for a PIV-processing with fixed squared interrogation windows, whereas the window deformation technique refers to the iterative adjustment of the IW size according to velocity gradients within the area of an IW (see section 4.5.4).

The vectors have been determined using 16×16px IW and the standard evaluation or the window deformation technique (case no. 1 or 2, respectively). The latter approach, however, resulted in less valid vectors compared to the standard evaluation with fixed squared IW. Therefore, in order to increase the number of valid samples the data of evaluation no. 2 (with window deformation) was combined with the corresponding results of the standard evaluation using 32×32px IW, but with 75% overlap, i.e. the grid spacing was eight pixel (case no. 3). This combined approach is denoted as case no. 4., and whenever a vector of the window deformation evaluation was invalid it was replaced by the corresponding vector of the evaluation no. 3.

The different cases, listed above, are compared in Figure 6.6 with respect to the time-averaged horizontal and vertical profiles of the streamwise and the wall-normal velocity component. Further, in Figure 6.7, the corresponding profiles of the turbulent kinetic energy

(TKE) k and the Reynolds shear stress $\langle u'v' \rangle$ are presented at the location of the horseshoe vortex (HV) centre.

The PIV results of all variations were compared among each other and to the numerical results of Schanderl (2018), who simulated the same flow configuration in terms of Re, y/D- and b/D-ratio around a wall-mounted cylinder using a Large-Eddy simulation (LES) with high spatial resolution. Additionally, the results of a single-pixel ensemble PIV-evaluation (SPE) by Strobl (2017) of the same experimental data set were taken as a reference. The cross-correlation function is, hereby, computed for every *single pixel*, and finally, added up to an time-averaged *ensemble* (Westerweel *et al.*, 2004; Kähler *et al.*, 2006). As the particle image density was low in the original data set, the final results appear to be rougher than the one of the IW-based PIV-evaluation, but provide more detailed information especially near surfaces.

The deviations of the numerical and the experimental results are obvious and one reason for this difference could be found in the so-called *slip boundary condition* modelling the nearly inviscid interface between water and air in the LES. The virtual water surface remained steady, whereas the real one was moving due to surface waves, and the approaching flow is separated into downflow and surface roller in the experiment (cf. Figure 3.1). In the LES, however, the location of the stagnation point at the cylinder edge defining downflow and surface roller could be affected by the lack of surface waves, and as it was shifted to the intersection of the virtual water surface and the cylinder no surface roller occurred. As a consequence, the top layer of the flow containing high momentum was also deflected downwards (instead of upwards) and formed the downflow driving the horseshoe vortex. Thus, the HV-system was stronger and more pronounced in the numerical simulation, and the centre of HV was located further upstream in the LES.

Nevertheless, all experimental data coincide with each other, as well as agree qualitatively with the LES data, only at some points the results deviate and reveal differences that have to be discussed in more detail. The profiles of $\langle u(x/D) \rangle$ (see Figure 6.6 a) match upstream of HV, but after changing sign in the region of the centre of HV, the 16×16px evaluations (fixed square and deformable IW) seem to overestimate the magnitude of $u-$component tremendously. The downflow directly at the edge of the cylinder, however, is determined correctly in all cases. The vertical velocity component in Figure 6.6 b) is coinciding in total, but is slightly underestimated by both 16×16px evaluations (case no. 1 and 2) upstream of the HV centre ($x < -0.7D$).

Both velocity profile plots in vertical direction (see Figure 6.6 c) and d)) show that the 16×16px evaluation with fixed squared IW is not representing the flow structure correctly. Near the wall, the amplitude of both the u- and the v-component is damped and not as pronounced as the remaining experimental and numerical results indicate. The overestimation of the $u-$component and the underestimation of the $v-$component underneath HV at the same time (see Figure 6.6 a) and d)) by the 16×16px standard evaluation (hollow red squares) revealed that the wall-parallel jet is more pronounced in this case, and the horseshoe vortex becomes smaller and less turbulent.

When analysing the profiles of the in-plane (2D) turbulent kinetic energy (cf. eq. 2.18) similar damping effects appear by the 16px-standard evaluation in Figure 6.7 a) and b), and the amplitude of the TKE is approximately 25% smaller than the one of the merged results, for example. Whereas, the Reynolds shear stress $\langle u'v' \rangle$ coincides for all evaluation methods

(see Figure 6.7 c) and d)); thus, is not as affected as the velocity profiles by the setting of the evaluation parameters.

Analyses by Jenssen *et al.* (2016*b*) concerning the impact of the PIV evaluation strategy on the wall shear stress distribution in front of the cylinder showed that the results of the 32×32px evaluation underestimated the velocity gradient directly at the wall. Moreover, the results obtained by a 16×16px evaluation could not fully resolve all details of the wall shear stress distribution, whereas the SPE results showed the highest level of detail.

This parameter variation analysis allows to conclude that the results of case no. 1 are accounted to be of lowest quality, whereas the merged data set, i.e. 16×16px window deformation combined with a 32×32px standard evaluation on the same grid (75% overlap), yields the best performance in general; thus, this hybrid technique was chosen for the evaluation of the flow field in front of the wall-mounted cylinder.
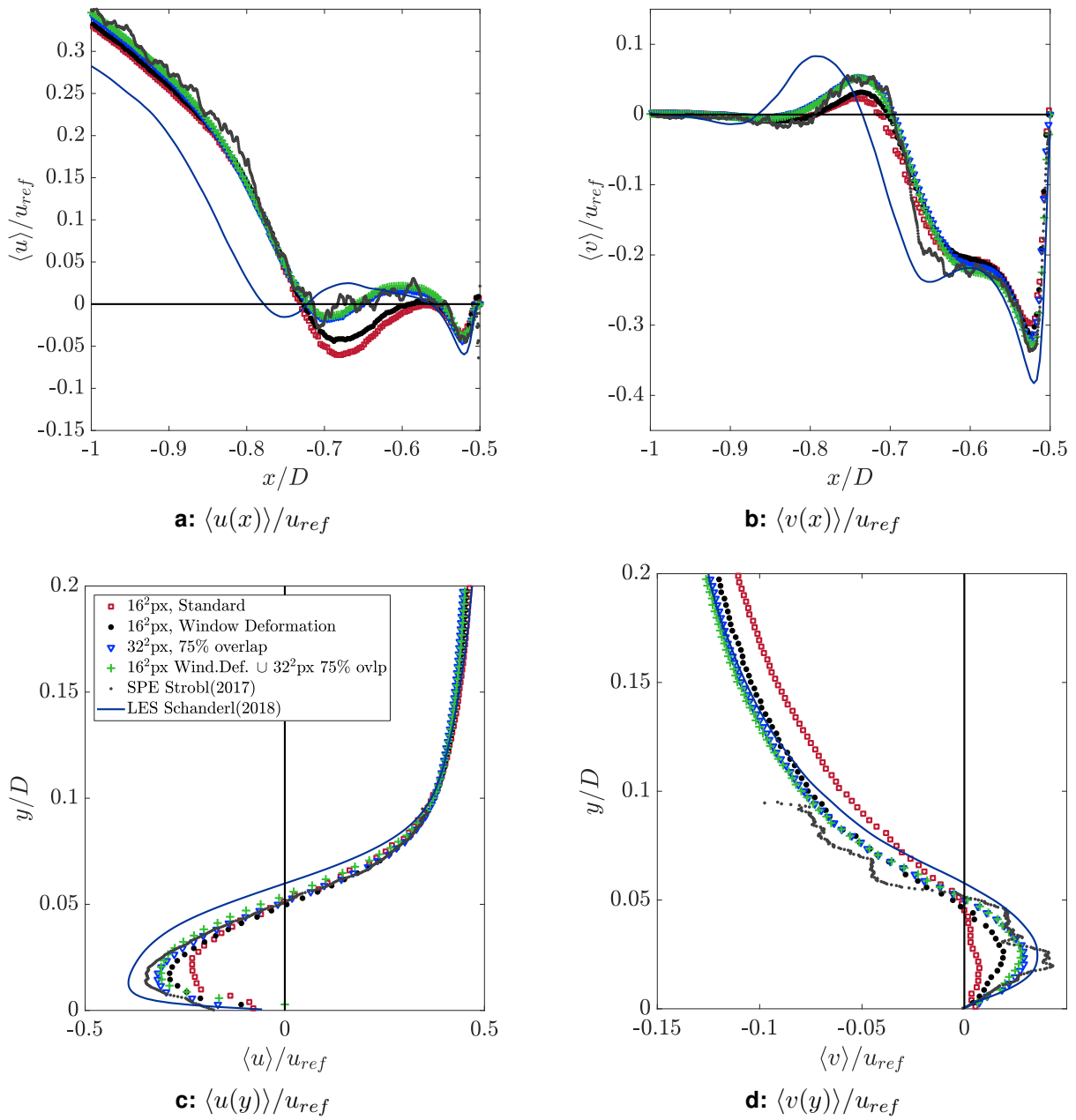
Figure 6.6: Time-averaged velocity profiles in front of wall-mounted cylinder at $Re = 39{,}000$. $u-$ and $v-$component shown along horizontal a) and b), and vertical c) and d) line through the centre of the horseshoe vortex
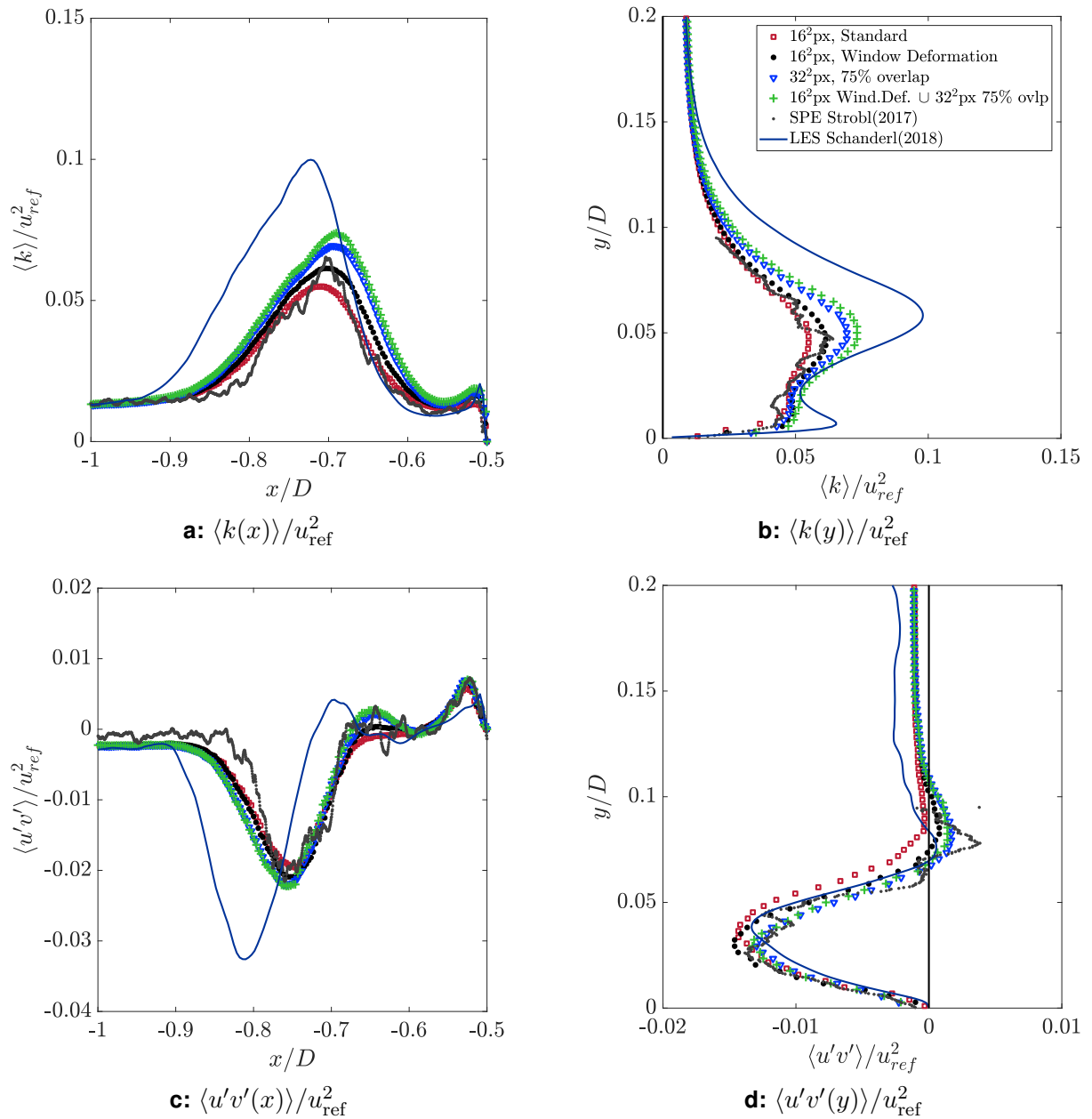
Figure 6.7: Time-averaged profiles of turbulent kinetic energy k a) and b) and Re shear stress c) and d) in front of wall-mounted cylinder at $Re = 39{,}000$ along a horizontal and a vertical line through the centre of the horseshoe vortex

6.6 Error Analysis

Studying turbulent flows requires statistical methods for describing their characteristics. Therefore, to record a "sufficient" number of samples N for a time which is "sufficiently" long is a crucial factor, but the definition of what number or what time was sufficient depends on the investigated flow situation. Basically, the time series of a velocity component is recorded at a certain point in space during an experiment. From this time series the probability density function (PDF) representing the number of occurrences (in terms of percentage) can be computed, and the characteristics of this PDF can be used to estimate the uncertainty of the measurement, which helps to quantify the reliability of the observed data.

6.6.1 Statistical background

The shape of a PDF $p(u)$ is described by the *central moments* defined in eq. 6.8 (Pope, 2013). For $n = 1$, the central moment represents the mean of the fluctuations (see eq. 2.13), which equals to zero. The second central moment is directly linked to the variance or to the square of the standard deviation, whereas the higher central moments ($n = 3$ and $n = 4$) refer to the skewness, and kurtosis of a PDF, respectively, when normalized by the standard deviation to the power of n. Due to mathematical definition, the "zeroth" moment equals always to one regardless of the variable u and its distribution.

$$M_n = \int u^n p(u) du = \langle (u - \langle u \rangle)^n \rangle = \langle (u')^n \rangle \tag{6.8}$$

The relative error ε_{rel} of the mean velocity $\langle u \rangle$ converges with the turbulence intensity T_u divided by the square root of the number of samples (Adrian & Westerweel, 2011):

$$\varepsilon_{\text{rel}} = \frac{\sigma(u)/\langle u \rangle}{\sqrt{N}} = \frac{T_{\text{u}}}{\sqrt{N}}. \tag{6.9}$$

According to eq. 6.9, the relative error is only defined for non-zero values of $\langle u \rangle$, therefore, yields corrupt values, when $\langle u \rangle$ approximates to zero, i.e. becomes very small with respect to the standard deviation. For turbulent flows with zero mean velocity, e.g. in the centre of oscillating vortices, the definition of the standard error ε_{std} of the mean has to be applied instead:

$$\varepsilon_{\text{std}} \left(\langle u \rangle \right) = \frac{\sigma(u)}{\sqrt{N}} = \frac{\sqrt{M_2(u)}}{\sqrt{N}}, \tag{6.10}$$

which is the ratio of the standard deviation to the square root of the number of samples. Furthermore, the standard error of higher-order correlations (e.g. $\langle u'^2 \rangle$ or $\langle u'^3 \rangle$) can be computed likewise:

$$\begin{aligned}
\varepsilon_{\text{std}}\left(\langle u'^n \rangle\right) &= \frac{\sigma\left(u'^n\right)}{\sqrt{N}}, \\
&= \frac{\sqrt{\langle (u'^n - \langle u'^n \rangle)^2 \rangle}}{\sqrt{N}}, \\
&= \frac{\sqrt{\langle u'^{2n} - 2u'^n \langle u'^n \rangle + \langle u'^n \rangle^2 \rangle}}{\sqrt{N}}.
\end{aligned} \tag{6.11}$$

By inserting eq. 6.8 in eq. 6.11, the standard error of a fluctuating quantity to the power of n can be rearranged as:

$$\varepsilon_{\text{std}}\left(\langle u'^n \rangle\right) = \frac{\sqrt{M_{2\text{n}} - M_\text{n}^2}}{\sqrt{N}}. \tag{6.12}$$

In chapter 2, the role of (co-)variances and triple (cross-)correlations was described in fluid mechanical terms: the Reynolds stress tensor consists of $\langle u_i' u_j' \rangle$, and the transport equation of the TKE requires the terms $\langle u_i' u_j' u_j' \rangle$ (see eq. 2.17 and eq. 2.23, respectively). The higher the order of a central moment becomes, the more samples are required to keep the standard error constant. Therefore, the trend of the nth central moment with respect to the number of samples should converge with increasing number of samples.

The standard error of one single measurement can be computed by applying eq. 6.10 and eq. 6.12. Repeating this experiment for many times, leads subsequently to a Gaussian distributed standard error. Therefore, the estimation of the standard error itself is uncertain, too, as the included number of samples is finite. To estimate the relative error of the standard error, the central moments of an ideal, i.e. noise-free, Gaussian distribution are considered. All odd central moments are zero in the ideal case due to symmetry. Central moments of even order, however, are proportional to the standard deviation of the distribution as listed in Table 6.3. Furthermore, the standard error of the nth central moment with respect to the standard deviation to the power of n is included for the first four central moments as well.

n	1	2	3	4	5	6	7	8
M_n	0	σ^2	0	$3\sigma^4$	0	$15\sigma^6$	0	$105\sigma^8$
$\varepsilon_{\text{std}}(M_\text{n})/\sigma^n$	$1/\sqrt{N}$	$\sqrt{2}/\sqrt{N}$	$\sqrt{15}/\sqrt{N}$	$\sqrt{96}/\sqrt{N}$				

Table 6.3: Central moments and the corresponding standard errors due to the number of samples of a Gaussian distribution

6.6.2 Standard error of the measurements

Table 6.4 shows the results of the error analysis for the mean, the second, third and fourth central moment using eq. 6.10 and eq. 6.12. The investigated time series of the $u-$components of each Re were recorded in the centre of the horseshoe vortex in front of

both the wall-mounted cylinder and the scoured cylinder. Due to a strong out-of-plane displacement, the loss of particles was high, the cross-correlation failed more often in this region to identify the correct in-plane displacements. Therefore, a minimum in the number of valid vectors (N_{valid}) was observed and at the same time a maximum of turbulent fluctuations occurred here.

The overall reliability of the measurements is related to the question whether the number of valid samples was large enough, which was analysed at the most critical point in the flow. For this reason the total number of recorded image pairs ($N_{\text{img. pairs}}$) had to be considerably larger than the number of valid vectors.

Re	$N_{\text{img. pairs}}$	N_{valid}	$\varepsilon_{\text{std}}(\langle u \rangle)/\sigma$	$\varepsilon_{\text{std}}(M_{\text{n}})/\sigma^n$		
				M_2	M_3	M_4
20,000 (Flat)	20,000	18,205	0.0075	0.0107	0.0293	0.0716
20,000 (Scour)	33,000	9,839	0.0101	0.0135	0.0348	0.0763
39,000 (Flat)	27,000	24,116	0.0065	0.0089	0.0237	0.0545
39,000 (Scour)	20,000	6,264	0.0126	0.0169	0.044	0.0975
78,000 (Flat)	46,400	39,119	0.0051	0.0069	0.0183	0.0419

Table 6.4: Standard error of mean and central moments of Mono / Stereo-PIV measurements in the symmetry plane in front of the wall-mounted and scoured cylinder

The standard error in estimating the mean based on the number of sample is very low and between 0.5 and 1.3%. As expected, the error grows with increasing order of the central moment: the second moment reveals an error between 0.7 and 1.7%, whereas the fourth moment is estimated with the largest error of 4 to 10%. Furthermore, the trends of the standard error of the mean and up to the fourth central moment are shown on a double-logarithmic scale in Figure 6.8. The blue lines correspond to the data in front of the wall-mounted cylinder, whereas the red lines refer to the scour-data at $Re = 39,000$. The standard errors of the experimental data reveal a Gaussian 'behaviour', as they approximate the trends of the Gaussian standard error (black lines) with increasing number of samples for each central moment (or the mean).

6.6.3 Trends of estimators

Each statistical estimator (mean, second, third and fourth central moment) was computed in a loop with increasing number of samples to test the statistical convergence, which is denoted as $\langle \tilde{u} \rangle$ for the mean or as $\langle \tilde{u}'^n \rangle$ for the nth central moment. The deviation of the trends with respect to the corresponding ensemble average are presented in Figures 6.9 a) to d), respectively. The trend of the mean value is normalized by the depth-averaged streamwise velocity in the symmetry plane of the flume (u_{ref}), whereas the central moments are normalized by the standard deviation to the power of n. The time series were recorded at the time-averaged position of the horseshoe vortex, and the trends were analysed for all measurements in the symmetry plane in front of the wall-mounted cylinder and of the scoured cylinder, as well as at the lateral position (45°) around the scoured cylinder.

The trends of the mean, second and third central moment indicate for all configurations that the deviation approximated a constant low value from 60% of the number of valid
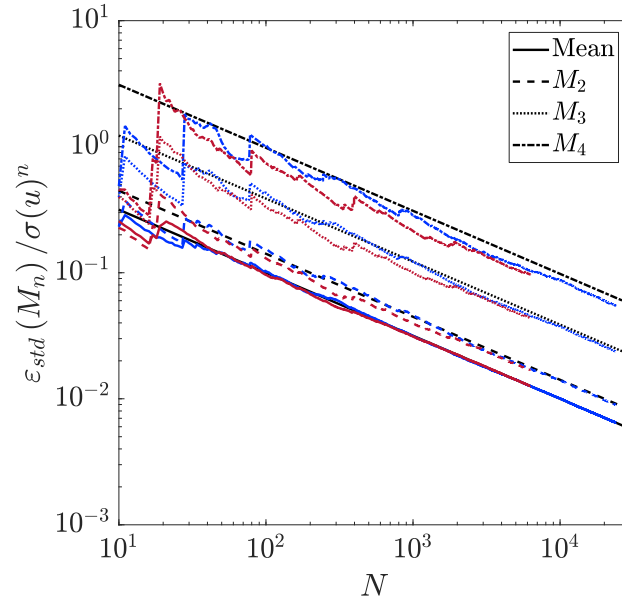
Figure 6.8: Decreasing standard error of the mean (solid lines), second (dashed lines), third (dotted lines) and fourth (dash-dotted lines) central moment obtained at the centre of the horseshoe vortex in front of the wall-mounted (blue) and scoured (red) cylinder at $Re = 39,000$. The black lines represent the reference trend of the standard error of the mean and the moments of a Gaussian distribution.

samples on. The statistical estimators converged to a constant value and the achieved number of valid samples in each flow configuration was, therefore, considered to be sufficiently large. The fourth central moment of all set-ups, however, shows still a significant deviation and can not be considered as converged.

Using the number of valid samples alone is not sufficient to quantify the statistical convergence of a measurement. The sampling frequency f_s of 7.25Hz has to be taken into account as well. A large number of samples recorded with a high frequency would result in a very short sampling time T, but this value has to be considered with respect to the flow situation. Therefore, the sampling time

$$T = \frac{N}{f_\mathrm{s}}, \tag{6.13}$$

has to be normalized by the macro scales of the flow:

$$T^* = T\frac{u}{L_\mathrm{c}} = T\frac{u_\mathrm{b}}{D} = \frac{N u_\mathrm{b}}{f_\mathrm{s} D}, \tag{6.14}$$

to relate the sampling time and frequency to the largest time scales of the flow, and to allow the comparison between different experiments or numerical simulations. Due to the limited computational capacity during the PIV-experiments, the data acquisition had to be subdivided into batches of 1,500 image pairs, which could be recorded at once. All

individual batches were afterwards united to one data set (measurement), in order to calculate the time-average statistics. The total number of valid samples of each data set was used to compute the relative sampling time T^* according to eq. 6.14, which is listed in Table 6.5.

Re	Flat bed	Scour 0°	Scour 45°
20,000	5,022	2,714	3,579
39,000	12,973	3,369	3,497
78,000	16,524	—	—

Table 6.5: Dimensionless sampling time T^* based on the total number of valid samples of each data set recorded in the centre of the horseshoe vortex

To conclude this analysis, the estimation of the mean, the variance and the third central moment, which are important for describing the physical processes in turbulent flows, can be provided with high accuracy and the collected data sets were large enough that a statistical convergence could be verified. Even though the fourth central moment was not converged yet using the specific number of samples, this sensitive statistical parameter could be estimated with an maximum standard error of about 10%. However, the fourth central moment is not relevant for the budget of the TKE (see eq. 2.21 to eq. 2.26).
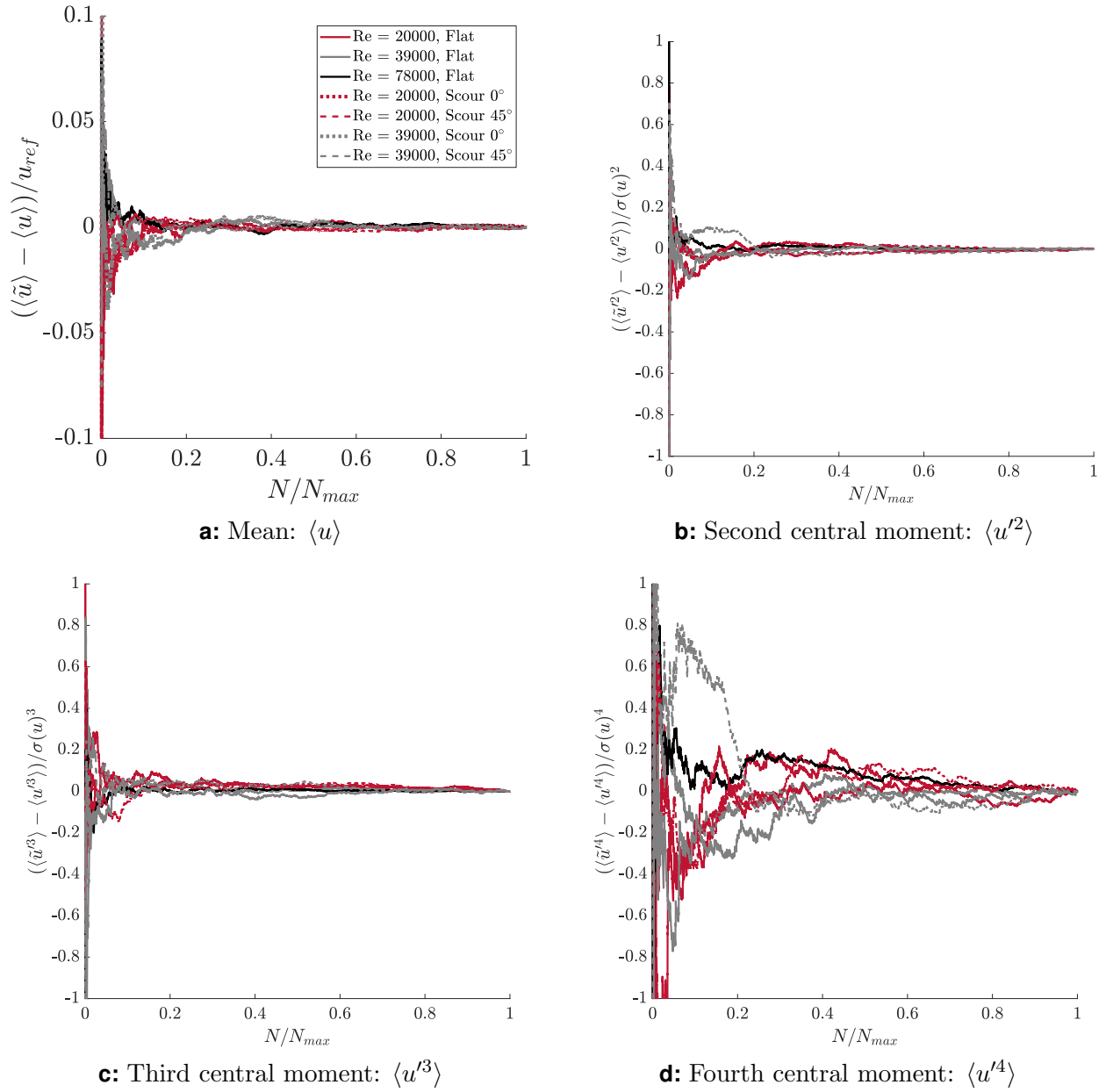
Figure 6.9: Trends of the deviation of the mean and the central moments for all *Re* at the wall-mounted and at the scoured cylinder observed in the centre of the horseshoe vortex.

7 Analysis of Measurement Results

The flow in front of a cylinder on a flat plate was investigated for three different Reynolds numbers (20,000, 39,000, and 78,000), which are in the subcritical range with respect to the coefficient c_D of the drag force acting on the cylinder (Sumer & Fredsøe, 2006). In order to provide insight into the flow structures, which come into play at a scoured cylinder, the results of the PIV experiments at the cylinder on a flat plate and inside a scour hole are presented. However, no measurements for the $Re = 78,000$ case were conducted at the scoured cylinder. In addition to the measurements in the symmetry plane, the flow field at the scoured cylinder was observed at an 45° angle of rotation with respect to the approaching flow.

The analysis of the results begins with a discussion of the magnitude of the velocity field, before the focus shifts to the vorticity, the Reynolds stresses, the turbulent kinetic energy, and the budget terms of the TKE on a time-averaged level. Furthermore, the probability density functions (PDF) of the velocity components are evaluated, and the wall shear stress distributions are examined. Finally, the vortex dynamics and coherent structures are analysed by using the proper orthogonal decomposition (POD).

7.1 The Time-Averaged Velocity Fields

7.1.1 In front of a cylinder on a flat plate

When the boundary layer approaches the cylinder, the pressure near the water surface increases with respect to the pressure near the bottom of the channel, due to the logarithmic shape of the velocity profile. The flow is redirected at the flow facing edge of the cylinder and a strong downflow develops (see section 3.1.1 and Figure 3.1). Fluid with high momentum from the upper part of the boundary layer is transported downward by this strong flow towards the bottom of the flume and defines stagnation point S3 (see Figure 7.1). At this point, the downflow is redirected again, on the one hand in the upstream direction forming a wall-parallel jet exerting a strong velocity gradient on the wall, i.e. high shear stress (see section 7.6). On the other hand, the downflow is deflected downstream in the direction towards the foot of the cylinder blocking this small-scale downstream jet, which in turn is redirected upwards and i) forms a small foot vortex V3, and ii) blocks the downflow along the cylinder surface leading to its separation, which is indicated by the stagnation point S4. The coordinates of these points of interest are listed in Table 7.1.

The horseshoe vortex system reveals only a slight Re dependence, as the time-averaged $x-$position of V1 and S1 move a little upstream with increasing Re, maintaining their relative distance at approximately $0.09D$. For $Re = 20,000$ and $39,000$, the vertical distance of V1 is constant at $y/D = 0.051$, whereas the vortex core has moved downward in the high Re case. The flow structures directly at the cylinder, i.e. S3, V3, and S4, seem to be

	$Re = 20,000$		$Re = 39,000$		$Re = 78,000$	
	$\frac{x}{D}$	$\frac{y}{D}$	$\frac{x}{D}$	$\frac{y}{D}$	$\frac{x}{D}$	$\frac{y}{D}$
$S1$	-0.765	0.033	-0.7875	0.0296	-0.7941	0.0227
$V1$	-0.6814	0.051	-0.6965	0.0512	-0.7052	0.0454
$S3$	-0.531	$-$	-0.5325	$-$	-0.5274	$-$
$V3$	-0.5133	0.0178	-0.5133	0.0171	-0.5111	0.0146
$S4$	-0.5068	0.0363	-0.5074	0.0362	-0.5038	0.0364

Table 7.1: Points of interest of flow structure in front of cylinder on a flat plate

unaffected by Re, as their locations in the time-averaged flow field do not differ systematically.

A major part of the approaching flow, i.e. $0.13 < y/D < y_0$, is directed downwards and dragged in the wall-parallel jet pointing upstream. However, this global downflow directly at the cylinder forces the other part from the inflow, which is closer to the wall ($0.03 < y/D < 0.13$), to roll up forming the horseshoe vortex V1. The inflow near the wall ($0 < y/D < 0.03$) separates from the wall upstream the horseshoe vortex at stagnation point S2 ($x/D < -0.9$) and forms a recirculation zone blocked by V1. The stagnation point S1 is located where this recirculation zone, the horseshoe vortex and the wall-parallel jet meet. Apsilidis *et al.* (2015) identified a second vortex (V2) instead of this recirculation zone for $Re = 29,000$, $47,000$, and $123,000$. However, analysing the profiles of the vertical velocity component in the streamwise direction at a wall distance $y/D = 0.01$ (see Figure 7.2), no positive values in the region upstream stagnation point S1 were observed in the flow cases of this study, thus no vortex. Looking at the streamline separating the horseshoe vortex from the wall-parallel jet (dashed line in Figure 7.1) reveals that with increasing Re more fluid forms the wall-parallel jet, as the vertical position of this streamline decreases from $y/D = 0.146$ to $y/D = 0.127$ at $x/D = -0.9$ meaning that the part of the approaching flow increased, which is transformed into the downflow.

7.1.2 Around a scoured cylinder

The time-averaged flow fields for the Reynolds numbers 20,000 and 39,000 were measured using Stereo-PIV. Figure 7.3 and Figure 7.4 show the results in the symmetry plane in front of the scoured cylinder (0° with respect to the approaching flow), and the results at a lateral position at 45° with respect to the inflow direction.

The approaching boundary layer separates when entering the scour hole; therefore, *Kelvin-Helmholtz*[1] vortices are generated at the edge of the scour hole similar to the flow at a backward facing step. A strong downflow develops along the cylinder as well, which transports high-momentum fluid towards the scour surface, similar to the flat-bed case. The downflow is deflected at the scour surface mainly in the uphill direction forming the horseshoe vortex or in the circumferential direction around the scoured cylinder. However, at the cylinder foot, which forms a sharp angle with the scour surface, the downflow is redirected upwards generating a recirculation zone rather than a corner vortex V3 as in front of the wall-mounted

---

[1] William Thomson, 1st Baron Kelvin (⋆1824, †1907)
    Hermann Ludwig Ferdinand von Helmholtz (⋆1821, †1894)

a: $Re = 20,000$
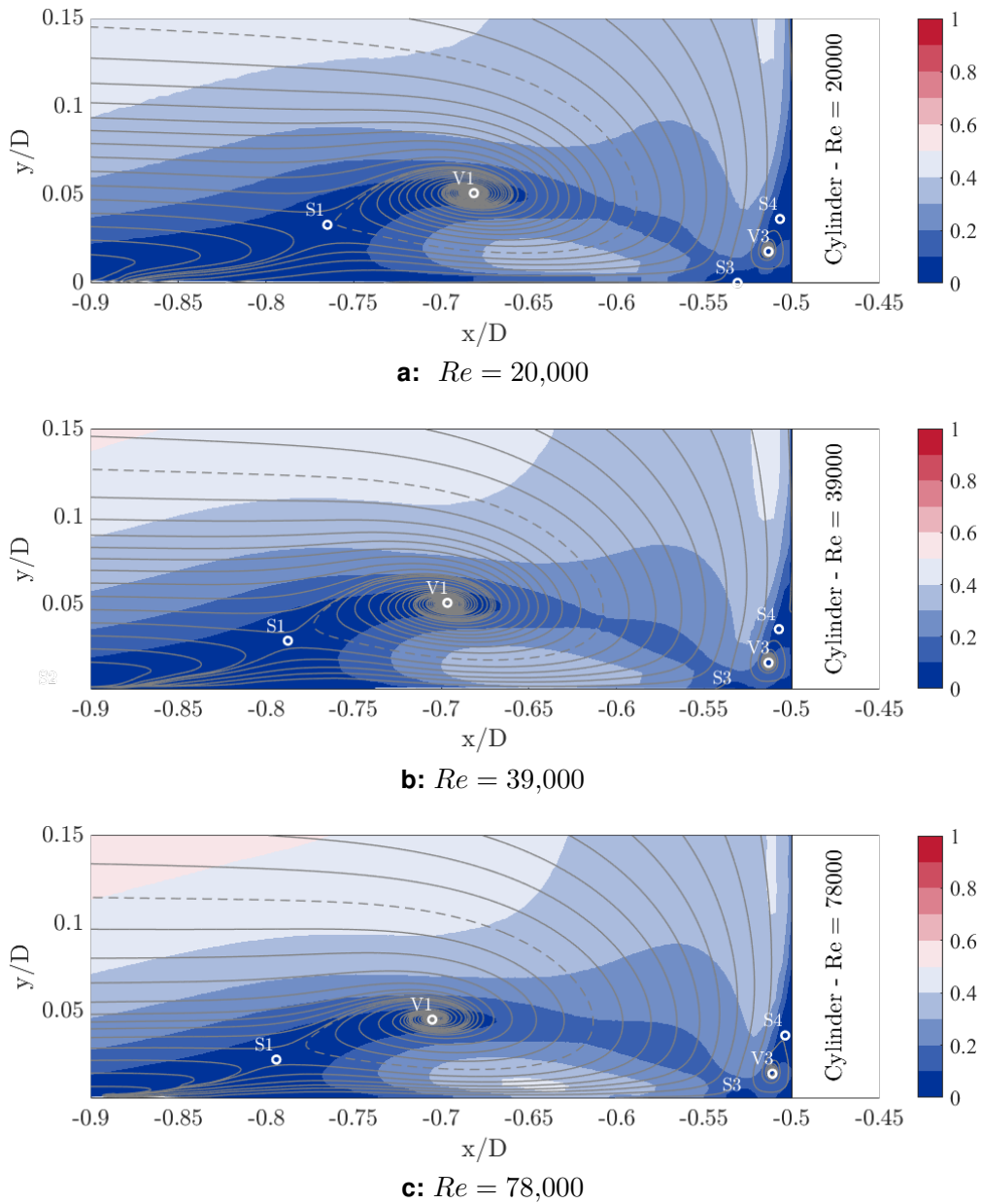
b: $Re = 39,000$

c: $Re = 78,000$

Figure 7.1: Time-averaged streamlines in front of a wall-mounted cylinder, flooded with the magnitude of the velocity field: a) $Re = 20,000$, b) $Re = 39,000$, c) $Re = 78,000$
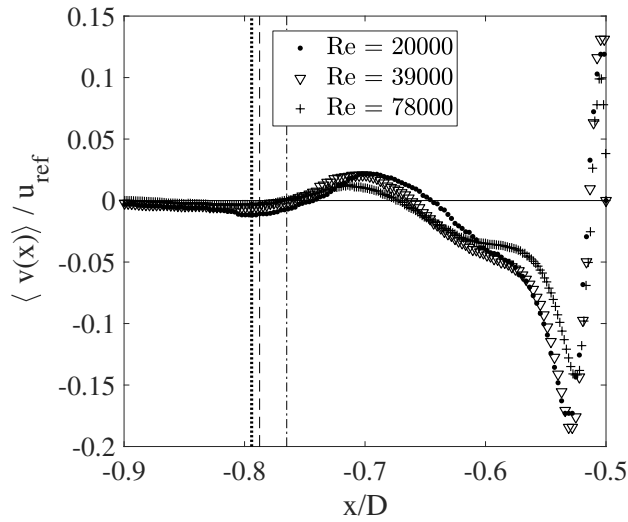
Figure 7.2: Vertical velocity profile in streamwise direction at $y/D = 0.01$. Vertical lines indicate position of stagnation point S1: Dash-dot $Re = 20{,}000$, dashed $Re = 39{,}000$, dotted $Re = 78{,}000$

cylinder. The major part of the impinging downflow, however, is redirected in the out-of-plane direction passing the cylinder sideways. The region upstream of the horseshoe vortex and underneath the separated boundary layer reveals no preferred flow direction or structure as the magnitude of the velocity is very low.

In the flat-bed case, a wall-parallel jet evolves from the point of impingement on and dominates the near-wall region underneath V1. According to the time-averaged flow fields in the scour hole, however, this jet could not be identified to be as pronounced as in the flat bed case and is possibly only developing further uphill. The region directly between the scour surface and HV reveals a velocity magnitude up to 60% of the depth-averaged approaching velocity. This strong uphill directed flow, however, stems from the clockwise rotation of the HV itself and is not caused by a wall-parallel jet originating from further downhill (see the streamlines in Figure 7.3 originating from the vortex and not from the deflected downflow further downhill).

The horizontal location of the HV shifted further upstream in the scour experiments compared to the situation at the wall-mounted cylinder and the vortex is completely embedded in the scour hole. In Table 7.2, the horizontal position of the HV centre as well as its distance normal to the bounding surface is listed. Δx_n refers to the distance normal to the scour surface, which was derived in a scour-oriented coordinate system (for the transformation of the coordinate system, see appendix 10). First, the normal distance of the HV centre in the symmetry plane does not significantly vary with Re. Secondly, the wall distance of the HV in the scour hole is approximately the same as in front of the wall-mounted cylinder. And thirdly, the horseshoe vortex centre moves further uphill and lifts at the same time from the scour surface while bending around the scoured cylinder.

In the flat-bed case, the maximum magnitude of the back-flow region underneath the horseshoe vortex is approximately $0.3u_{\mathrm{ref}}$ and in the vertical downflow at the cylinder front, the magnitude is about $0.4u_{\mathrm{ref}}$. In the symmetry plane in front of the scoured cylinder, however, these values increased to about $0.5u_{\mathrm{ref}}$ and $0.7u_{\mathrm{ref}}$, respectively. The flow structure

	0°		45°		Flat bed	
	$\frac{x}{D}$	$\frac{\Delta x_n}{D}$	$\frac{x}{D}$	$\frac{\Delta x_n}{D}$	$\frac{x}{D}$	$\frac{y}{D}$
$Re = 20{,}000$	-0.8946	0.053	-0.9124	0.09	-0.6814	0.051
$Re = 39{,}000$	-0.9225	0.055	-0.98	0.0834	-0.6965	0.0512

Table 7.2: Horizontal position and the wall distance of the horseshoe vortex at $0°$ and $45°$ in front of the scoured cylinder and in the flat-bed case for $Re = 20{,}000$ and $Re = 39{,}000$

around a scoured cylinder changes when leaving the symmetry plane: The magnitude of the downflow at the cylinder front increases substantially from about 70% of the reference velocity to more than 100%. Furthermore, the w-component of the velocity field becomes stronger as the flow passes the cylinder sideways. Therefore, the velocity magnitude at the cylinder foot increased from about $0.2u_{\mathrm{ref}}$ in the symmetry plane to about $0.6u_{\mathrm{ref}}$ at the lateral position. However, a calm region between V1 and the rim of the scour hole is still present, as the approaching flow separates there irrespectively of the angular position. The horseshoe vortex bends around the cylinder and moves uphill, at the same time the vortex widens up and does not appear to be as concentrated as in the symmetry plane.
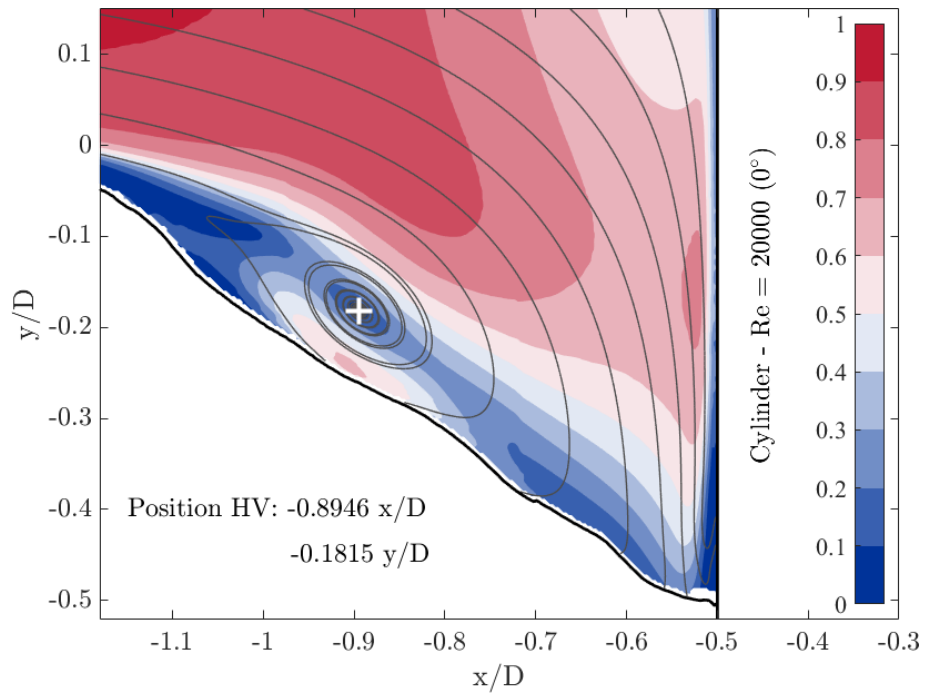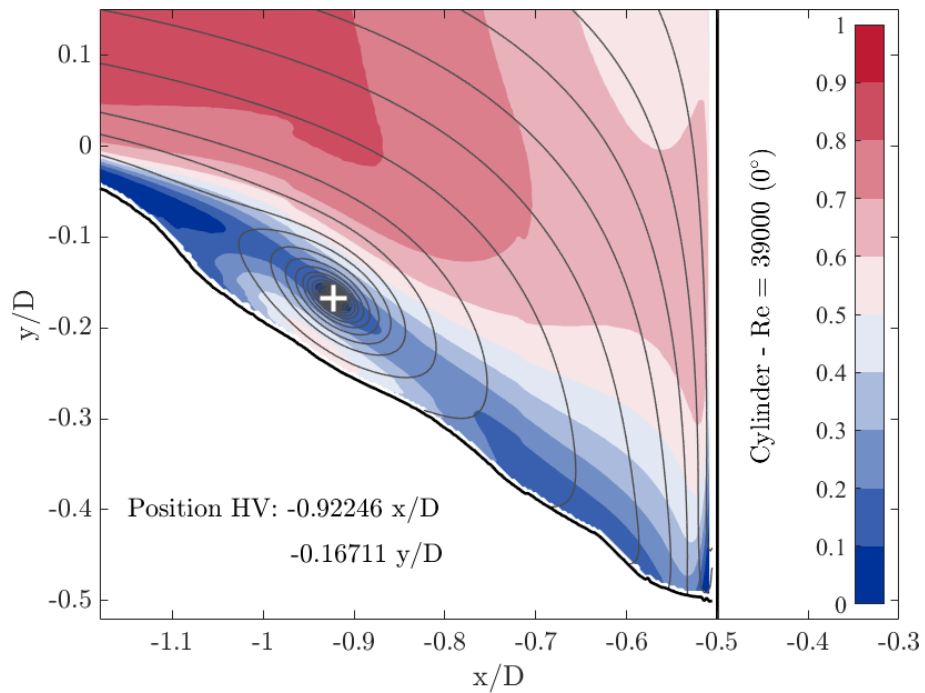
a: $Re = 20,000$

b: $Re = 39,000$

Figure 7.3: Time-averaged streamlines of the velocity field in the symmetry plane $0°$ in front of a scoured cylinder, flooded with the magnitude of the 3D-velocity field normalized by u_{ref}: a) $Re = 20,000$, b) $Re = 39,000$; white cross indicates time-averaged position of HV.
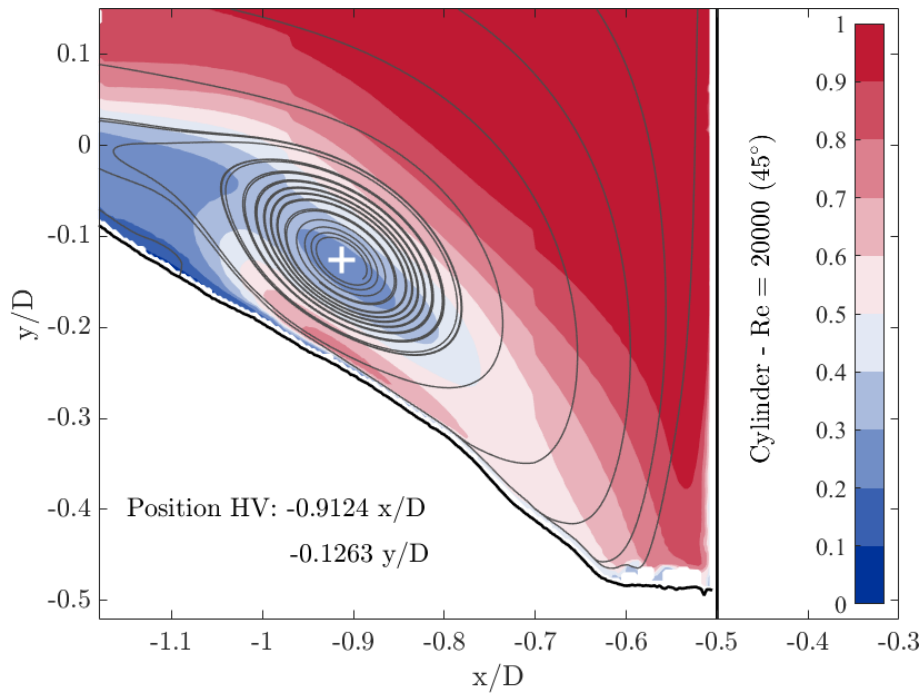
a: $Re = 20{,}000$
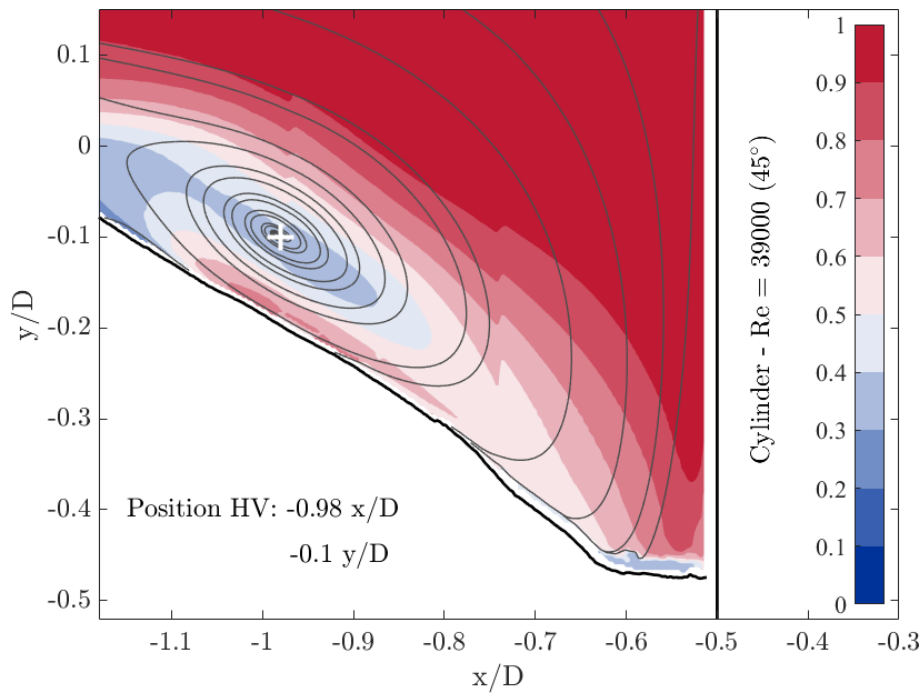
b: $Re = 39{,}000$

Figure 7.4: Time-averaged streamlines of the velocity field at 45° at the side of a scoured cylinder, flooded with the magnitude of the 3D-velocity field normalized by u_{ref}: a) $Re = 20{,}000$, b) $Re = 39{,}000$; white cross indicates time-averaged position of HV.

7.2 Vorticity of the Velocity Field

In turbulent flows, the rotation of fluid elements is given by the vorticity, which is defined as:

$$\omega = \nabla \times \mathbf{u}, \tag{7.1}$$

$$\begin{pmatrix} \omega_x \\ \omega_y \\ \omega_z \end{pmatrix} = \begin{pmatrix} \frac{\partial w}{\partial y} - \frac{\partial v}{\partial z} \\ \frac{\partial u}{\partial z} - \frac{\partial w}{\partial x} \\ \frac{\partial v}{\partial x} - \frac{\partial u}{\partial y} \end{pmatrix}.$$

In both, Mono-PIV and Stereo-PIV a planar velocity field is measured; thus, the spatial gradients $\partial/\partial z$ cannot be calculated. Therefore, eq. 7.1 reduces to ω_z, which refers to the rotation of the fluid elements around the z-axis. Consequently, the vortex transport equation $\frac{D\omega}{Dt} = (\omega\nabla)\mathbf{u} + \nu\nabla^2\omega$ cannot be discussed in detail here.

7.2.1 In front of a cylinder on a flat plate

Figures 7.5 present the time-averaged vorticity fields normalized by D/u_{ref} computed in the symmetry plane in front of the wall-mounted cylinder. Negative values of ω_z refer to a clockwise rotation and vice versa due to the selected orientation of the coordinate system. To link regions of strong vorticity to the flow field, thinned-out streamlines have been placed on the top together with the positions of the vortex cores and the stagnation points.

Both, distributions and magnitudes of the normalized vorticity are independent of Re. The strong downflow along the cylinder surface generates a zone of positive rotation, due to a developing turbulent boundary layer. This layer of high vorticity separates from the cylinder surface starting from $y/D = 0.1$ on towards the cylinder-wall junction and coincides with the small but intense vortex V3 at the cylinder foot.

The wall-parallel jet upstream of the stagnation point S3 generates a thin layer of strong positive rotation expanding underneath the horseshoe vortex. Further upstream of V1, the jet meets the approaching boundary layer and leads to its separation from the bottom plate that is indicated by the broad area of negative rotation upstream S1.

The centre of the horseshoe vortex, V1, coincides with a region of strong negative (clockwise) rotation, but V1 is not located in the centre of this area of negative vorticity. This off-centre position of V1 is similar for each Re and might be caused by an asymmetric behaviour of the HV (cf. section 3.1.2). However, this is not a distinct coherence as the vorticity contains also shear; thus, strong vorticity does not necessarily coincide with a vortex.

The region of negative vorticity at the cylinder-wall junction and underneath V3 indicates a rotation in the opposite direction of the corner vortex and gives a hint to the presence of a small-scale jet underneath V3, which developed there analogously to the wall-parallel jet underneath the HV.

a: $Re = 20,000$
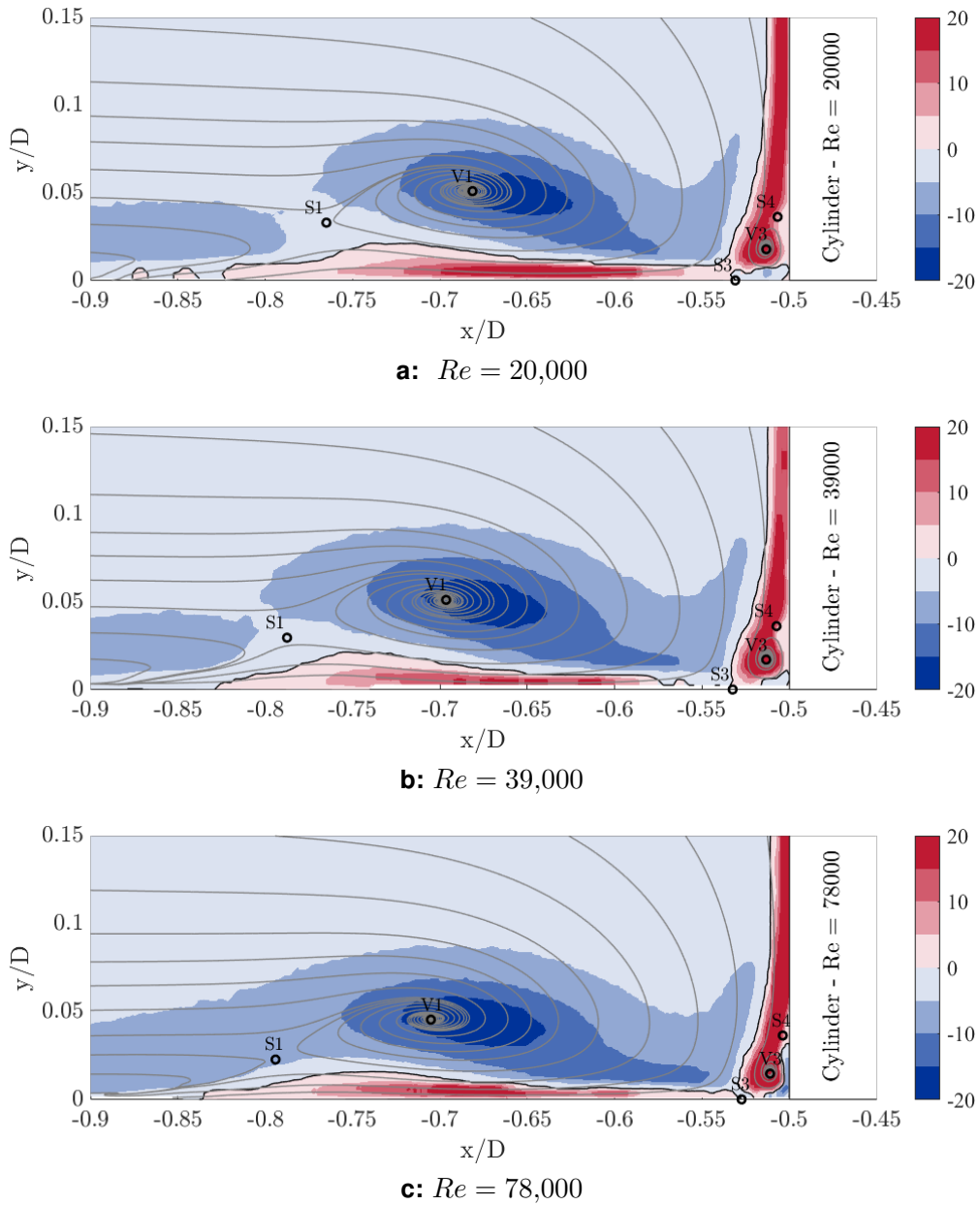
b: $Re = 39,000$

c: $Re = 78,000$

Figure 7.5: Time-averaged normalized vorticity $\omega_z = \left(\frac{\partial \langle v \rangle}{\partial x} - \frac{\partial \langle u \rangle}{\partial y} \right) \cdot \frac{D}{u_{\mathrm{ref}}}$ in front of a wall-mounted cylinder including the points of interest: a) $Re = 20,000$, b) $Re = 39,000$, c) $Re = 78,000$. Solid black line indicates zero-isoline of ω_z.

7.2.2 Around a scoured cylinder

The structure of the time-averaged vorticity in front of a scoured cylinder is presented in Figures 7.6. Similar to the flat-bed case, the downflow induces high (positive) vorticity along the cylinder surface as discussed in section 7.2.1. However, this developing boundary layer does not seem to separate from the cylinder surface near the cylinder foot as neither the time-averaged flow field (i.e. streamlines, see section 7.1.2) nor the vorticity give an indication to the presence of a corner vortex, which would force the downflow to detach. The time-averaged flow field does not indicate the development of a scour-parallel jet along the scour surface in the same manner as in the flat bed case (cf. Figure 7.3). The jet appears to be less pronounced and the vorticity along the scour surface is, therefore, small.

The approaching boundary layer from upstream detaches at the edge of the scour hole and induces strong negative vorticity along a shear layer, which merges with the HV. A thin layer of positive vorticity is recognisable underneath the main vortex, which might indicate that a weak jet-like structure developed in the scour, too, starting from a point closer to the HV. This near-wall shear layer enlarges when being ejected by the HV in the uphill direction and forms a region of positive vorticity spatially restricted by the approaching shear layer. The LES-results of Kirkil *et al.* (2005), who simulated this flow at a similar Reynolds number (18,000), indicate a second and third vortex in this region. Based on Figure 7.3 and Figure 7.6 a) and b), a second small vortex is likely to be located in that area trapped between the HV on one side and the entering shear layer on the other side. However, the PIV-results do not clearly support this assumption.

The presented Stereo-PIV results reveal much more detailed insight into the vorticity structure than previous experiments from literature. Dey & Raikar (2007) and Dey *et al.* (2008) measured the flow field around a scouring cylinder at different stages of development using acoustic Doppler velocimetry (ADV). Their results show homogeneous positive vorticity in the symmetry plane of the scour hole indicating only the global direction of rotation of the HV. However, neither the developing boundary layer along the cylinder surface, nor the region underneath the HV, nor the detached shear layer of the approaching flow from upstream were observed by the authors.

When analysing the results obtained at the 45° rotated position (see Figure 7.6 c) and d), the same vorticity structures can be identified as in the symmetry plane (cf. Figure 7.6 a) and b). The downflow is recognisable along the cylinder surface although the corresponding layer of positive rotation became thinner with respect to the symmetry plane. Further, the amplitude of vorticity around the HV decreased as well. As a circumferential velocity component is predominant at this location in the scour hole, a strong out-of-plane velocity transports the flow around the cylinder; therefore, the downflow is not parallel to the cylinder axis any more, but curling around in a helix. The HV widens out apparently while bending around the cylinder and the in-plane shear decreases. The same applies for the entering shear layer from upstream as the vorticity, i.e. the in-plane shear, shows much lower values here. At the same time, the layer of positive rotation underneath the HV expanded due to the dominating circumferential velocity component.

The analysis of the vorticity showed for both the flow in front of the wall-mounted cylinder as well as in the scour hole that the vorticity is (i) independent of the Reynolds number and (ii) the vorticity in the scour hole is as strong as in the flat-bed case.

a: $Re = 20,000$

b: $Re = 39,000$
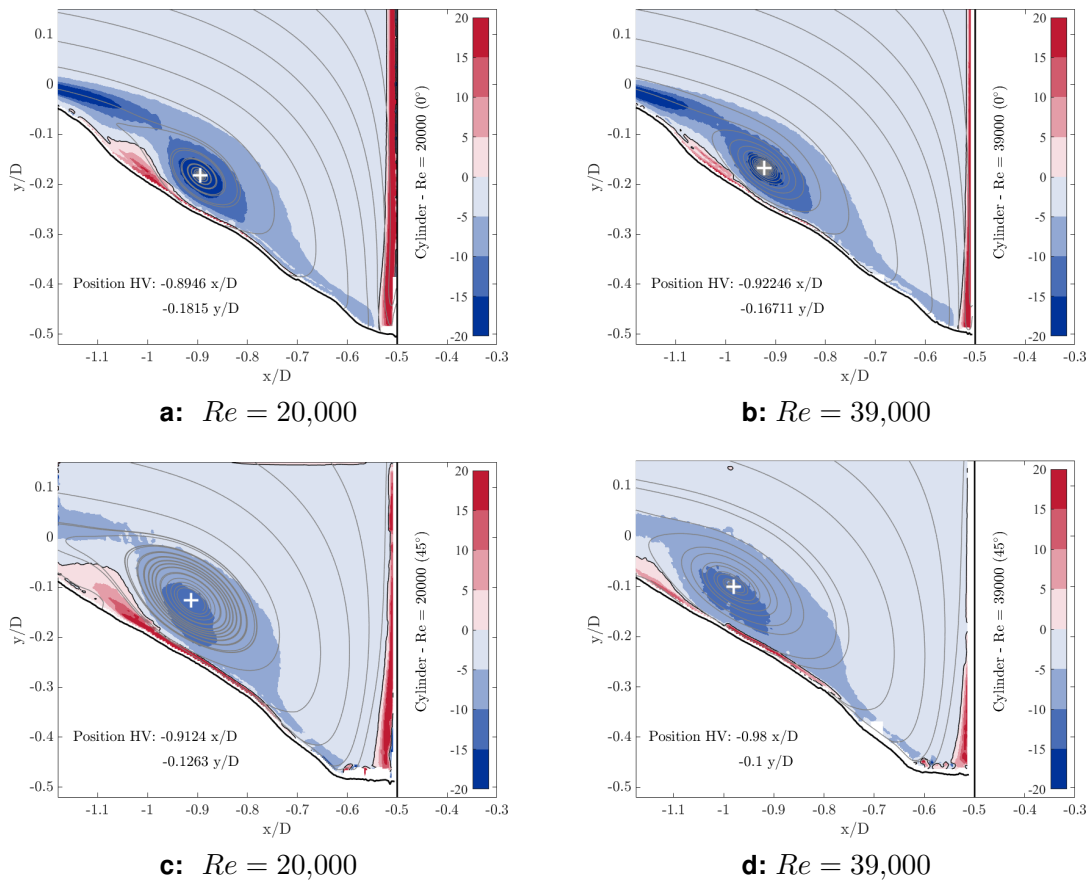
c: $Re = 20,000$

d: $Re = 39,000$

Figure 7.6: Time-averaged normalized vorticity $\omega_z = \left(\frac{\partial \langle v \rangle}{\partial x} - \frac{\partial \langle u \rangle}{\partial y} \right) \cdot \frac{D}{u_{\text{ref}}}$ in the symmetry plane $0°$ (top) and at $45°$ (bottom) around a scoured cylinder: $Re = 20,000$ (left), $Re = 39,000$ (right). White cross indicates the time-averaged position of the HV and the solid black line the zero-isoline of ω_z.

7.3 Reynolds Stresses and Turbulent Kinetic Energy

7.3.1 In front of a cylinder on a flat plate

The time-averaged two dimensional turbulent kinetic energy (TKE), normalized by u_{ref}^2, is documented in Figure 7.7 and reveals the c-shape pattern of the horseshoe vortex as described by Schanderl *et al.* (2017); Schanderl & Manhart (2016); Apsilidis *et al.* (2015); Kirkil & Constantinescu (2015); Escauriaza & Sotiropoulos (2011); Paik *et al.* (2007). The distribution of the TKE is concentrated around the centre of the vortex and has a branch reaching towards the bottom of the flume. The region of the downflow does not show significant turbulence, whereas the corner vortex (V3) is clearly represented by a local maximum of TKE. A slight *Re*-dependency is noticeable when looking at the maximum values in the region of the horseshoe vortex core: $0.1u_{\text{ref}}^2$ for $Re = 20,000$ to $0.06u_{\text{ref}}^2$ for $Re = 78,000$. Accordingly, the higher the Reynolds number, the lower the turbulence level of the horseshoe vortex with respect to the approach flow.

The turbulent kinetic energy at the vortex centre V1 is generated by velocity fluctuations in the streamwise and wall-normal directions, due to the horizontal oscillations of V1. However, the lower branch of the c-shaped TKE distribution is only caused by the Reynolds normal stresses in the streamwise direction (see Figure 7.8). The entire vortex structure oscillates, but these oscillations are not totally random and reveal two preferred flow states according to Devenport & Simpson (1990). They identified a back-flow and a zero-flow mode, meaning that the wall-parallel jet is either strongly pronounced in the upstream direction or has collapsed. The maximum value of the streamwise fluctuations at approximately $x/D = -0.7$ (underneath V1) stems from this alternating pattern of the jet that was described by Schanderl *et al.* (2017) as the 'flapping' of the jet when it detaches from the wall in the zero-flow mode. The amplitude of $\langle u'u'\rangle/u_{\mathrm{ref}}^2$ increases with Re in this region, whereas the fluctuations in the wall-normal direction $\langle v'v'\rangle/u_{\mathrm{ref}}^2$, which are the strongest in the centre of the horseshoe vortex, decrease from $Re = 20{,}000$ to $Re = 78{,}000$. In other words, the dynamics of the horseshoe vortex are reciprocally proportional to Re, whereas those of the wall-parallel jet are directly proportional to Re.

7.3.2 Around a scoured cylinder

The horseshoe vortex in the symmetry plane of the scour hole with a vertical cylinder shows a similar structure of turbulent kinetic energy as in the flat-bed case. The TKE has again a c-shaped spatial distribution with a maximum level around the vortex core branching towards the scour surface (see Figures 7.9 a and b). The levels of the TKE-intensity at the HV centre in both experimental configurations (flat bed and scour) match well with each other (e.g. $k_{\mathrm{flat},Re=20{,}000} \approx 0.09$ and $k_{\mathrm{scour},Re=20{,}000} \approx 0.1$). However, the relation between the TKE and the Re is more pronounced in the flat-bed set-up than in the scoured case: the amplitudes of the TKE at the HV are almost equal for both Reynolds numbers ($k_{\mathrm{scour},Re=20{,}000} \approx 0.1$ and $k_{\mathrm{scour},Re=39{,}000} \approx 0.094$), in contrast to the flat-bed case, where the TKE decreases with increasing Re.

The detaching approaching boundary layer of the flat-bed case does not seem to introduce additional turbulence to the HV-system, as Figure 7.7 does not show increased TKE levels trailing from upstream towards V1. Nevertheless, the detachment of the boundary layer at the scour rim appears to generate fluctuations that are also fed to the horseshoe vortex system (see Figure 7.9). The corner vortex that occurred at the cylinder-wall junction in the flat-bed case is represented by a region of increased TKE. However, no indication of this vortex structure can be observed when analysing the TKE at the scoured cylinder.

The TKE maintains its c-shaped structure, while the HV bends around the cylinder. Figures 7.9 c) and d) show that the HV widens out at the lateral measurement position and, therefore, loses TKE as the decreased amplitudes at the HV centre indicate. The lower branch appears to become more pronounced when the HV bends around the cylinder, whereas the entire TKE distribution is shifted uphill corresponding to the time-averaged position of the HV.

The TKE-structure shows high similarity between the wall-mounted cylinder and the scoured set-up irrespectively of the Re, which is not the case for each individual contributor to the TKE ($\langle u_i'u_i'\rangle$). The turbulent kinetic energy represents the trace of the Reynolds

a: $Re = 20,000$
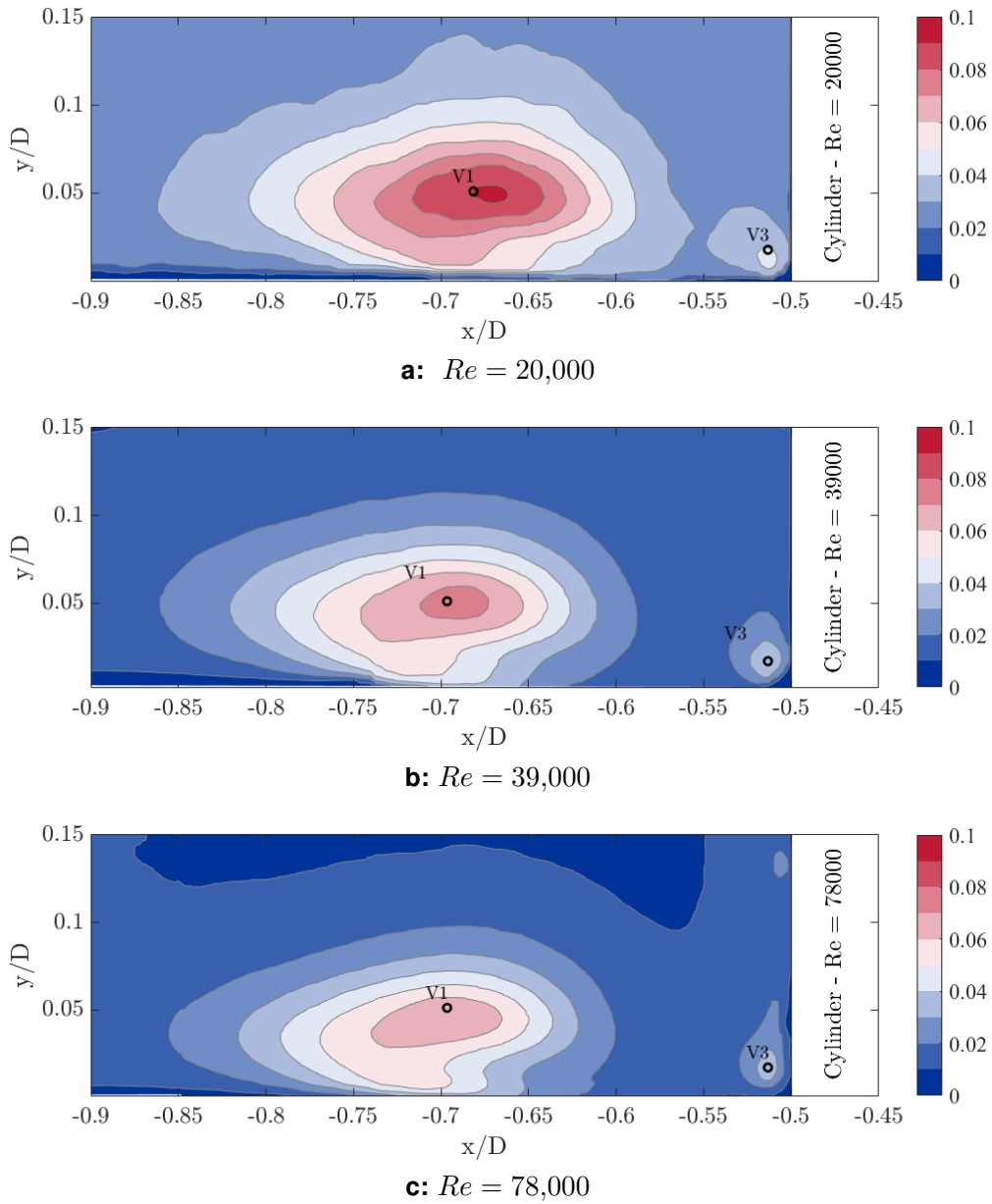
b: $Re = 39,000$

c: $Re = 78,000$

Figure 7.7: Time-averaged turbulent kinetic energy k in front of a wall-mounted cylinder on flat bed, normalized by u_{ref}^2: a) $Re = 20,000$, b) $Re = 39,000$, c) $Re = 78,000$

a: $Re = 20,000 : \langle u'u'\rangle/u_{\mathrm{ref}}^2$

b: $Re = 20,000 : \langle v'v'\rangle/u_{\mathrm{ref}}^2$

c: $Re = 39,000 : \langle u'u'\rangle/u_{\mathrm{ref}}^2$

d: $Re = 39,000 : \langle v'v'\rangle/u_{\mathrm{ref}}^2$

e: $Re = 78,000 : \langle u'u'\rangle/u_{\mathrm{ref}}^2$
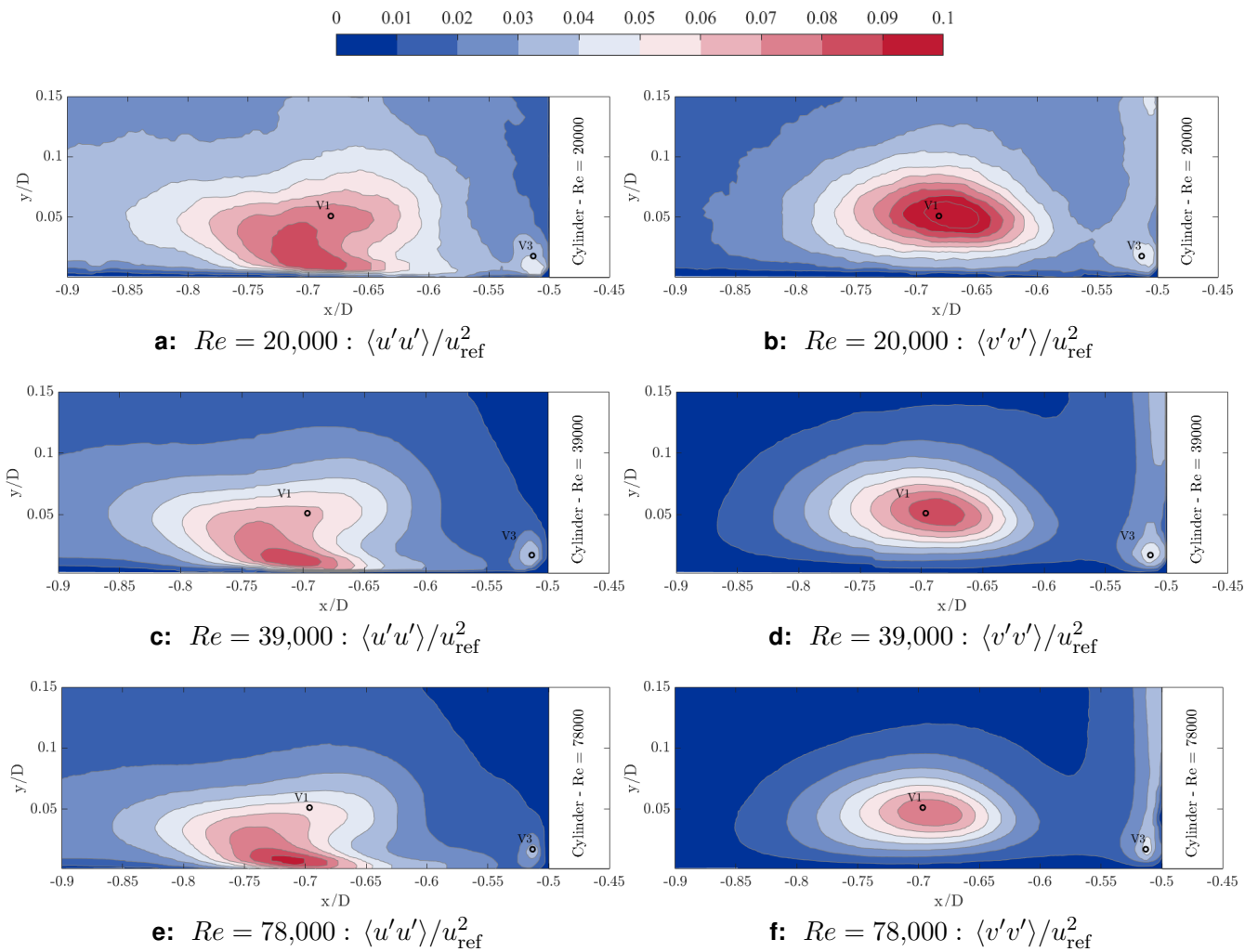
f: $Re = 78,000 : \langle v'v'\rangle/u_{\mathrm{ref}}^2$

Figure 7.8: Time-averaged Reynolds normal stresses in front of a wall-mounted cylinder on flat bed. Left:$\langle u'u'\rangle/u_{\mathrm{ref}}^2$, right: $\langle v'v'\rangle/u_{\mathrm{ref}}^2$. Top to bottom row: $Re = 20,000$, $Re = 39,000$, $Re = 78,000$

stress tensor (see section 2.2.5) and, therefore, is a scalar field, which is independent of the orientation of the reference frame. When analysing each normal stress component individually, however, the orientation of the reference frame is of major importance. The flow topology and the stress acting on a fluid element are dominated by the obstacle and the orientation of the bounding wall in case of wall-junction flows. The Cartesian orientation of the PIV-images, which defines the reference frame for the velocity components, coincides with the orientation of the physical stress tensor in front of the wall-mounted cylinder, which is not the case at the scour hole, as the scour surface and the cylinder do not square off.

Therefore, to analyse the similarity of the Reynolds stresses, their reference frame is rotated into a scour-oriented coordinate system (see appendix 10), and consequently, the coordinates and velocity components are no longer horizontal and vertical within the measurement plane, but become wall-normal (u_n and X_n) and wall-parallel (u_r and X_r) to the scour surface, while the parallel direction refers additionally to the radial direction of the cylinder. The coordinate system is rotated around the z-axis, which remains unchanged by this transformation. The circumferential direction is referred to as the azimuthal direction (u_a and X_a).

7.3.3 Effect of coordinate transformation on the *Re* stresses

Figure 7.10 shows the distributions of the Reynolds normal stresses in radial, wall-normal, and azimuthal direction, and the turbulent kinetic energy as the sum of the normal stresses in the scour-oriented as well as in the Cartesian frame for $Re = 39{,}000$. The effect of the transformation is clearly recognisable considering this juxtaposition.

The fluctuations $\langle u'_\mathrm{n} u'_\mathrm{n} \rangle$ are elliptically shaped similar to the flat-bed case (see right column of Figure 7.8). The amplitude in the centre of HV is slightly smaller than in the flat-bed case, whereas the TKE in the scour is larger. This difference can be explained by the contributions of the KH-vortices in the shear layer detaching from the edge of the scour hole.

Before the transformation, the distribution of the normal stresses in the horizontal direction showed three separate regions, whereas after transforming the reference frame, the stresses in radial direction $\langle u'_\mathrm{r} u'_\mathrm{r} \rangle$ reveal a similar near-wall structure as the corresponding term in front of the wall-mounted cylinder. Moreover, the fluctuations in the radial direction show a more complex distribution than in the flat-bed configuration with three different regions. Due to the rotation of the coordinate system, the regions of $\langle u'u' \rangle$ (see section 7.3.2) became more pronounced, and the near-wall structure is now fully contained in the wall-parallel stress. The interaction of the approaching boundary layer with the HV is represented by the increased $\langle u'_\mathrm{r} u'_\mathrm{r} \rangle$ values uphill the HV.

The fluctuations $\langle w'w' \rangle$ and $\langle u'_\mathrm{a} u'_\mathrm{a} \rangle$ are identical as the axis of rotation is parallel to the $z-$axis. Furthermore, the TKE-distribution does not change significantly in shape as this scalar field is independent of the corresponding orientation of the coordinate system (see Figure 7.10 e to h).

Lastly, the in-plane Reynolds shear stresses $\langle u'v' \rangle$ and $\langle u'_\mathrm{r} u'_\mathrm{n} \rangle$ are presented in Figure 7.11. In the Cartesian orientation, the shear stress is amplified where the approaching boundary
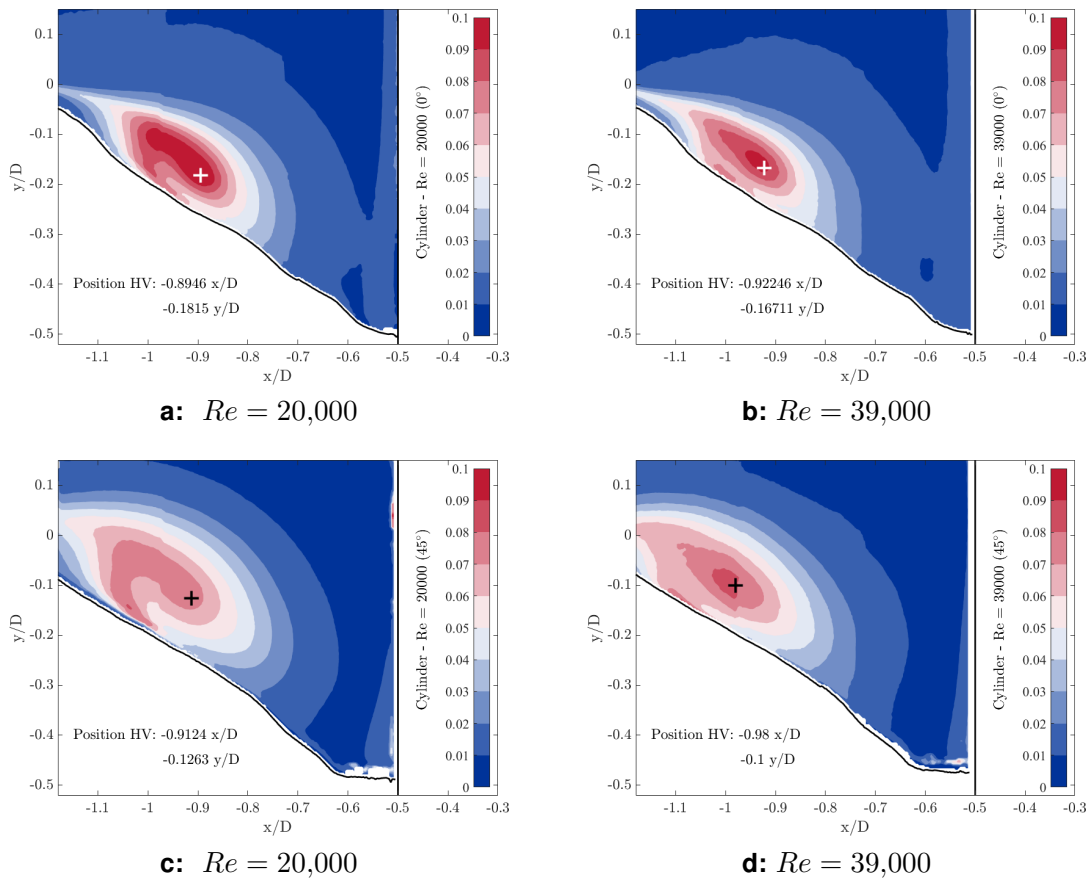
Figure 7.9: Time-averaged turbulent kinetic energy k in the symmetry plane 0° and at 45° around a scoured cylinder, normalized by u_{ref}^2: $Re = 20{,}000$ (left), $Re = 39{,}000$ (right). Black / white cross indicates the time-averaged position of the HV.

layer detaches and enters the scour hole. Further, the shear stress is increased as well underneath the horseshoe vortex at the scour surface. Both regions reveal negative values meaning that the correlation between u and v is negative. For the first region, when the flow enters the scour hole, v is negative and u is positive (pointing downwards and to the right, respectively). At the scour underneath HV the situation is reversed: the flow is going in the uphill direction (i.e. v is positive and u is negative). The HV is not indicated by amplified values of the shear stress. However, after the transformation into the scour-oriented system, the shear stress distributions changed completely. The HV is clearly indicated by strong negative values, whereas the entering shear layer cannot be identified any more. The entering shear layer induces normal stresses in the radial direction (parallel to the orientation of the scour surface), which were contained in both the u- and v-component of the velocity before the transformation.

When analysing a stress tensor, the orientation of the reference frame has to be considered, as normal stresses can be transformed into shear stresses and vice versa depending on the perspective. Therefore, referring to 'shear' or 'normal' stress in the flow around a scoured cylinder is strongly depending on the coordinate system. The TKE, however, corresponds to the trace of the stress tensor, which is the first invariant and, therefore, independent of the perspective.

a: $\langle u'u'\rangle/u_{\mathrm{ref}}^2$

b: $\langle u_{\mathrm{r}}'u_{\mathrm{r}}'\rangle/u_{\mathrm{ref}}^2$

c: $\langle v'v'\rangle/u_{\mathrm{ref}}^2$

d: $\langle u_{\mathrm{n}}'u_{\mathrm{n}}'\rangle/u_{\mathrm{ref}}^2$

e: $\langle w'w'\rangle/u_{\mathrm{ref}}^2$

f: $\langle u_{\mathrm{a}}'u_{\mathrm{a}}'\rangle/u_{\mathrm{ref}}^2$

g: $\langle k\rangle/u_{\mathrm{ref}}^2$

h: $\langle k\rangle/u_{\mathrm{ref}}^2$
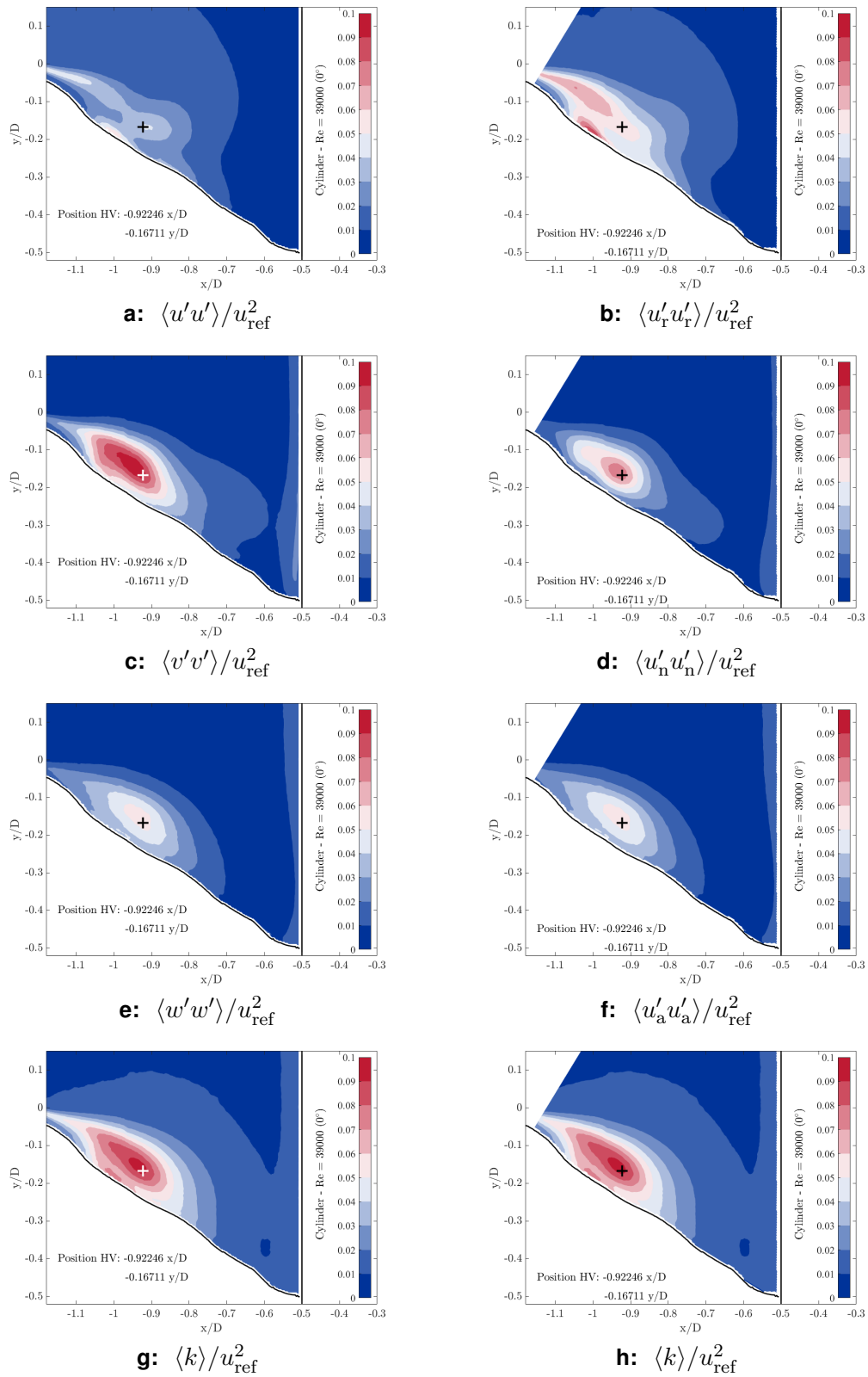
Figure 7.10: Time-averaged Reynolds normal stresses and TKE in Cartesian (left) and scour-oriented (right) coordinates for $Re = 39{,}000$ at $0°$ in front of a scoured cylinder, normalized by u_{ref}^2. Black / white cross indicates the time-averaged position of HV.

a: $\langle u'v'\rangle/u_{\mathrm{ref}}^2$ **b:** $\langle u'_{\mathrm{r}}u'_{\mathrm{n}}\rangle/u_{\mathrm{ref}}^2$
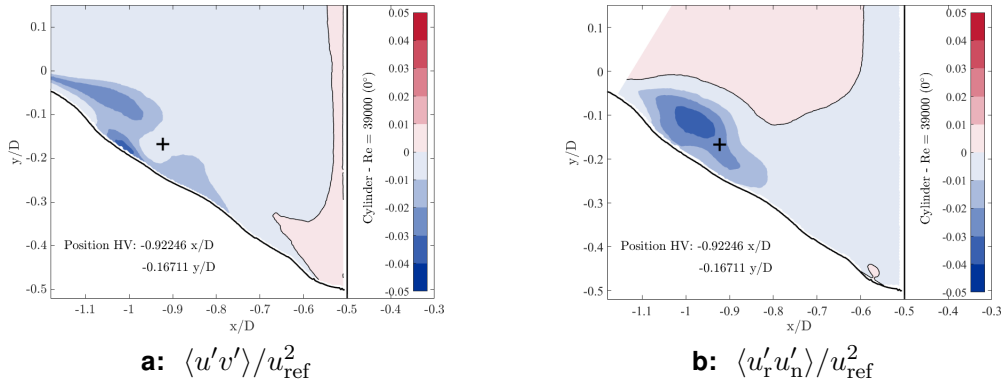
Figure 7.11: Time-averaged Reynolds shear stress in Cartesian a) and scour-oriented b) coordinates for $Re = 39{,}000$ at $0°$ in front of a scoured cylinder, normalized by u_{ref}^2. Black cross indicates the time-averaged position of HV.

7.4 Budget of the Turbulent Kinetic Energy

In section 2.3, the terms balancing the turbulent kinetic energy such as production, dissipation, convection and turbulent diffusion were presented. Each process will be discussed together for both flow configurations (wall-mounted and scoured cylinder) in the following section.

7.4.1 Production

The sum of the in-plane production of turbulent kinetic energy in front of the wall-mounted cylinder is depicted in Figure 7.12, i.e. only the terms of the first two dimensions are evaluated from the Mono-PIV results (P_{11} to P_{22} of eq. 7.2). In contrast, Figure 7.13 shows the total in-plane production in front of the scoured cylinder, which includes the two-dimensional terms plus the in-plane normal and shear stress production of the $w-$component measured using Stereo-PIV. The three dimensional Stereo-PIV results are reconstructed (see section 4.6.4), which means that the time series of all three velocity components are known and, thus, the cross-correlations $\langle u'w'\rangle$ and $\langle v'w'\rangle$ (entries P_{31} and P_{32}) are also shown. However, the results are still limited by the planar light sheet. Therefore, the derivatives $\partial/\partial z$ are impossible to evaluate using these data sets (grey-coloured terms in eq. 7.2). This lack of information is negligible at $0°$, as the terms $\partial u/\partial z$ and $\partial v/\partial z$ are approximately zero due to symmetry. Nevertheless, the gradient $\partial w/\partial z$ can be calculated indirectly based on the gradients $\partial u/\partial x$ and $\partial v/\partial y$ and assuming the incompressibility of water (cf. eq. 2.8).

$$P_{i,j} = -\langle u'_i u'_j\rangle \frac{\partial \langle u_i\rangle}{\partial x_j} = -\begin{bmatrix} \langle u'u'\rangle\frac{\partial\langle u\rangle}{\partial x} & \langle u'v'\rangle\frac{\partial\langle u\rangle}{\partial y} & \langle u'w'\rangle\frac{\partial\langle u\rangle}{\partial z} \\ \langle u'v'\rangle\frac{\partial\langle v\rangle}{\partial x} & \langle v'v'\rangle\frac{\partial\langle v\rangle}{\partial y} & \langle v'w'\rangle\frac{\partial\langle v\rangle}{\partial z} \\ \langle u'w'\rangle\frac{\partial\langle w\rangle}{\partial x} & \langle v'w'\rangle\frac{\partial\langle w\rangle}{\partial y} & \langle w'w'\rangle\frac{\partial\langle w\rangle}{\partial z} \end{bmatrix} \qquad (7.2)$$

In front of the wall-mounted cylinder, the down-flow is deflected at S3 in the upstream direction by the bottom plate. The total production becomes negative when the wall-parallel jet develops and accelerates; turbulent kinetic energy is transferred into mean kinetic energy. However, the jet decelerates when passing the horseshoe vortex, which entails significant normal stress production in the streamwise direction (lower branch of the total in-plane production). Furthermore, the characteristic bimodal dynamics of the horseshoe vortex contribute to the normal and shear stress production terms in front of the wall-mounted cylinder and indicate a large energy transfer into turbulent kinetic energy in the region of V1, which is discussed in detail by Schanderl *et al.* (2017). The corner vortex V3 is indicated by a large in-plane production of TKE at the location where the down-flow separates from the cylinder surface.
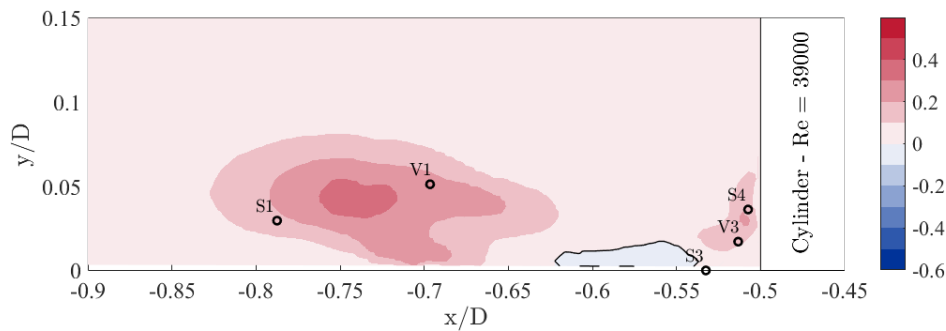
Figure 7.12: Time-averaged in-plane production of TKE $P = -\langle u_i' u_j' \rangle \frac{\partial \langle u_i \rangle}{\partial x_j} \cdot \frac{D}{u_{\mathrm{ref}}^3}$ in front of a wall-mounted cylinder on flat bed ($Re = 39,000$). The solid black line indicates the zero-isoline of P.

The mechanisms of stress production in front of the scoured cylinder are on the one hand similar to the flat-bed case due to the similarity of the down-flow, which introduces high-momentum fluid into the HV-system. On the other hand, additional structures occur because of the shape of the scour hole, which reveals similarities to a backward-facing step where a layer of Kelvin-Helmholtz (KH) instabilities develops from the edge of the step on, which is analogue to the rim of the scour hole.

Along the cylinder surface in the scour, the down-flow develops and the total production is slightly negative (see Figure 7.13). The downwards acceleration in the vertical direction towards the scour surface (see Figure 7.3) causes a transformation of turbulent kinetic energy into mean kinetic energy. After the deflection of the down-flow in the uphill direction, the production remains negative at the scour surface like in the flat-bed case, which indicates the development of a wall-parallel jet. Further uphill, the horseshoe vortex is indicated by a significantly large TKE-production. In contrast to the situation in front of the wall-mounted cylinder, the production of TKE has an additional structure of KH-vortices (entering shear layer), which produce normal stresses. The KH-vortices shed from the scour rim interfere with the horseshoe vortex, which is indicated by large shear stress production (see Figure 7.13).

When the flow bends around the cylinder, the horseshoe vortex widens at the expense of its strength. Analysing the total production of TKE at 45° (see Figures 7.13 c and d), an increasing difference between the corresponding distributions at 0° in front of both a scoured and a wall-mounted cylinder can be observed.

In Figure 7.14, the total production of TKE is separated into the sum of normal stress production and into the sum of shear stress production in the scour-oriented reference frame. The single contributors to these summed terms, however, are not presented. The normal stress production is the trace of the production tensor in eq. 7.2, whereas the shear stress production refers to the sum of the remaining elements. According to this decomposition, the total production of TKE consists mainly of shear stress production, which is caused by the entering KH-vortices interfering with the horseshoe vortex approximately at $x/D = -1.0$ and $y/D = -0.1$, i.e. upstream (uphill) of HV. Within the shear stress production, the term $-\langle u'_{\mathrm{r}} u'_{\mathrm{n}} \rangle \frac{\partial \langle u_{\mathrm{r}} \rangle}{\partial x_{\mathrm{n}}}$ is generally predominant, while the contribution of the out-of-plane components is small due to symmetry. At the HV centre, the shear production is damped by $-\langle u'_{\mathrm{r}} u'_{\mathrm{n}} \rangle \frac{\partial \langle u_{\mathrm{n}} \rangle}{\partial x_{\mathrm{r}}}$, which has a negative amplitude there.

a: $Re = 20,000$

b: $Re = 39,000$
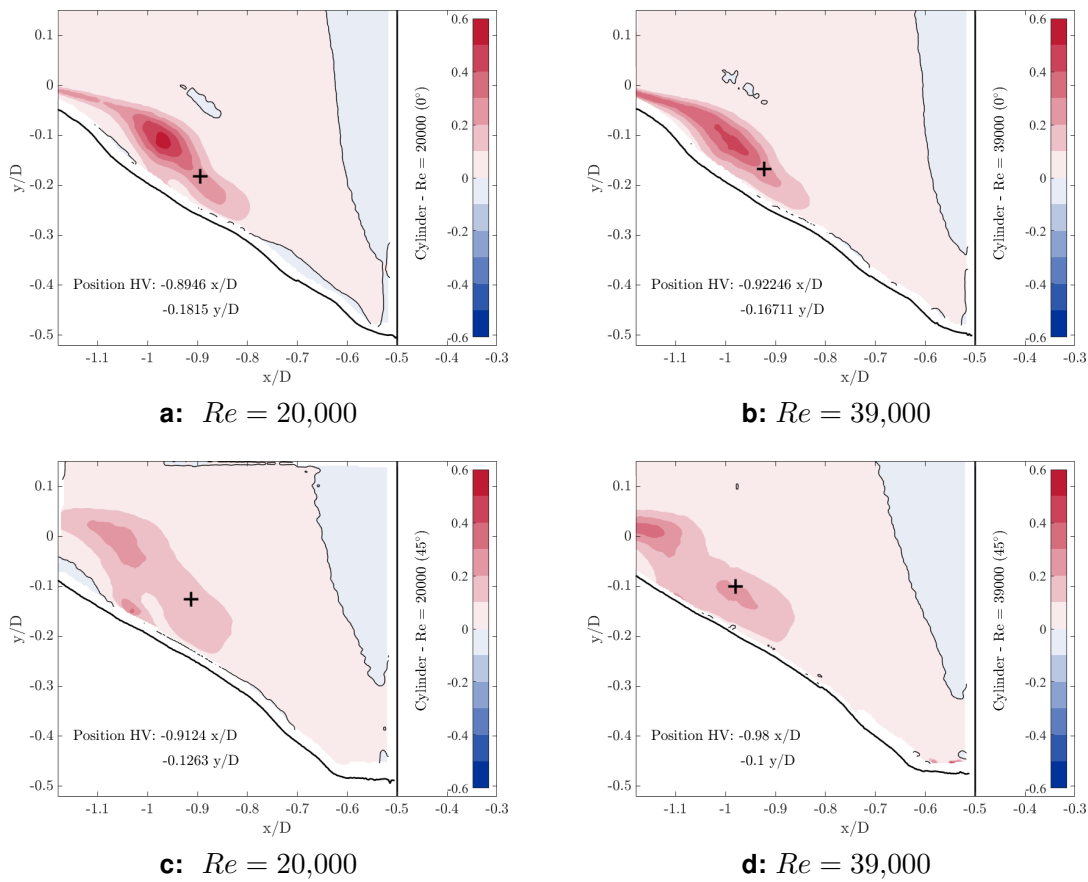
c: $Re = 20,000$

d: $Re = 39,000$

Figure 7.13: Time-averaged production of TKE $P = -\langle u'_i u'_j \rangle \frac{\partial \langle u_i \rangle}{\partial x_j} \cdot \frac{D}{u_{\mathrm{ref}}^3}$ in the symmetry plane 0° (top) and at 45° (bottom) around a scoured cylinder: $Re = 20,000$ (left), $Re = 39,000$ (right). Black cross indicates time-averaged position of HV and the solid black line the zero-isoline of P.

Within the layer of KH-vortices that detached from the edge of the scour hole, the normal stress is exclusively produced by the radial component $-\langle u'_{\mathrm{r}} u'_{\mathrm{r}} \rangle \frac{\partial \langle u_{\mathrm{r}} \rangle}{\partial x_{\mathrm{r}}}$. In the region of the HV, the normal stress production is close to zero, as the radial and the surface-normal contributions of the stress production cancel each other out. The flow is only rotated when following a streamline into the horseshoe vortex. This means the normal stress stemming

a: P_{normal} $Re = 20,000$

b: P_{normal} $Re = 39,000$

c: P_{shear} $Re = 20,000$

d: P_{shear} $Re = 39,000$
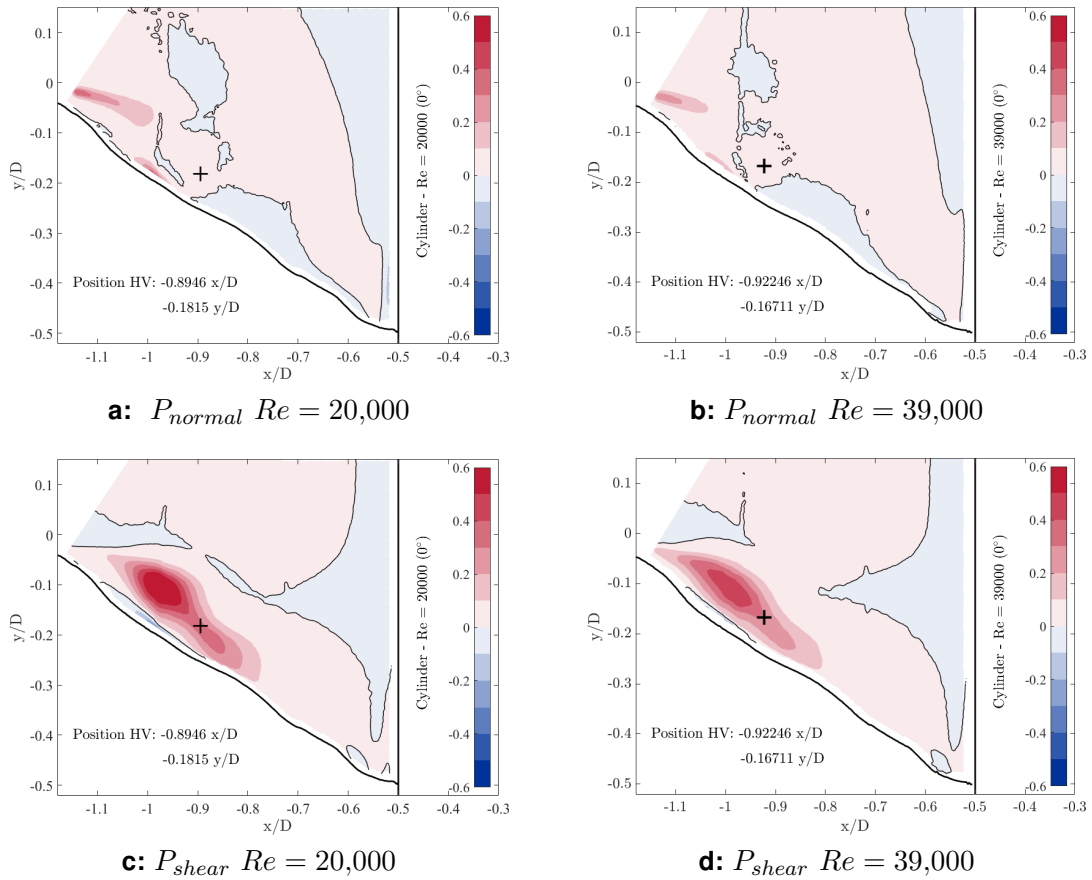
Figure 7.14: Time-averaged production of normal stresses (top) $P_{i,i} = -\langle u_i' u_i' \rangle \frac{\partial \langle u_i \rangle}{\partial x_i} \cdot \frac{D}{u_{\mathrm{ref}}^3}$ at $Re = 20,000$ a) and $Re = 39,000$ b). Time-averaged production of shear stresses (bottom) $P_{i,j} = -\langle u_i' u_j' \rangle \frac{\partial \langle u_i \rangle}{\partial x_j} \cdot \frac{D}{u_{\mathrm{ref}}^3}$, for $i \neq j$ at $Re = 20,000$ c) and $Re = 39,000$ d) in front of the scoured cylinder ($0°$). Black cross indicates time-averaged position of HV and the solid black line the zero-isoline.

from u_r-fluctuations upstream from the vortex is transferred into u_n-fluctuations due to the rotation by the HV. However, the small region at the scour surface uphill from the centre of the HV reveals a positive residual of normal stress production, which is linked to the lower branch of the c-shaped TKE distribution stemming from fluctuations parallel to the scour surface, i.e. in the radial direction.

7.4.2 Dissipation

The dissipation of turbulent kinetic energy ϵ acts as a sink term in eq. 2.21 on the smallest flow scales (i.e. Kolmogorov scales, see eq. 2.4 to eq. 2.6) and transforms TKE in internal energy, thus heat. Figure 7.15 shows the distribution of the time-averaged dissipation rate in front of the wall-mounted cylinder for $Re = 39,000$. Three characteristic regions of high dissipation with values of $0.09 < \epsilon < 0.12 \cdot \frac{u_{\mathrm{ref}}^3}{D}$ can be identified: i) in the horseshoe vortex (V1); ii) in the corner vortex (V3); and iii) in the wall-parallel jet underneath V1. The large peak of ϵ at V1 is caused by the horizontal oscillations of the horseshoe vortex inducing large

gradients of the fluctuations u' and v'.

The down-flow separates from the cylinder surface and forms the corner vortex V3, which entails a region of large dissipation. As this structure is enclosed by the outer part of the down-flow and the cylinder, the TKE produced in that region cannot be transported within the symmetry plane. Thus, it has to be either dissipated or transported in out-of-plane direction.

Upstream stagnation point S3, when the jet develops (accelerates), TKE is re-transformed into mean kinetic energy (see section 7.4.1). Consequently, the dissipation is small in this region, too. As soon as the jet decelerates and becomes more unstable, the dissipation rate increases and reveals a local near-wall peak in the amplitude.

The spatial distribution of ϵ is similar to that of the TKE and its production, but does not fully match. The peak of the total production is located upstream of V1, whereas the largest dissipation is observed downstream of the horseshoe vortex. This disparity indicates that the flow configuration is not in an equilibrium state, since the horseshoe vortex bends around the cylinder evoking a strong out-of-plane transport.
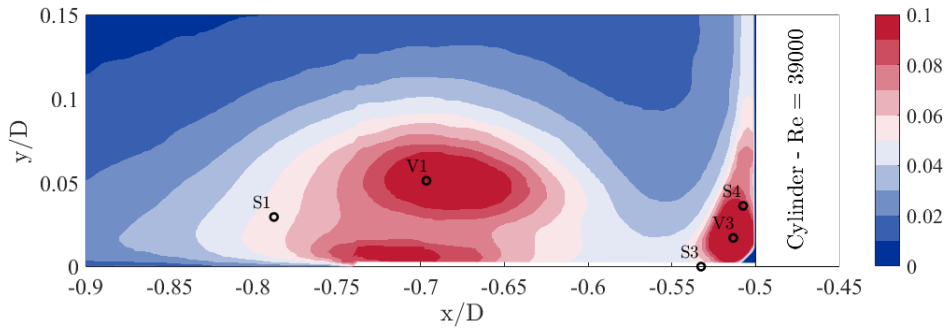
Figure 7.15: Time-averaged dissipation of TKE $\epsilon = 2\nu\langle s_{ij}s_{ij}\rangle \cdot \frac{D}{u_{\text{ref}}^3}$ in front of a wall-mounted cylinder on flat bed ($Re = 39{,}000$).

At the scoured cylinder, the distribution of TKE dissipation consists of two main structures (see Figures 7.16). The location of the HV centre is located within the region of the largest dissipation. In contrast to the flat-bed case, downstream of the HV no dissipation can be observed at all. Furthermore, the approximately zero dissipation rate in the corner of the scour and the cylinder indicates that no corner vortex is present. The amplitude in the centre of the HV in front of the scoured cylinder is approximately half as large as at the wall-mounted cylinder ($\epsilon_{\text{V1, flat, }Re=39{,}000} \approx 0.11 \cdot \frac{u_{\text{ref}}^3}{D}$ and $\epsilon_{\text{HV, scour, }Re=39{,}000} \approx 0.06 \cdot \frac{u_{\text{ref}}^3}{D}$)

In the region where the KH-vortices interfere with the horseshoe vortex (upstream of the HV centre), the dissipation reveals amplified values as well. Furthermore, the trace of the approaching separated shear layer is indicated by a thin layer of large dissipation. The large values of ϵ underneath the horseshoe vortex at the surface of the scour are probably artefacts caused by the surface reflections rather than reliable values. The c-shaped structure of the TKE is contained by the dissipation at the side of the scoured cylinder, but the amplitude decreased with respect to the symmetry plane.

a: $Re = 20,000$

b: $Re = 39,000$
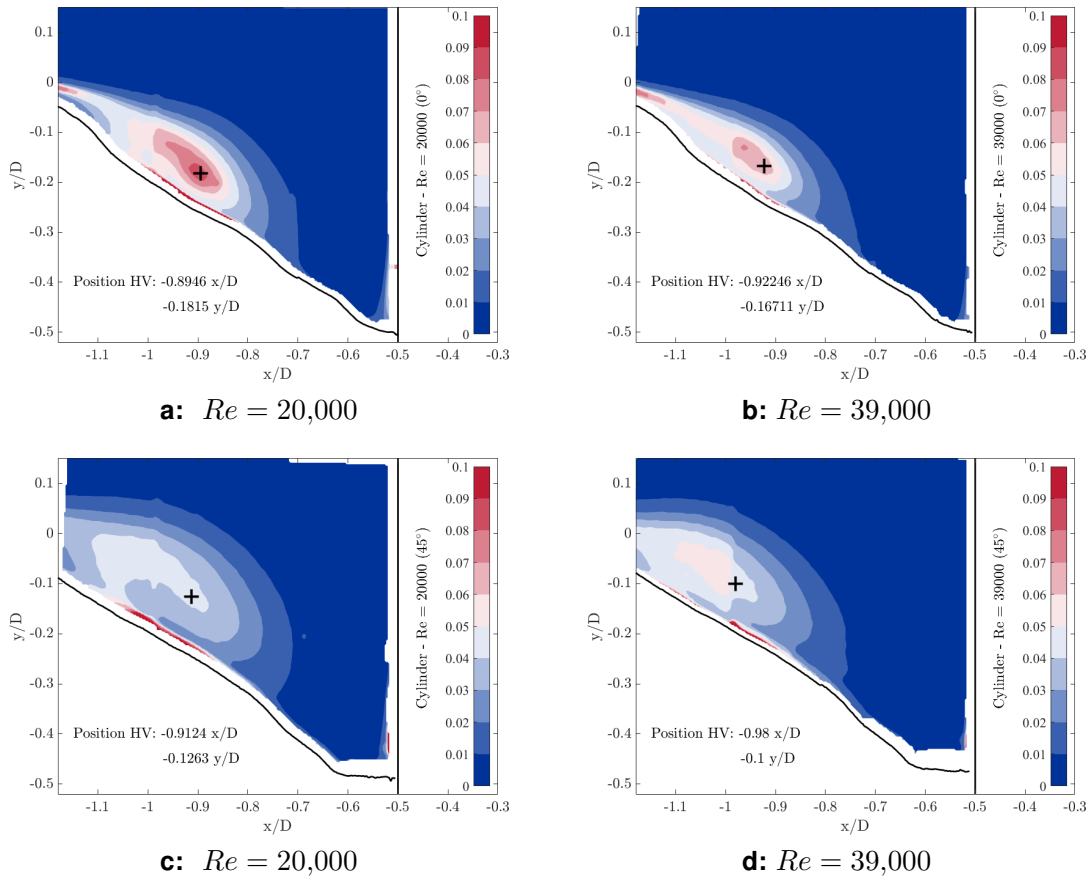
c: $Re = 20,000$

d: $Re = 39,000$

Figure 7.16: Time-averaged dissipation of TKE $\epsilon = 2\nu\langle s_{ij}s_{ij}\rangle \cdot \frac{D}{u_{\mathrm{ref}}^3}$ in the symmetry plane $0°$ (top) and at $45°$ (bottom) around a scoured cylinder: $Re = 20,000$ (left), $Re = 39,000$ (right). Black cross indicates the time-averaged position of the HV.

7.4.3 Diffusion

The turbulent transport of TKE in space occurs due to velocity and pressure fluctuations, as well as, due to viscosity; and in this diffusion process no production or degeneration of TKE takes place. In turbulent flows with high Reynolds numbers, the influence of the viscous diffusion term of eq. 2.23 (see section 2.3) is orders of magnitudes smaller than the remaining two. According to Schanderl *et al.* (2017), the viscous term is negligible in front of a wall-mounted cylinder. For the scoured-cylinder configuration, this term was evaluated for $Re = 20,000$ and will not be further discussed, as it is about $2-3$ orders of magnitude smaller than the transport due to velocity fluctuations. Furthermore, the velocity-pressure correlations $-\nabla\frac{1}{\rho}\langle u_i'p'\rangle$ are impossible to obtain from PIV data. However, the influence of the pressure and the corresponding fluctuations are expected to be important for the TKE transport mechanisms.

The remaining part of the diffusion term is that referring to the turbulent fluctuations $-\nabla\frac{1}{2}\langle u_i'u_j'u_j'\rangle$, which is presented in Figure 7.17 in front of the wall-mounted cylinder and $Re = 39,000$. Negative areas indicate that TKE is being transported away from them and vice versa. The negative region between the horseshoe vortex (V1), the stagnation point

upstream (S1) and the bottom of the flume coincides with the region of main production of TKE. Thus, the TKE generated in this region is going to be either dissipated or transported upwards. Up- and downstream of V1, two pairs of negative-positive diffusion can be observed, respectively, due to the horizontal oscillations of the horseshoe vortex. The small corner vortex V3 reveals similar transport structures in upwards direction corresponding to the direction of the rotation. The layer of large positive transport along the cylinder surface might be biased by errors in calculating the gradient of triple correlations of the velocities near a wall rather than referring to physical flow structures.
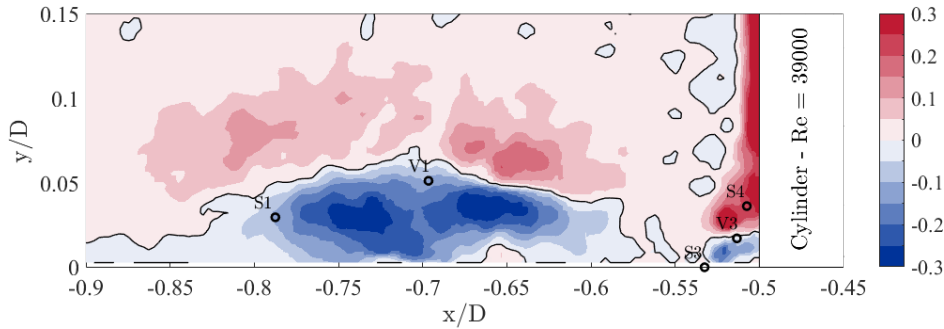
Figure 7.17: Time-averaged turbulent diffusion of TKE $\nabla T = -\frac{1}{2}\frac{\partial \langle u_i' u_j' u_j' \rangle}{\partial x_i} \cdot \frac{D}{u_{\mathrm{ref}}^3}$ in front of a wall-mounted cylinder on flat bed ($Re = 39{,}000$). The solid black line indicates the zero-isoline of T.

Figures 7.18 show the turbulent diffusion of the TKE around the scoured cylinder for both Re. Following the entering shear layer at the scour rim in the symmetry plane, a region of positive turbulent diffusion lays on top of a negative region. The centre of the horseshoe vortex and the region of interference with the incoming shear layer are characterized by negative turbulent diffusion. Thus, TKE is being transported out of these areas. In the figures representing the symmetry plane a) and b), an isoline of the total production ($P \geq 0.4 \cdot \frac{u_{\mathrm{ref}}^3}{D}$) is included as well. The area of largest negative transport due to the velocity fluctuations coincides well with the area of large production. This counterbalancing pattern of the turbulent diffusion and the production term was also documented by Schanderl *et al.* (2017) in front of the wall-mounted cylinder.

The amplitude of turbulent transport decreases with Re as it is the case for the production. Furthermore, a similarity between the symmetry plane and the lateral position at 45° can be observed, as well as the effect of the widening horseshoe vortex.

7.4.4 Convection

The time-averaged convection of turbulent kinetic energy C in front of the wall-mounted cylinder for $Re = 39{,}000$ is presented in Figure 7.19 together with the zero-isoline and points of interest. Areas of negative mean-flow convection indicate that TKE increases along a streamline and vice versa. The horseshoe vortex blocks the incoming flow and the wall-parallel jet penetrates the boundary layer near the wall acting as a wedge, which forces the detachment of the flow further upstream. This detached flow becomes unstable, and consequently, the TKE increases along the streamlines (negative values of C) when approaching the horseshoe vortex.

a: $Re = 20,000$ **b:** $Re = 39,000$
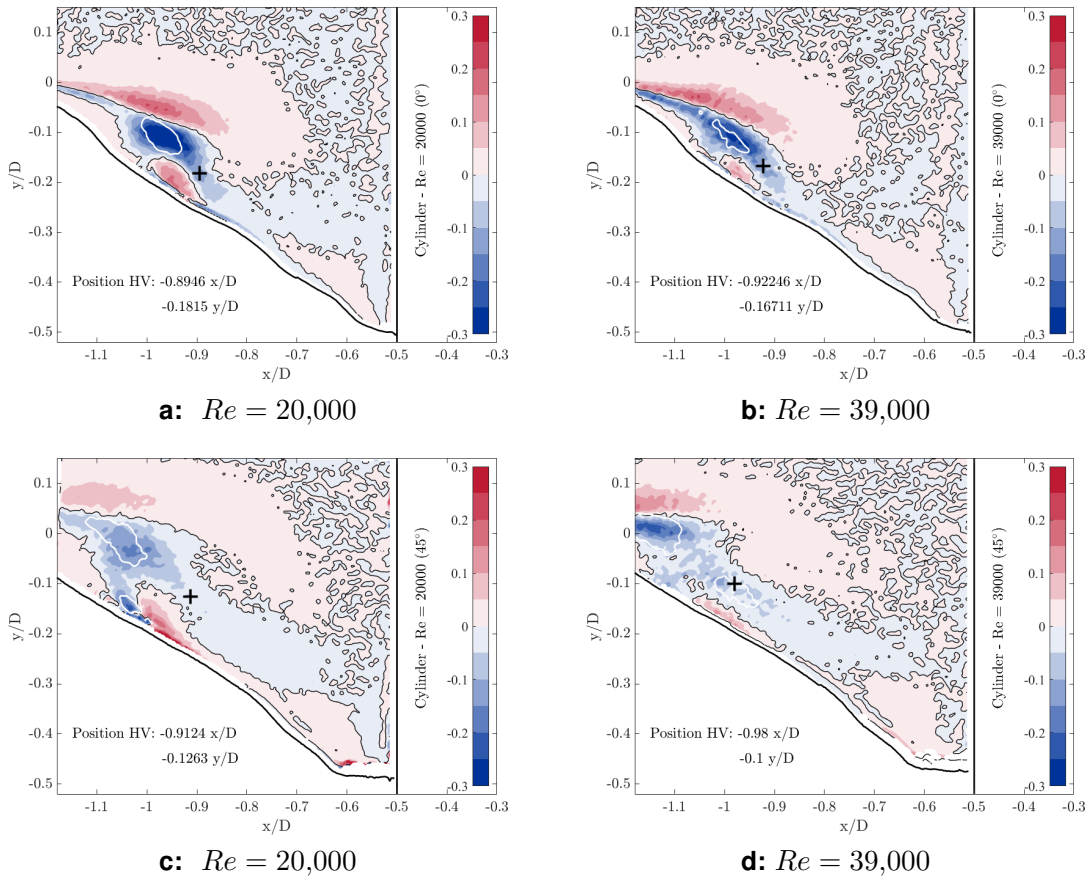
c: $Re = 20,000$ **d:** $Re = 39,000$

Figure 7.18: Time-averaged turbulent diffusion of TKE $\nabla T = -\frac{1}{2}\frac{\partial \langle u_i' u_j' u_j' \rangle}{\partial x_i} \cdot \frac{D}{u_{\mathrm{ref}}^3}$ in the symmetry plane $0°$ (top) and at $45°$ (bottom) around a scoured cylinder: $Re = 20,000$ (left), $Re = 39,000$ (right). Black cross indicates the time-averaged position of the HV and the solid black line refers to the zero-isoline of T. The solid white line highlights the region of large production $P \geq 0.4 \cdot \frac{u_{\mathrm{ref}}^3}{D}$ in a) and b), and $P \geq 0.2 \cdot \frac{u_{\mathrm{ref}}^3}{D}$ in c) and d)

At point S3, the down-flow is deflected in upstream direction and the wall-parallel jet develops. The redirection is indicated by positive mean-flow convection, which refers to a decreasing TKE. The longer the wall-parallel jet can evolve, the more TKE can increase, which is represented by a large negative mean-flow convection at $-0.7 < x/D < -0.6$. As soon as the jet passes V1, the convection C changes sign and becomes positive (TKE decreases). The lower branch of the c-shaped distribution of the TKE and of the production (see Figures 7.7 and 7.12, respectively) coincide with the zero-isoline of C in that region. The stagnation points S1 and S4 are located on top of the zero-isoline of the mean-flow convection. Furthermore, the vortex cores V1 and V3 are located close to areas of zero mean-flow convection, meaning that changes of the TKE in the centre of a vortex are small in average. The interaction of the down-flow and the corner vortex is indicated by the negative mean convection above V3 and increases the TKE level in this region.

Figure 7.20 shows the convection of TKE for $Re = 20,000$ and $Re = 39,000$ at $0°$ and $45°$ around the scoured cylinder. The shear layer that detached at the edge of the scour hole introduces instabilities and, therefore, the mean convection is negative referring to an
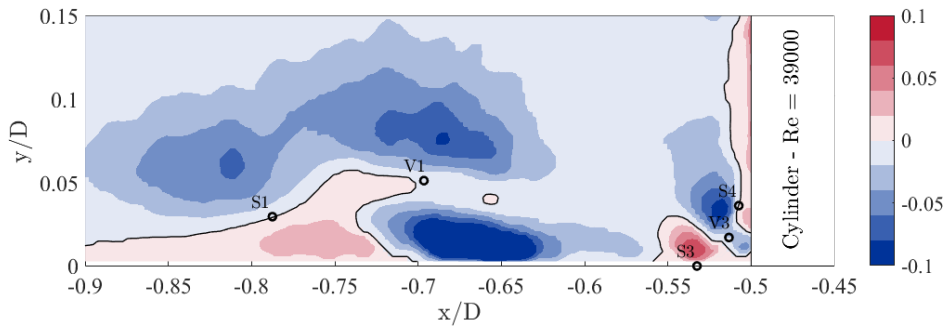
Figure 7.19: Time-averaged convection of TKE $C = -\langle u_i \rangle \frac{\partial k}{\partial x_i} \cdot \frac{D}{u_{\text{ref}}^3}$ in front of a wall-mounted cylinder on flat bed ($Re = 39{,}000$). Solid black line indicates the zero-isoline of C.

increasing TKE. Moreover, both the time-averaged distribution of the TKE as well as the production of TKE (see Figure 7.9 and Figure 7.13, respectively) reveal a tail from the horseshoe vortex towards the scour rim due to this effect.

The vortex core is located on top of a zero-isoline of C around the scoured cylinder, encircled by positive and negative mean convection. In contrast to the flat-bed case, the TKE decreases in the upper half of the horseshoe vortex. Whereas, near the scour surface the TKE increases. As in the flat-bed results, the mean convection changes sign along the bounding surface after passing the horseshoe vortex, while the zero-isoline of this change of sign coincides again with the lower branch of the c-shaped distribution of the TKE and the production. Along the scour surface, when the down-flow is redirected uphill, the mean convection is negative, i.e. TKE increases in this region. However, the production term as well as the turbulent diffusion (see Figure 7.18) are negative, too, which means that TKE is either transformed into mean kinetic energy ($P < 0$) or transported away from the wall ($\nabla T < 0$), and therefore, does not explain the increasing TKE at the scour surface.

7.4.5 Residual of the TKE balance

The pressure transport term (see eq. 2.23) in the TKE balance consists of pressure-velocity correlations $u_i' p'$, which cannot be evaluated using PIV-data. Furthermore, velocity gradients can only be measured within the light sheet plane. As the contributors of the TKE budget in the symmetry plane of the cylinder do not balance, the question arises which term that cannot be evaluated from the PIV-data has such considerable impact to be responsible for this imbalance.

Due to reasons of symmetry, the out-of-plane velocity gradients $\partial u / \partial z$ and $\partial v / \partial z$ (e.g. in eq. 7.2), however, can be assumed to be small. The contribution of the viscous diffusion ($2\nu \langle u_j' s_{ij} \rangle$) to the turbulent transport, is small, too (e.g. (Schanderl et al., 2017)).

Therefore, the pressure fluctuations are suspected to be responsible for transporting TKE towards the scour surface and to be the missing piece in the balance. This hypothesis is supported by analysing the residual of all terms. According to eq. 2.21, the production (P), the transport mechanisms (∇T), and the dissipation (ϵ) balance the mean-flow convection

a: $Re = 20,000$ **b:** $Re = 39,000$
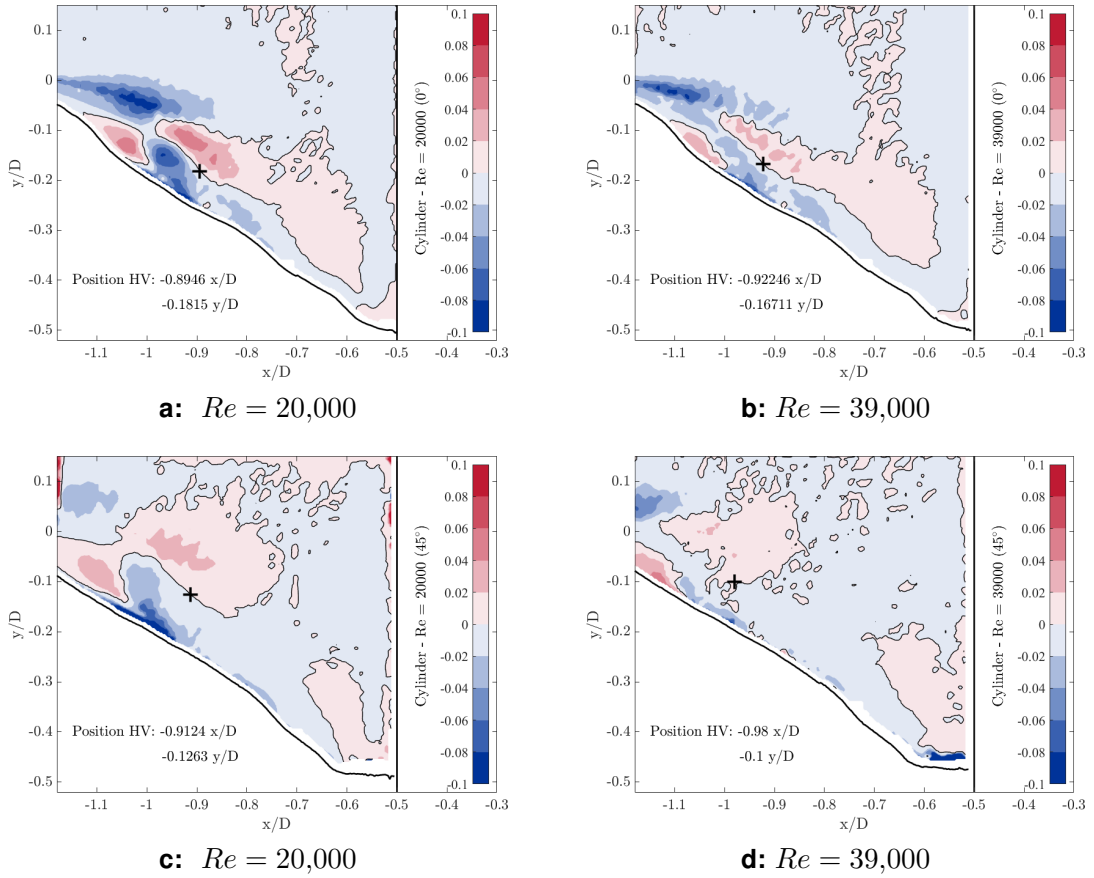
c: $Re = 20,000$ **d:** $Re = 39,000$

Figure 7.20: Time-averaged convection of TKE $C = -\langle u_i \rangle \frac{\partial k}{\partial x_i} \cdot \frac{D}{u_{\text{ref}}^3}$ in the symmetry plane 0° (top) and at 45° (bottom) around a scoured cylinder: $Re = 20,000$ (left), $Re = 39,000$ (right). Black cross indicates time-averaged position of HV and the solid black line the zero-isoline of C.

(C). Therefore, the residual R of the balance:

$$R = C + \nabla T_{\text{turb. fluct.}} + P - \epsilon, \tag{7.3}$$

is assumed to be related to the pressure transport $-\frac{1}{\rho}\langle u_i' p' \rangle$. The residual in the symmetry plane in front of the wall-mounted cylinder (see Figure 7.21) matches the structure and magnitude of the pressure transport evaluated by Schanderl *et al.* (2017) using a Large-Eddy simulation, and therefore, supports the hypothesis that the pressure transport is the only missing term of the PIV-results in the TKE balance equation, i.e. $R \approx -\nabla T_{\text{pres.}}$. According to Schanderl *et al.* (2017), the pressure transport is positive in the wall-parallel jet, whereas it is negative up- and downstream of the horseshoe vortex. Both vortices (V1 and V3) are located close to the zero-isoline indicating that the pressure transport close to the vortex cores is small; however, negative at V1 and positive at V3.

Comparing the residual of the flat-bed results and that of the scour-results reveals substantial differences as the residual in the scour hole is entirely positive in the region of the

incoming shear layer and of the horseshoe vortex. Along the scour surface downhill of the HV, the residual turns negative and gives rise to the conclusion that the pressure fluctuations, which are, therefore, positive here, transport TKE towards the scour surface similar to the flat-bed case.

Furthermore, the residual in the outer part of the measurement plane is small $(\pm 0.05 D/u_{\mathrm{ref}}^3)$, which means that eq. 7.3 approximately balances above the horseshoe vortex and in the region of the down-flow. Within the shear layer uphill the HV and in the region of the vortex itself, the residual has a magnitude of approximately $0.2 D/u_{\mathrm{ref}}^3$ in the symmetry plane. According to the numerical results of Schanderl *et al.* (2017), the pressure transport in front of the wall-mounted cylinder is approximately $\pm 0.2 D/u_{\mathrm{ref}}^3$, and therefore, the transport due to pressure fluctuations is assumed to be in this range, too, at the scoured cylinder. In the region of the horseshoe vortex, the residual reveals a magnitude of about $0.1 D/u_{\mathrm{ref}}^3$, which exceeds that of the flat-bed case.
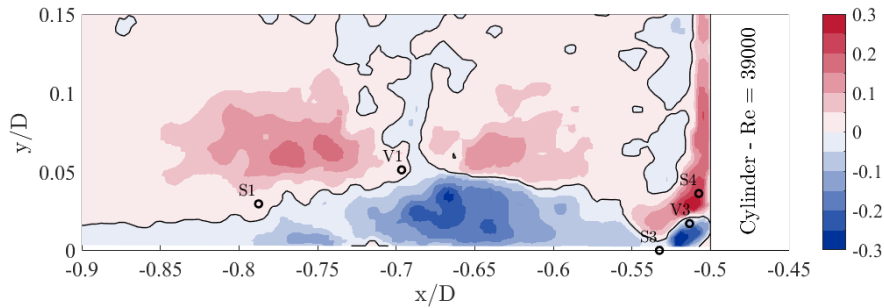
Figure 7.21: Residual of the TKE transport equation $R = C + \nabla T + P - \epsilon$ in front of a wall-mounted cylinder on flat bed ($Re = 39{,}000$). Solid black line indicates the zero-isoline of R.
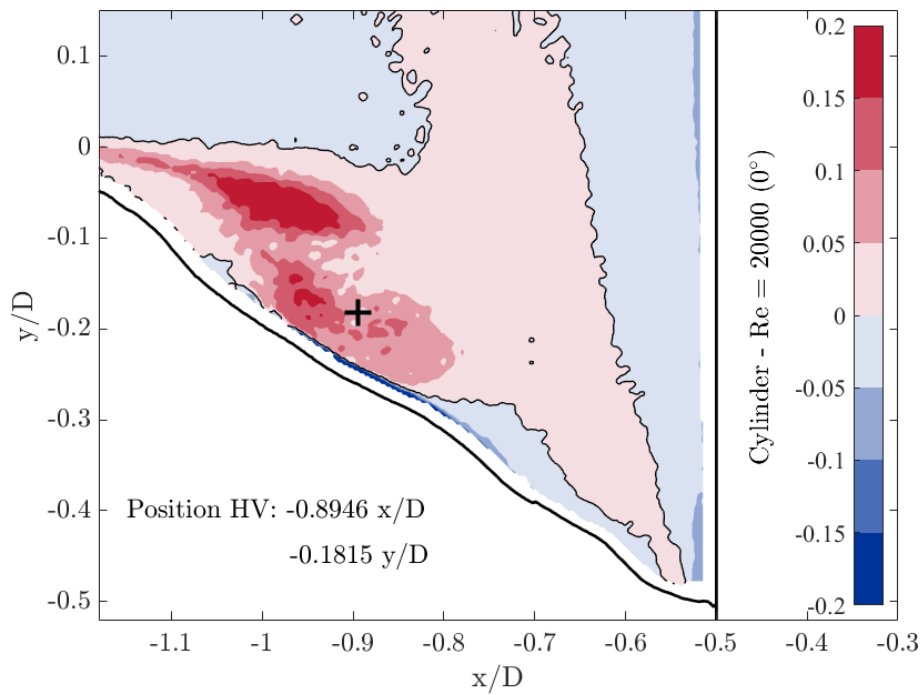
a: $Re = 20{,}000$
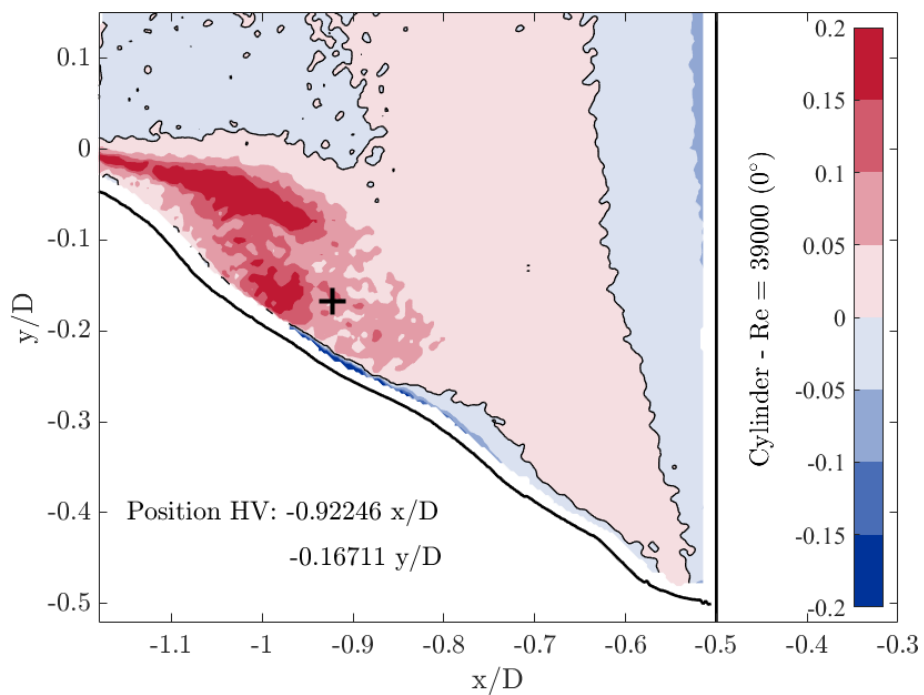
b: $Re = 39{,}000$

Figure 7.22: Residual of the TKE transport equation $R = C + \nabla T + P - \epsilon$ in the symmetry plane $0°$ around a scoured cylinder: $Re = 20{,}000$ (left), $Re = 39{,}000$ (right). Black cross indicates the time-averaged position of the HV and the solid black line refers to the zero-isoline of R.

7.5 Quadrant Analysis of the Velocity Fluctuations

In this section, the probability density functions (PDF) of the in-plane velocity fluctuations in front of the wall-mounted cylinder and around the scoured cylinder will be analysed at selected positions within the flow field, which were defined as follows:

$P1$: Centre of the HV

$P2$: Maximum value of the velocity magnitude underneath the HV

$P3$: Maximum value of the TKE production

$P4$: Inside the lower branch of the c-shaped TKE.

When analysing the PDFs of the Mono-PIV data, the so-called *peak locking* (Raffel *et al.*, 2007) or alternatively referred to as *pixel locking* (Adrian & Westerweel, 2011) effect has been detected. A periodic bias error can occur when discretising the displacements (cf. 4.5.3), and the estimated sub-pixel displacements tend to integer values. Fortunately, the impact of the peak locking effect was small enough to be able to analyse the time-averaged flow structures as discussed in the previous sections. However, these biased results should not be used for analysing PDFs. Therefore, the velocity signals were extracted from a Stereo-PIV measurement at $Re = 39,000$, which was conducted in front of the wall-mounted cylinder to validate the Stereo-PIV system by comparing the results to the previous Mono-PIV results of the same flow configuration and to data from the literature. The reconstruction of the three dimensional velocity vectors is based on the information obtained from two different perspectives (see section 4.6.4); therefore, this discretisation error vanishes during the Stereo-PIV processing.

Raupach (1981) conducted a quadrant analysis to investigate the turbulence generating pattern of a boundary layer with zero-pressure gradient. Accordingly, the turbulent fluctuations of the streamwise and the wall-normal velocity components are normalized by their standard deviation and the single-point correlation within the $u'v'$ sample space is analysed. Finnigan (2000), too, used this method of conditional sampling to examine the coherent structures of canopy turbulence. The joint probability density function (jPDF) of $u'v'$ is separated into four quadrants: (I) outward interaction if $u' > 0$ and $v' > 0$; (II) sweep if $u' > 0$ and $v' < 0$; (III) inward interaction if $u' < 0$ and $v' < 0$; (IV) ejection if $u' < 0$ and $v' > 0$. If the velocities are uncorrelated, the jPDF has a circular shape, whereas an elliptical structure refers to a correlation between the velocities. For canopies and boundary layers, the sweep events, i.e. positive fluctuations of u and negative fluctuations of v at the same time, transport high-momentum fluid from the outer part of the boundary layer towards the wall, whereas low-speed fluid erupts upwards during ejections. These two events are characterized by a negative product of $u'v'$ and cause positive production of TKE according to eq. 2.24 (Pope, 2013).

Furthermore, the correlation of two random variables u and v can be quantified by determining the linear correlation coefficient ϱ, which is defined as their covariance normalized by the product of the corresponding standard deviations. Like the Re shear stress, which corresponds to the covariance, the correlation coefficient ϱ is also dependent on the orientation

of the coordinate system.

$$\varrho_{uv} = \frac{cov(u,v)}{\sigma(u)\sigma(v)} = \frac{\langle u'v'\rangle}{\sqrt{\langle u'^2\rangle}\sqrt{\langle v'^2\rangle}} \tag{7.4}$$

7.5.1 In front of a cylinder on a flat plate

In Figures 7.23 and 7.24, the jPDFs of the streamwise and the wall-normal velocities for $Re = 39,000$ are presented in the bottom left plot, respectively. The individual PDFs are added above (u') and at the right (v') of the jPDF, and the location of the current position is shown in the top right plot with respect to either the magnitude ($P2$) or the TKE ($P1$, $P3$ and $P4$) of the velocity field. Both, the PDFs and the jPDF, are normalized to unit integral, and all the fluctuations have a zero mean by definition. The ticks on the horizontal and vertical axis of the marginal distributions in the top left and bottom right plots indicate the zero value of the corresponding instantaneous velocity component (e.g. $u = 0$).

a: $P1 : x/D = -0.7018$, $y/D = 0.0522$ **b:** $P2 : x/D = -0.654$, $y/D = 0.012$
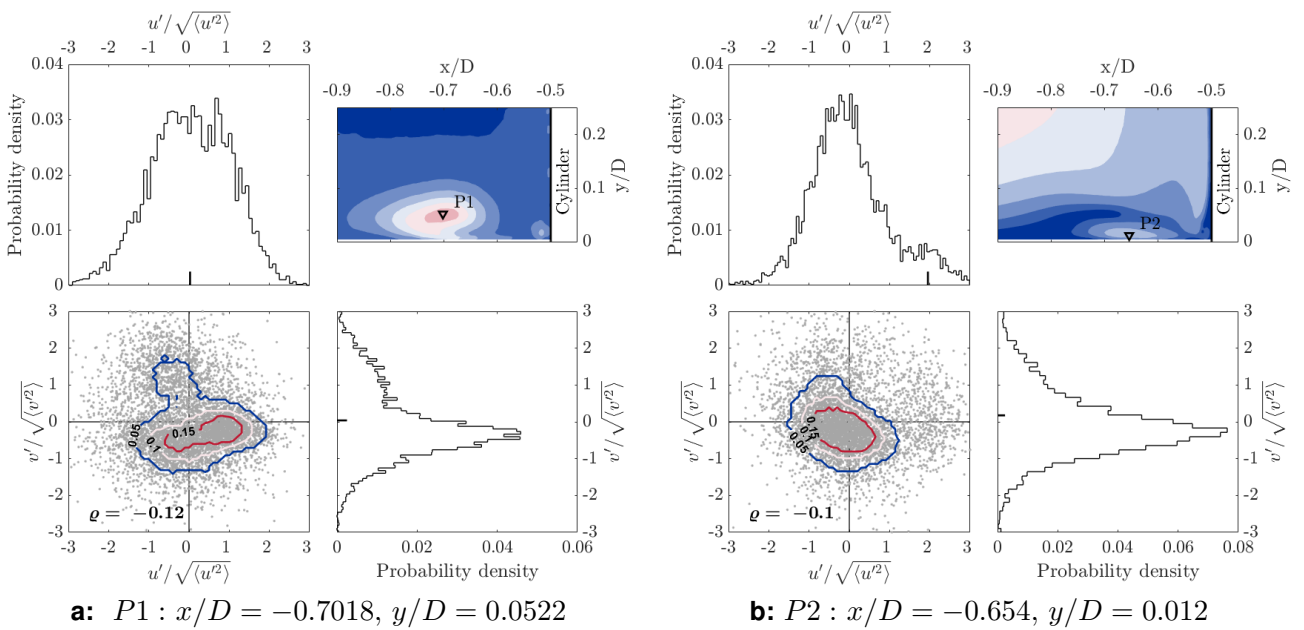
Figure 7.23: (Joint) probability density functions of u and v at $P1$ and $P2$ in front of the wall-mounted cylinder for $Re = 39,000$. Black ticks indicate $u = 0$ and $v = 0$.

The jPDF at the horseshoe vortex centre ($P1$) is presented in Figure 7.23 a). The correlation coefficient is $\varrho = -0.12$ and indicates that u' and v' are nearly uncorrelated. The PDF of the streamwise fluctuations has a broad (flat) peak, which is caused by the absence of vertical oscillations of the vortex, and the PDF of v' reveals a skewed distribution with a sharp peak and a tail in the positive direction (positive skewness). The observation point $P1$ records most of the time vertical velocity values being close to zero or slightly negative. The strong positive values results from oscillations towards the cylinder, the upwards rotating part of the vortex is then shifted to the location of $P1$ and, therefore, the fluctuations of v become positive.

a: $P3 : x/D = -0.736, y/D = 0.044$ **b:** $P4 : x/D = -0.712, y/D = 0.012$
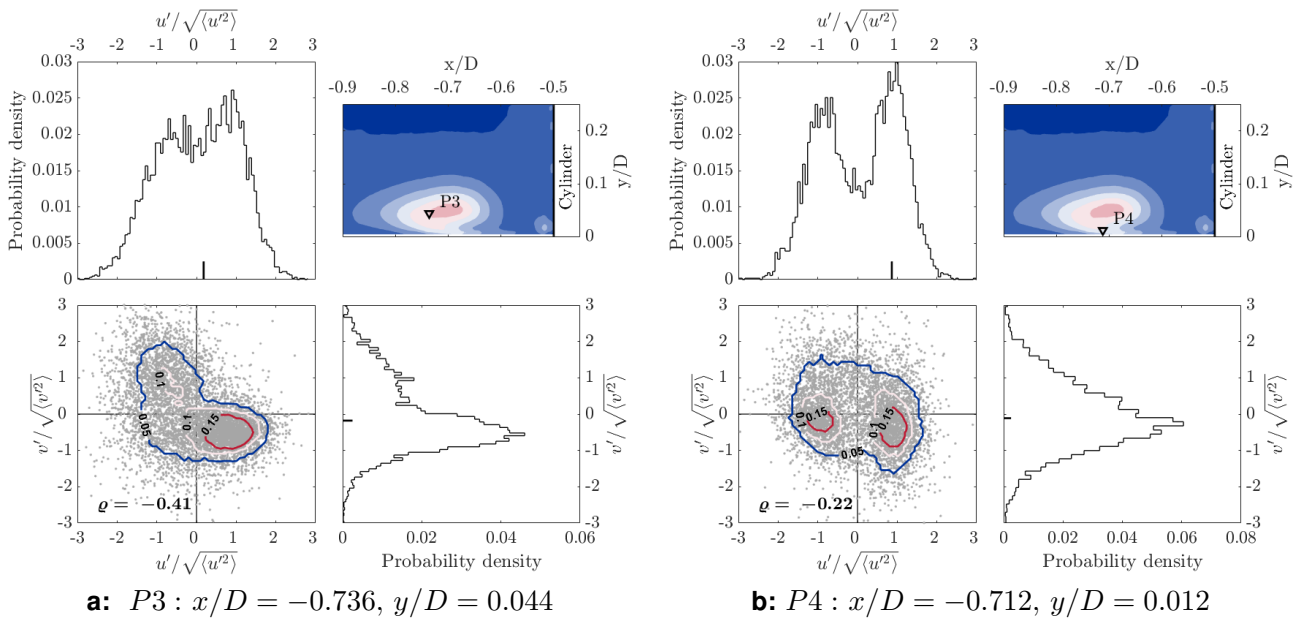
Figure 7.24: (Joint) probability density functions of u and v fluctuations at $P3$ and $P4$ in front of the wall-mounted cylinder for $Re = 39{,}000$. Black ticks indicate $u = 0$ and $v = 0$.

At the position of the largest near-wall magnitude of the velocity ($P2$), the fluctuations u' and v' are again only weakly correlated indicated by the shape of the jPDF, which does not reveal a distinct direction (see Figure 7.23 b) and $\varrho = -0.1$. The streamwise fluctuations are distributed with positive skewness, and the tail in the positive direction contains a secondary peak at $u = 0$, and therefore, indicates the zero-flow mode with fluctuations in the positive direction towards the cylinder. The main peak of the PDF around zero refers to the back-flow mode of the wall-parallel jet, and accordingly, the fluctuations are less intense in this flow mode. The vertical fluctuations of the velocity component show a skewed distribution with a slender peak (low standard deviation), i.e. the velocity in the jet is mainly horizontally aligned (parallel to the wall), which is also the direction of the main turbulent dynamics.

Figure 7.24 a) shows the quadrant analysis of u' and v' at $P3$. This sampling point is located in the area of the largest TKE production; therefore, the fluctuations are expected to be large as well. According to the shape of the jPDF and to the correlation coefficient $\varrho = -0.41$, the fluctuations correlate and the most likely event is identified as $u' > 0$ and $v' < 0$. Such a combination is either possible when the horseshoe vortex has moved towards the cylinder and the approaching flow from upstream dominates the region of $P3$, or when the HV moved further upstream and $P3$ is located in the downwards rotating part of the vortex. The jPDF reveals a secondary event indicated by $u' < 0$ and $v' > 0$, which is the case when $P3$ records the upwards rotating part of the vortex or when the jet flaps in the vertical direction. Moreover, there is also the case of $u' < 0$ and $v' < 0$ occurring at the same time referring to an upstream directed flow event. In the distribution of u' the bimodality of the vortex-jet system is indicated, while the v'-distribution reveals a positive skewness with a secondary peak in the positive region.

The last probe $P4$ is located inside the wall-parallel jet where the lower branch of the

c-shaped TKE distribution reaches the wall. The jPDF, the corresponding marginal PDFs in Figure 7.24 b) and ϱ indicate a weak $u'v'$-correlation. The vertical fluctuations are symmetrically distributed, whereas the $u-$fluctuations reveal a strong bimodality and it is approximately equally likely that u' is positive or negative. The positive $u-$fluctuations coincide with an instantaneous zero-velocity ($u = 0$). This pattern indicates, therefore, the zero- and back-flow mode reported by Devenport & Simpson (1990). The wall-parallel jet is either strongly pronounced pointing upstream (back-flow) or has collapsed (zero-flow mode) and, consequently, produces turbulent kinetic energy by this alternating behaviour.

7.5.2 Around a scoured cylinder

In Figure 7.25 a) and b), the jPDFs and the corresponding marginal PDFs at position $P1$ in the symmetry plane and at 45° around the scoured cylinder are presented, respectively. The quadrant analysis of the scour case was conducted for the fluctuations in the scour-oriented coordinate system (i.e. u'_r and u'_n) and includes the results of both $Re = 20{,}000$ (dashed red lines) and $Re = 39{,}000$ (solid lines).

a: $P1(0°) : x/D = -0.9225,\ y/D = -0.1671$ **b:** $P1(45°) : x/D = -0.98,\ y/D = -0.1$

Figure 7.25: (Joint) probability density functions of u_r and u_n fluctuations at $P1$ in the symmetry plane (left) and at 45° (right) around a scoured cylinder for $Re = 20{,}000$ (dashed red lines) and $Re = 39{,}000$ (solid lines). Ticks indicate $u_\mathrm{r} = 0$ and $u_\mathrm{n} = 0$.

Except for the wall-normal fluctuations in the symmetry plane, which are positively skewed, all other distributions are symmetrically shaped at the sampling point in the centre of the horseshoe vortex ($P1$). The elliptical shapes of both jPDFs indicate a negative correlation of u'_r and u'_n, which appears to intensify when the horseshoe vortex bends around the cylinder ($\varrho_{0°} = -0.37$ and $\varrho_{45°} = -0.51$). The HV might oscillate parallel to the scour surface as u'_r is positive when u'_n is negative and vice versa. Furthermore, the u'_n component at $P1$ is mainly negative; thus, the HV is mainly located in the uphill direction of $P1$ and the

skewed distribution indicates that oscillations in the downhill direction occur occasionally shifting the upwards rotating part of the vortex to $P1$.

a: $P2(0°) : x/D = -0.9407, y/D = -0.2161$ **b:** $P2(45°) : x/D = -0.9907, y/D = -0.1824$

Figure 7.26: (Joint) probability density functions of u_r and u_n fluctuations at $P2$ in the symmetry plane (left) and at $45°$ (right) around a scoured cylinder for $Re = 20,000$ (dashed red lines) and $Re = 39,000$ (solid lines). Ticks indicate $u_\mathrm{r} = 0$ and $u_\mathrm{n} = 0$.

The distributions observed at sampling point $P2$ are given in Figure 7.26 a) and b). The distributions of the radial fluctuations are skewed in the positive direction, whereas the wall-normal fluctuations are symmetrically distributed. The shape of the jPDF reveals again a negative correlation that increases from the symmetry plane to the lateral measurement plane ($\varrho_{0°} = -0.32$ and $\varrho_{45°} = -0.43$). The near-wall flow underneath the horseshoe vortex is directed uphill and parallel to the surface, as the radial velocity is in average negative and the wall-normal velocity component close to zero. Occasionally, the radial fluctuations underneath the HV show rare positive values (see right tail of the distribution), which coincide with $u_\mathrm{r} \to 0$ indicating a shift of the HV in the downhill direction and, accordingly, the wall-normal fluctuations become negative.

Location $P3$ was selected, in order to analyse the interaction of the approaching shear layer, which detached at the scour edge, with the horseshoe vortex (see Figure 7.27 a and b). Therefore, the in-plane production of the TKE has its maximum value at this position. In the symmetry plane, the correlation between the fluctuations is comparatively large ($\varrho_{0°} = -0.57$), and the shape of both marginal distributions is symmetric. The most likely event is identified by the jPDF when $u_\mathrm{r}' < 0$ and $u_\mathrm{n}' > 0$ representing the horseshoe vortex at its time-averaged position; thus, $P3$ is located in the upwards rotating part of the vortex. However, when the HV moves in the downhill direction, the radial and wall-normal fluctuations turn positive and negative, respectively, as the approaching shear layer dominates the situation at $P3$ in this case. Due to these oscillations, the shear stress term $\langle u_\mathrm{r}' u_\mathrm{n}' \rangle$ is in average negative and shows its amplitude in this region (see Figure 7.11 b). Accordingly, the shear production of the TKE at this position is large, too, as the time-averaged gradients

a: $P3(0°) : x/D = -0.976, y/D = -0.1191$ **b:** $P3(45°) : x/D = -1.055, y/D = -0.0603$
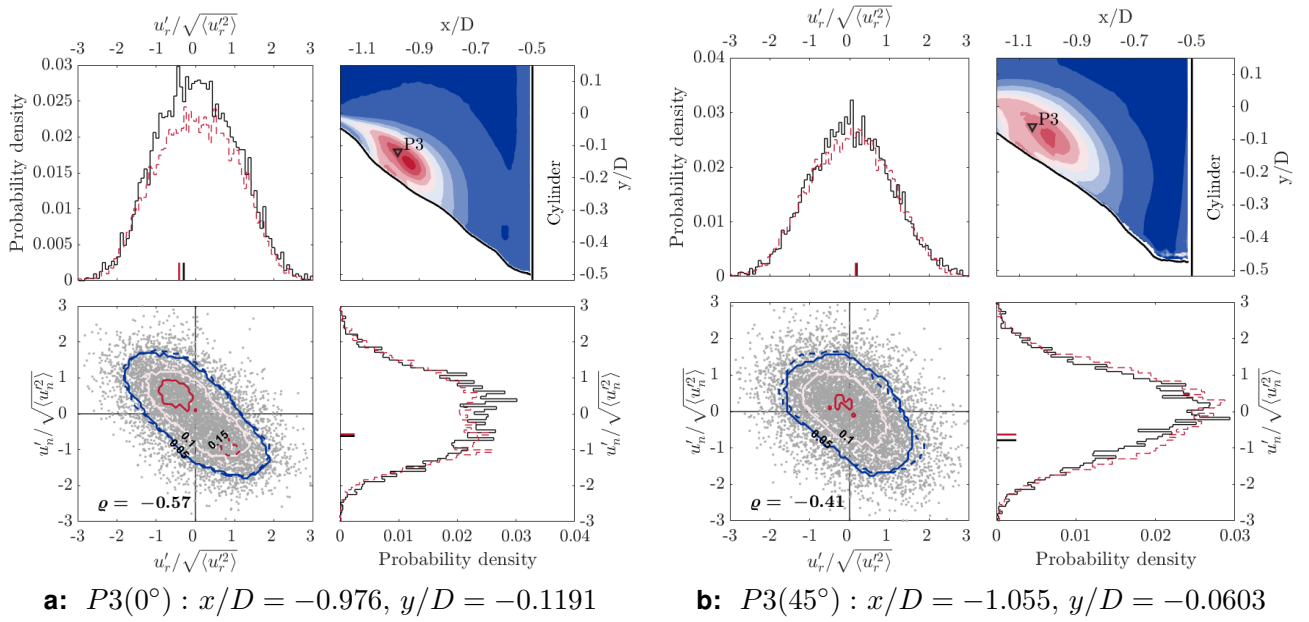
Figure 7.27: (Joint) probability density functions of u_r and u_n fluctuations at $P3$ in the symmetry plane (left) and at $45°$ (right) around a scoured cylinder for $Re = 20{,}000$ (dashed red lines) and $Re = 39{,}000$ (solid lines). Ticks indicate $u_r = 0$ and $u_n = 0$.

of the velocities $\partial\langle u_r\rangle/\partial x_n$ and $\partial\langle u_n\rangle/\partial x_r$ are positive. In contrast to the previous sampling points, the correlation decreases when the horseshoe vortex bends around the cylinder. The shear layer entering from the scour rim is deflected by the dominating azimuthal velocity component and the interaction with the horseshoe vortex becomes weaker out of the symmetry plane.

When analysing the jPDF in the lower branch of the c-shaped TKE ($P4$, see Figures 7.28), a bimodal pattern becomes apparent. The radial fluctuations show two almost equal peaks that are just about to be separated from each other. The slightly lower peak coincides with an instantaneous zero value of u_r (see ticks on $x-$axis of u_r'), whereas the main peak appears when $u_r < 0$ and, therefore, indicate the zero and back-flow mode, respectively. The distribution of the wall-normal fluctuations is negatively skewed, and most of the time the fluctuations are close to zero and turn only occasionally to be negative or positive. The correlation coefficient indicates a slight negative correlation as the negative $u_r'-$fluctuations coincide with positive $u_n'-$fluctuations and vice versa. Therefore, two flow modes, similar to the zero- and back-flow modes of the flat-bed case, are identified, whereas the flow mode pointing in the uphill direction (back-flow), is identified to be predominant in the scour. At the lateral position, the predominance in the bimodality shifts even more towards the back-flow mode. The zero-flow mode occurs less frequently, as the difference between the two u_r' peaks increases while the u_n' distribution accumulates more around zero, i.e. surface parallel flow. In particular at $P4_{45°}$, a trend corresponding to the Reynolds number appears. The back-flow mode dominates with increasing Re. However, the correlation between the in-plane fluctuations does not change from the symmetry plane to the $45°$ plane.

The quadrant analysis of the in-plane fluctuations confirmed the oscillating behaviour in

a: $P4(0°) : x/D = -0.9995, y/D = -0.1779$ **b:** $P4(45°) : x/D = -1.055, y/D = -0.1489$
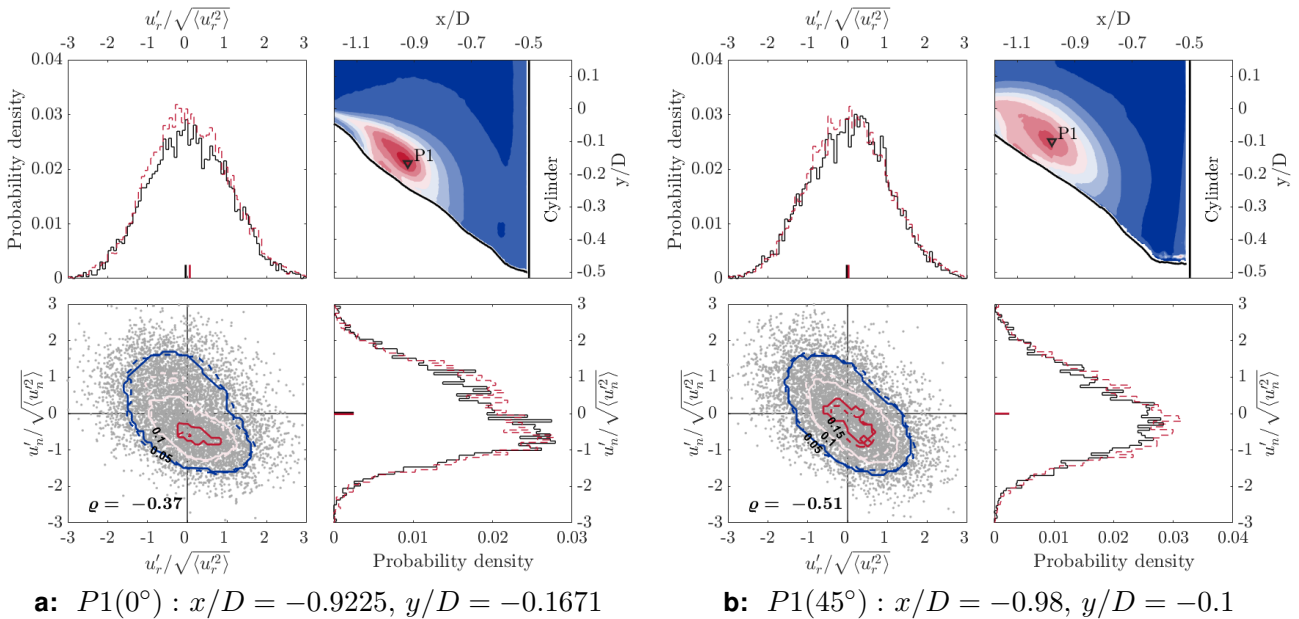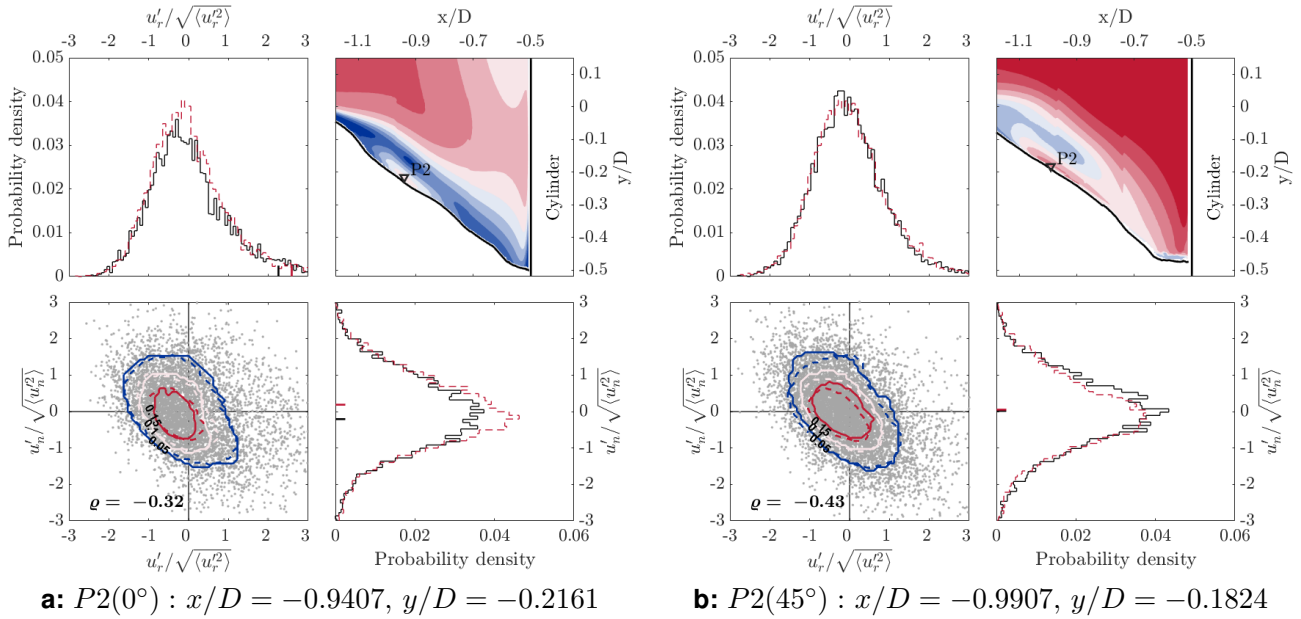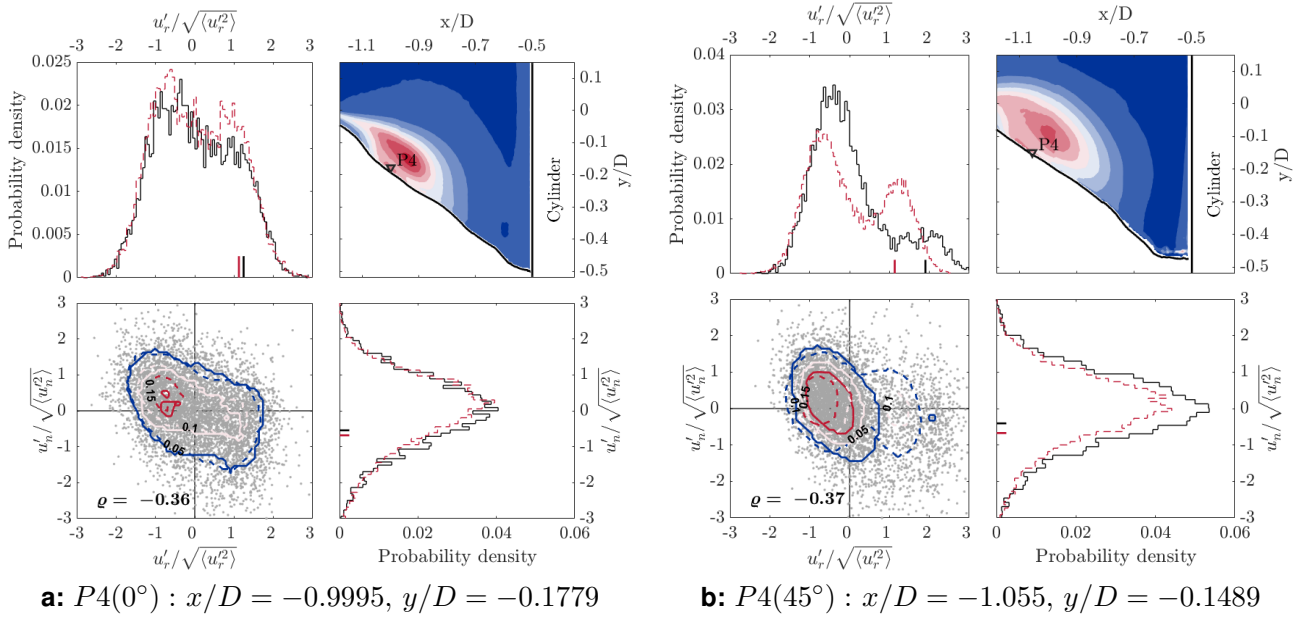
Figure 7.28: (Joint) probability density functions of u_r and u_n fluctuations at $P4$ in the symmetry plane (left) and at $45°$ (right) around a scoured cylinder for $Re = 20,000$ (dashed red lines) and $Re = 39,000$ (solid lines). Ticks indicate $u_r = 0$ and $u_n = 0$.

the horizontal direction of the HV and the bimodality of the wall-parallel jet in the flat-bed case. In the scour hole, oscillations of the HV are indicated as well, which occur mainly parallel to the scour surface independent of Re. Furthermore, a bimodal pattern in the wall-parallel velocity component underneath the HV is also identified, which becomes more distinct out of the symmetry plane (sample point $P4$) and seems to increase with increasing Re.

7.6 Near-wall Flow

7.6.1 Wall shear stress

To measure the wall shear stress, a high spatial resolution is required and the result can vary widely, according to Jenssen *et al.* (2016*b*). The spatial resolution of the PIV images was about $36\mu m/px$. Using a standard evaluation technique based on interrogation windows (IW) with a size of $16 \times 16px$ overlapping by 50%, resulted in a grid spacing of $8px$. Furthermore, when the surface of the wall intersected with an IW in the images, the corresponding vectors were considered to be biased, which occurred in particular in the scour measurements. A vector represents the spatial average of the corresponding IW and, therefore, the vector of an intersected window would no longer be located in the centre of the IW and the true position would be the centroid of the area, which refers to the flow.

For this reason, the first vector corresponding to an IW that was not intersected by the wall was considered to be the first valid grid point and is listed in Table 7.3. Furthermore, the results of a Large-Eddy simulation by Schanderl *et al.* (2017) and of a single-pixel ensemble

(SPE) evaluation performed by Strobl (2017) are added as well. The numerical results were validated by Schanderl & Manhart (2016) and, therefore, are taken as a reference for the wall shear stress evaluation. The data of Strobl (2017) are presented, in order to validate the experimental data irrespectively of the applied evaluation technique. The resolution of the LES was about three times finer than the one of the standard-PIV and the SPE data were about four times finer resolved than the data of the standard-PIV. Therefore, the results of the near-wall flow analysis using the standard-PIV in both configurations, flat-bed and scour hole, have to be treated with caution.

Flat-bed experiments

Re	$y_1[\mathrm{m}]$	$y_1/D[-]$	$y_1[\mathrm{px}]$
20,000	$3.808 \cdot 10^{-4}$	$3.808 \cdot 10^{-3}$	10.33
39,000	$3.063 \cdot 10^{-4}$	$3.063 \cdot 10^{-3}$	8.31
Schanderl (2018) 39,000	$1 \cdot 10^{-4}$	$1 \cdot 10^{-3}$	–
Strobl (2017) 39,000	$7.372 \cdot 10^{-5}$	$7.372 \cdot 10^{-4}$	2
78,000	$4.011 \cdot 10^{-4}$	$2.507 \cdot 10^{-3}$	11.05

Scour experiments

Re	$x_{\mathrm{n},1}[\mathrm{m}]$	$x_{\mathrm{n},1}/D[-]$	$x_{\mathrm{n},1}[\mathrm{px}]$
20,000	$4.920 \cdot 10^{-4}$	$4.920 \cdot 10^{-3}$	13.11
39,000	$4.861 \cdot 10^{-4}$	$4.861 \cdot 10^{-3}$	12.99

Table 7.3: Wall distance of first valid interrogation windows centres

a: Flat bed: $c_\mathrm{f}(x/D)$

b: Scour: $c_\mathrm{f}(x/D)$

c: Flat bed: $c_\mathrm{f}(\tilde{x})$

d: Scour: $c_\mathrm{f}(\tilde{x})$
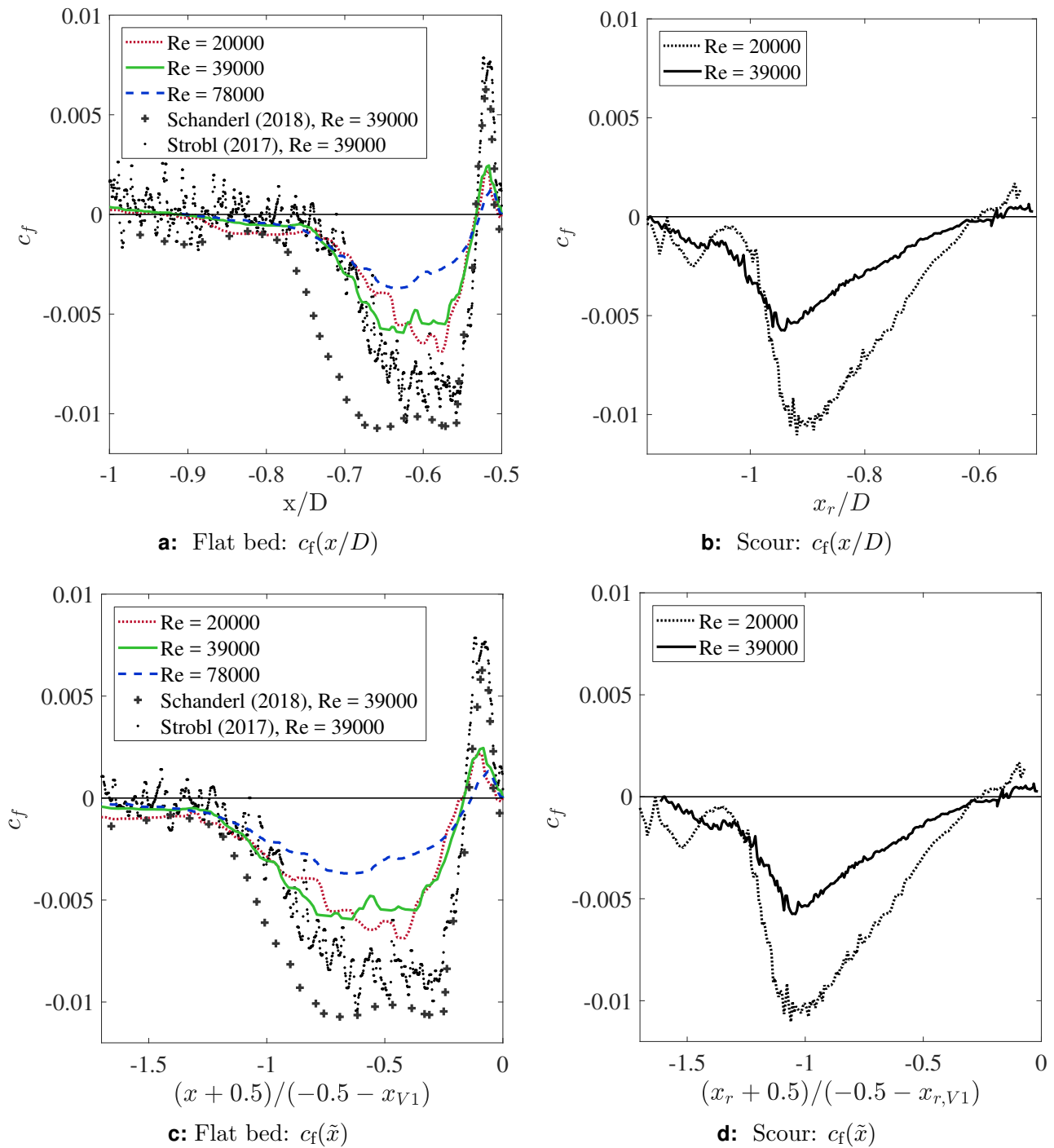
Figure 7.29: Distribution of the friction coefficient c_f in front of a wall-mounted cylinder (left) and in front of a scoured cylinder (right).

Figure 7.29 a) shows the distributions of the friction coefficients c_f in the symmetry plane in front the wall-mounted cylinder using eq. 2.2. The down-flow is deflected in all directions when reaching the bottom plate at stagnation point S3 (see Figures 7.1); therefore, the wall shear stress becomes zero in S3, as the gradient $\partial\langle u\rangle/\partial y$ is zero as well, irrespectively of the Re and the type of data.

From S3 on towards the cylinder, a sharp positive peak of c_f develops, as the flow accelerates strongly in the positive x-direction due to the corner vortex V3. Approximately underneath the centre of this corner vortex, the wall shear stress reaches a local maximum before it decreases towards zero directly at the cylinder. Due to the small spatial scales, the IW-based PIV cannot resolve the dynamics correctly and damps the true velocities by the spatial averaging, whereas the SPE indicates even larger values than the LES.

The wall-parallel jet develops in the upstream direction of S3 and induces a strong negative velocity gradient $\partial\langle u\rangle/\partial y$ along the bottom plate exerting a large shear stress. The jet accelerates and the wall shear stress distribution increases until a plateau is reached. While passing the horseshoe vortex, the jet decelerates and, correspondingly, the wall shear stress decreases. The jet fades until approximately $x/D = -0.9$ and the wall shear stress becomes positive further upstream due to the approaching flow.

In the region of the strongly accelerating jet, the spatial resolution of the PIV appears to be too coarse to estimate the wall shear stress amplitude correctly, as the LES and the SPE data reveal a friction coefficient of $c_f \approx -0.01$, whereas the PIV results reach $c_f \approx -0.005$. However, the shape of the c_f-distribution seems to be represented correctly by the standard-PIV.

Even though the numerical and experimental data are generally consistent, both, the standard PIV and the SPE results indicate that the jet had a smaller spatial extend in the experiment. This difference between the numerical and the experimental data stems from the difference in the position of the HV, which is located more upstream in the LES and, therefore, the wall shear stress distribution is wider in the simulation. To accommodate this difference, the x-coordinate was normalized by the time-averaged location of the HV centre (V1) as follows:

$$\tilde{x} = \frac{x/D + 0.5}{-0.5 - x_{V1}/D}. \tag{7.5}$$

The distribution of the friction coefficient c_f with respect to $\tilde{x}$ is presented in Figure 7.29 c). The cylinder is located at $\tilde{x} = 0$, whereas $\tilde{x} = -1$ refers to the position of the HV. When applying this normalization, the numerical and experimental results get closer together, and their similarity increases. However, the incapability of the IW-based PIV-algorithm reconstructing strong velocity gradients is still obvious, particularly in the region of the strongest acceleration in the wall-parallel jet. On the contrary, when the jet decelerates underneath V1, the results of the standard-PIV and the SPE match. Furthermore, a difference with respect to the Re can be observed as well. The data for $Re = 20,000$ and $Re = 39,000$ coincide, whereas the friction coefficient in the $Re = 78,000$ case is smaller. However, Schanderl *et al.* (2018) observed a clear trend in c_f corresponding to Re: the wall shear stress took the largest values for $Re = 20,000$ and decreased with increasing Re. Schanderl (2018) found that the shear stress within the jet scales in accordance to a laminar boundary

layer, which is proportional to $1/\sqrt{Re}$. Therefore, when the c_f value is adjusted as follows:

$$c_{\mathrm{f}_*} = c_\mathrm{f} \cdot \sqrt{Re}, \tag{7.6}$$

the amplitudes of the scaled $c_{f_*}-$curves coincide irrespectively of the Re (see Figure 7.30 a). This indicates a re-laminarisation of the jet between S3 and V1.
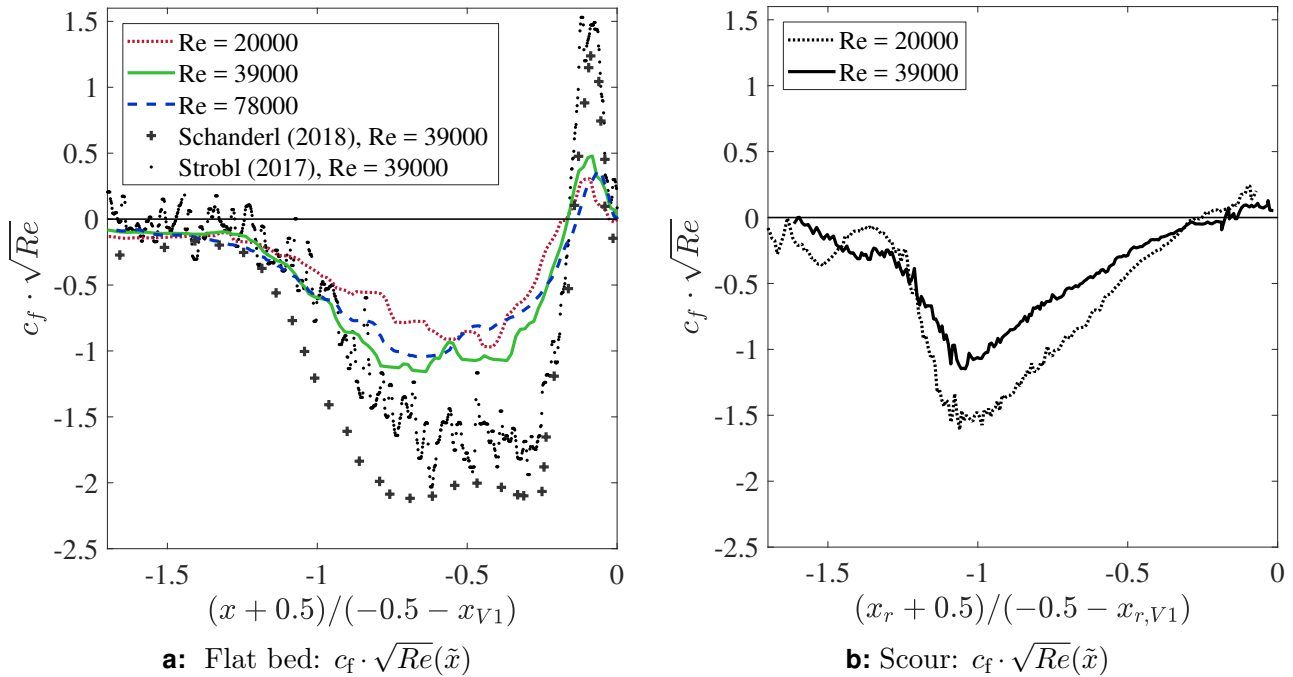
Figure 7.30: Scaling of friction coefficient c_f using $c_\mathrm{f} \cdot \sqrt{Re}$ in front of a wall-mounted cylinder (left) and in front of a scoured cylinder (right).

The wall shear stress in front of the scoured cylinder was obtained using the gradient of the wall-parallel velocity according to the scour-oriented reference frame. Since the light sheet was aligned with the symmetry plane, the time-averaged azimuthal component was small and the dominating velocity gradient was $\partial\langle u_\mathrm{r}\rangle/\partial x_n$. The distribution of the friction coefficient in front of the scoured cylinder shows only little similarity to that in the flat-bed case (see Figure 7.29 b and d). The stagnation point where the down-flow reaches the surface of the scour is indicated by $c_\mathrm{f} = 0$ and positive and negative values down- and upstream of it. Even if no clear corner vortex developed in the scour hole, a positive shear stress can be observed due to a deflection of the down-flow towards the cylinder. From the stagnation point on uphill, the friction coefficient increases almost linearly until a peak is reached directly under the HV, and further uphill the c_f value declines rapidly towards zero. In the $Re = 20,000$ case a secondary local peak appears and indicates a recirculation zone with an uphill directed flow as the friction coefficient remains negative. This recirculation in the uphill direction was also assumed by analysing the magnitude of the velocity field (see Figure 7.3 a).

The amplitude of c_f inside the scour hole is of the same order of magnitude than on the flat bed. Furthermore, a clear Re dependency can be observed as well. The resolution

of the PIV experiment, however, might be too coarse to estimate the amplitude of the
wall shear stress in the scour hole correctly, but the shapes of the distributions seem to
reproduce all structures in detail. The sharp peak of the friction coefficient c_{f} between the
stagnation point and the HV indicates that the wall shear stress inside the scour hole is
dominated by the HV rather than by a wall-parallel jet, which would cause a plateau-shape
of c_{f}.

When the x-coordinate in the radial direction is normalized to the location of the HV,
according to eq. 7.5, the position of the peaks of c_{f} coincide for both Re (see Figure 7.29
d). However, when the suggested laminar scaling using $\sqrt{Re}$ is applied to the results in the
scour hole, the amplitudes of c_{f} of both Re still do not match (see Figure 7.30 b). Therefore,
the laminar scaling law for the wall shear stress is suspected not to be valid inside the scour
hole.

a: $c_{\mathrm{f}} \cdot Re(\tilde{x})$ **b:** Positions of wall profiles along scour surface
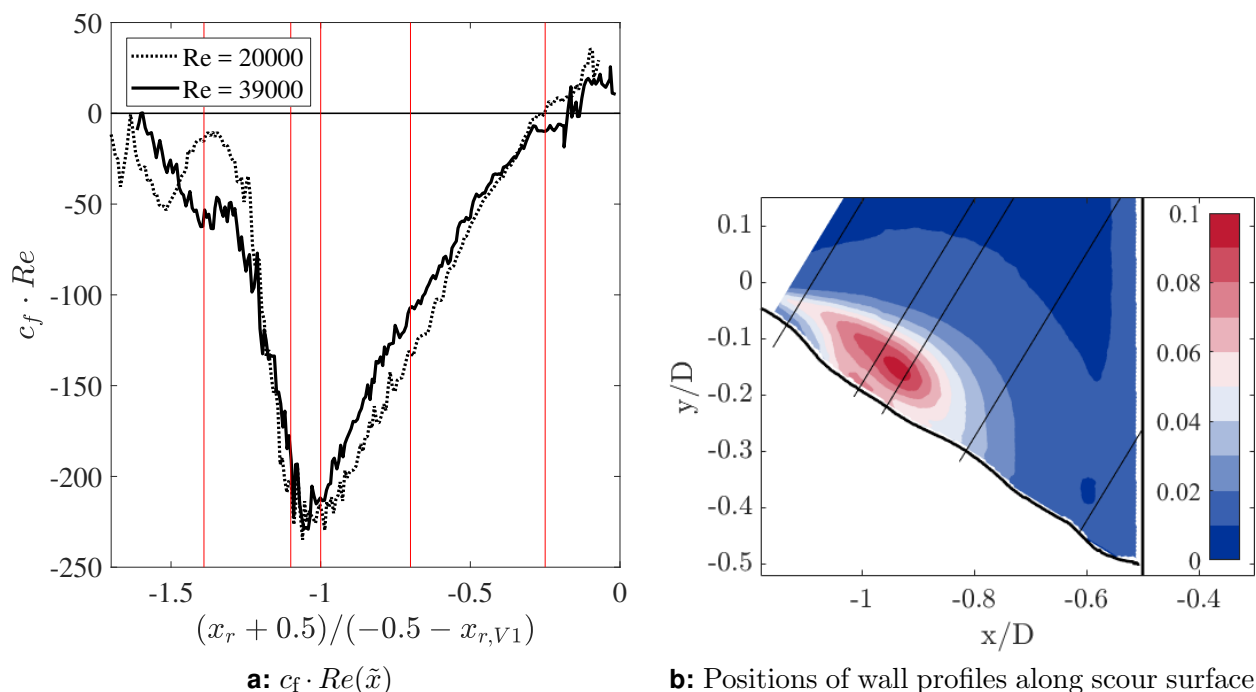
Figure 7.31: Scaling of friction coefficient c_{f} using $c_{\mathrm{f}} \cdot Re$ in front of a scoured cylinder, red lines
indicate positions of wall profiles (left). TKE distribution in scour hole at $Re = 39{,}000$,
black lines indicate positions of wall profiles (right).

Moreover, when the friction coefficient is multiplied with the corresponding Re and plotted
versus the adjusted x-coordinate $\tilde{x}$, the distributions of c_{f} for both Re coincide surprisingly
well (see Figure 7.31 a). Since the distribution of the friction coefficient in front of the
scoured cylinder does not reveal a plateau-like structure and does not follow the scaling
law of a laminar boundary layer, the near-wall flow in the uphill direction between the
stagnation point and the HV is considered to be neither laminar nor to be governed by a
strong wall-parallel jet.

7.6.2 Wall-normal velocity profiles

The solid red lines in Figure 7.31 a) indicate the positions in the symmetry plane along the scour surface at which wall-normal profiles at $Re = 39,000$ of the surface parallel velocity component $\langle u_r \rangle$, the Re stresses $\langle u_r' u_n' \rangle$, $\langle u_r' u_r' \rangle$ and $\langle u_n' u_n' \rangle$ were extracted and plotted in Figures 7.32 a) to d), respectively. As reference, the corresponding profiles in front of the wall-mounted cylinder were added at $\tilde{x} = -1.0$ and $\tilde{x} = -0.7$. The dashed lines refer to the LES results of Schanderl (2018) and the dots were obtained from the Mono-PIV data. The positions of these wall-profiles are also related to the spatial distribution of the TKE in the scour hole (see black lines in Figure 7.31 b).

The position $\tilde{x} = -1.4$ refers to the shear layer that detached from the scour rim. At the scour surface the velocity component $\langle u_r \rangle$ takes small negative values, which indicates an uphill directed flow underneath the shear layer, which comes into play with increasing wall distance and, consequently, the radial velocity component increases strongly. The Re shear stress at the wall is negative and peaks inside the shear layer at approximately $x_n/D = 0.04$ where the normal stresses in the radial direction also reveal a maximum amplitude. The wall-normal stress amplitude is by a factor of $2 - 3$ smaller than the stresses due to radial fluctuations.

At $\tilde{x} = -1.1$, the lower branch of the c-shaped TKE distribution meets the scour surface, the TKE reveals a local peak and the wall shear stress is close to its maximum value (see Figure 7.31 a and b). This position corresponds to $P4$ of the quadrant analysis in section 7.5. The velocity component $\langle u_r \rangle$ indicates the HV by strong uphill directed values at the surface, which turn in the downhill direction above the centre of HV. The shear stress $\langle u_r' u_n' \rangle$ is consistently negative and reaches its maximum absolute value of $-0.037 u_{ref}^2$ at $x_n/D = 0.064$, which coincides with the region of largest total and shear TKE production (see Figure 7.13 b) and Figure 7.14 d, respectively). This large amplitude of Re shear stress results from the approaching shear layer detaching from the scour edge. The wall-normal stress has its maximum value of $-0.064 u_{ref}^2$ also at this wall distance, which is approximately equal to the secondary peak of the radial stress here. The largest stress $\langle u_r' u_r' \rangle$ can be observed at the wall ($0.09 u_{ref}^2$) and similar to the flat-bed case the lower branch of the TKE distribution is mainly caused by wall-parallel fluctuations.

At the location of the HV ($\tilde{x} = -1.0$), the uphill directed flow is the strongest and, consequently, the wall shear stress is the largest here, too. The maximum absolute value of $\langle u_r \rangle$ exceeds the one of the LES by a factor of 1.4 and that of the Mono-PIV by a factor of 1.8. The shape of the velocity profile, however, is similar to that of the flat-bed case and the gradient of the wall-parallel velocity at the HV appears to be similar, too. Therefore, the strength of the HV in both flow configurations is considered to be equal as well. Above the HV, the velocity in the scour hole is about 1.8 times larger than in front of the wall-mounted cylinder. The shear stresses $\langle u_r' u_n' \rangle$, too, exceed the values in front of the wall-mounted cylinder, which is due to the interaction of the shear layer and the HV. The shapes of the Re normal stresses $\langle u_r' u_r' \rangle$ and $\langle u_n' u_n' \rangle$ in the scour are similar to the flat-bed case revealing a peak at the centre of the HV and a wall-peak of the wall-parallel stresses. The amplitudes of both stress profiles, however, are smaller with respect to the flat bed case. The wall-parallel oscillations of the HV are indicated by the $\langle u_n' u_n' \rangle$-peak at the height of the HV centre. The wall-peak of the $\langle u_r' u_r' \rangle$ is by a factor of $1.5 - 2$ below the Mono-PIV and LES-results of the flat bed case. In front of the wall-mounted cylinder, the wall-parallel jet dominates the region

close to the wall by a strong upstream directed flow and, therefore, the wall-parallel stresses are large, too. As these stresses are considerably weaker in the scour hole, the near-wall flow is considered to be less pronounced and not dominated by such a strong wall-parallel jet.

Further downstream at $\tilde{x} = -0.7$, the scour surface has a local bump, which seems to border the HV in the downhill direction (cf. 7.3 b). The surface-parallel flow, however, has a strong uphill directed component, whose amplitude is about 75% of $\langle u_r \rangle$ at $\tilde{x} = -1.1$, but only 66% of the wall-peak of the LES results at $\tilde{x} = -0.7$. The corresponding normal stress profile $\langle u_r' u_r' \rangle$ reveals a wall-peak here, too, which is approximately as large as in the flat-bed case. These observations indicate that there is a similar upstream directed structure along the scour surface as the wall-parallel jet of the flat-bed case, which is, however, not as strongly developed even though the stresses due to the fluctuations are equally large. The shape of the Re shear stress and the wall-normal stress do not match at all and the latter does not reveal such a characteristic peak at the height of the HV as in the flat-bed case. Therefore, the HV is considered not to pass this location in the scour hole as no corresponding footprint in the wall-normal stress profile $\langle u_n' u_n' \rangle$ can be observed.

The position $\tilde{x} = -0.25$ is characterised by a low wall shear stress as the down-flow impinges at the scour surface around this location. Consequently, the wall-profiles reveal no characteristic shape here, as the uphill directed flow starts to develop from this position onwards.

a: $\langle u_{\mathrm{r}} \rangle / u_{\mathrm{ref}}$

b: $\langle u_{\mathrm{r}}' u_{\mathrm{n}}' \rangle / u_{\mathrm{ref}}^2$

c: $\langle u_{\mathrm{r}}' u_{\mathrm{r}}' \rangle / u_{\mathrm{ref}}^2$

d: $\langle u_{\mathrm{n}}' u_{\mathrm{n}}' \rangle / u_{\mathrm{ref}}^2$
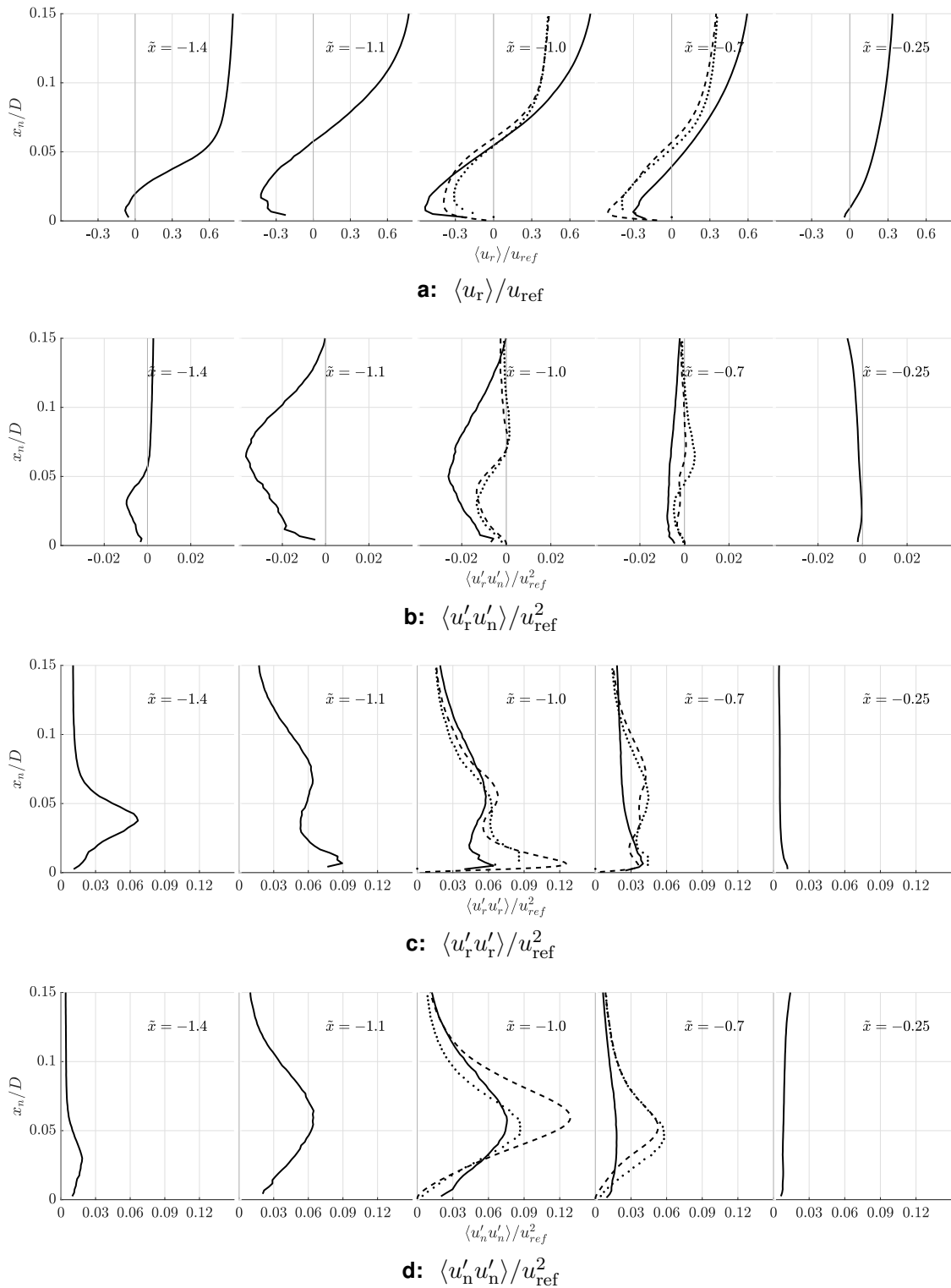
Figure 7.32: Time-averaged wall-normal profiles of $\langle u_{\mathrm{r}} \rangle$ (a), $\langle u_{\mathrm{r}}' u_{\mathrm{n}}' \rangle$ (b), $\langle u_{\mathrm{r}}' u_{\mathrm{r}}' \rangle$ (c) and $\langle u_{\mathrm{n}}' u_{\mathrm{n}}' \rangle$(d) in the symmetry plane along the scour surface at the adjusted positions $\tilde{x} = -1.4, -1.1, -1.0, -0.7, -0.25$. At $\tilde{x} = -1.0$ and -0.7 results in front of the cylinder on a flat bed are added: dashed lines stem from the LES of Schanderl (2018) and the dots represent the Mono-PIV data. All data refer to $Re = 39{,}000$.

7.7 Proper Orthogonal Decomposition

In this section, the data sets of the flat-bed and scour measurements for $Re = 39{,}000$ are examined for coherent structures, which can be done by the *Proper Orthogonal Decomposition* (POD). This deterministic tool was independently developed in parallel and, therefore, has several names such as *Karhunen-Loève*[2] expansion (Tropea *et al.*, 2007). It was first introduced to the field of fluid mechanics by Lumley (1967), in order to describe coherent structures in the flow; Berkooz *et al.* (1993) and Aubry (1991) give an overview of the historical background of POD, especially in relation to fluid mechanics. POD is a linear technique decomposing the flow into a sum of statistically independent deterministic spatial basis functions and their corresponding time coefficients. These related components form the so-called modes in which the *"the latter is the time evolution of the former and the former is the spatial configuration of the latter"* (Aubry, 1991). Furthermore, the advantage of this technique is that no a priori knowledge is required; thus, no assumptions have to be taken.

7.7.1 Mathematical background

Direct POD   The following theoretical description and notation of the POD is extracted from Tropea *et al.* (2007). First, consider a measured velocity vector field with finite representations in time and space: $\mathbf{u}(\mathbf{x}, t)$. In order to extract coherent flow structures, which contain spatial and temporal parts, the vector field can be approximated by a linear combination of random coefficients $a_k(t)$ with deterministic basis functions $\Phi_k(\mathbf{x})$, the first refer to the variation in time, whereas the latter represent the spatial distribution.

$$\mathbf{u}(\mathbf{x}, t) \approx \sum_{k=1}^{K} a_k(t)\Phi_k(\mathbf{x}) \tag{7.7}$$

For an infinite number of combinations ($K \rightarrow \infty$), the expansion in eq. 7.7 becomes exact in terms of reconstructing the vector field $\mathbf{u}(\mathbf{x}, t)$. Each basis function $\Phi_k(\mathbf{x})$ represents the "best match" of one realization of $\mathbf{u}(\mathbf{x})$. This can be mathematically expressed as a maximization problem of the normalized averaged inner product[3] of $\mathbf{u}(\mathbf{x})$ and $\Phi(\mathbf{x})$, see expression 7.8, and results in the best projection of the velocity field onto a basis function.

$$\frac{\langle |\mathbf{u} \cdot \Phi|^2 \rangle}{\|\Phi\|^2} \tag{7.8}$$

with $\mathbf{u} \cdot \Phi = \int_{\Omega} \mathbf{u}(\mathbf{x})\Phi^*(\mathbf{x})d\mathbf{x}$, where Φ^* stands for the complex conjugate of Φ

---

[2]Kari Karhunen ($\star$1915, $\dagger$1992)
   Michel Loève ($\star$1907, $\dagger$1979)
[3]In Euclidean space: scalar product

Expression 7.8 can be rewritten as an eigenvalue problem, which leads to the Fredholm[4] integral:

$$\int_{\Omega} R(\mathbf{x}, \mathbf{x}')\Phi(\mathbf{x}')d\mathbf{x}' = \lambda\Phi(\mathbf{x}), \tag{7.9}$$

$$R(\mathbf{x}, \mathbf{x}') = \frac{1}{N_T}\sum_{i=1}^{N_T} u(\mathbf{x}, t_i)u(\mathbf{x}', t_i). \tag{7.10}$$

$R(\mathbf{x}, \mathbf{x}')$ denotes the two-point correlation tensor in space, and the kth basis function that maximizes expression 7.8, corresponds to the kth eigenvalue of 7.9. The goal of the POD is to find a set of statistically independent basis functions, which represent the velocity field $\mathbf{u}(\mathbf{x})$; therefore, every mode $\Phi_k(\mathbf{x})$ has to be orthonormal to each other, which means:

$$\int_{\Omega} \Phi_{k_1}(\mathbf{x})\Phi_{k_2}(\mathbf{x})d\mathbf{x} = \delta_{k_1 k_2}, \tag{7.11}$$

with $\delta_{k_1 k_2}$ as the Kronecker delta. The orthonormal basis functions ensure that each time coefficient a_k is only dependent on the corresponding spatial mode $\Phi_k(\mathbf{x})$, and that the time coefficients are uncorrelated as well, i.e. they are referred to as orthogonal:

$$\frac{1}{N_T}\int_{T} a_{k_1}(t)a_{k_2}(t)dt = \lambda_{k_1}\delta_{k_1 k_2}, \tag{7.12}$$

with λ_{k_1} as the eigenvalue of the combination k_1. Due to the orthonormal characteristic in eq. 7.11, the time coefficients are determined as follows:

$$a_k(t) = \int_{\Omega} u(\mathbf{x}, t)\Phi_k(\mathbf{x})d\mathbf{x}. \tag{7.13}$$

Snapshot POD   According to Sirovich (1987a,b,c), the velocity signal can be decomposed into orthonormal spatial modes and temporal orthogonal coefficients by applying the temporal correlation tensor for the eigenvalue problem substitutional to the spatial one. Thus, eq. 7.9 reads:

---

[4]Erik Ivar Fredholm ($\star$1866, $\dagger$1927)

$$\int\limits_T C(t,t')a(t')dt' = \lambda a(t), \tag{7.14}$$

$$C(t,t') = \frac{1}{N_P} \sum_{i=1}^{N_P} u(\mathbf{x},t)u(\mathbf{x},t'). \tag{7.15}$$

Subsequently, the spatial modes are obtained as:

$$\Phi_k(\mathbf{x}) = \frac{1}{N_T \lambda_k} \int\limits_T a_k(t)u(\mathbf{x},t)dt, \tag{7.16}$$

and the velocity field is finally reconstructed by applying eq. 7.7.

The direct and the snapshot POD lead in general to similar results, but depending on the size of the input data, the computational effort can be different. In the direct method, the size of the spatial correlation matrix $R(\mathbf{x},\mathbf{x}')$ corresponds to the number of grid points in space, whereas the size of the temporal correlation matrix $C(t,t')$ of the snapshot technique corresponds to the number of observed time steps. While solving the eigenvalue problem of those correlation matrices, the number of operations increases exponentially with the number of matrix elements. According to Coppersmith & Winograd (1990), the computational effort is proportional to $n^{2.376}$. Therefore, the decision of which approach to apply should be based on the size of the available data set. The velocity data are observed at N_P points in space at N_T points in time, and structured as follows:

$$U = \begin{bmatrix} u_1(x_1,t_1) & \dots & u_1(x_1,t_{N_T}) \\ \vdots & \ddots & \vdots \\ u_3(x_{N_P},t_1) & \dots & u_3(x_{N_P},t_{N_T}) \end{bmatrix}. \tag{7.17}$$

Thus, the input matrix (see eq. 7.17) for POD has a size of $(N_C \cdot N_P) \times N_T$. N_C is the number of measured velocity components, N_P stands for the number of grid points in space and N_T for the number of snapshots. The spatial correlation tensor of the direct POD approach (in eq. 7.9) has, therefore, a size of $(N_C \cdot N_P) \times (N_C \cdot N_P)$, whereas the temporal correlation tensor (see eq. 7.15) of the snapshot POD has the size $N_T \times N_T$.

7.7.2 Treatment of outliers

When performing a POD using experimental data, outliers have to be considered in particular, as they will falsify the result. By correlating valid velocity values with implausible vectors, an additional noise is generated in the individual modes, which leads to the incorrect calculation of the respective energy fractions of the modes. A possible strategy to avoid this bias in the energy fractions is to interpolate the outliers from the surrounding vectors of each instantaneous vector field in a first step, before the actual POD is performed.

However, the interpolation, too, has an impact on the correlation tensor and biases the outcome.

For this reason, a novel approach to neglect outliers in the instantaneous vector fields is introduced here. First, the input matrix U, according to eq. 7.17, was multiplied with an indicator function m, which consisted of ones and zeros depending on the quality of each vector. As a result, the masked matrix $\tilde{U}$ became zero, wherever a vector was treated as an outlier, which occurred either when the signal-to-noise ratio of the cross-correlation function during the PIV-processing was below 1.5, or when the velocity magnitude was larger than half the size of an interrogation window. The latter criterion was applied due to the potential loss of particle image pairs, which increases towards the edge of an interrogation window.

In a second step, the correlation tensor of the masked input matrix was obtained as follows:

$$\tilde{R}(\mathbf{x}, \mathbf{x}') = \tilde{U}\tilde{U}^T. \tag{7.18}$$

The indicator function used in the first step, was correlated in the same manner, which resulted in a matrix $\tilde{N}_R$ that contained the number of valid correlations at each location in space. In order to obtain the time-averaged correlation tensor $R(\mathbf{x}, \mathbf{x}')$, the matrix $\tilde{R}(\mathbf{x}, \mathbf{x}')$ was divided element-by-element by the matrix $\tilde{N}_R$, instead of dividing by the total number of snapshots N_T.

The subsequent steps to solve the eigenvalue problem of the correlation tensor, and to obtain the spatial modes as well as the time coefficients were identical to eq. 7.11 until eq. 7.13. The advantage of this technique was that only the valid vectors of each time step were taken into account and no spatial or temporal interpolation influenced the correlation tensor. However, this approach is based on the assumption that statistically converged samples are used so that the correlation tensor is also statistically converged, otherwise this method would probably fail. The convergence of the samples, i.e. the sufficient number of samples, was shown in section 6.6, see Figure 6.8 and Figure 6.9.

7.7.3 Strategy of the POD analysis

As introduced previously, the POD provides two approaches, which lead in general to similar results but differ in the dimension of the correlation tensor (spatial or temporal). In the direct POD, the velocities are correlated in space and, therefore, the solution of the Fredholm integral (see eq. 7.9) corresponds to the spatial modes $\Phi(x)$. In the snapshot POD, though, the samples are correlated in time and the eigenvalue problem results in the time coefficients (see 7.14). The outcomes ($\Phi(x)$ and $a(t)$) of solving the eigenvalue problem following one or the other method are correct as long as the assumption of the statistical convergence of U holds true.

Subsequently, the instantaneous vector fields assembled in the input matrix U are used to compute the time coefficients or the spatial modes in the direct or snapshot method, respectively. Therefore, the quality of $a(t)$ or $\Phi(x)$ depends on the quality of the input matrix U. Due to the neglected outliers, the matrix U contains NaN-values, wherever a velocity vector is spurious, and consequently, the result of eq. 7.13 or eq. 7.16 are affected accordingly.

For this reason, both POD approaches are compared using the data of the flat-bed case, in order to evaluate mutually the quality of the POD parameters. Figures 7.33 a) and b) show the correlation of the basis functions $\Phi(x)$ and of the time coefficients $a(t)$, respectively, which is calculated using the vector norm of each parameter to normalize the scalar product of two modes, similar to eq. 7.8. This indicator is also referred to as the *relevance index R_k* of two modes (Chen *et al.*, 2012; Liu & Haworth, 2011):

$$R_k = \frac{\Phi_{\text{direct}}^k \cdot \Phi_{\text{snapshot}}^k}{\|\Phi_{\text{direct}}^k\| \|\Phi_{\text{snapshot}}^k\|}. \tag{7.19}$$

The diagonal of the resulting matrix (dashed white line in Figure 7.33) corresponds to the relevance index, which equals to 1 if both parameters are identical, and to -1 if the parameters are identical, but different in sign. In case of no correlation, eq. 7.19 would be zero. The colour bar is scaled to ± 0.5 for better recognition. The small plots inside Figures 7.33 a) and b) correspond to a zoom to the first 35 modes. In general, the modes of both POD approaches correlate well as the diagonal entries of the matrix are close to ± 1, whereas the remaining entries are close to zero. Moreover, for the first seven modes (see zoomed area), the relevance index is $\geq \pm 0.95$, which indicates a strong correlation of the most energetic modes. The correlation for the higher POD modes, however, decreases, which can be observed by the increasing scattering along the diagonal in Figures 7.33 a) and b). Consequently, the similarity between the modes of the direct and the snapshot approach decreases likewise, and the modes can no longer be related. Therefore, the time coefficients and the basis functions of both approaches are considered to be similar in the first modes, but not in the higher modes.

Furthermore, the number of modes containing 90% of the total kinetic energy differs as well. In the direct POD, 360 modes are required, whereas in the snapshot POD only 30 modes are sufficient to reconstruct this percentile of the energy. For this reason, a hybrid POD approach is used to test if the reconstructed velocity fields following one or the other POD approach suffer from the quality of the input matrix U. Doing so, the velocity field is reconstructed using the first 30 basis functions $\Phi(x)_{\text{direct}}$ of the direct POD method combined with the first 30 time coefficients $a(t)_{\text{snapshot}}$ of the snapshot POD approach. When solving the eigenvalue problem of the correlation matrix, for example $R(\mathbf{x}, \mathbf{x}')$ in the direct POD approach, the obtained parameter $\Phi(x)$ represent the eigenvectors, and therefore, their signs are random. The time coefficients $a(t)$ are calculated using the vector field and the eigenvectors (see eq. 7.13), and vice versa for the snapshot POD. Therefore, when reconstructing the vector fields, the random signs of the eigenvectors are adapted by that parameter, which is determined from the vector field, i.e. $a(t)$ using the direct POD and $\Phi(x)$ in the snapshot POD. When combining the two POD approaches, the random signs of $a(t)_{\text{snapshot}}$ have to be adapted accordingly to those of $a(t)_{\text{direct}}$, in order to result in a reconstructed vector field of correct signs. Due to the normalization of the basis functions, the reconstructed velocity field is only qualitatively correct and has to be multiplied by $\sqrt{N_{\text{modes}}}$, in order to reveal the amplitude of the vector field, too (see eq. 7.20). The total number of modes corresponds to that of the direct POD approach: number of velocity components N_{C} times the number of

points in space N_P.

$$U_\mathrm{reconstructed} = \Phi_\mathrm{direct}\,|a|_\mathrm{snapshot}\,\mathrm{sgn}(a_\mathrm{direct})\sqrt{N_C \cdot N_P} \qquad (7.20)$$

Figure 7.34 shows the PDFs of the horizontal velocity component at P4 (see section 7.5) inside the wall-parallel jet underneath the horseshoe vortex in front of the wall-mounted cylinder. The time series were reconstructed using the direct, the snapshot and the hybrid POD approach. As described in section 7.5, the Mono-PIV data were biased by the peak locking effect. When applying a POD (direct or snapshot) on these biased Mono-PIV data, the peak locking effect vanished, and the expected bimodal structure of the horizontal velocity component appears. Furthermore, the probability distributions stemming from the direct and the snapshot POD coincide well with each other as the mean values differ by less than 1% and the standard deviation by about 6%. The reconstructed time series using the hybrid approach is close to those of the other methods (error in the mean value: $\varepsilon \approx 15\%$, and in the standard deviation: $\varepsilon \approx 9\%$). However, when comparing the three reconstructed time series to the measured one, the mean values differ by $7 - 8\%$ in each POD approach, and the standard deviation varies by 14% and 18% using the direct and the snapshot POD, respectively, and by 6% in the hybrid approach.

Even though the hybrid approach appears to be promising in general, and the results seem to be acceptable, the reconstruction of the velocity fields and further analyses using this method are not recommended in this case. Only 15 modes in total reveal a relevance index (correlation) of more than ± 0.90, i.e. these modes of the direct and the snapshot POD can be considered to be more or less identical, whereas the remaining modes do not correspond to each other. The lower the relevance index between two modes is, the larger the error in the reconstructed time signal becomes using the hybrid approach. The intention of testing this hybrid POD approach was to show that the influence of the quality of the input matrix is small, and therefore, validated the strategy of neglecting spurious vectors instead of interpolating the remaining 'holes'. Furthermore, the final results of both traditional POD approaches (direct or snapshot) appeared to be reliable and can be used for further analyses.

Definition of the input matrix

The POD is commonly conducted using the fluctuating velocity fields only; thus, the ensemble average field $\langle U \rangle$ is subtracted from the input matrix (see eq. 7.17), before one of the decomposition methods (snapshot or direct) is applied. Whether the POD should be applied to the velocity fields or to the fluctuating fields depends on the 'perspective'. The hypothesis that the mean velocity field is orthogonal to the fluctuations might hold true for boundary layers, for example. In such a flow situation, the small-scale fluctuations occurring in the flow field can be considered to be uncorrelated, and therefore, the POD of the fluctuating fields would be chosen. Furthermore, if a POD was applied on the velocity fields, the time coefficient of the most energetic POD mode, which corresponded to the mean flow field, would be constant.

However, in front of a wall-mounted cylinder, the flow field oscillates simultaneously and fluctuations in the direction of the mean flow occur. Oscillations in the approaching flow

a: Basis functions $\Phi(x)$ **b:** Time coefficients $a(t)$

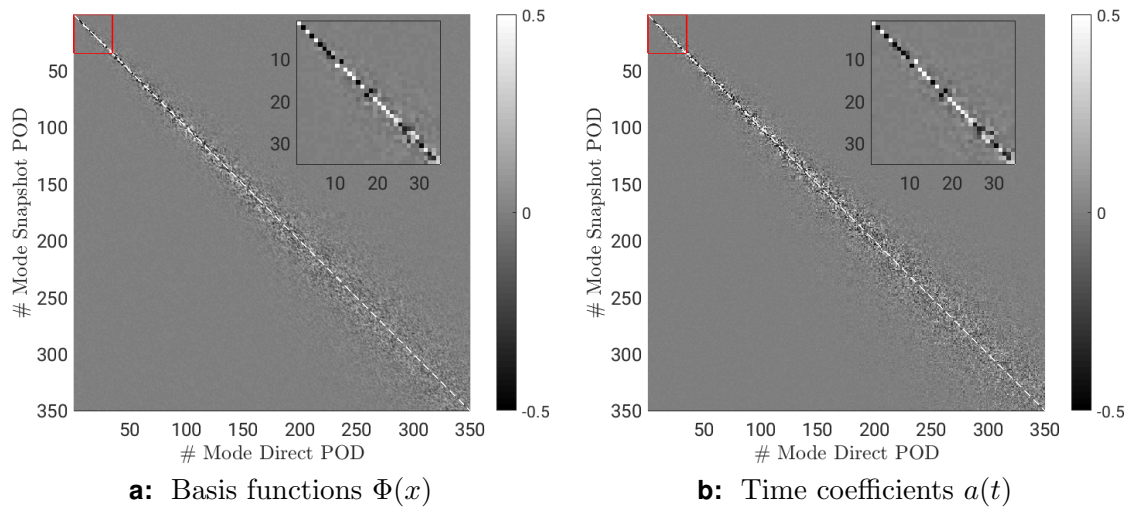**Figure 7.33:** Correlation of POD parameters of the direct and snapshot POD in front of the wall-mounted cylinder of the first 350 modes. The dashed white line highlights the diagonal of the correlation matrix.
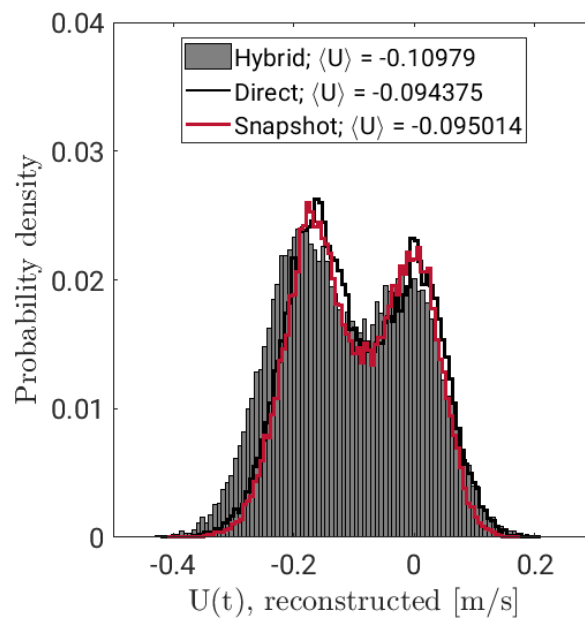
Figure 7.34: Reconstructed time series of the u-component in front of the wall-mounted cylinder using the direct, snapshot and the hybrid POD approach at $P4 : x/D = -0.712$, $y/D = 0.012$

are assumed to correlate with those of the entire horseshoe vortex system as the incoming flow is redirected by the cylinder, and therefore, are linked to the vortex dynamics. As a result, when the POD is applied to the velocity fields, the most energetic mode varies in time in opposition to the common assumption. Furthermore, this variance in time is redistributed to the remaining POD modes when the fluctuations are considered only and might generate additional POD modes, which are not directly linked to physical flow structures. Chen *et al.* (2012) analysed the directed and undirected flow inside combustion engines and discussed the quality of the POD results using the velocities and the fluctuations as input. Simultaneous fluctuations in the direction of the mean flow occurred as well, and according to the conclusions of Chen *et al.* (2012), the POD considering the velocities was of greater use. From the mathematical point of view, there is no difference in the POD with or without the ensemble average. However, the interpretation of the outcomes is different.

When the POD is applied on the velocity fields, the first (most energetic) mode is similar to the mean velocity field. Therefore, this mode is here referred to as the zeroth mode Φ_0 for simplicity in comparing to the modes of the POD using the fluctuating fields only. When applying the POD on the velocity and on the fluctuating fields, following relevance indices were obtained:

# mode	1	2	3	4	5	$\langle U_i \rangle$
0	-0.6220	0.6564	-0.1406	-0.2114	0.1041	-0.9937
1	0.7788	0.5933	-0.0654	-0.1371	0.0483	-0.0470
2	-0.0410	0.1905	0.9757	0.0569	0.0304	-0.0059
3	0.0592	-0.3122	0.1233	-0.9205	0.1215	-0.0173
4	-0.0510	0.1316	0.0078	-0.1944	-0.9528	-0.0070

Table 7.4: Relevance indices for the snapshot POD using velocities (rows) and fluctuations (columns) as input matrix, based on measurements in front of the wall-mounted cylinder. Additionally, the velocity POD modes are compared to the mean velocity field (rightmost column)

The relevance indices in Table 7.4 are obtained from eq. 7.19 using the spatial modes Φ of the snapshot POD with both the velocity fields and the fluctuating fields as input matrix in front of the wall-mounted cylinder. The results indicate that the first two modes of the POD using the fluctuations combined are similar to the POD mode #1 of the velocity decomposition. Furthermore, the zeroth POD mode of the velocity decomposition shows high similarity to the mean velocity field and from the third mode on, both methods show similarity again. In Figures 7.35, the spatial distributions of the POD modes, which show the highest similarity, are compared to each other. As expected, the spatial distribution of the zeroth POD mode matches the one of the mean velocity magnitude. The mode #1 of the velocity-POD reveals a similar distribution as the first and second mode of the fluctuation-POD, and the mode #2 of the velocity decomposition is similar to the mode #3 of the fluctuation-POD. Based on these results, the following hypothesis is formulated:

$$\Phi_{0,\,\text{veloc}} \cdot a(t)_{0,\,\text{veloc}} + \Phi_{1,\,\text{veloc}} \cdot a(t)_{1,\,\text{veloc}} \approx \langle U_i \rangle + \Phi_{1,\,\text{fluc}} \cdot a(t)_{1,\,\text{fluc}} + \Phi_{2,\,\text{fluc}} \cdot a(t)_{2,\,\text{fluc}}. \quad (7.21)$$

7.7.4 Results of the POD

The POD was conducted following the direct approach (cf. section 7.7.1) using the velocity fields for both the flat-bed configuration as well as for the data set of the scoured cylinder for $Re = 39,000$. Furthermore, the regions of interest were concentrated to the area around the time-averaged location of the horseshoe vortex; 58×189 data points were included in the POD in front of the cylinder on a flat plate. From the Mono-PIV results, two dimensional velocity fields were obtained. Therefore, the maximum number of POD modes in this flow case was $58 \times 189 \times 2 = 21,924$. In front of the scoured cylinder, the analysed area covered 141×101 data points, which would have resulted theoretically in $141 \times 101 \times 3 = 42,723$ modes due to the reconstruction of the entire three dimensional vector field using Stereo-PIV. However, due to the inclined surface of the scour model, the rectangular frame of 141×101 data points representing the region of interest was intersected by the scour model, and therefore, 5,083 data points of the velocity field contained no information, i.e. the maximum number of attainable POD modes reduced to $42,723 - 3 \times 5,083 = 27,474$.

Energy fractions

In Figure 7.36 a), the energy spectra of the POD-analyses in front of the wall-mounted cylinder and the scoured cylinder are given on a logarithmic scale. Note, that the mode #0 is mathematically the mode with index 1, but for the sake of comparability it is called zeroth mode here. The energy of the POD modes corresponds to the Eigenvalues of each mode. The linear trends of both data sets indicate the logarithmic decay of the energy from the dominant energetic modes to the less energetic modes of higher order. The energy contents of the first modes are similar for both flow configurations, and the zeroth mode contains approximately 80% of the total energy. However, the energy decay in the scour-case appears to be much smaller than in the flat-bed case.

Figure 7.36 b) shows the energy fractions of the modes #1 to #20 of the flat-bed case, the scour-results and of the POD results published by Apsilidis *et al.* (2016). As the velocity fields were used as input for the POD, the Eigenvalue of the zeroth mode (λ_0) was subtracted, in order to enable the comparison to the data of Apsilidis *et al.* (2016), who decomposed fluctuating fields. The energy fraction of the kth mode is, therefore, defined as:

$$EF_k = \frac{\lambda_k}{\sum \lambda - \lambda_0} \cdot 100. \tag{7.22}$$

Apsilidis *et al.* (2016) conducted Mono-PIV measurements of the flow in front of a wall-mounted cylinder at $Re = 47,000$ and performed a POD according to the snapshot approach on the fluctuating velocity fields using 3,270 snapshots with a sampling rate of $1 kHz$. The first two modes contained approximately 25% of the TKE, whereas 10 modes were required for 50% and 145 modes for covering 90% of the TKE. The energy content of the individual modes and the energy decay is similar to the results obtained in the present analysis of both configurations (scour and flat-bed). The energy content of the POD mode #1 is $EF_{1, \text{ Flat bed}} \approx 20\%$, $EF_{1, \text{ Scour } 0°} \approx 18\%$ and $EF_{1, \text{ Apsilidis et al. 2016}} \approx 14\%$, and the number of modes that cover 50% of the energy is approximately the same (see Ta-

ble 7.5). The number of modes containing 90% of the energy, however, is different, which is in accordance with the energy decay: in the flat-bed case 360 modes are required, while Apsilidis *et al.* (2016) identify 145 modes and at the scoured cylinder there are only 29 modes.

The POD-analyses applied to the cylinder-on-flat-bed configurations reveal a difference between the energy fractions of the first and the second mode by approximately a factor of two ($EF_{1,\text{Flat bed}} = 20.64\%$ and $EF_{2,\text{Flat bed}} = 9.13\%$). The decomposition of the data at the scoured cylinder shows that the energy of the first POD mode exceeds the one of the second mode by a factor of 1.4 ($EF_{1,\text{Scour } 0°} = 17.87\%$ and $EF_{2,\text{Scour } 0°} = 12.39\%$). The energy fractions in the first 10 modes, approximately, are similar between the flat-bed and the scour configuration.

Cum. EF [%]	Flat bed	Scour 0°	Apsilidis *et al.* (2016)
25	2	2	2
50	8	7	10
75	49	19	
90	360	29	145

Table 7.5: Number of modes required for covering characteristic cumulative energy fractions without the zeroth POD mode

Spatial distribution of the POD modes

Figures 7.37 a) to d) show the pseudo-streamlines of the zeroth and the first POD modes flooded with the corresponding magnitude for both experimental configurations in the symmetry plane in front of the cylinder for $Re = 39{,}000$. As expected, the zeroth POD modes of both configurations show similarity to the time-averaged magnitude of the velocity field.

According to Figure 7.37 b), the first POD mode in the flat-bed case can be related to the dynamics of the wall-parallel jet, as a flow structure at a similar position of the lower branch of the c-shaped TKE distribution can be observed (see Figure 7.7). The flapping of the jet causes velocity fluctuations in the horizontal direction, which in turn induces kinetic energy represented by the first POD mode. Furthermore, the horseshoe vortex is affected by this flapping as the first mode reveals a second patch downstream of the time-averaged location of the HV. Whenever the jet detaches from the bottom plate, the vortex moves subsequently towards the cylinder. This flapping behaviour of the jet is assumed to be random as the PDF of the horizontal velocity component shows a certain flatness instead of a distinct bimodality (see Figure 7.23 a).

The spatial distribution of the first POD mode inside the scour hole shows a different shape than in the flat-bed case (see Figure 7.37 d) as the underlying physical process is different, too. The peak of this mode is located upstream of the HV centre and coincides with the peak production of turbulent kinetic energy (see the 0.35 isoline of the TKE production term). Furthermore, the tail of the distribution in the uphill direction corresponds to the region of the shear layer separating from the scour edge, and thus to the tail of the distribution of the TKE production. Therefore, the first POD mode appears to be the major source of TKE

inside the scour hole and refers to the interference of the approaching shear layer with the HV and not to the dynamics of a wall-parallel jet.

The POD modes #2 and #3 are presented in the Figures 7.38 a) to d). These two modes together are considered to represent the oscillations of the entire vortex-jet system. The peaks of the second and third POD mode are located up- and downstream of the time-averaged location of the HV, respectively. The offset of the peaks of the modes #2 and #3 refers to the horizontal oscillations of the HV that induce vertical velocity fluctuations according to the orientation of the corresponding pseudo-streamlines. When the (clockwise) rotating vortex passes a certain observation point, the vertical velocity component changes both magnitude and sign (positive to zero to negative and vice versa). Therefore, fluctuations in the vertical direction occur and form the upper part of the time-averaged TKE distribution around the HV centre (see Figure 7.7 b). The bimodality of the jet, as observed by Devenport & Simpson (1990), cannot directly be related to several single POD modes (e.g. second and third). An assignment of the back-flow and zero-flow mode to POD modes individually would imply that these two flow modes would be orthogonal to each other. The jet, however, is either in the back-flow, in the zero-flow or in an intermediate mode while the transition takes place. Therefore, the energy content of the back-flow and zero-flow mode is assumed to be constant, and consequently, to be represented in the same POD mode. Furthermore, these events are expected to be negatively correlated (one suppresses the other) and not to be mutually independent.

The analysis of the PDFs of the velocity components in the scour hole (see section 7.5.2) revealed a skewed PDF of the wall-normal fluctuations indicating an occasional lift of the vortex in this direction. At the time-average location of the centre of the HV, the POD mode #2 has a local peak representing the dynamics of the vortex corresponding to the lift from the surface (see Figure 7.38 c). Further uphill, the second POD mode reveals an other peak, which marks the location of the lower branch of the c-shaped TKE distribution. The PDF of the radial velocity component approximates a bimodal shape in this region, too (see Figure 7.28 a). Therefore, the lift of the vortex is directly linked to the dynamics of the radial velocity component in this area. The lifting vortex induces the radial fluctuations and vice versa, because of the fluid rotating around the vortex, which is, subsequently, accelerated underneath the HV in the radial direction pointing uphill. In contrast to the situation in front of the wall-mounted cylinder, apparently no surface-parallel jet is indicated by the pseudo-streamlines of mode #2 in the scour. The second POD mode is, therefore, related to the dynamics of the HV alone, while the first mode, is related to the interference of the shear layer and the vortex.

The third POD mode shown in Figure 7.38 d) can be related to the oscillations of the HV parallel to the surface. As in the flat-bed case, these oscillations induce surface-normal fluctuations that are represented by the peaks of the third POD mode. The peak uphill from the time-averaged vortex is at the same location as the peak of the first mode and, therefore, is also related to the interference of the shear layer and the vortex. The fluctuations of the shear layer are linked to the oscillating behaviour of the HV, according to the distribution of the third POD mode.

a: #0, Velocity-POD

b: $\sqrt{\langle U \rangle^2 + \langle V \rangle^2}$

c: #1, Velocity-POD

d: #1, Fluctuation-POD

e: #2, Fluctuation-POD

f: #2, Velocity-POD
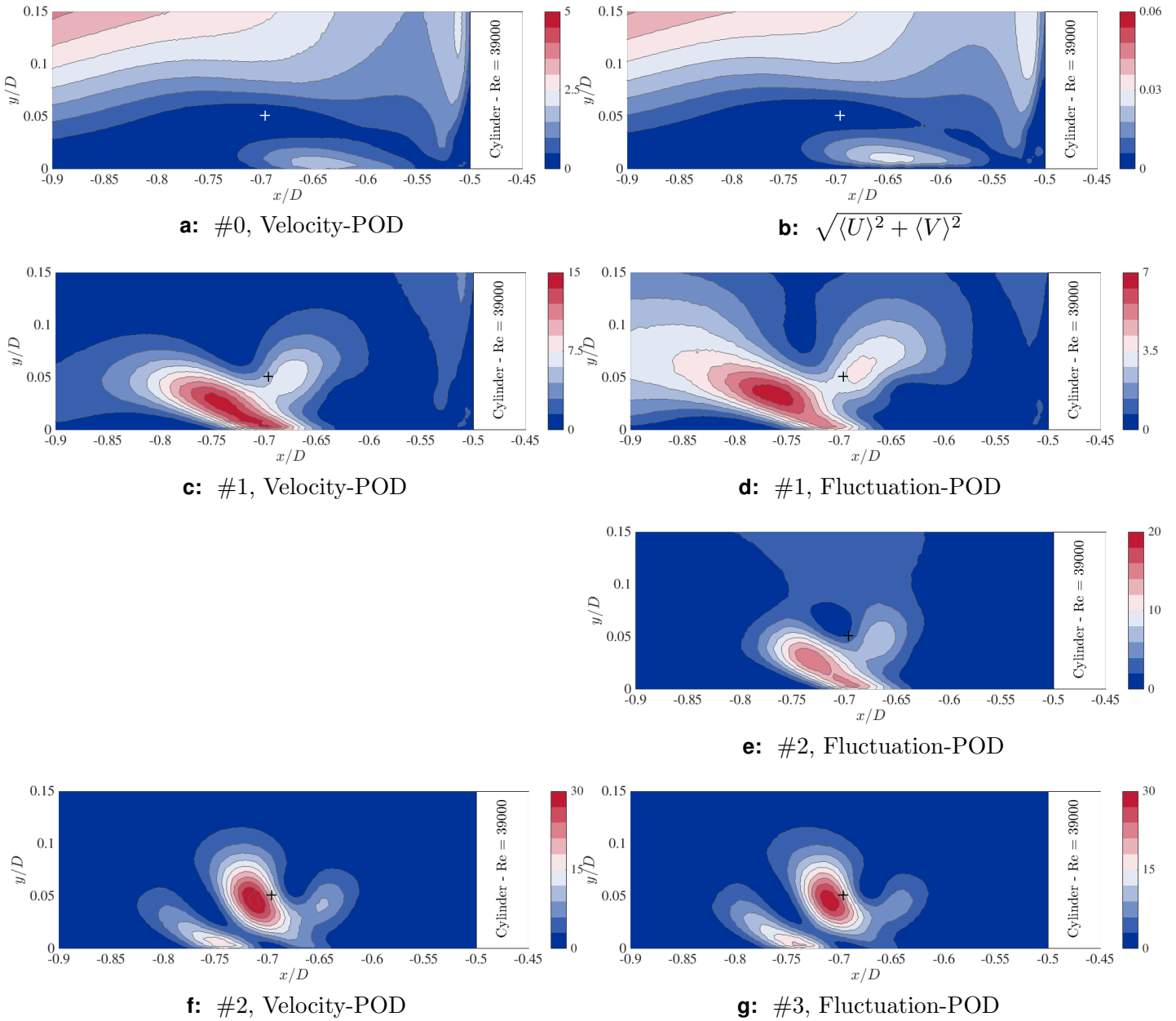
g: #3, Fluctuation-POD

Figure 7.35: Spatial distribution of the magnitude of the basis functions $\Phi(\mathbf{x})$ of the velocity-POD (left) and the fluctuation-POD (right) using the snapshot approach in front of the wall-mounted cylinder

a: Energy spectrum

b: Energy fraction of mode #1 to #20
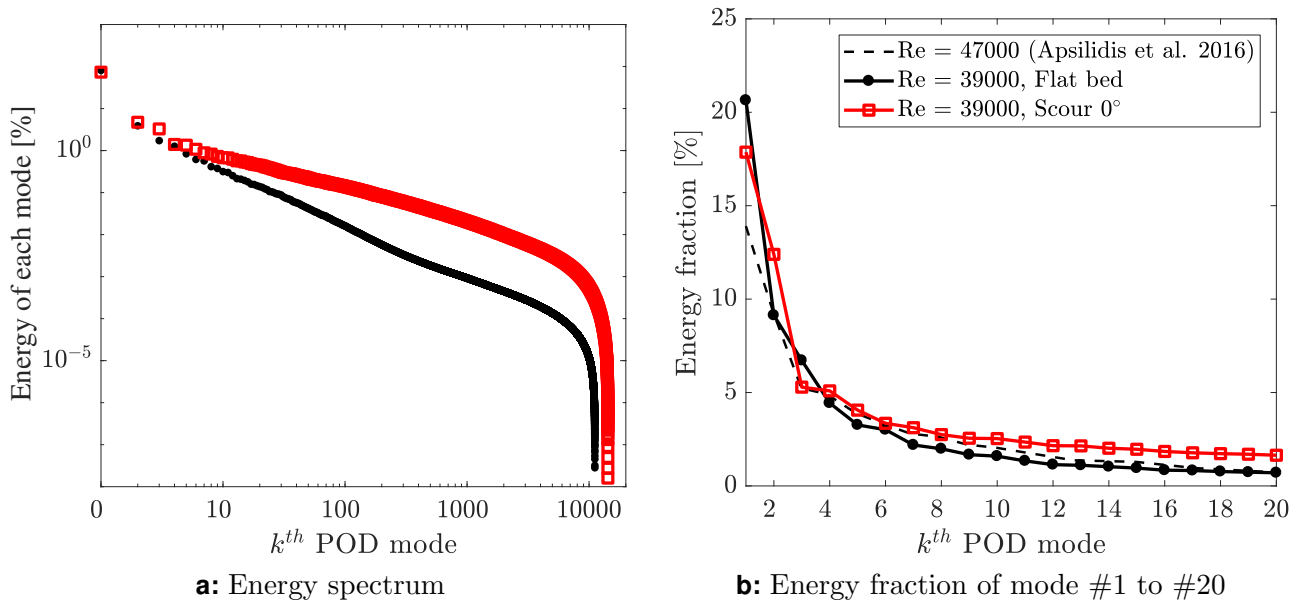
Figure 7.36: Energy spectra of the POD modes for $Re = 39{,}000$ in front of the wall-mounted cylinder (black dots) and the scoured cylinder (red squares) (right), and Energy fractions of modes #1 to #20 together with data from Apsilidis *et al.* (2016) (dashed line) (right).

a: #0, Flat bed

b: #1, Flat bed

c: #0, Scour 0°

d: #1, Scour 0°
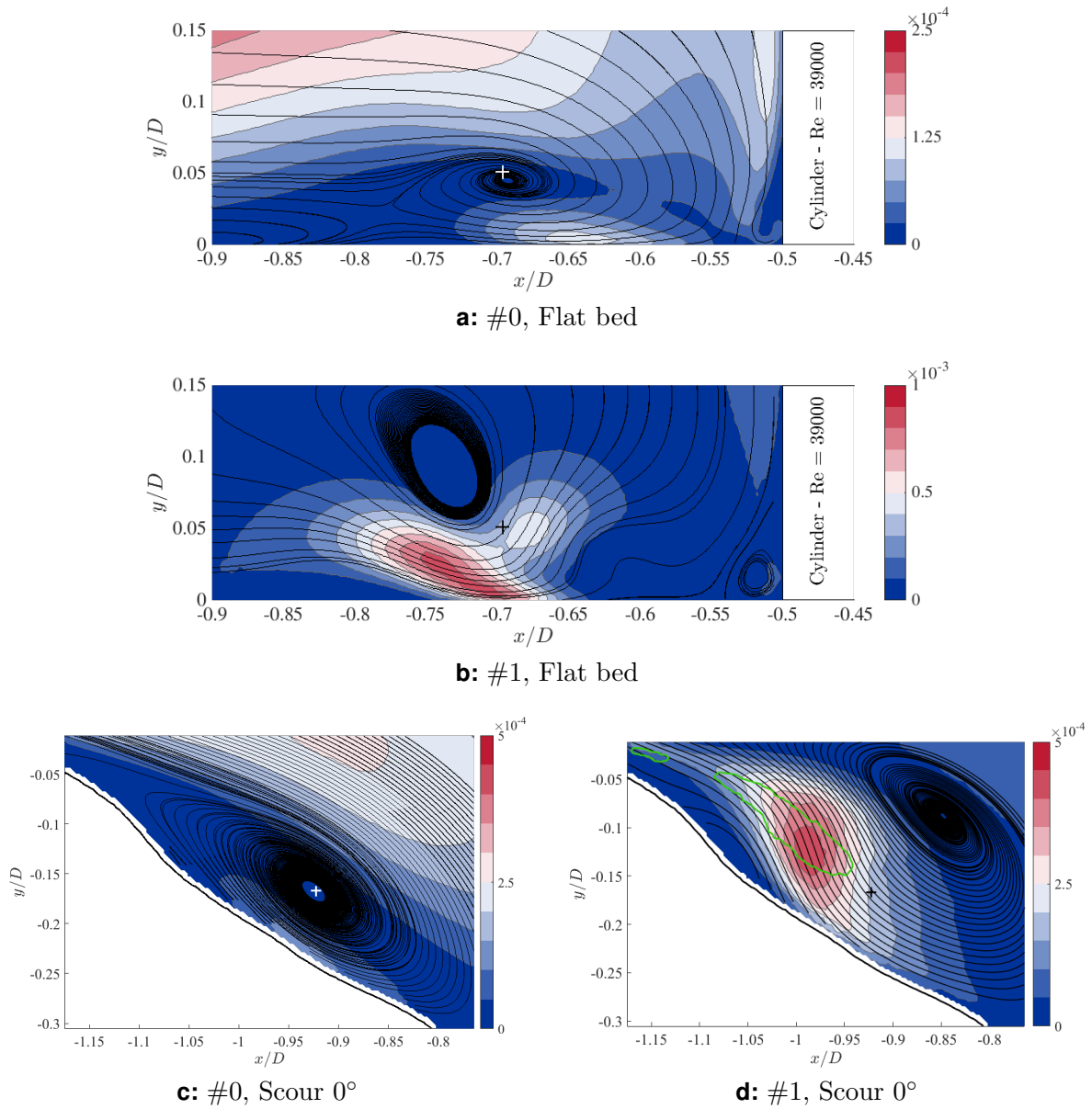
Figure 7.37: Spatial distribution of the POD modes #0 and #1. The time-averaged location of horseshoe vortex is indicated by the plus symbol. The green line in Figure d) refers to the 0.35 isoline of TKE production.

a: #2, Flat bed

b: #3, Flat bed

c: #2, Scour 0°

d: #3, Scour 0°
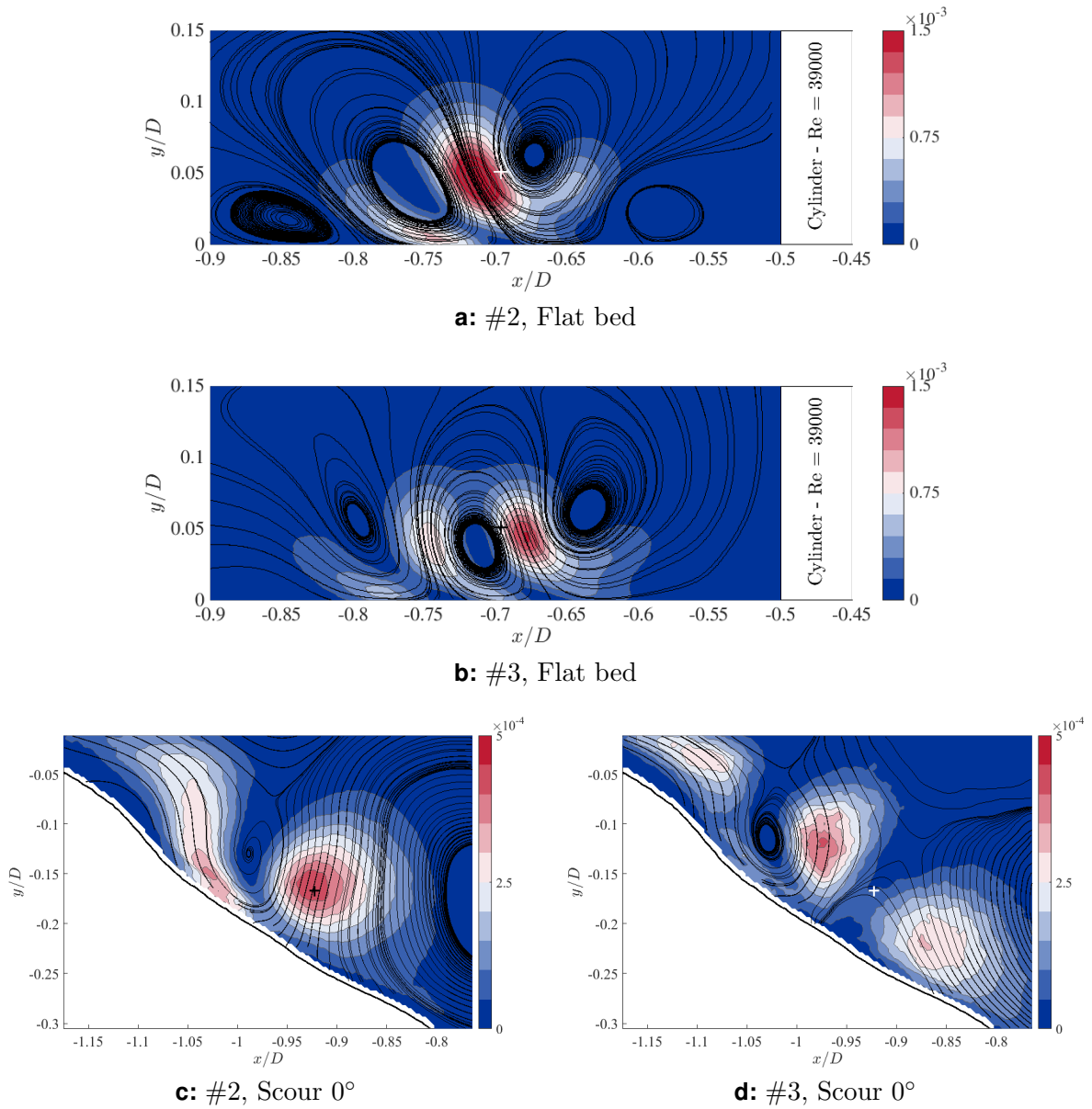
Figure 7.38: Spatial distribution of the POD modes #2 and #3. The time-averaged location of horseshoe vortex is indicated by the plus symbol.

Combinations of POD modes

The resulting POD modes span an orthogonal vector space, which represents the solution space of a dynamical system, for example the flow field $\mathbf{u}(\mathbf{x}, t)$. Such a flow field is expressed as the linear combination of the spatial functions $\Phi_k(\mathbf{x})$ with the time coefficients $a_k(t)$ of the kth mode (see section 7.7.1). Furthermore, the flow *"corresponds to solutions belonging to the attractor of a dynamical system such as the Navier-Stokes equations"* (Tropea *et al.*, 2007, p. 1358). Therefore, when inserting the POD expansion $\sum_{k=1}^{K} a_k(t)\Phi_k(\mathbf{x})$ (see eq. 7.7) in the Navier-Stokes equations (NSE) (see eq. 2.12), a reduced-order model for this dynamical system can be derived. The time coefficients a_k in the NSE are then determined by a Galerkin[5] projection onto the POD subspace using $\Phi_{n,i}$ for $n = 1 \ldots K$ (Tropea *et al.*, 2007). The Galerkin projection is demonstrated using the viscous term of the NS and substituting u_i by the expansion $\sum_{k=1}^{K} a_k(t)\Phi_{k,i}(\mathbf{x})$:

$$
\nu \frac{\partial^2}{\partial x_j^2} \left(\sum_{k=1}^{K} a_k(t)\Phi_{k,i}(\mathbf{x}) \right) \quad \bigg| \cdot \Phi_{n,i}
$$

$$
= \int_{\Omega} \Phi_{n,i} \, \nu \left(\sum_{k=1}^{K} a_k(t) \frac{\partial^2 \Phi_{k,i}}{\partial x_j^2} \right) d\Omega
$$

$$
= \nu \sum_{k=1}^{K} a_k(t) \int_{\Omega} \Phi_{n,i} \frac{\partial^2 \Phi_{k,i}}{\partial x_j^2} d\Omega, \tag{7.23}
$$

$\Phi_{n,i}$ and $\frac{\partial^2 \Phi_{k,i}}{\partial x_j^2}$ are not orthogonal, and the spatial integral $\int_{\Omega} d\Omega$ in eq. 7.23 results in a non-diagonal matrix D_{kn}. The same applies for the remaining terms of the NS, such that $\partial a_k/\partial t$ becomes a set of Ordinary Differential Equations (ODE):

$$
\frac{\partial a_k}{\partial t} = f(a_k, a_l, a_m, \ldots). \tag{7.24}
$$

The function on the right hand side of eq. 7.24 refers to the interconnection of the time coefficients a_n for $n = 1 \ldots K$ and, therefore, to the interconnection of the dynamics of the single POD modes.

This interconnection might be counterintuitive and is further demonstrated using Figure 7.39. Consider a flow field in the sample space $X_1 X_2$ represented as the grey ellipse on the left hand side of Figure 7.39. Without subtracting the mean value (velocity POD, red axes) the zeroth POD mode (#0) is similar to the mean locating the process in 'space', whereas the first POD mode (#1) is orthogonal to the previous mode. When applying the POD on the fluctuations (blue axes), the first and second POD mode refer to the first and second principal axis of the ellipse, respectively. Therefore, the modes obtained by the velocity decomposition do not necessarily align with the principal axes of the ellipse.

In the remainder of this section, the time coefficients of the velocity decomposition are evaluated with respect to a mutual interaction. Doing so, the time coefficients are cen-

---

[5]Boris Grigorjewitsch Galjorkin ($\star$1871, $\dagger$1945)
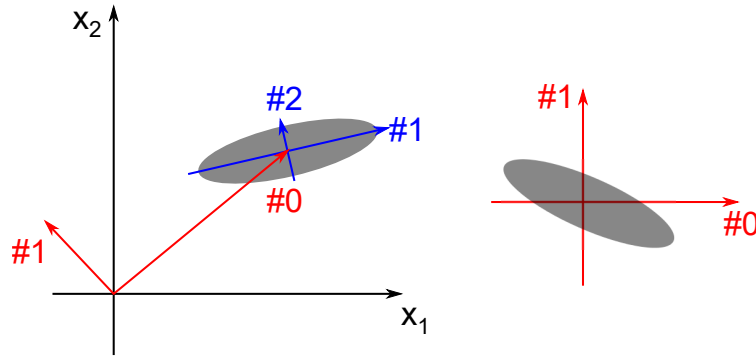
Figure 7.39: Sketch of a process (grey ellipse) in the $X_1 X_2$ sample space (black), in the POD subspace of zeroth and first mode as in the velocity decomposition (red), and the POD subspace of first and second mode as in the fluctuation decomposition (blue)

tred and normalized as: $(a_k(t) - \langle a_k(t) \rangle)/\sigma(a_k(t))$, and the joint probability density functions of the modes m and n are calculated similar to section 7.5. Furthermore, the linear correlation coefficient of these centred time coefficients is calculated according to eq. 7.4:

$$\varrho_{m,n} = \frac{\langle a'_m a'_n \rangle}{\sigma(a_m)\sigma(a_n)}. \tag{7.25}$$

The time coefficients are orthogonal (see eq. 7.12):

$$\langle a_m a_n \rangle = \begin{cases} \lambda, & \text{for } m = n \\ 0, & \text{else} \end{cases} \tag{7.26}$$

The term $\langle a_m a_n \rangle$ can be rewritten as:

$$\langle a_m a_n \rangle = \langle a_m \rangle \langle a_n \rangle + \langle a'_m a'_n \rangle. \tag{7.27}$$

Therefore, the correlation coefficient $\varrho_{m,n}$ is not necessarily zero. If $\varrho_{m,n} \neq 0$, it follows from eq. 7.27 that the mean values of the time coefficients are non-zero, which is logically consistent when applying a POD on the velocity fields. The mean values of the time coefficients $\langle a_k(t) \rangle$ of both configurations, flat-bed and scour, are listed in Table 7.6. The correlation of the fluctuations of the time coefficients is demonstrated on the right hand side of Figure 7.39. The centring of the time coefficients shifts the process to the origin of the subspace #0 #1. As the POD modes might not align with the principal axes of the ellipse, a rotation of the process with respect to the subspace #0 #1 remains causing $\varrho_{m,n} \neq 0$.

Figure 7.40 shows the joint PDFs of the time coefficients of the zeroth, first and second POD mode in the flat-bed case. The combination of the zeroth and the first mode (a) reveals a slight positive correlation of these two modes ($\varrho_{0,1} = 0.43$), which means that the fluctuations of the zeroth mode are linked to those of the first mode. The zeroth POD mode agrees with the mean flow field to a large extend (see Table 7.4). The fluctuations in the direction of the mean flow, therefore, are mainly responsible for the variance of the time coefficient of the zeroth mode (otherwise $a_0(t)$ would be constant). Furthermore, these

# mode	Flat bed	Scour 0°
0	−15.14	−12.53
1	0.1579	−0.9498
2	0.1013	0.2403
3	0.0898	0.4161

Table 7.6: Mean values of the time coefficients of the first four POD modes according to the velocity decomposition of the flat-bed and scour data

fluctuations are transported to the first POD mode as the correlation coefficient indicates. The flow approaching to the wall-mounted cylinder fluctuates. Due to the blocking of the flow by the cylinder, the down-flow is generated, and consequently, high momentum fluid is transported into the horseshoe vortex system. Thus, the fluctuations of the approaching flow (zeroth POD mode) are related to those of the jet due to the redirection of the streamlines of the approaching flow. Therefore, the flapping of the jet, which is interpreted to be represented by the first POD mode, is interconnected to the fluctuations of the down-flow; thus, the approaching flow.

The linear correlation between the first and the second mode (see Figure 7.40 b) is zero. The jPDF, however, appears to be heart-shaped as the distribution of $a_1'(t)$ has a broad (bimodal) peak and that of $a_2'(t)$ is skewed. The first POD mode represents the flapping of the wall-parallel jet, whereas the second mode refers to the horizontal oscillations of the HV, and, according to the heart-shaped distribution, the flapping of the jet occurs only when the vortex moves in the positive direction (towards the cylinder). In case of $a_2'(t) < 0$, the vortex moves in the upstream direction, which seems to suppress the flapping of the jet. As the distribution of $a_2'(t)$ is skewed, the vortex oscillates predominantly in the positive direction (towards the cylinder), and excursions in the negative direction, thus further upstream than the time-averaged position, occur occasionally.

The analysis of the jPDF of the second and third POD mode has shown that these modes are both uncorrelated and completely independent of each other, so that no other combinations of POD modes are further discussed here.

The jPDFs of the zeroth and the first, and of the first and the second POD mode of the flow field in the scour hole are presented in Figure 7.41 a) and b), respectively. In contrast to the correlation coefficient $\varrho_{0,1}$ of the flat-bed case, the correlation of the zeroth and the first POD mode of the scour data is slightly negative and the distributions of the fluctuations of the time coefficients of both modes reveal a sharp peak. The interference of the shear layer and the HV is influenced by the fluctuations in the mean flow direction. In case of positive fluctuations of $a_0(t)$, the interference of the shear layer and the vortex moves in the downward direction towards the scour surface and vice versa. As the fluctuations of the shear layer are represented by the fluctuations in the mean flow direction, this relation between the zeroth and the first POD mode is not surprising. The jPDF of the first and second POD mode, however, does not provide further details of the dynamics and their relations. The jPDF indicates symmetry and uncorrelated fluctuations of the time coefficients $a_1(t)$ and $a_2(t)$ of the scour data.

Figure 7.42 shows the jPDF of the second and third POD mode. In contrast to the uncorrelated corresponding distributions in the flat-bed case, these POD modes, in front of

Figure 7.40: (Joint) probability density functions of the POD time coefficients of the zeroth and first mode (left) and of the first and second mode (right) in front of the wall-mounted cylinder

the scoured cylinder, reveal a certain dependency as the correlation coefficient $\varrho_{2,3} = 0.2$. Both $a'_2(t)$ and $a'_3(t)$ are approximately symmetrically distributed and the corresponding POD modes are related to the oscillations of the horseshoe vortex: the second mode refers to the surface-normal movements, whereas the third mode is linked to the motions parallel to the scour surface. The positive correlation of these two modes reveals that oscillations in positive radial direction might coincide with positive wall-normal oscillations, i.e. lift from the scour surface. However, this is only a weak dependence and other combinations of the vortex oscillations occur as well.

Reconstruction of the horseshoe vortex position

The original vector fields of the PIV measurements may contain spurious vectors; therefore, any analyses on an instantaneous level suffer from missing or unreliable data. The POD, however, is a powerful tool to reconstruct the instantaneous velocity fields using the spatial modes $\Phi(x)$ and the corresponding time coefficients $a(t)$ according to eq. 7.7. Using these reconstructed instantaneous velocity fields, the position of the HV centre and the corresponding joint PDF was determined. In order to detect vortex structures, the so-called *Q-criterion* was applied (Jeong & Hussain, 1995). The Q-criterion is defined as $Q = \frac{1}{2}(\Omega^2 - S^2)$, with S and Ω as the symmetric and antisymmetric part of the velocity gradient tensor, respectively. If $Q > 0$, the rate of rotation dominates the strain rate and vice versa. The positions of the maximum value of Q is then assumed to coincide with the HV centre.

In the flat-bed case, the Q-criterion was successfully applied to detect the HV centre. However, in the scour hole, the Q-criterion was not an appropriate measure to extract the
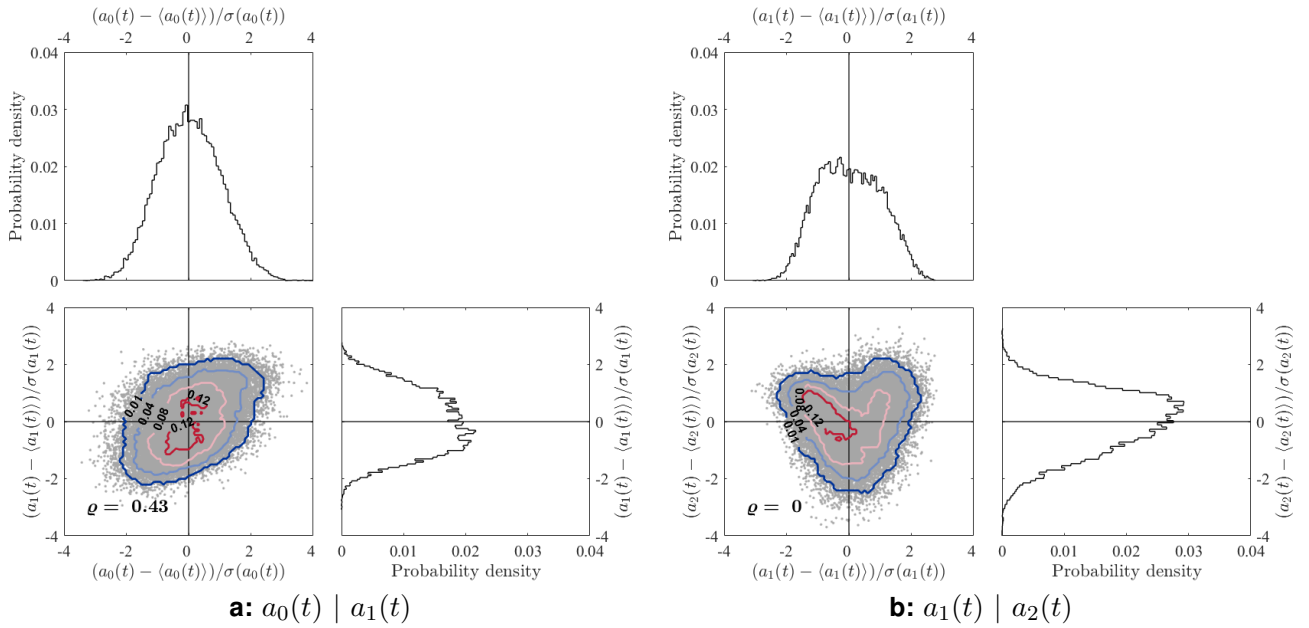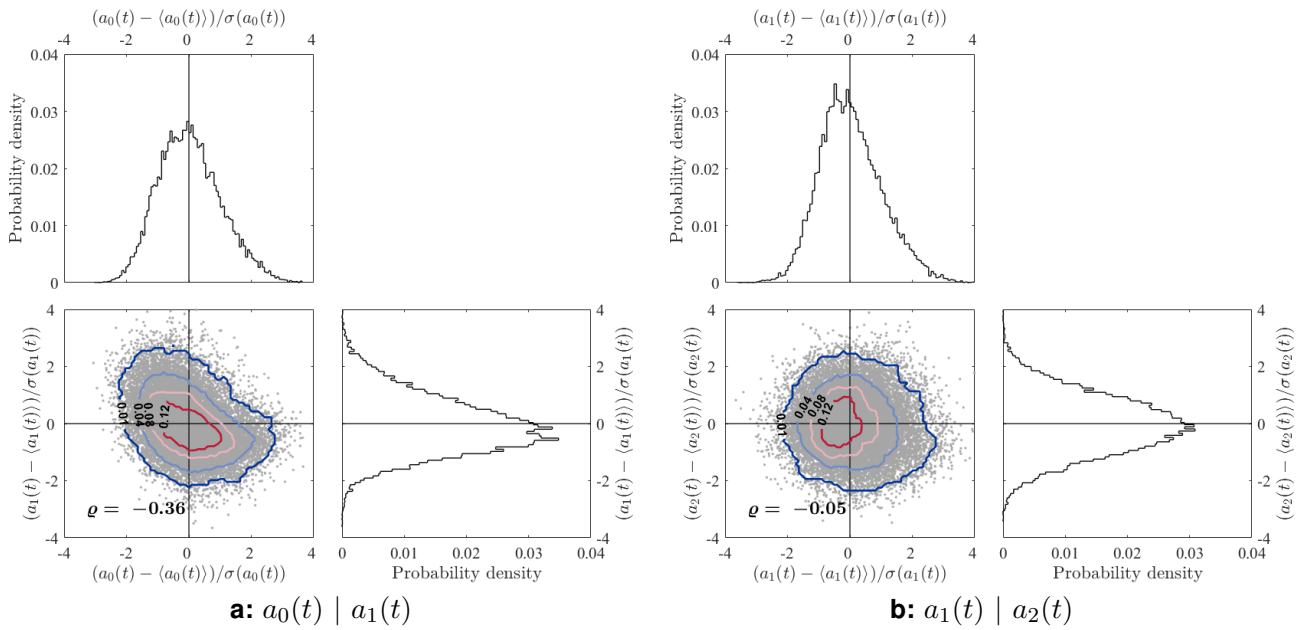
Figure 7.41: (Joint) probability density functions of the POD time coefficients of the zeroth and first mode (left) and of the first and second mode (right) in front of the scoured cylinder

positions of the HV centre. Instead of the instantaneous HV positions, vortical structures in the approaching shear layer were detected indicating the Kelvin-Helmholtz vortices. In order to detect the HV, an alternative method was applied by assuming the centre of the HV to be characterised by a zero in-plane velocity magnitude. The point of intersection of the corresponding zero isolines of the velocity components was, therefore, considered to coincide with the centre of the HV. From the coordinates of the points of the intersection (scour) or of the points with the maximum value of Q (flat-bed) the joint PDFs of the position of the HV centre were derived. The results represent the most likely positions of the HV, the extend as well as the main direction of the vortex oscillations that have occurred with a certain probability.

Figures 7.43 show the jPDFs of the coordinates of the HV centre for the flat-bed (a) and the scour (b) set-up. The number of modes reconstructing the instantaneous velocity fields corresponded to that representing 90% of the cumulative energy. Thus, 360 modes in the flat-bed case and 29 modes in the scour set-up (see Table 7.5). The jPDFs are normalized such that their integrals equal to one. The isolines of the jPDFs represent the probability levels 0.05, 0.1 and 0.15, respectively. Additionally, the centre of the HV obtained from the time-averaged velocity fields is indicated by the cross symbols. The elliptical shape and the orientation of the jPDF indicate that the HV oscillates mainly parallel to the bounding wall in both flow configurations. The extend of the wall-parallel movements is about $4 - 5$ times larger than the range of the wall-normal oscillations, according to the size of the elliptical $0.05-$isoline. The principal axis of this probability contour has in both cases (flat-bed and scour) approximately the same length ($0.16D$); therefore, the HV appears to oscillate to the same extend irrespectively of the inclination of the bounding wall.

The most likely location of the HV is within the $0.15-$isoline. In front of the wall-mounted
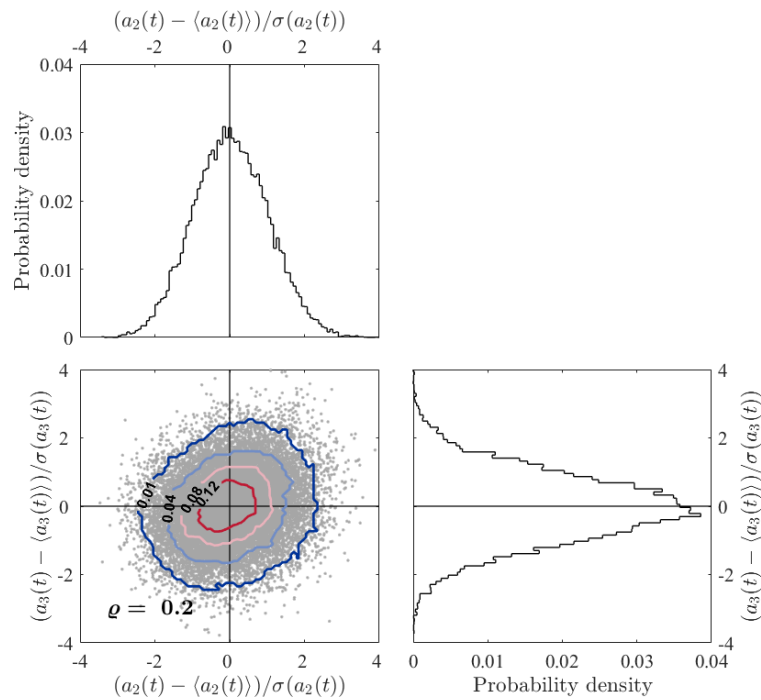
Figure 7.42: (Joint) probability density functions of the POD time coefficients of the second and third POD mode in front of the scoured cylinder

cylinder, the time-averaged position is off-centred in the upstream direction with respect to this isoline, which indicates that the HV is mainly located slightly downstream of its time-averaged position. Inside the scour hole, however, the time-averaged HV centre is located slightly downhill of the centre of the $0.15-$isoline revealing that the most likely location of the HV is uphill its time-averaged location.

a: Flat-bed   **b:** Scour 0°
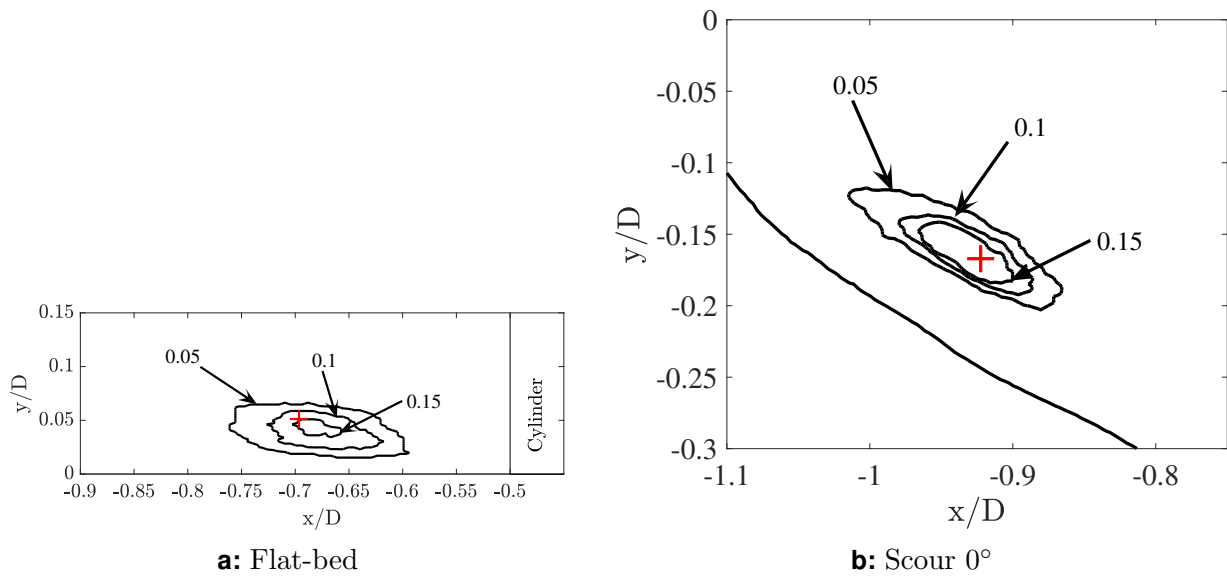
Figure 7.43: Joint PDF of the horseshoe vortex centre in the symmetry plane in front of a wall-mounted cylinder (left) and of a scoured cylinder (right) at $Re = 39,000$. Crosses indicate the time-averaged position of the HV centre.

8 Conclusions

8.1 Main Results

In order to measure and analyse the flow around a scouring cylinder experimentally, a stereo-scopic particle image velocimetry (Stereo-PIV) set-up was designed in the hydraulic laboratory of the Professorship of Hydromechanics at the Technical University of Munich. A scour model based on the geometry measured by Pfleger (2011) was used to represent an eroded sand bed of a bridge pier. The present study focusses on observing the flow structure inside a given scour hole and how this flow structure changes with respect to the initial state, i.e. a cylinder on a flat plate. Therefore, the flow in the symmetry plane in front of a wall-mounted cylinder at three Reynolds numbers (Re) $Re = 20,000$, $Re = 39,000$ and $Re = 78,000$ was analysed and compared to the flow in front of a scoured cylinder at $Re = 20,000$ and $Re = 39,000$. Additionally, the flow field inside the scour hole was observed at a lateral position with an 45° angle of rotation with respect to the symmetry plane of the channel. Therefore, data of a fully three dimensional scour set-up with high resolution was obtained, which was to the best of my knowledge not available in the literature so far. Unger & Hager (2007) studied the flow inside a scour hole, too. However, they used a semi-circular cylinder mounted on the side wall of a water channel; thus, the symmetry plane of the cylinder coincided with the side wall of the flume. Afzalimehr *et al.* (2018) measured the flow field inside a scour hole as well by applying an ADV probe, which disturbed the flow.

The approaching flow conditions of the open channel were studied and validated by reference data in the literature as the flow and turbulence structure of the hydraulic boundary condition is of major importance for the structure of a wall-junction flow. In particular, when using water for conducting fluid mechanical experiments, the entry length of the channel is a crucial factor for the generation of a fully developed turbulent boundary layer. When conducting physical experiments, the reproducibility of the hydraulic boundary conditions has to be ensured in order to collect reliable data. Uncertainties introduced by the pump or the varying temperature of the fluid were estimated and the experiments can be reproduced with an uncertainty of $1 - 5\%$, depending on the Re. The number of valid samples of each experiment made it possible to estimate up to the third central moment of the probability density functions of the velocities with an error of less than 5%.

PIV measurements require the application of a high power laser as a light source, in order to provide high quality particle images. These images are then correlated with each other to determine the most likely displacement vectors of particle clusters. Therefore, surface reflections in wall-junction flows are a source of error because they lower the quality of the particle images; particularly in the region close to the wall, no valid vectors can be obtained when the surface reflections are too strong. Several approaches to treating walls were tested to avoid surface reflections: (i) transmitting material, (ii) light absorbing, and

(iii) fluorescent surface. For the cylinder-on-flat-plate experiments, the camera was mounted perpendicularly at the side of the glass channel. Therefore, a major portion of the light energy passed through the transparent bottom wall, and the remaining reflections occurring at the glass surface did not affect the quality of the particle images. Moreover, the mirrored particle images were used to determine the position of the wall surface in the images with an accuracy of $1 - 2$px. For the scour-experiments, however, the Stereo-PIV was used to observe the flow field inside the three-dimensional scour hole. Therefore, the cameras had to be mounted above the water surface and recorded the scour surface and the light reflections with an 45° angle from above, which resulted in highly disrupted particle images with a strong illumination gradient. The aluminium scour model was black-anodized to absorb the light energy, but a fluorescent Rhodamine B coating also had to be applied as the absorbing effect of the anodized surface was not sufficient.

A companion project that numerically studied the flow around a wall-mounted cylinder by performing a Large-Eddy Simulation (LES) (Schanderl, 2018) was used to validate the corresponding experimental results. The similarity of the PIV and LES results was sufficiently high, and the PIV parameters, such as the interrogation window size, were selected based on the comparison to the LES-results in the symmetry plane of the wall-mounted cylinder. Furthermore, the particle images were analysed using a single-pixel ensemble PIV (SPE) approach developed by Strobl (2017). In contrast to the interrogation window based PIV evaluation, the SPE provides displacement vectors for every single pixel, thus results with a high spatial resolution. These SPE results were additionally used as a reference and validation for the data evaluated by the standard PIV.

The results showed that the flow structure in front of a cylinder, with and without a scour hole present, is similar: the down-flow impinges at the bottom wall and forms a horseshoe vortex (HV) bending around the cylinder. The HV oscillates in both cases parallel to the wall and the bimodality (Devenport & Simpson, 1990) of the wall-parallel velocity component underneath the HV occurred in the scour hole, too. However, in the symmetry plane in the scour hole, this bimodal distribution of the surface-parallel velocity is not as strongly pronounced as in the flat-bed case, and the bimodality becomes more distinct when the HV bends around the cylinder. The distribution of the TKE is c-shaped in both configurations in the symmetry plane as well as at the side of the cylinder, where the amplitude decreases. The lower branch is generated by surface-parallel fluctuations underneath the HV, whereas the TKE peak around the HV centre stems from wall-normal fluctuations induced by oscillations of the HV. These similarities between the Re stresses became visible only after the Cartesian coordinate system of the scour data was transformed into a scour-oriented reference frame. Therefore, the orientation of the coordinate system plays a major role when discussing 'normal' and 'shear' stresses.

The TKE at the wall-mounted cylinder decreases with Re and is mainly produced at the centre of the vortex or underneath the vortex near the wall. In the scour hole, however, the TKE amplitude remains constant with Re due to an additional process contributing to the TKE production. The approaching boundary layer detached at the edge of the scour hole and formed a shear layer, which merged with the horseshoe vortex and introduced a large amplitude of TKE production. This shear layer containing Kelvin-Helmholtz instabilities is one of the main differences between the flow structures in front of a wall-mounted cylinder and a scoured cylinder. Furthermore, the residual of the TKE budget indicated that the

transport of TKE due to pressure fluctuations might be responsible for transporting TKE towards the scour surface. However, these findings are of implicit character as they were derived from the residual and compared to the pressure transport distribution in front of the wall-mounted cylinder by Schanderl *et al.* (2017).

The analysis of the normalized vorticity showed that the distribution and the amplitude are both independent of the Re and that the amplitude in the scour hole is as large as in front of the wall-mounted cylinder. Furthermore, no vortex at the cylinder-wall junction (foot vortex) was observed in the scour hole, whereas in front of the wall-mounted cylinder a strong vortex occurred at the junction.

The dynamics of the HV system in front of the wall-mounted cylinder is strongly governed by the formation of a wall-parallel jet from the point onwards where the down-flow hits the bottom wall. In the scour hole, this jet is not as pronounced and appears to be not as strong as in the flat-bed case. As a consequence, the wall shear stress distribution, which showed a characteristic footprint of the jet (plateau distribution) at the wall-mounted cylinder, is mainly governed by the HV in the scour hole as it revealed a sharp peak underneath the HV centre with a strong gradient before and after. The wall shear stress in front of the wall-mounted cylinder scaled with $\sqrt{Re}$ similar to a laminar boundary layer, whereas the wall shear stress in the scour hole scaled with Re showing that the near wall flow is not laminar. The results of the near-wall flow analysis, however, have to be treated with caution as the wall-resolution of the data might be too coarse, in order to fully resolve the viscous layer.

Finally, a proper orthogonal decomposition (POD) was conducted to identify coherent structures in the flow following the direct as well as the snapshot approach. Since the instantaneous velocity fields of the PIV measurements contained spurious vectors, a novel approach to calculate the correlation tensor ignoring these biased vectors instead of interpolating from the neighbouring data was developed. Therefore, a combined approach was tested to reconstruct the velocity fields using the time coefficients of the snapshot POD and the spatial modes of the direct POD. The reconstructed time series of this method approximated those using both traditional POD approaches. However, a comparison of the corresponding modes showed that such a combined POD approach cannot be recommended in this case, as the number of modes, which could be directly related to each other was too little. Furthermore, the POD on the velocity fields as well as on the fluctuating part only revealed that an additional mode appeared in the latter analysis and that the bimodality of the jet is not indicated using the fluctuating fields. Therefore, the direct POD on the instantaneous velocity fields was conducted and the bimodal behaviour of the jet in front of the wall-mounted cylinder was identified in a single POD mode, but not in front of the scoured cylinder. The second and third POD of both flow configurations revealed even some similarities supporting the conclusion that the flow structure in the scour hole is similar to that in front of a wall-mounted cylinder. Furthermore, the jPDFs of the HV centre in front of both the wall-mounted and the scoured cylinder were derived from reconstructed instantaneous velocity fields using the number of modes covering about 90% of the energy. The analysis revealed that the oscillations of the HV in both configurations are mainly oriented parallel to the bounding wall being about $4-5$ times larger than the wall-normal oscillations and that the extend of the oscillations is similar as well.

8.2 Future Work

Based on the findings of this study, the flow structure inside a scour hole can be linked to the sediment transport processes, which are responsible for the development of the local scour. The wall shear stress and the TKE distribution could be used to set up sophisticated morphodynamic models simulating the erosion process in greater detail. Furthermore, the proability density functions of the velocity components could be used to derive a probabilistic sediment transport model.

Measurements could be performed at higher Reynolds numbers, too, while covering the flow around a scoured cylinder on a finer raster with respect to the angle of rotation and using the experimental set-up outlined in this dissertation. These data would help on one hand to obtain a clearer view on the role of the Re, and on the other hand help to understand the HV dynamics at the side of the cylinder. Additionally, the influence of the pressure fluctuations could be investigated along the cylinder and bottom wall surface to support the hypothesis of the role of the pressure transport in the TKE budget. The Stereo-PIV approach was a useful tool to measure the in-plane instantaneous velocity fields. However, the reliability of the data close to the bounding wall could be further improved by the application of other evaluation techniques, such as the particle tracking velocimetry (PTV) or the single pixel ensemble PIV (SPE). In general, the temporal and spatial resolution of the data could be improved as well, in order to obtain better results concerning the wall shear stress distribution, the dissipation of the TKE, and the time scales of the flow field, which would help to gain a deeper insight into the turbulent processes of a scoured cylinder and the related sediment transport.

Finally, the presented POD analysis revealed coherent structures in the flow and interconnections of the dynamics of the single POD modes. However, this investigation scratched only the surface, as further detailed studies could be carried out on this basis: concerning the heart-shaped structure of the time coefficients of the POD modes #1 and #2 using the data in front of the cylinder on a flat plate, for example. One possibility would be to reconstruct the velocity fields using different combinations of $a_0(t)$, $a_1(t)$ and $a_2(t)$ (and their basis functions $\Phi_k(\mathbf{x})$) that correspond to the three regions of the heart-like structure, e.g. the top left part, which occurs when $a_0' \in [-1; -0.5] \cap a_1' \in [-1; -0.5] \cap a_2' \in [0; 1]$. It is to be expected that corresponding characteristics will occur in the reconstructed instantaneous velocity fields.

Bibliography

ACHENBACH, E. 1968 Distribution of local pressure and skin friction around a circular cylinder in cross-flow up to $re = 5 \times 10^6$. *Journal of Fluid Mechanics* **34** (4), 625–639.

ADRIAN, R. J. 1984 Scattering particle characteristics and their effect on pulsed laser measurements of fluid flow: speckle velocimetry vs particle image velocimetry. *Appl. Opt.* **23** (11), 1690–1691.

ADRIAN, R. J. 1991 Particle-imaging techniques for experimental fluid mechanics. *Annual review of fluid mechanics* **23** (1), 261–304.

ADRIAN, R. J. & WESTERWEEL, J. 2011 *Particle Image Velocimetry*. Cambridge: Cambridge University Press.

AFZALIMEHR, H., MORADIAN, M. & SINGH, V. P. 2018 Flow Field around Semielliptical Abutments. *Journal of Hydrologic Engineering* **23** (2).

ALFAYA, P. 2016 Influence of a top plate on the flow around a wall-mounted cylinder. Master's thesis, Technical University of Munich.

APSILIDIS, N., DIPLAS, P., DANCEY, C. L. & BOURATSIS, P. 2015 Time-resolved flow dynamics and Reynolds number effects at a wall-cylinder junction. *Journal of Fluid Mechanics* **776**, 475–511.

APSILIDIS, N., DIPLAS, P., DANCEY, C. L. & BOURATSIS, P. 2016 Effects of wall roughness on turbulent junction flow characteristics. *Exp. Fluids* **57** (12).

ARMITT, J. & COUNIHAN, J. 1968 The simulation of the atmospheric boundary layer in a wind tunnel. *Atmospheric Environment* **2**, 49–71.

ASHFORTH-FROST, S., DOBBINS, B. N., JAMBUNATHAN, K., WU, XI. & JU, X. 1993 Comparison of interrogation methods for particle image velocimetry. In *Optical Diagnostics in Fluid and Thermal Flow*, , vol. 2005, pp. 478–490. International Society for Optics and Photonics.

ASTARITA, T. & CARDONE, G. 2005 Analysis of interpolation schemes for image deformation methods in PIV. *Experiments in Fluids* **38** (2), 233–243.

AUBRY, N. 1991 On the hidden beauty of the proper orthogonal decomposition. *Theoretical and Computational Fluid Dynamics* **2** (5), 339–352.

BAGHBADORANI, D. A., BEHESHTI, A. & ATAIE-ASHTIANI, B. 2017 Scour hole depth prediction around pile groups: review, comparison of existing methods, and proposition of a new approach. *Natural Hazards* **88** (2), 977–1001.

BAKER, C. J. 1979 The laminar horseshoe vortex. *Journal of Fluid Mechanics* **95** (2), 347–367.

BAKER, C. J. 1980 The turbulent horseshoe vortex. *Journal of wind engineering and industrial aerodynamics* **6**, 9–23.

BERKOOZ, G., HOLMES, P. & LUMELY, J. L. 1993 The proper orthogonal decomposition in the analysis of turbulent flows. *Annual Reviews of Fluid Mechanis* **25**, 539–575.

BLANCKAERT, K., DUARTE, A. & SCHLEISS, A.J. 2010 Influence of shallowness, bank inclination and bank roughness on the variability of flow patterns and boundary shear stress due to secondary currents in straight open-channels. *Advances in Water Resources* **33** (9), 1062–1074.

BREUSERS, H. N. C., NICOLLET, G. & SHEN, H. W. 1977 Local Scour Around Cylindrical Piers. *Journal of Hydraulic Research* **15** (3), 211–252.

BRUNS, J., DENGEL, P. & FERNHOLZ, H. H. 1992 Mean flow and turbulence measurements in an incompressible two-dimensional turbulent boundary layer. Part I: data. *Tech. Rep.*. Herman-Föttinger-Institut für Thermo- und Fluiddynamik, TU Berlin.

CANNY, J. 1986 A computational approach to edge detection. *IEEE Transactions on pattern analysis and machine intelligence* **PAMI-8** (6), 679–698.

CAO, X., LIU, J., JIANG, N. & CHEN, Q. 2014 Particle image velocimetry measurement of indoor airflow field: A review of the technologies and applications. *Energy and Buildings* **69**, 367–380.

CHABERT, J. & ENGELDINGER, P. 1956 *Étude des affouillements autour des piles de ponts*. Chatou, France: Laboratoire National d'Hydraulique.

CHEN, H., REUSS, D.L. & SICK, V. 2012 On the use and interpretation of proper orthogonal decomposition of in-cylinder engine flows. *Measurement Science and Technology* **23** (8).

CLAUSER, F.H. 1954 Turbulent boundary layer in adverse pressure gradients. *Journal of the Aeronautical Sciences* **21**, 91–108.

COPPERSMITH, D. & WINOGRAD, S. 1990 Matrix Multiplication via Arithmetic Progressions. *J. Symbolic Computation* **9**, 251–280.

COUNIHAN, J. 1969 An improved method of simulating an atmospheric boundary layer in a wind tunnel. *Atmospheric Environment* **3**, 197–214.

DARGAHI, B. 1989 The turbulent flow field around a circular cylinder. *Experiments in Fluids* **8** (1-2), 1–12.

DEMUREN, A. O. & RODI, W. 1984 Calculation of turbulence-driven secondary motion in non-circular ducts. *Journal of Fluid Mechanics* **140**, 189–222.

DEVENPORT, W. J. & SIMPSON, R. L. 1990 Time-dependent and time-averaged turbulence structure near the nose of a wing-body junction. *Journal of Fluid Mechanics* **210**, 23–55.

DEY, S. & RAIKAR, R. V. 2007 Characteristics of horseshoe vortex in developing scour holes at piers. *Journal of Hydraulic Engineering* **133** (4), 399–413.

DEY, S., RAIKAR, R. V. & ROY, A. 2008 Scour at Submerged Cylindrical Obstacles under Steady Flow. *Journal of Hydraulic Engineering* **134** (1), 105–109.

ESCAURIAZA, C. & SOTIROPOULOS, F. 2011 Reynolds Number Effects on the Coherent Dynamics of the Turbulent Horseshoe Vortex System. *Flow, Turbulence and Combustion* **86** (2), 231–262.

ETTEMA, R. 1976 Influence of Bed Material Gradation on Local Scour.

ETTEMA, R., KIRKIL, G. & MUSTE, M. 2006 Similitude of Large-Scale Turbulence in Experiments on Local Scour at Cylinders. *Journal of Hydraulic Engineering* **132** (1), 33–40.

ETTEMA, R., MELVILLE, B. W. & BARKDOLL, B. 1998 Scale Effect in Pier-Scour Experiments. *Journal of Hydraulic Engineering* **124** (6), 639–642.

FERNHOLZ, H. H. & FINLEY, P. J. 1996 The incompressible zero-pressure-gradient turbulent boundary layer: an assessment of the data. *Progress in Aerospace Sciences* **32**, 245–311.

FINNIGAN, J. 2000 Turbulence in plant canopies. *Annual Review of Fluid Mechanics* **32** (1), 519–571.

GESSNER, F. B. 1973 The origin of secondary flow in turbulent flow along a corner. *Journal of Fluid Mechanics* **58** (01), 1.

GOODMAN, JOSEPH W 2005 *Introduction to Fourier optics*. Roberts and Company Publishers.

GOVERNMENT OF QUEENSLAND (AUS) 2013 *Bridge Scour Manual*, 1st edn. Department of Transport and Main Roads, State of Queensland, Australia.

GRAYSON, K, DE SILVA, CM, HUTCHINS, N & MARUSIC, I 2018 Impact of mismatched and misaligned laser light sheet profiles on PIV performance. *Experiments in Fluids* **59** (1), 2.

HJORTH, P. 1975 Studies on the nature of local scour. PhD thesis, University of Lund.

HUANG, H.T., FIEDLER, H.E. & WANG, J.J. 1993*a* Limitation and improvement of PIV. Part 1. *Experiments in Fluids* **15** (3), 168–174.

HUANG, H.T., FIEDLER, H.E. & WANG, J.J. 1993*b* Limitation and improvement of PIV. Part 2. *Experiments in Fluids* **15** (3), 263–273.

VAN DE HULST, H.C. 1957 *Light scattering by small particles*. Courier Corporation.

JAMBUNATHAN, K., JU, X.Y., DOBBINS, B.N. & ASHFORTH-FROST, S. 1995 An improved cross correlation technique for particle image velocimetry. *Measurement Science and Technology* **6** (5), 507.

JENKINS, F. A. & WHITE, H. E. 2001 *Fundamentals of Optics*, 4th edn. McGraw-Hill.

JENSSEN, U., SCHANDERL, W. & MANHART, M. 2016*a* Cylinder wall junction flow: Particle Image Velocimetry and Large Eddy Simulation. In *11th International ERCOFTAC Symposium on Engineering Turbulence Modelling and Measurements*. Palermo.

JENSSEN, U., STROBL, C. & MANHART, M. 2016*b* High resolution Particle Image Velocimetry near-wall measurements of non-equilibrium flow at a wall-mounted cylinder. In *11th European Fluid Mechanics Conference*. Seville.

JEONG, J. & HUSSAIN, F. 1995 On the identification of a vortex. *Journal of Fluid Mechanics* **285**, 69–94.

KÄHLER, C.J., SCHOLZ, U. & ORTMANNS, J. 2006 Wall-shear-stress and near-wall turbulence measurements up to single pixel resolution by means of long-distance micro-PIV. *Experiments in Fluids* **41**, 327–341.

KÄHLER, C. J., SCHARNOWSKI, S. & CIERPKA, C. 2012 On the uncertainty of digital PIV and PTV near walls. *Experiments in Fluids* **52** (6), 1641–1656.

KARSTENS, T & KOBS, K 1980 Rhodamine b and rhodamine 101 as reference substances for fluorescence quantum yield measurements. *The journal of physical chemistry* **84** (14), 1871–1872.

KEANE, R. D. & ADRIAN, R. J. 1992 Theory of cross-correlation analysis of PIV images. *Applied Scientific Research* **49**, 191–215.

KESHAVARZI, A., SHRESTHA, C. K., MELVILLE, B., KHABBAZ, H., RANJBAR-ZAHEDANI, M. & BALL, J. 2018 Estimation of maximum scour depths at upstream of front and rear piers for two in-line circular columns. *Environmental Fluid Mechanics* **18** (2), 537–550.

KIRKIL, G. & CONSTANTINESCU, G. 2010 Flow and turbulence structure around an instream rectangular cylinder with scour hole. *Water Resources Research* **46** (11).

KIRKIL, G. & CONSTANTINESCU, G. 2015 Effects of cylinder Reynolds number on the turbulent horseshoe vortex system and near wake of a surface-mounted circular cylinder. *Physics of Fluids* **27** (7).

KIRKIL, G., CONSTANTINESCU, G. & ETTEMA, R. 2005 The Horseshoe Vortex System Around a Circular Bridge Pier on Equilibrium Scoured Bed. In *World Water and Environmental Resources Congress* (ed. American Society of Civil Engineers).

KIRKIL, G., CONSTANTINESCU, G. & ETTEMA, R. 2008 Coherent Structures in the Flow Field around a Circular Cylinder with Scour Hole. *Journal of Hydraulic Engineering* **134** (5), 572–587.

KUNDU, P. K. & COHEN, I.M. 2004 *Fluid Mechanics*, 3rd edn. Elsevier Academic Press.

LAURSEN, E. M. & TOCH, A. 1956 Scour around bridge piers and abutments. *Tech. Rep.*. Iowa Institute of Hydraulic Research.

LINDON, J. C., TRANTER, G. E. & KOPPENAAL, D. 2016 *Encyclopedia of spectroscopy and spectrometry*. Academic Press.

LINK, O. 2006 Untersuchung der Kolkung an einem schlanken, zylindrischen Pfeiler in sandigem Boden. PhD thesis, Technische Universität Darmstadt.

LINK, O., PFLEGER, F. & ZANKE, U. 2008 Characteristics of developping scour-holes at sand-embedded cylinder. *International Journal of Sediment Research* **23**, 258–266.

LIU, K. & HAWORTH, D.C. 2011 Development and Assessment of POD for Analysis of Turbulent Flow in Piston Engines. In *SAE Technical Paper*. SAE International.

LUMLEY, J.L. 1967 *Atmospheric Turbulence and Radio Wave Propagation*, chap. The structure of inhomogeneous turbulent flows, pp. 166–178. Moscow: Nauka.

MARTINUZZI, R. & TROPEA, C. 1993 The Flow Around Surface-Mounted, Prismatic Obstacles Placed in a Fully Developed Channel Flow. *Journal of Fluids Engineering* **115** (1), 85–92.

MELLING, A. 1997 Tracer particles and seeding for particle image velocimetry. *Measurement Science and Technology* **8**, 1406–1416.

MELVILLE, B. W. & CHIEW, Y. M. 1999 Time scale for local scour at bridge piers. *J. Hydraul. Eng.* **125** (1), 59–65.

MELVILLE, BRUCE W. & COLEMAN, STEPHEN E. 2000 *Bridge Scour*. Highlands Ranch, USA: Water Resources Publications, LLC.

MELVILLE, B. W. & RAUDKIVI, A. J. 1977 Flow characteristics in local scour at bridge piers. *Journal of Hydraulic Research* **15** (4), 373–380.

MELVILLE, B. W. & SUTHERLAND, A. J. 1988 Design method for local scour at bridge piers. *Journal of Hydraulic Engineering* **114**, 1210–1226.

MONIN, A. S. & YAGLOM, A. M. 2007 *Statistical fluid mechanics: mechanics of turbulence*, , vol. 1. Courier Corporation.

NOGUEIRA, J., LECUONA, A. & RODRÍGUEZ, P. A. 1999 Local field correction PIV: on the increase of accuracy of digital PIV systems. *Experiments in Fluids* **27** (2), 107–116.

OERTEL, H. JR., BÖHLE, M. & REVIOL, T. 2015 *Strömungsmechanik-für Ingenieure und Naturwissenschaftler*, 7th edn. Berlin Heidelberg New York: Springer-Verlag.

PAIK, J., ESCAURIAZA, C. & SOTIROPOULOS, F. 2007 On the bimodal dynamics of the turbulent horseshoe vortex system in a wing-body junction. *Physics of Fluids* **19**, 045107.

PATERNA, E, MOONEN, P, DORER, V & CARMELIET, J 2013 Mitigation of surface reflection in PIV measurements. *Measurement Science and Technology* **24** (5).

PFLEGER, F. 2011 Experimentelle Untersuchung der Auskolkung um einen zylindrischen Brückenpfeiler. PhD thesis, Technische Universität München, german.

PICKERING, C. J. D. & HALLIWELL, N. A. 1984 Laser speckle photography and particle image velocimetry: photographic film noise. *Appl. Opt.* **23** (17), 2961–2969.

POPE, S. B. 2013 *Turbulent Flows*, 11th edn. Cambridge University Press.

PRASAD, A. K. 2000 Stereoscopic particle image velocimetry. *Experiments in Fluids* **29** (2), 103–116.

PRASAD, A. K. & JENSEN, K. 1995 Scheimpflug stereocamera for particle image velocimetry in liquid flows. *Applied Optics* **34**, 7092–7099.

QI, M., LI, J. & CHEN, Q. 2016 Comparison of existing equations for local scour at bridge piers: parameter influence and validation. *Natural Hazards* **82** (3), 2089–2105.

QUEZADA, M., TAMBURRINO, A. & NIÑO, Y. 2018 Numerical simulation of scour around circular piles due to unsteady currents and oscillatory flows. *Engineering Applications of Computational Fluid Mechanics* **12** (1), 354–374.

RAFFEL, M., WILLERT, C. E., SCARANO, F., KÄHLER, C. J., WERELEY, S. T. & KOMPENHANS, J. 2018 *Particle Image Velocimetry : A Practical Guide*, 3rd edn. Springer International Publishing AG.

RAFFEL, M., WILLERT, C. E., WERELEY, S. T. & KOMPENHANS, J. 2007 *Particle Image Velocimetry : A Practical Guide*, 2nd edn. Berlin, New York: Springer.

RAPP, C. 2009 Experimentelle Studie der turbulenten Strömung über periodische Hügel. PhD thesis, Technische Universität München, german.

RAUDKIVI, A. J. & ETTEMA, R. 1983 Clear-water scour at cylindrical piers. *Journal of Hydraulic Engineering* **109**, 338–350.

RAUPACH, M. R. 1981 Conditional statistics of Reynolds stress in rough-wall and smooth-wall turbulent boundary layers. *Journal of Fluid Mechanics* **108**, 363–382.

RENNIE, S. E., BRANDT, A. & FRIEDRICHS, C. T. 2017 Initiation of motion and scour burial of objects underwater. *Ocean Engineering* **131**, 282–294.

RESCH, G. A. & BÖSNER, H. J. T. 1821 *Die Steinerne Brücke zu Regensburg*. Stadtamhof, Regensburg: Schaupp.

REYNOLDS, O. 1883 An Experimental Investigation of the Circumstances Which Determine Whether the Motion of Water Shall Be Direct or Sinuous, and of the Law of Resistance in Parallel Channels. *Philosophical Transactions of the Royal Society of London* **174**, 935–982.

REYNOLDS, O. 1895 On the dynamical theory of incompressible viscous fluids and the determination of the criterion. *Philosophical Transactions of the Royal Society of London* **186**, 123–164.

RICHARDSON, E. V. & DAVIS, S. R. 2001 Evaluating scour at bridges. *Tech. Rep.*. National Highway Institute.

ROSTAMY, N., SUMNER, D., BERGSTROM, D.J. & BUGG, J.D. 2012 Local flow field of a surface-mounted finite circular cylinder. *Journal of Fluids and Structures* **34**, 105–122.

ROTTA, J. C. 2010 *Turbulente Strömungen-eine Einführung in die Theorie und ihre Anwendung*, *Göttinger Klassiker der Strömungsmechanik Bd. 8*, vol. 8. Göttingen: Universitätsverlag Göttingen.

ROULUND, A., MUTLU SUMER, B., FREDSOE, J. & MICHELSEN, J. 2005 Numerical and experimental investigation of flow and scour around a circular pile. *Journal of Fluid Mechanics* **534**, 351–401.

SCARANO, F. & RIETHMULLER, M. L. 1999 Iterative multigrid approach in PIV image processing with discrete window offset. *Experiments in Fluids* **26** (6), 513–523.

SCARANO, F. & RIETHMULLER, M. L. 2000 Advances in iterative multigrid PIV image processing. *Experiments in Fluids* **29** (1), S051–S060.

SCHANDERL, W. 2018 Large-Eddy Simulation of the flow around a wall-mounted cylinder. PhD thesis, Technische Universität München, München.

SCHANDERL, W., JENSSEN, U., STROBL, C. & MANHART, M. 2017 The structure and budget of turbulent kinetic energy in front of a wall-mounted cylinder. *Journal of Fluid Mechanics* **827**, 285–321.

SCHANDERL, W., JENSSEN, U., STROBL, C. & MANHART, M. 2018 Reynolds scaling of outer and inner flow in front of a wall-mounted cylinder. *Unpublished-Submitted to Journal of Fluid Mechanics on 08 May 2018*.

SCHANDERL, W. & MANHART, M. 2016 Reliability of wall shear stress estimations of the flow around a wall-mounted cylinder. *Computers and Fluids* **128**, 16–29.

SCHLICHTING, H. & GERSTEN, K. 2006 *Grenzschicht-Theorie (German Edition)*. Springer.

SCHUSTER, U., QUOSDORF, D., RITTER, K. & MANHART, M. 2015 Surface reflection of 3D scour models in Particle-Image-Velocimetry experiments. In *10th Pacific Symposium on Flow Visualization and Image Processing*. Naples.

SCIACCHITANO, A. & SCARANO, F. 2014 Elimination of PIV light reflections via a temporal high pass filter. *Measurement Science and Technology* **25** (8).

SHIELDS, A. 1936 Anwendung der Ähnlichkeitsmechanik und der Turbulenzforschung auf die Geschwiebebewegung. *Mitteilungen der Preußischen Versuchsanstalt für Wasserbau und Schiffbau* **36**.

SHIRHOLE, A. & HOLT, R. 1991 Planning for a comprehensive bridge safety program. *Tech. Rep.* 1290. Transportation Research Board, National Research Council.

SIMPSON, R. L., CHEW, Y. T. & SHIVAPRASAD, B. G. 1981 The structure of a separating turbulent boundary layer. Part 1. Mean flow and Reynolds stresses. *J. Fluid Mech.* **113**, 23–51.

SIROVICH, L. 1987*a* Turbulence and the Dynamics of Coherent Structures, Part I: Coherent Structures. *Quartely of Applied Mathematics* **45**, 561–571.

SIROVICH, L. 1987*b* Turbulence and the Dynamics of Coherent Structures, Part II: Symmetries and Transformations. *Quartely of Applied Mathematics* **45**, 573–582.

SIROVICH, L. 1987*c* Turbulence and the Dynamics of Coherent Structures, Part III: Dynamics and Scaling. *Quartely of Applied Mathematics* **45**, 583–590.

STANISLAS, M. & MONNIER, J.C. 1997 Practical aspects of image recording in particle image velocimetry. *Measurement Science and Technology* **8**, 1417–1426.

STROBL, C. 2017 Single Pixel Particle Image Velocimetry for Measurements of Two-Dimensional Joint Velocity Distributions. PhD thesis, Technische Universität München, München.

SUMER, B. M. & FREDSØE, J. 2006 *Hydrodynamics around cylindrical structures*, *Advanced Series on Ocean Engineering*, vol. 26. Singapore: World Scientific.

SUMER, B. M. & FREDSØE, J. 2012 *The Mechanics of Scour in the Marine Environment*, 3rd edn., *Advanced Series on Ocean Engineering*, vol. 17. Singapore: World Scientific.

TANAKA, T. & EATON, J. K. 2007 A correction method for measuring turbulence kinetic energy dissipation rate by PIV. *Experiments in Fluids* **42** (6), 893–902.

TISON, L. J. 1940 Érosion autour de piles de pont en rivière. *Ann. des Travaux Publics de Belgique* **41** (6), 813–871.

TOMINAGA, A., NEZU, I., EZAKI, K. & NAKAGAWA, H. 1989 Three-dimensional turbulent structure in straight open channel flows. *Journal of Hydraulic Research* **27** (1), 149–173.

TROPEA, C., YARIN, A. & FOSS, J. F. 2007 *Springer Handbook of Experimental Fluid Mechanics*. Berlin Heidelberg: Springer Science & Business Media.

TRUCKENBRODT, E. 1987 *Lehrbuch der angewandten Fluidmechanik*, 2nd edn. Springer-Verlag.

UNGER, J. 2006 Strömungscharakteristika um kreiszylindrische Brückenpfeiler. PhD thesis, Eidgenössische Technische Hochschule Zürich, german.

UNGER, J. & HAGER, W. H. 2007 Down-flow and horseshoe vortex characteristics of sediment embedded bridge piers. *Experiments in Fluids* **42** (1), 1 –19.

WARDHANA, K. & HADIPRIONO, F. C. 2003 Analysis of Recent Bridge Failures in the United States. *Journal of Performance of Constructed Facilities* **17** (3), 144–150.

WEI, T., SCHMIDT, R. & MCMURTRY, P. 2005 Comment on the Clauser chart method for determining the friction velocity. *Experiments in Fluids* **38** (5), 695–699.

WESTERWEEL, J. 1997 Fundamentals of digital particle image velocimetry. *Meas. Sci. Technol.* **8**, 1379–1392.

WESTERWEEL, J. 2008 On velocity gradients in PIV interrogation. *Experiments in Fluids* **44** (5), 831–842.

WESTERWEEL, J., GEELHOED, P. F. & LINDKEN, R. 2004 Single-pixel resolution ensemble correlation for micro-PIV applications. *Experiments in Fluids* **37**, 375–384.

9 Appendix A: Design parameters of the experimental campaigns

Re	20,000	39,000	78,000
b	1.17 m	1.17 m	1.17 m
D	0.1 m	0.1 m	0.16 m
y_0	0.15 m	0.15 m	0.24 m
u_b	0.20 m/s	0.39 m/s	0.49 m/s
u_ref	0.2091 m/s	0.3986 m/s	0.5219 m/s
$u_\mathrm{ref}/u_\mathrm{b}$	1.0455	1.022	1.0651
A	0.1755 m^2	0.1755 m^2	0.2808 m^2
Q	0.035 m^3/s	0.068 m^3/s	0.136 m^3/s
b/D	11.7	11.7	7.3
b/y_0	7.8	7.8	4.875
Fr	0.165	0.32	0.318
Fr_D	0.2	0.39	0.39
$\frac{\Delta y}{D} = \frac{u_\mathrm{b}^2}{2g \cdot D}$	0.02	0.077	0.076
$R_h = \frac{A}{U}$	0.12	0.12	0.17
L/D	200	200	125
L/y_0	133	133	83
L/R_h	167	167	117
L/D_h	41.7	41.7	29.4
c_f	0.0047	0.0041	0.0036
$\lambda^* = 4 \cdot c_f$	0.0187	0.0162	0.0143
Re_h	96,000	187,200	333,200

Table 9.1: Scaling and design of the experimental campaigns

10 Appendix B: Transformation of the Coordinate System

The transformation of the Cartesian coordinate system (black) into a scour oriented one (magenta) is illustrated in Figure 10.1. The angle of rotation φ depends on the position in the scour hole and, thus, is a function of x and has to be determined locally ($\varphi(x)$). When doing so, the wall-normal axis at a certain position might intersect with a neighbouring axis and would lead to disturbing stripes when entire fields of velocities or of Reynolds stresses are rotated. In order to avoid this bias, an average angle of rotation φ_m is taken instead for vector field rotations. However, when computing the wall shear stress distribution (see section 7.6), the exact angle of rotation at each position along the scour surface is computed in order to generate results as accurate as possible.
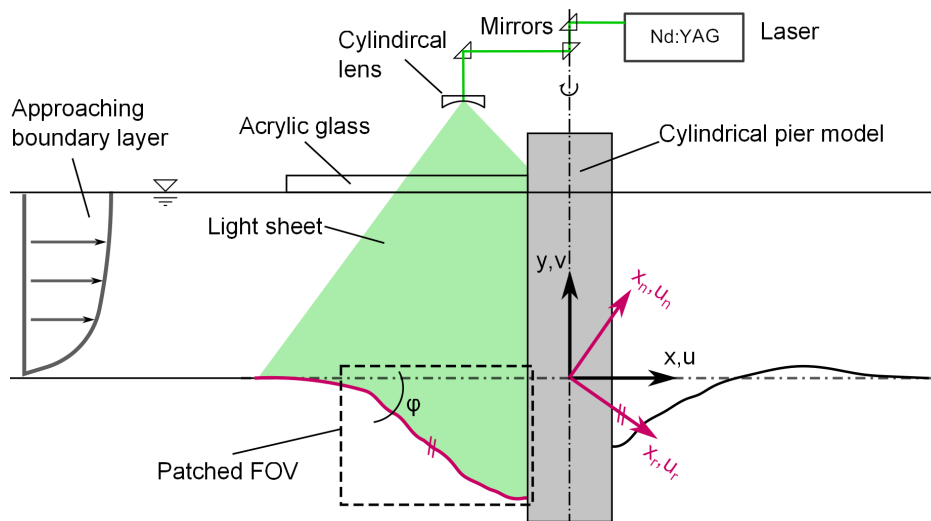

Figure 10.1: Scour oriented coordinate system in the 0° degree case

Following the right-hand rule, the coordinates and the velocity fields resulting from the Stereo-PIV experiments around the scoured cylinder, have to be rotated clockwise, which corresponds to a negative rotation in a mathematical sense. The trigonometric relations for deriving this transformation of a reference frame to another are illustrated in Figure 10.2. The absolute location P in space with respect to a reference point (origin) is a scalar value, whereas reaching point P from the origin is dependent on the coordinate system applied. Based on the sketched trigonometry, the Cartesian system (x_P and y_P) can be transformed

into an arbitrary one ($\hat{x}_P$ and $\hat{y}_P$) as follows:

$$\begin{pmatrix} \hat{x}_{\mathrm{P}} \\ \hat{y}_{\mathrm{P}} \\ \hat{z}_{\mathrm{P}} \end{pmatrix} = \underbrace{\begin{pmatrix} cos\varphi & -sin\varphi & 0 \\ sin\varphi & cos\varphi & 0 \\ 0 & 0 & 1 \end{pmatrix}}_{\text{transformation matrix T}} \begin{pmatrix} x_{\mathrm{P}} \\ y_{\mathrm{P}} \\ z_{\mathrm{P}} \end{pmatrix}. \tag{10.1}$$
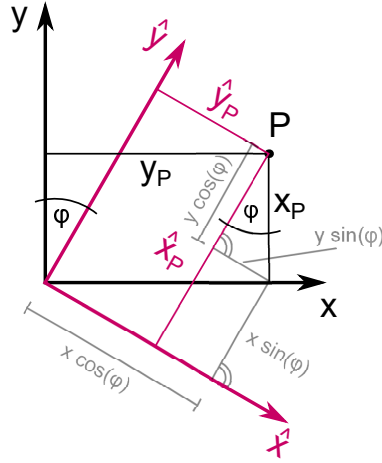

Figure 10.2: Clockwise rotation of a coordinate system

The Cartesian velocity field $\mathbf{u} = (u, v, w)^T$ is rotated accordingly by using eq. 10.1, which results in $\hat{\mathbf{u}} = (u_{\mathrm{r}}, u_{\mathrm{n}}, u_{\mathrm{a}})^T$. The subscripts refer to: i) **radial**, i.e. parallel to the scour surface and pointing towards the centre of the cylinder, ii) **normal** to the scour surface, and iii) **azimuthal**, i.e. parallel to the scour surface, but pointing in the perimetric direction of the cylinder.

Furthermore, the Reynolds normal stresses in the scour-oriented coordinate system are determined by the transformation of the Cartesian fluctuations. Therefore, the Reynolds *normal* stresses in the rotated system (see eq. 10.2 and eq. 10.3) also depend on the Cartesian *shear* stresses due to the second order binomial expansion:

$$u'_{\mathrm{r}} = u'cos\varphi - v'sin\varphi,$$
$$\langle u'_{\mathrm{r}}u'_{\mathrm{r}} \rangle = \left(\langle u' \rangle cos\varphi - \langle v' \rangle sin\varphi \right)^2,$$
$$\langle u'_{\mathrm{r}}u'_{\mathrm{r}} \rangle = \langle u'^2 \rangle cos^2\varphi - 2\langle u'v' \rangle cos\varphi\, sin\varphi + \langle v'^2 \rangle sin^2\varphi, \tag{10.2}$$

$$u'_{\mathrm{n}} = u'sin\varphi + v'cos\varphi,$$
$$\langle u'_{\mathrm{n}}u'_{\mathrm{n}} \rangle = \left(\langle u' \rangle sin\varphi + \langle v' \rangle cos\varphi \right)^2,$$
$$\langle u'_{\mathrm{n}}u'_{\mathrm{n}} \rangle = \langle u'^2 \rangle sin^2\varphi + 2\langle u'v' \rangle cos\varphi\, sin\varphi + \langle v'^2 \rangle cos^2\varphi. \tag{10.3}$$

The shear stress in the radial-normal direction is likewise rotated by applying the transfor-

mation for each contributor separately:

$$\langle u'_\mathrm{r} u'_\mathrm{n} \rangle = \underbrace{(u'cos\varphi - v'sin\varphi)}_{u'_\mathrm{r}} \cdot \underbrace{(u'sin\varphi + v'cos\varphi)}_{u'_\mathrm{n}},$$

$$\langle u'_\mathrm{r} u'_\mathrm{n} \rangle = \left(\langle u'^2 \rangle - \langle v'^2 \rangle\right) cos\varphi\, sin\varphi + \langle u'v' \rangle \left(cos^2\varphi - sin^2\varphi\right). \tag{10.4}$$

However, when the azimuthal component comes into play, the transformation simplifies, as $u'_\mathrm{a} = w'$ (see eq. 10.1):

$$\langle u'_\mathrm{r} u'_\mathrm{a} \rangle = \underbrace{(u'cos\varphi - v'sin\varphi)}_{u'_\mathrm{r}} \cdot w' = \langle u'w' \rangle cos\varphi - \langle v'w' \rangle sin\varphi, \tag{10.5}$$

$$\langle u'_\mathrm{n} u'_\mathrm{a} \rangle = \underbrace{(u'sin\varphi + v'cos\varphi)}_{u'_\mathrm{n}} \cdot w' = \langle u'w' \rangle sin\varphi + \langle v'w' \rangle cos\varphi. \tag{10.6}$$